Mars and Phobos Related Impact Processes:

The formation and degradation of craters in the Northern Lowland Plains and the transfer of Martian material to the surface of Phobos

Jack E. J. Finch

Submitted for the degree of Doctor of Philosophy





Centre for Astrophysics and Planetary Science,
University of Kent,
Canterbury.

Acknowledgements

I would like to thank my supervisor team throughout this PhD project. Firstly, Dr. Penny Wozniakiewicz as not only my supervisor, but also as my undergraduate academic advisor, for the guidance and support over the past 10 years. Dr. Jon Tandy for the guidance and advice with the chemistry applications of the project and for always encouraging my chaos in the lab. Prof. Mark Burchell for the almost limitless advice and guidance on how to navigate the world of academia. Dr. Elliot Sefton-Nash providing a fresh perspective on problems.

I would also like to thank my collaborators Dr. Chrysa Avdellidou and Dr. Detlef Koshcny, as well as the Exolith team for the aid and opportunities provided, as well as making this project a possibility. In terms of academic acknowledgements, I would finally like to thank both the University of Kent and the European Space Agency OSIP scheme for providing the funding allowing me to complete this project. I would also like to thank everyone in 104 who without a doubt made completing a PhD bearable, and the numerous staff within the department. I would also like to thank the Student Support and Wellbeing department at the University of Kent for their support and guidance throughout my time at the university. A special thank you also extends to Dr. Vassilia Spathis as both a friend and colleague for her help with analysing data and for providing greatly appreciated support through very difficult times.

I would like to thank my family for their continued support throughout my time at university and my closest friends for always being there, no matter what (or how often I distract you from work).

A final enormous thank you goes to Tomorrowland, for a lifetime of amazing memories, and the wonderful soundtrack to the many days and night spend writing this thesis.

Selected via the Open Space Innovation Platform (https://ideas.esa.int) as a Co-Sponsored Research Agreement and carried out under the Discovery programme of, and funded by, the European Space Agency. Contract number: 4000139252/22/NL/GLC/my

We are shadows in their eternal light.

Abstract

Despite extensive efforts to study Mars, with more than 40 spacecraft returning data from it to date, our red neighbour remains a subject of intense study within the field of planetary science. The work presented in this thesis focuses on the process of impact cratering at Mars and its moons, conducting experimental impacts using the one and two stage light gas gun at the University of Kent to provide insights into two topics: 1. The quantity of ice within the Northern Lowland Plains on Mars, and 2. The transfer of material to the Martian moon Phobos.

It has long been thought that the morphological features of an impact crater can be related to the surface properties of the target, including whether or not ice is present within it. Past experimental investigations into the influence of target ice content, however, have typically focused on ice-silicate mixtures in the range of $0 - 50$ wt% silicate content. Whilst this may be appropriate for ice-rich bodies in the outer solar system, it leaves a wide range of silicate-dominated mixtures unstudied (ones which may be more appropriate for Mars for example). Here, 80 wt% JSC Mars-1 content targets are impacted with the Kent Light Gas Gun over the velocity range of $1 - 5$ km/s with 1.5 mm diameter spherical copper projectiles. For comparison to this, targets with a 50 wt% content of either JSC Mars-1 or kiln dried sand are impacted over the same velocity range with either 1.5 mm copper of 1.5 mm basalt (for JSC Mars-1 targets) spherical projectiles.

The results of this showed that, whilst little difference is present when considering the size of craters formed in silicate-dominated mixtures compared to those formed in 50 wt% content targets, subtle differences could be observed between the interior morphologies of the produced craters. Additionally, Martian simulant craters formed by the impact of a copper projectile presented central pit features, forming craters similar in appearance to terraced craters on Mars. In contrast, those formed by a basalt projectile showed a linear-to-bowl shaped profile. This suggests that the formation of terraced craters of Mars may be due to the impact of a metallic (i.e., relatively dense) projectile, rather than the properties of the target surface.

To investigate the transfer of Martian material to Phobos, a series of shots was carried out using custom 3D-printed shells containing a europium-doped MGS-1 Martian simulant material. These were fired over a velocity range of $620 - 1620$ m/s into cemented PCA-1 Phobos simulant targets. An ejecta collection system was designed for this series of shots with samples being collected from four shots, whilst two failed to collect a measurable quantity of ejecta. Projectiles are thought to have passed through three distinct stages of emplacement: at the lowest speeds projectiles rebounded producing highly contaminated ejecta, while at higher speeds the projectile was largely emplaced, decreasing the level detected within ejecta and at the highest speeds, projectile material was ejected along with target material. Collected ejecta showed the presence of projectile material with the quantity ranging from $260 - 7833$ ppm. This indicates that the levels of Martian material planned to be detected on Phobos by the future MMX mission may be more localised than previously assumed.

The thesis then concludes by recommending improvements to the design of the various experiments reported, along with suggestions for how the work can be taken further to tackle the questions studied in more depth and detail.

Contents

Acknowledgements i
Abstract i
List of Figures v
List of Tables ix

1 The Geology and Craters of Mars **1**
1.1 Comparative Planetology 2
1.2 The Geological History of Mars 3
1.3 Martian Water 4
1.3.1 Ancient Fluvial Action 5
1.4 Martian Ice and Permafrost 9
1.4.1 Ice Related Morphology 10
1.4.2 Martian Icy Craters 10
1.4.3 Direct Detections of Martian Ice 12
1.5 The Martian Crater Population 12
1.6 Martian Crater Databases 14
1.6.1 Crater Degradation States 16
1.6.2 Abrupt Terminus Ejecta (ATE) Craters 19
1.6.3 Central Pit Craters 22
1.7 Conclusions 22

2 Impact Craters in the Solar System **24**
2.1 Deciphering the Impact Crater 25
2.1.1 The Origin of Crater Investigations 25
2.1.2 Explosive Cratering and Underlying Mechanisms 27
2.1.3 The Crater Formation Process 30
2.2 Contact and Compression 30
2.2.1 Impact Jetting (Ejecta Transport 1) 31
2.2.2 Projectile Unloading 33
2.3 Excavation 34
2.3.1 Shock Wave Propagation 36

2.3.2 The NSIZ and Spallation (Ejecta Transport 2) . . . 36
2.4 Modification . . . 37
2.4.1 Transitional and Complex Craters . . . 38
2.4.1.1 Transitional Craters . . . 39
2.4.1.2 Complex Craters . . . 41
2.4.2 Target Composition and Stratigraphy . . . 41
2.5 Crater Relaxation . . . 42
2.5.1 Effects of Target Viscosity . . . 43
2.6 Conclusions . . . 43

3 Crater Morphology and Volatiles 44
3.1 Crater Morphology . . . 45
3.2 Crater Classifications . . . 45
3.2.1 Transitional and Complex Craters . . . 46
3.2.2 Multi-ring Basins . . . 48
3.3 Crater Ejecta Deposits . . . 49
3.3.1 Abrupt Terminus Ejecta (ATE) Deposits . . . 49
3.3.2 Formation Without Target Volatiles . . . 50
3.3.2.1 Volatile-Rich Projectiles . . . 51
3.3.2.2 Atmospheric Interactions . . . 51
3.4 Central Pit Craters . . . 52
3.4.1 Volatile-Rich Targets . . . 54
3.4.2 Volatile-Enhanced Targets (Mars and Ceres) . . . 55
3.4.3 Volatile-Poor Targets . . . 56
3.4.4 Formation Mechanisms . . . 56
3.4.4.1 Volatile-Based Formation . . . 57
3.4.4.2 Non-Volatile-Based Formation . . . 58
3.5 Central Dome Craters . . . 60
3.6 Conclusions . . . 62

4 Experimental Equipment 63
4.1 Light Gas Gun (LGG) . . . 64
4.1.1 One-Stage Operation . . . 64
4.1.2 Two-Stage Operation . . . 66
4.1.3 Target Placement . . . 67
4.1.4 Projectile Speed calculations . . . 68
4.2 Material Characterisation Techniques . . . 70
4.2.1 X-Ray Fluorescence (XRF) . . . 70
4.2.2 Scanning Electron Microscope (SEM) . . . 73

4.3 conclusions . . . 75

5 Planetary Simulant Materials **77**

5.1 Mars and Phobos Simulant Materials . . . 78
5.2 Experimental Protocol . . . 79
5.2.1 Sample Preparation . . . 80
5.2.2 Ball Milling . . . 81
5.3 Geotechnical Properties of Martian Simulants . . . 81
5.4 Compositional Properties of MGS-1 and PCA-1 Simulants . . . 84
5.5 MGS-1 Geopolymer Reactions . . . 85
5.5.1 MGS-1 Ball Milling . . . 87
5.6 MGS-1 Martian Permafrosts . . . 90
5.7 Chapter Summary . . . 94

6 A Changing Silicate Material **95**

6.1 Ice-Silicate Mixtures in the Laboratory . . . 96
6.2 Experimental Protocol . . . 98
6.2.1 Target Construction . . . 98
6.2.2 Target Analyses . . . 98
6.2.2.1 Depth Profile Processing . . . 99
6.2.2.2 Crater Volumes . . . 100
6.3 Results . . . 101
6.4 Influences of Silicate Type . . . 102
6.4.1 Crater Dimensions . . . 103
6.4.2 Morphological Comparisons . . . 107
6.4.3 Unusual Crater Morphologies . . . 108
6.4.3.1 Shot 2 . . . 108
6.4.3.2 Shot 5 . . . 108
6.4.3.3 Shot 11 . . . 109
6.4.4 Copper or Basalt Projectiles . . . 111
6.5 Silicate-Dominated Mixtures . . . 116
6.6 Conclusions . . . 119

7 The Mysterious Martian Potato **121**

7.1 Presenting the Problem . . . 122
7.1.1 Projectile Emplacement . . . 124
7.2 Method Development . . . 124
7.2.1 Projectile Design Iteration . . . 127
7.2.1.1 Shell Filling Methods . . . 127
7.2.1.2 Shell Lids . . . 129

7.2.2 Target Construction . . . 132
7.3 Results . . . 133
7.4 Crater Analysis . . . 133
7.5 Ejecta Analysis . . . 135
7.6 Conclusions . . . 138

8 Conclusions **140**
8.1 Introduction to the Thesis . . . 141
8.2 Simulant Materials . . . 141
8.3 Impacts into Varying Simulants . . . 142
8.4 Phobos . . . 143
8.5 Possible Future Improvements in Experimental Design . . . 144
8.6 Topics for Further Investigation . . . 146
8.7 Closing Remarks . . . 148

Bibliography **149**

A Chapter 6 Depth Profiles **175**
A.1 50 wt% Kiln Dried Sand Craters . . . 175
A.2 50 wt% JSC Mars-1 Craters . . . 179
A.2.1 Copper Projectiles . . . 179
A.2.2 Basalt Projectiles . . . 186
A.3 80 wt% JSC Mars-1 Craters . . . 193

List of Figures

1.1 Geological map of Mars . . . 3
1.2 Martian geological timeline . . . 4
1.3 Terrestrial and Martian valley networks . . . 6
1.4 Martian and terrestrial deltas . . . 7
1.5 small-scale signatures of water . . . 8
1.6 Hydrated mineral sights on Mars . . . 9
1.7 A collection of ice-related features . . . 11
1.8 Phoenix Lander excavated trenches . . . 13
1.9 Filtered Martian crater population . . . 15
1.10 Martian crater density distribution . . . 15
1.11 Martian crater population degradation states 1 . . . 17
1.12 Martian crater population degradation states 2 . . . 18
1.13 Degradation states density distributions . . . 19
1.14 Mars crater population ATE craters . . . 21
1.15 Layered ejecta density distributions . . . 22
1.16 Mars crater population central pit craters . . . 23
1.17 Central pit crater density distributions . . . 23

2.1 Lunar surface sketches . . . 26
2.2 Meteor Crater, Arizona . . . 27
2.3 Sedan Nuclear Crater . . . 28
2.4 Terrestrial Craters . . . 29
2.5 Contact and compression . . . 31
2.6 Thin-plate theory of jetting . . . 33
2.7 Spherical impact theory of jetting . . . 34
2.8 Excavation . . . 35
2.9 Simple and complex craters . . . 39
2.10 Transitional crater profiles . . . 40
2.11 Central peak and peak ring craters . . . 41

3.1 Central crater morphologies . . . 46
3.2 Martian central pits . . . 47
3.3 Multi-Ring Basin Examples . . . 49
3.4 Central pit craters in the Solar System . . . 53
3.5 Stage of peak collapse . . . 59
3.6 Central dome crater, Ganymede . . . 61

4.1 Kent light gas gun . . . 65
4.2 Single stage burst disc . . . 66
4.3 Single use nylon LGG piston . . . 67
4.4 Blast tank target holders . . . 67
4.5 Segmented sabot schematic . . . 68
4.6 Projectile velocity measurements . . . 69
4.7 XRF process . . . 71
4.8 Atomic electron transitions . . . 71
4.9 The PANalytical Epsilon3 EDXRF spectrometer . . . 72
4.10 XRF sample holders . . . 73
4.11 Scanning electron microscope . . . 74
4.12 SEM mounting stub . . . 75
4.13 Phobos block mounting method . . . 76

5.1 Mixer mill . . . 82
5.2 Simulant microscopy images . . . 83
5.3 Sieved simulant trends . . . 85
5.4 MGS-1 cement ‘crust’ . . . 86
5.5 Pozzolanic cement testing . . . 87
5.6 MGS-1 paste . . . 88
5.7 MGS-1 ball milling results . . . 89
5.8 Cryogenic vacuum chamber system . . . 91
5.9 Chamber systems . . . 92
5.10 Permafrost analogue test . . . 93

6.1 Depth gauge set-up . . . 99
6.2 Depth Profile Processing Example . . . 100
6.3 Crater Volume Example . . . 101
6.4 Silicate comparison crater diameter . . . 104
6.5 Silicate comparison crater depths . . . 105
6.6 Silicate comparison crater volumes . . . 106
6.7 Silicate comparison radial profiles . . . 107
6.8 Shot 2 impact crater . . . 109

6.9 Shot 2 depth profiles . . . 109
6.10 Shot 5 impact crater . . . 110
6.11 Shot 5 depth profiles . . . 110
6.12 Shot 11 impact crater . . . 111
6.13 Shot 11 depth profiles . . . 111
6.14 Projectile comparison crater diameters . . . 112
6.15 Projectile comparison crater depths . . . 113
6.16 Projectile comparison crater volumes . . . 114
6.17 Projectile comparison average radii . . . 115
6.18 Ice quantity variation crater diameters . . . 116
6.19 Ice quantity variation crater depth . . . 117
6.20 Ice quantity variation crater volumes . . . 118
6.21 Ice quantity variation average radii . . . 119

7.1 Annotated overview of Phobos . . . 123
7.2 Experimental set-up . . . 125
7.3 Ejecta capture cell schematic . . . 126
7.4 First attempt shell filling . . . 128
7.5 Second attempt filling shell . . . 128
7.6 Chemically damaged shells . . . 129
7.7 Lidded shell test . . . 130
7.8 Lidded shell . . . 131
7.9 Pre-impact target surface . . . 132
7.10 Phobos block comparison . . . 133
7.11 Formed Phobos impact features . . . 135
7.12 Shot two projectile debris . . . 136
7.13 shot six projectile debris . . . 136
7.14 Normalised XRF data . . . 138

A.1 Shot 1 depth profiles . . . 175
A.2 Shot 2 depth profiles . . . 176
A.3 Shot 3 depth profiles . . . 177
A.4 Shot 4 depth profiles . . . 178
A.5 Shot 5 depth profiles . . . 179
A.6 Shot 6 depth profiles . . . 180
A.7 Shot 7 depth profiles . . . 181
A.8 Shot 8 depth profiles . . . 182
A.9 Shot 9 depth profiles . . . 183
A.10 Shot 10 depth profiles . . . 184

A.11 Shot 11 depth profiles 185
A.12 Shot 12 depth profiles 186
A.13 Shot 13 depth profiles 187
A.14 Shot 14 depth profiles 188
A.15 Shot 15 depth profiles 189
A.16 Shot 16 depth profiles 190
A.17 Shot 17 depth profiles 191
A.18 Shot 18 depth profiles 192
A.19 Shot 19 depth profiles 193
A.20 Shot 20 depth profile 194
A.21 Shot 21 depth profiles 195
A.22 Shot 22 depth profiles 196
A.23 Shot 23 depth profiles 197
A.24 Shot 24 depth profiles 198
A.25 Shot 25 depth profiles 199
A.26 Shot 26 depth profiles 200

List of Tables

1.1 Martian ATE crater breakdown 20

2.1 Simple-to-complex transition range 38

3.1 Central pit characteristics 53

5.1 Sieve stack parameters 80
5.2 Simulant geotechnical properties 82
5.3 Simulant sieving distribution 84
5.4 Simulant bulk compositions 85
5.5 Milling sample matrix 88

6.1 Past investigative parameters 97
6.2 Target constituent masses 98
6.3 Shot programme results 102

7.1 Shot parameters 134
7.2 Raw XRF results 137

Chapter 1

The Geology and Craters of Mars

"A luminous beacon across the heavens

and connects us all to the very essence of the Universe"

The Voice of Tomorrow

The Mars system presents some of the largest mysteries within planetary science, despite the high level of study the planet has been subjected to. Two of the biggest mysteries within this planetary system are investigated within this thesis. These are the level of ice thought to be present within the Northern Lowlands region of Mars and the origin of the Martian satellites. Impact craters and the crater formation process may provide a means to answer both of these questions. Craters provide a way to investigate the subsurface of planets, reaching depths far beyond those achievable by the current generation of spacecraft [1]. This allows the sub-surface composition to be analysed, and the influence of the sub-surface on crater morphology and size [2–4] provides a means to indirectly investigate the structure and composition. Additionally, during the formation of an impact crater, the projectile and target material become mixed. This occurs through both impactor emplacement contaminating the target surface [5, 6] and the mixing of projectile and target fragments in the formation of ejecta [3, 7]. These processes are thought to be key to understanding the possible origin of the Martian satellites. Thus experimental studies of how projectile material can be mixed into the target during impacts and how it can be carried in ejecta may provide invaluable insight into this mystery.

Before investigating these processes later in this thesis, however, it is useful to consider the geological history and present state of the Martian surface. The remainder of this chapter focuses on this. First a brief discussion of a past Mars where liquid water is thought to have flowed across the surface introduces the extensive collection of hydrological features identified on Mars. The potential influence of this hydrological activity on the current day surface can then be investigated. Next, Mars presents an extensive crater population which has undergone an unparalleled level of investigation. This provides an almost unique opportunity to study the influence of changing sub-surface structures and compositions on recent impact crater morphologies. Whilst this chapter does not introduce the crater formation process or the formation of morphological features thought to be related to the presence of ice (covered in Chapters 2 and 3 respectively), it provides a useful step to understanding the context of the work presented within this thesis. It is thus useful to introduce the general study of Mars here, allowing the formation of impact craters and the morphological features typically associated with volatile materials to be understood within a Martian context.

1.1 Comparative Planetology

Whilst recent in-situ measurements taken by landers and rovers have aided in understanding aspects of Mars, a large portion of its geological history has come from the study of comparative planetology. This area of study forms the core of much of planetary science; focusing on understanding the observed features on a body via our understanding of features elsewhere in the Solar System. In its most basic form for example, comparative planetology has enabled regions of Mars to be relatively dated via crater counting [8, 9]. The simplest assumption within studies of crater populations is that: craters form at the same rate across a planetary surface, therefore no region of a surface should be preferentially cratered [3]. Hence, a surface presenting a higher crater density is assumed to be older

than one possessing a much lower crater density. On Mars, this assumption has been used to date the Northern Lowlands and Tharsis as some of the youngest surfaces on Mars [9], whilst Arabia and Noachis Terrae are identified as being the oldest on the planet [10]. These named regions are shown within the geological map of Mars shown in Figure 1.1. A more complex application of comparative planetology is to investigate the origins of 'familiar'-appearing morphological features across the Solar System. Whilst this has some pitfalls as a method, such as miss-assigning formation mechanisms to an observed feature - e.g. the origin of lunar craters as discussed in section 2.1 - it enables powerful insights to be made; some of which will be discussed in the following chapter.

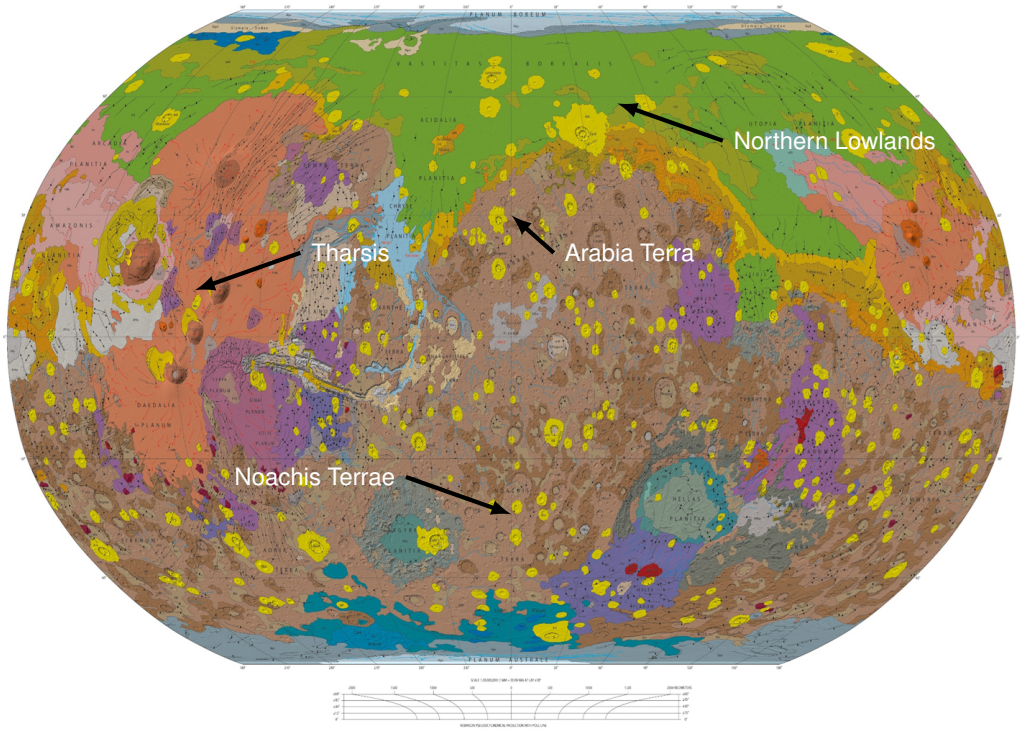

Figure 1.1: Geological map of Mars showing geological units and named regions provided by the USGS [11]. The map provides context to the named regions discussed within this chapter. Named features and regions can be see when zoomed in on the map.

1.2 The Geological History of Mars

The geological history of Earth has been refined over time and follows the chronological rock history record [12]. Defining such a time scale for a planetary surface, allows insight into its evolution. On Mars, however, this record remains largely unavailable for our study. Thus, the geological time scales of Mars have been defined predominantly through the application of observational and inference methods [9, 13, 14]; recent measurements performed by the suite of Mars system spacecraft have allowed this sequence to be further elaborated [8, 13]. Currently, there are two accepted timescales for the geological history of Mars - shown in Figure 1.2. The most recent of these is based on the mineral alteration phases of Mars, linking the geological and climate history together [13]. The

most widely used time scale, however, divides the history of Mars into four geological periods: pre-Noachian, Noachian, Hesperian, and Amazonian in terms of the observed crater density [8, 9]. Not only do these periods present differing levels of impact activity, they also represent varying levels of hydrological activity [8, 13], allowing the fluid history of Mars to be further understood.

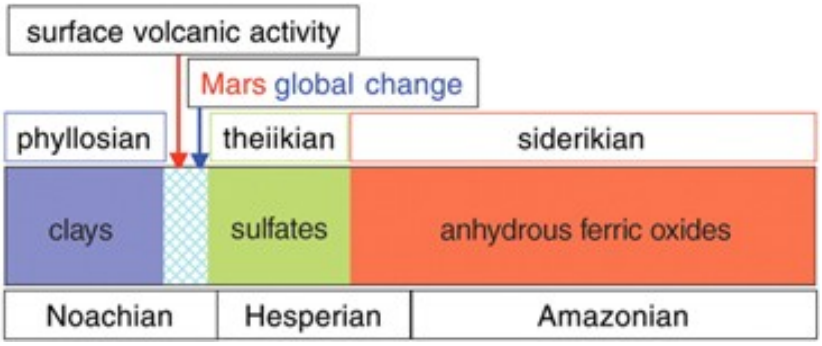

Figure 1.2: Timeline of the geological history of Mars [13] showing the current two timescales for Martian history (oldest on the left, youngest on the right). The top timeline is based on mineral alteration phases identified on Mars [13] whilst the lower timeline is based on the observed intensity of impact activity [8]. The region between the two timelines indicates materials or activities associated with these times.

1.3 Martian Water

Mars presents a complex network of evidence supporting the existence of substantial hydrological activity having shaped the surface in the geological past [8]. One of the most significant, yet enigmatic, features thought to support this is the Martian dichotomy - presenting a scarp boundary between the traditional Southern Highland and Northern Lowland regions [15]. The lowland region (largely consisting of the Vastitas Borealis sedimentary formation [16]) is often thought to represent the remnants of a long dried global ocean [10, 16–19], with the dichotomy boundary thought to represent a paleoshoreline [17, 19]. Studies along the dichotomy boundary have identified a significant number of apparent outflow channels, thought to have transported water from the Southern Highlands into the global ocean [17]. Within several of these, thumbprint terrain and evidence of back-washing is thought to provide evidence for the occurrence of several tsunami events in the history of Mars [10, 18]. When considering a large global Martian ocean, one of the main problems today is where all of the water has gone [17]. Morphological investigations of the Martian crater population, however, show many features supporting the existence of sub-surface ice layers within Mars [16, 20–23] - within craters considerably younger than the proposed global ocean [24–29].

An in-depth discussion on crater morphology relating to the presence of volatiles and their implications can be found in chapter 3 - with a discussion of these as relating to Mars being found in section 1.5 in this chapter. The continually increasing fleet of spacecraft orbiting and landing on Mars has found direct evidence to support the current day presence of volatiles within the near-

surface region of Mars [19, 30–35]. Of these, for the research presented here, a significant early observation was that found by the Phoenix Lander [33, 36]. Instrumentation on the lander capable of digging into the shallow near-surface region uncovered the existence of bright ice deposits in numerous trenches - indicative of relatively pure ice - along with the presence of darker ice deposits within some trenches [36]. Further evidence supporting the current-day presence of water-ice in the Martian near-surface is the indication of hydrogen in neutron spectrometer data [30]. Whilst this may indicate the presence of hydrated minerals (which have been located on the surface of Mars by rover missions [34,35]), it is thought that the most probable explanation for detection of substantial levels of hydrogen across large areas of the Martian surface is the presence of water-ice in these regions [36].

1.3.1 Ancient Fluvial Action

Evidence for past fluid activity over the surface of Mars can be seen on both large and small scales. Whilst orbital images first identified large scale features indicative of fluid activity [17, 18, 21], subsequent analyses by lander and rover missions have further identified medium and small scale indications of a previously flowing liquid [37]; with in-depth chemical analysis by orbital and rover spectroscopic instruments indicating this fluid to have been water [36–38]. The past expanse and nature of this water is not the key focus of the work presented in this thesis, however, it is an important aspect of Martian history to cover when looking to understand the inventory of ice and ice-related features on the surface today. Analysis of the evidence for water having existed on the surface of Mars strongly indicates it to have pooled - forming lakes or oceans [17]. Many of these are thought to have been within craters (crater lakes [21]) and many have inferred the existence of a large global ocean thought to have once filled large portions of the Northern Lowlands region [17, 18]. Evidence supporting this is found on both the largest scales in the form of extensive valley networks dissecting the surface and on the smallest scales with rounded ‘pebbles’ and ‘blueberries’ (iron-rich mm-scale spherules) having been identified by both lander and rover missions.

Viking Lander-era imagery revealed that valley networks on Mars appear to be concentrated in Noachian terrains [8, 40]. The branching appearance of these features (as can be seen in Figure 1.3), mimicking that of terrestrial valley networks, indicates these features to be hydrological in nature [40]. Contrasting with terrestrial valley features, however, Martian valleys are not observed to divide upstream into smaller valley, with valleys smaller than $100\ \mathrm{km}$ being rare [40]. Many valleys on the Martian surface are seen to span several $100's\ \mathrm{km}$ [8, 40]; with some measured to be $< 1000\ \mathrm{km}$ in length [8]. Most of the networks observed in the highlands of Mars are found to be local only [8,40], they are observed to drain into local depressions, rather than water and sediment having been transported to a regional or planetary low [8]. Observed local lows (commonly impact crater features) are seen to possess both inflow and outflow channels [8, 40, 41], with some depressions seen to link chains of valley networks covering $1000 - 4500\ \mathrm{km}$ across the Martian surface extending towards the Northern Lowlands [8]. These chains form a network of valley and channel features too long and complex to have been carved by lava, leading many to assume that the valleys on Mars have been

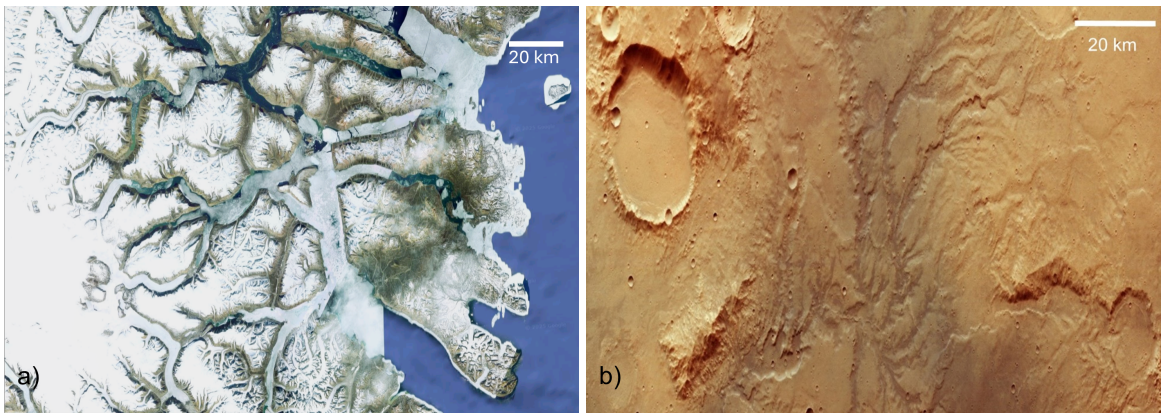

Figure 1.3: a) Terrestrial valley network on the east coast of Greenland located near the Traill Øer island, image courtesy of Google Earth 2024, Airbus Landsat/Copernicus. b) Unnamed dried valley system in the Southern Highlands located to the north of Hellas basin, imaged by the High Resolution Stereo Camera (HRSC) onboard Mars Express, image courtesy of ESA/DLR/FU Berlin [39]. Both networks can be seen to have similar branching (root structure) patterns indicative of features formed through hydraulic actions.

formed by water [8, 17, 40].

Analysis of the ends of these channels on the surface of Mars provides further support for the fluvial nature of these features. Whilst some of the channels leading to local topographic lows are found to be analogous to lunar or Venusian rilles [8], a few of the identified outflow channels are observed to posses features comparable to terrestrial river deltas [8, 42, 43] (see Figure 1.4). Whilst these features are relatively rare [44], their study has the potential to provide unparalleled insights into the past hydrological cycle of Mars [42–45]. Despite their relatively high level of study, uncertainty remains surrounding the formation and implications of deltas on Mars, with much of this arising from their often direct comparison to terrestrial deltas [45]. Their formation is heavily dependent on a delicate balance of parameters [44], the largest being both the type of sediment capable of being deposited and the rate of sedimentation occurring [42, 44]. Some level of indication regarding these can be found through the observed morphology of the river delta [42, 43, 45]. Stepped deltas (morphologically similar to Gilbert Deltas on Earth) are indicative of coarse grain sediment being deposited by a relatively fast flow [43].

A wide fan-shaped delta (such as that in Eberswalde crater, a 65 km diameter Martian crater at 24° S, 33° W), however, is typical of finer grained sediment being deposited by a much slower flow [44, 45]. Further, the relative scarcity of river delta features can also provide insights into past flows over the Martian surface [42–44] (an in depth review on the process of river delta formation is far beyond the scope of this thesis, information on this process can be found within Duy, *et al.* [48] and references within). The lack of delta formation within areas suspected of once possessing lakes on Mars indicates the flow to have been rapid enough to suppress sedimentation [44]. Flows insufficient to fill topographical lows will have also led to either the incision and terracing of deltas [43], or to the suppression of delta formation [44].

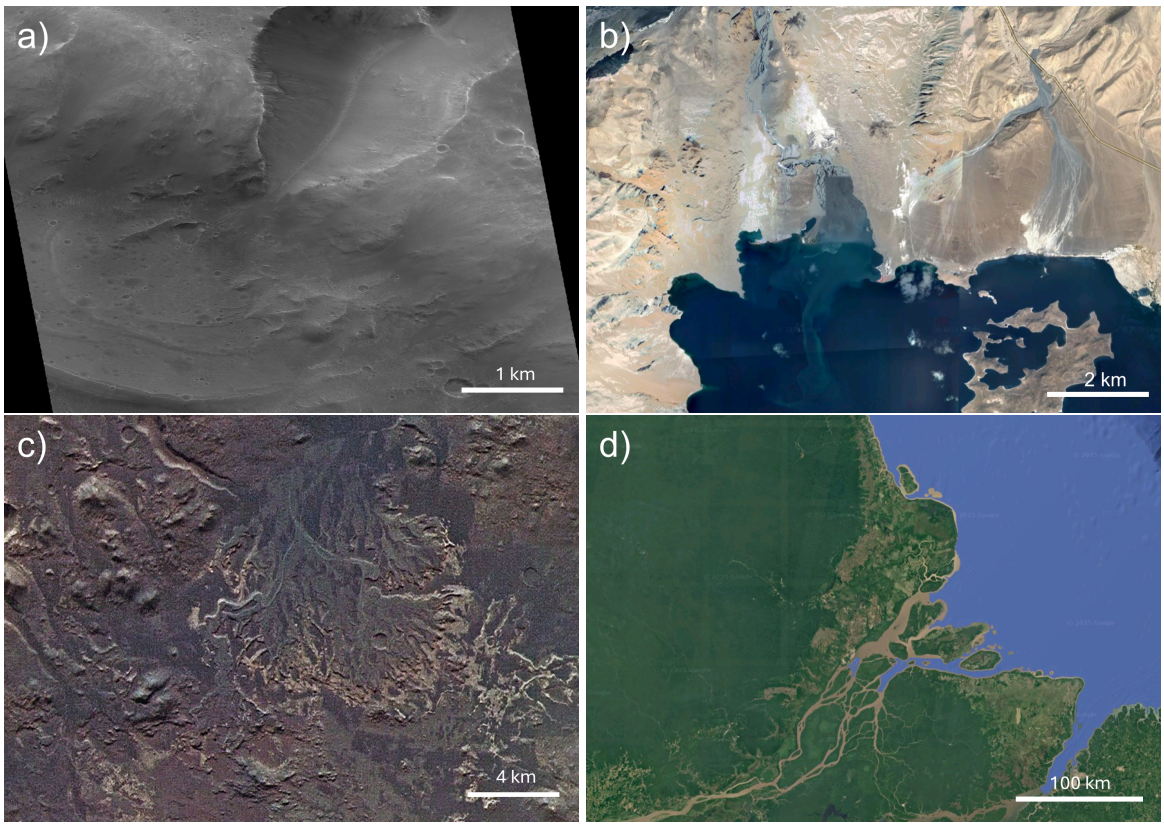

Figure 1.4: Panel a) shows a terraced delta within an unnamed crater imaged by HiRISE [46]. Panel b) shows a Gilbert type delta flowing into Karakul Lake in the Himalayas, image courtesy of Google Earth 2024, Airbus Landsat/Copernicus. Panel c) shows a fan-type delta feeding into Ebserwalde Crater on Mars imaged by Mars Express [47]. Panel d) shows the Amazon river fan-type delta in Brazil, image courtesy of Google Earth 2024, Airbus Landsat/Copernicus.

The exploration of Mars has, to date, largely focused around one variable: the planet's ability to have supported past life. As such, an extremely high level of interest has been paid to the topographical lows thought to once possess lakes, following the water in the attempt to find signs of past life - a key step in astrobiology [49]. The result of this extensive study within several potential paleolakes has been the identification of small-scale features and chemical evidence to support the existence of past liquid water on Mars [34, 37, 50, 51].

The in-depth investigation into the paleolakes identified on Mars has been carried out by the fleet of rover spacecraft that have previously and are currently exploring the surface of Mars. These vehicles, forming a mobile geochemistry laboratory, carry a range of equipment providing the ability to analyse both surface and shallow near-surface deposits [34, 37, 55]. Additionally, their cameras provide a new perspective of geomorphological features, enabling them to be observed from both the ground and different angles rather than solely from above (see Figure 1.5). Their examination of the areas identified from orbit as potential deltas has provided even further evidence for their hydrological nature. Images from both the Curiosity and Perseverance rovers have identified rounded boulders and 'pebbles' (Figure 1.5), similar to smoothed terrestrial rocks formed through their interaction with water [56]. Furthermore, images from channels flowing into topographical lows have identified 'blue-

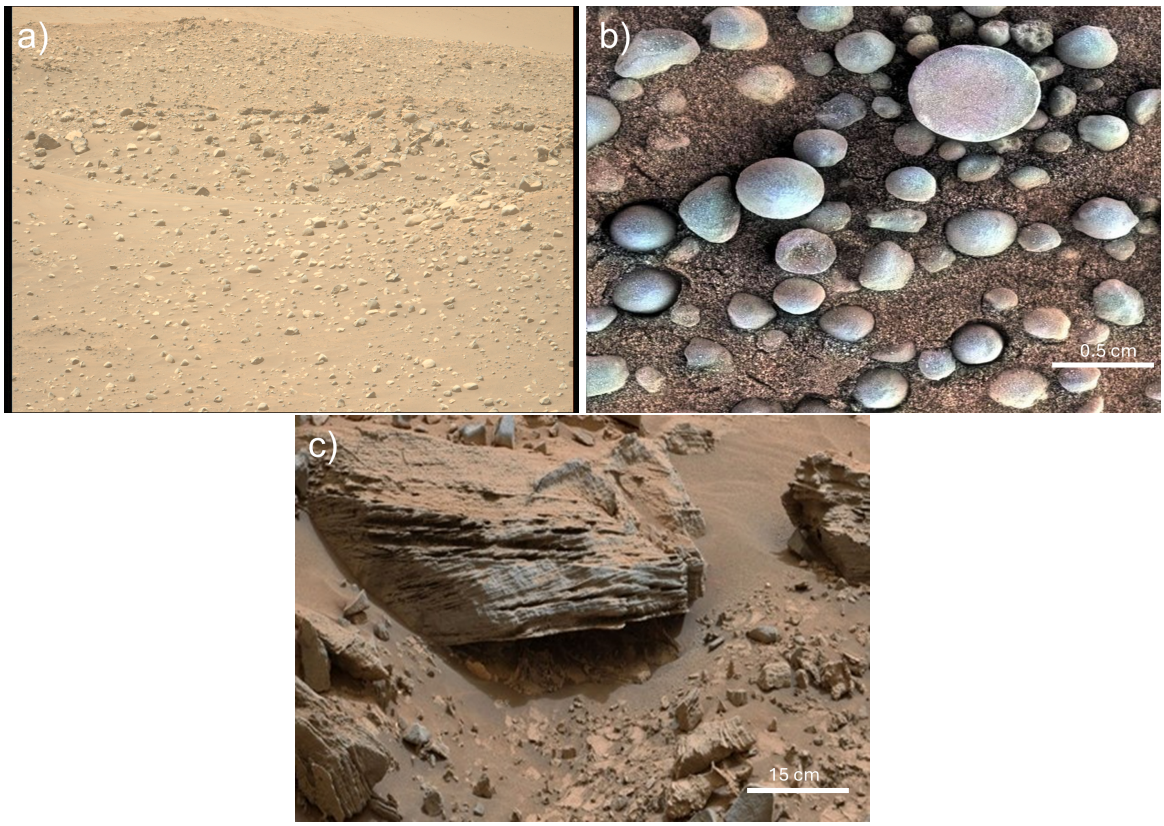

Figure 1.5: Panel a) shows an image captured by the Mastcam onboard Perseverance Rover on Sol 996 [52]. The image appears to show a field of smoothed pebbles that are thought to be indicative of water having once flowed through this region. Panel b) shows an image captured by the microscopic imager and PanCam onboard Opportunity Rover on Sol 84 [53]. The image shows mm-scale features termed blueberries. They are iron-rich spherules thought to form in the presence of water. Panel c) shows an image captured by the Mastcam onboard Curiosity Rover on Sol 796. The image shows cross-bedding identified at the base of Mount Sharp within Gale Crater [54]. Cross-bedding on the scale of 30 cm is thought to be caused by the waves within a body of water carrying sediment material.

berries' (shown in figure 1.5) which are iron-rich spherules on the surface of Mars [57]. Analysis of these morphological features have heavily suggested their formation to require the presence of water. The close-up imaging of rocks surfaces within craters has also revealed the presence of cross-bedding (figure 1.5). Whilst it is possible for this to occur via aeolian and abrasive processes, the scale of cross-bedding seen - particularly within Gale crater - is thought to only be possible through the action of fluid waves [58].

The evidence seen on the surface of Mars shows not only was there once a flowing fluid over the surface, but that it existed in substantial quantities. This leaves us today with two main questions: 1) what was this flowing fluid, and 2) where did it all go? Whilst it has been assumed that the features seen on Mars are due to the action of water, this is not the only possibility. Smoothed 'pebbles' have similarly been identified on the surface of Titan [61]; whilst these are almost certainly the evidence of a fluid having flowed over this surface, the conditions on Titan entirely rule out this fluid having been water. Hence, analysis is required to identify this fluid. This is where the chemical analysis

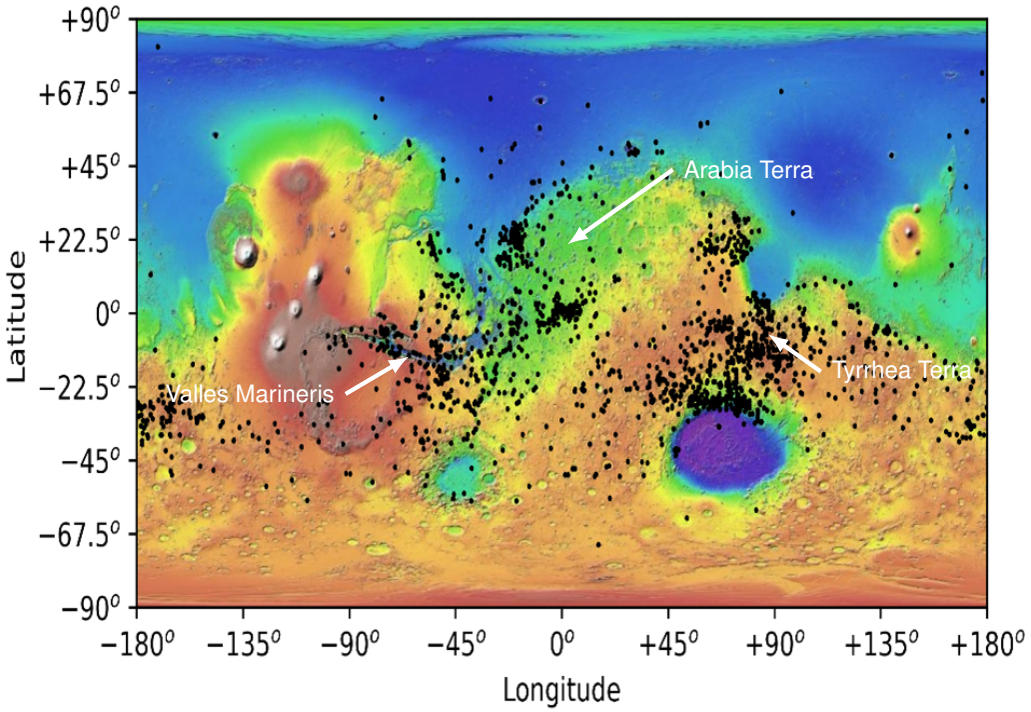

Figure 1.6: Data showing the locations of detected hydrated minerals on the surface of Mars. The data [59] is overlaid on a Mars Orbiter Laser Altimeter (MOLA) height map of Mars [60] to provide geographical context. It shows detected hydrated minerals to be heavily concentrated within the regions of Arabia Terra and Tyrrhena Terra, a concentration can also be seen along Valles Marineris. These concentrations are indicative of the regions having undergone considerable aqueous alteration at some point in the geological history of Mars.

undertaken by landers [36], rovers [34, 37], and orbital spectrometers [59, 62] provide the required information. Analysis has identified numerous hydrated minerals and phyllosilicates on the surface of Mars [59] (see Figure 1.6), especially in regions showing further evidence of hydrological activity [62]. The identification of these minerals, containing water, is highly indicative of the fluid having previously flowed over the surface of Mars to be water. This, however, does not help in answering the second question posed.

1.4 Martian Ice and Permafrost

In order to investigate where the water once present on Mars went, potential sinks for it to have been stored in are required. Whilst identifying hydrated minerals and its loss to space provide two possible sinks [17, 21, 63], neither is thought to be sufficient to account for the quantities required to produce the morphological features seen. Another potential sink for this past water is the presence of ice on and within the Martian surface. The presence of surface and near-surface ice on Mars in non-polar regions was, for a long time, was a contentious topic. Its existence was initially inferred through the analysis of morphological features [64–66] and crater morphologies [23, 67, 68] across the surface

of Mars. Additionally, data collected by synthetic aperture radar and spectrometer instrumentation in orbit around Mars was highly indicative of ice material being present within and underlying the surface. Indirect evidence was further acquired through the appearance of viscously relaxed surface features [69] and the near-surface abundances of hydrogen [70] The debate continued, however, until the direct detection of ice on the surface of Mars. This was accomplished through both the near-surface excavation in the area surrounding the Phoenix lander [36] and through the ejection of sub-surface material during impact crater formation [21, 71]. The phase diagram for ice shows a wide range of ice types can form [72, 73]. For Mars, however, the surface and sub-surface region of Mars is assumed in this work to be analogous to the environment on Earth [73]. Within this work, it is assumed that predominantly hexagonal ice is present on Mars with some cubic ice present at lower temperatures. These detections showed bright deposits of ice to be prevalent throughout the near-surface region of Mars. In addition to this, studies of freshly exposed scarps at mid-latitudes have found fresh ice deposits in the near-surface region [74].

1.4.1 Ice Related Morphology

Many of the morphological features observed on Mars are thought to be indicative of ice within the surface. Whilst some of these features are located within and close to impact features, they are thought to be the result of processes distinct from that of crater formation. Pitted terrain [66], molards [64], pingos [65, 75], and morains [76] are some of the key morphological features on the surface indicative of ice having influenced the terrain - examples are shown in Figure 1.7. The extent and occurrence of these features on the surface of Mars provides evidence for not only the presence of ice, but also to its extent. When combined, they are indicative of not only an ice-rich sub-surface environment, but also one having been influenced by glacial processes. These features are common at higher latitudes [66, 77]. This decrease in occurrence of ice-related features with decreasing latitude is suggestive of either the quantity of ice within the surface decreasing equatorwards, or the cryosphere starting at greater depth.

1.4.2 Martian Icy Craters

The craters on the surface of Mars present an extensive and unique population. Many aspects of the population are thought to be related to the presence of ice on and within the surface of Mars at the time of the impact. Whilst the morphology and formation of these features will be discussed in both chapters 2 and 3 of this thesis, it is important to look at the distribution of these crater morphologies over the surface of Mars and at what they can tell us about the presence of ice within the Martian surface. There are some crater types unique to Mars. These are pedestal craters [82], excess ejecta craters [16], layered ejecta craters [77], and low aspect-ratio layered ejecta (LARLE) craters [68]. Whilst the formation mechanisms behind these craters are not precisely known, the most supported mechanisms behind these unique crater forms are all thought to be related to the presence of volatiles and ice on Mars. The discussion in section 3.3.1 shows that Abrupt Terminus Ejecta (ATE)-appearing

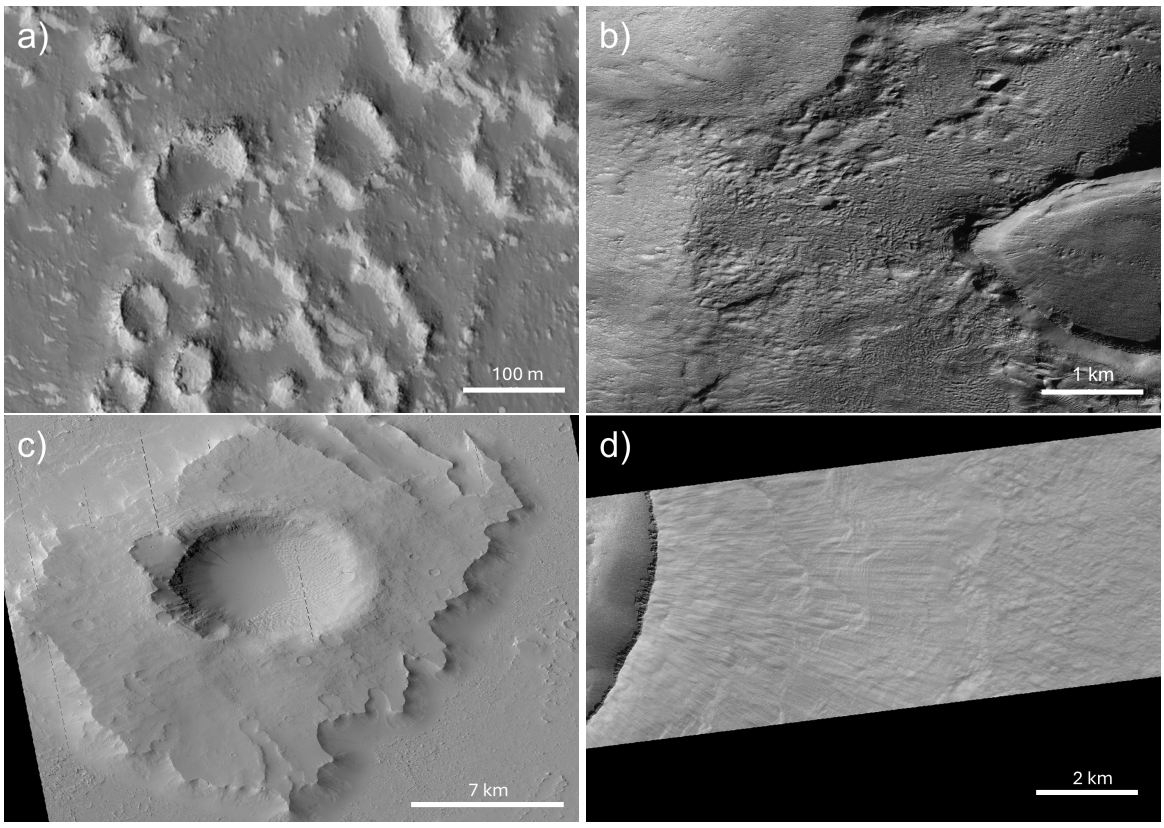

Figure 1.7: Panel a) shows a collection of pingos on the Martian surface [78]. Panel b) shows pitted terrain on the ejecta blanket of an unnamed crater near Reull Vallis to the east of Hellas Basin [79]. Panel c) shows an unnamed pedestal crater within the Amazonis Region on Mars [80]. Panel d) shows a fresh unnamed DL crater in the Northern Lowlands region of Mars [81].

deposits around craters are also often attributed to the presence of volatile materials within the target surface. It is unknown why on Mars they appear possessing layers within the deposits, where they are found to possess either a: single layer (SL), double layer (DL), or multi-layer (ML) morphology [71].

Formation mechanisms for the layering of deposits typically relies on sequential depositional processes [23] - due to the inner layers appearing to overly the outermost ones. This would indicate that material within the Martian crust became fluidised to differing extents during the crater formation process, generating layer boundaries at the extent of each flow. Additionally, interactions between the Martian atmosphere and the propagating ejecta may lead to differentiation of the material, causing its emplacement to be altered [3, 83]. This has been proposed for the formation mechanism behind LARLE craters [68]. These craters possess an extensive, extremely thin outer deposit extending a substantial distance from the crater. It is thought to be the result of base surge processes pushing the fine-grained debris from an ice-rich mantling deposit away from the crater [68]. Impacts into similar mantling deposits are thought to lead to the production of the Martian pedestal craters [25, 82], which have also been suggested to be a heavily degraded form of LARLE craters [68]. These craters stand above the their surrounding terrain, with steep scarps separating the edge of their associated ejecta blanket from the surrounding low-lying plains (similar to terrestrial mesa features). Whilst they possess a morphological similarity to mesas, their formation mechanism is thought to be very different.

Rather than forming via erosion processes, the pedestal crater morphology is suggested to form via terrain deflation. At the time of their formation, it has been assumed that pedestal craters were formed in ice-rich deposits [82]. As the Martian environment was altered over time, the ice within these geological units began to sublimate, ultimately lowering the elevation of the terrain. The ground overlain by the ejecta deposit, however, was protected from this process [25, 82], with the ice remaining trapped within the near-surface material. Thus, it became perched above the now low-lying surrounding region. Suggested to form via the same mechanism but with differing results to this are excess ejecta craters. These are craters whose proximate ejecta volume is considerably greater than their estimated cavity volume [16]. This is suggested to result from terrain deflation after impact into an ice-covered terrain unit, rather than an ice-rich deposit. As such, the ice in the material surrounding the crater was susceptible to subsequent sublimation except where it was protected by the ice-poor ejecta which remained largely unmodified [16, 68]

1.4.3 Direct Detections of Martian Ice

Whilst the morphology of the Martian terrain and its craters are highly suggestive to the presence of ice, it was not until its direct detection that the scientific community could say for certain that this ice was present and was formed by water. As already stated, one of the first detections of ice within the Martian crust came from the Phoenix lander [33]. Throughout the mission, the robotic arm experiment excavated twelve trenches, within eight of which ice was detected [33, 36] (examples of these can be seen in Figure 1.8). Ice within the trenches was found in two forms, bright and dark ice. Spectral analysis of these distinct ice deposits found the bright ice to be relatively pure water-ice whilst the darker ice material is thought to have been in the form of an ice-silicate mixture with an ice content between $20 - 30\ \mathrm{wt}\%$ [36]. This detection and subsequent analysis not only shows that permafrost materials are present close to the Martian surface, but also provides a good approximation for their ice content. These detections, however, are only for the very near-surface region. Whilst other spacecraft have attempted to reach further into the Martian crust, the current explored limit is $< 2\ \mathrm{km}$ in depth with this being reached by radar-based instruments [84, 85]. Hence, for the direct detections of ice material at deeper levels, other features have to be investigated; ones capable of displacing and ejecting material from depths far beyond those reachable by the current fleet of spacecraft on Mars.

1.5 The Martian Crater Population

Covering a large portion of the planet's surface, the crater population of Mars presents a substantial and very useful dataset. The high level of interest surrounding Mars and its past and future habitability mean that this crater population is one of the most heavily studied in the Solar System. Multiple aspects of the population remain current areas of high interest for research (e.g. cratering rates [88], small crater populations [89], interior morphology [17, 90], ejecta distribution [64, 91, 92], crater de-

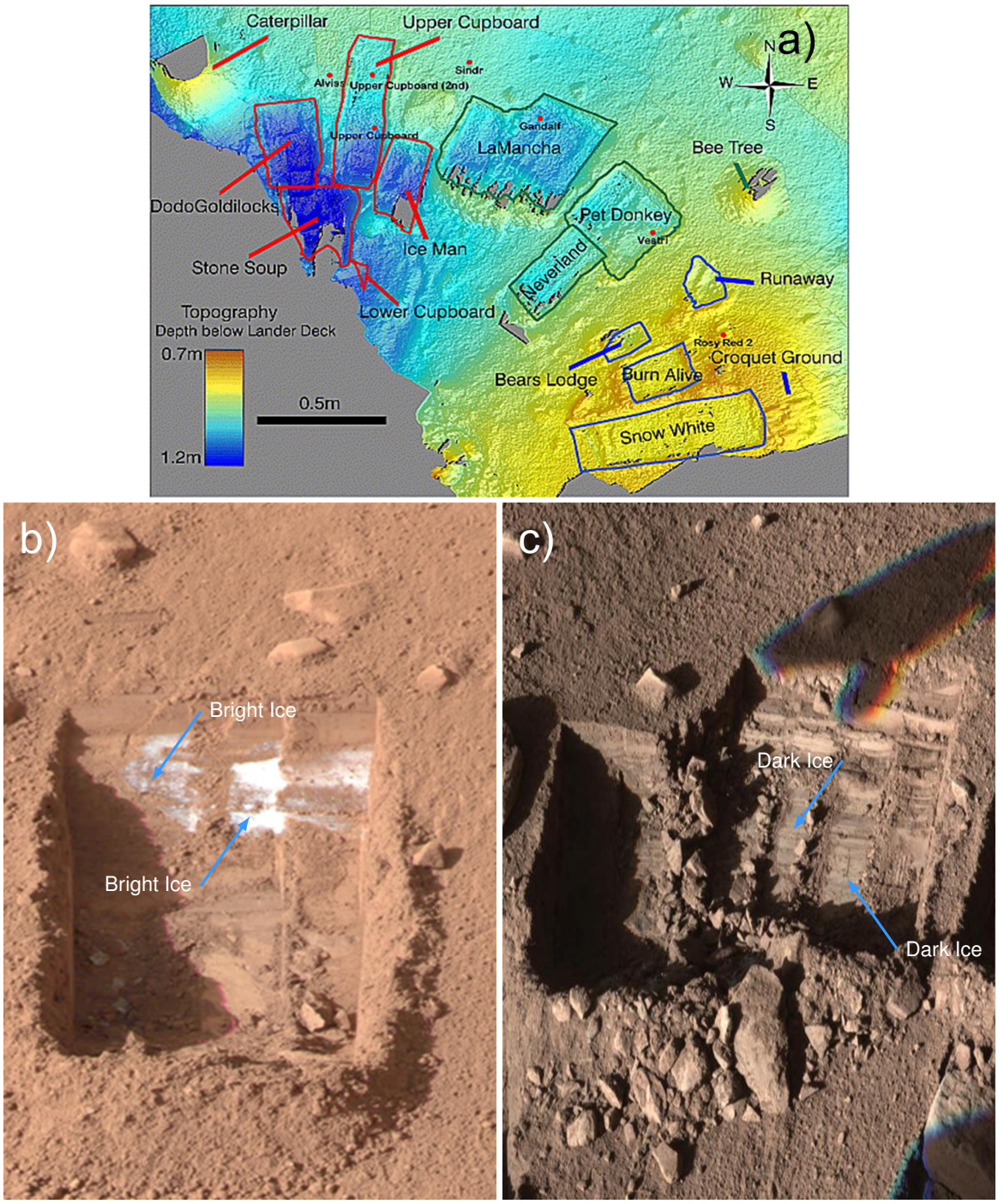

Figure 1.8: Images of trenches excavated by the Phoenix lander. Differences in the brightness of the ice deposits are thought to be due to variations in composition or deposition mechanism [36]. Panel a) shows the location and scale of the trenches excavated throughout the mission with the excavated trenches highlighted and labelled. Panel b) show bright ice deposits within the Dodo-Goldilocks [86] excavated on Sol 20. Panel b) shows dark ice deposits within the La Mancha [87] excavated on Sol 148. Trenches were up to 38 cm long and typically 5 cm in depth.

tection [93], in-situ volatile measurements [37], etc.). Mars presents a unique population of craters possessing features of both rocky and icy targets - see chapter 3. For example, at larger sizes complex craters on Mars are found to follow a unique size-morphology evolution. Central peaks, peak

rings, and central pits are all common on the surface but the central domes that are observed on Ceres, however, are missing. A size-evolution of this nature has led to many suggestions that the near-surface region of Mars contains a substantial level of volatile materials [67]. Additionally, as already stated the ejecta deposits surrounding Martian craters have also come under intense investigation, leading to the identification of crater classes unique to Mars, specifically LARLE [68, 94], Excess Ejecta (EE) [16], and pedestal (Pd) [71] craters.

1.6 Martian Crater Databases

Consisting of a total of $42,284$ craters, the first large-scale database of Martian craters was compiled by N. Barlow in 1988 [95]. More recently, taking advantage of the increased resolution available within newer images of the Martian surface, a new database of the Martian crater population has been compiled by Robbins and Hynek in 2012 [96], containing a total of $384,343$ craters. Overlying MOLA data [60, 97], the population of Martian craters within the 2012 compiled database is shown in Figure 1.9; the population presented in Figure 1.9 has been filtered to only contain craters with both an associated confidence level and degradation state (as assigned by Robbins and Hynek when compiling the database) where the confidence level is a subjective impact-interpretation of the feature and the degradation state is a measure of the crater freshness. Whilst initial observations of the Martian crater population may appear to show a somewhat uniform distribution, particularly within the mid-latitude regions of Mars, important trends can be identified. The most prominent, and most important for the research presented here, is that of the apparent lower crater density within the Northern Lowland region of Mars, commonly attributed to the younger age of the planetary surface in this region [17, 18, 98].

Some caution is needed in analyses of this data set. For example, the boundary between the Northern Lowlands and the higher lands to the south is a region of great interest. Therefore, it has been studied in detail, with many craters being identified. This leads to an apparent increase in the crater flux within this area. Thus, the increased crater density in this area (particularly noticeable within the Martian crater database once filtering has taken place) is likely a simple observation bias. Contrasting the higher crater density along this boundary, several areas in the Southern Highland region can be seen to have substantially lower crater density values. When comparing the crater distribution to the shown MOLA data, many of these regions possessing a decrease in crater density coincide with easily identifiable large impact features e.g. the Hellas and Argyre Basins' which will have overwritten earlier features. However, to the south of the dichotomy, the most extensive region presenting a decreased crater density corresponds to the Tharsis volcanic region. Within Tharsis, several large volcanic features can be identified (including Olympus Mons). As such, the noticeably lower crater density within this region is likely due to extensive resurfacing processes (volcanic resurfacing, sediment deposition, etc.) having occurred at several times during the past.

Figure 1.10 shows the latitudinal and longitudinal crater density (the number of craters per degree)

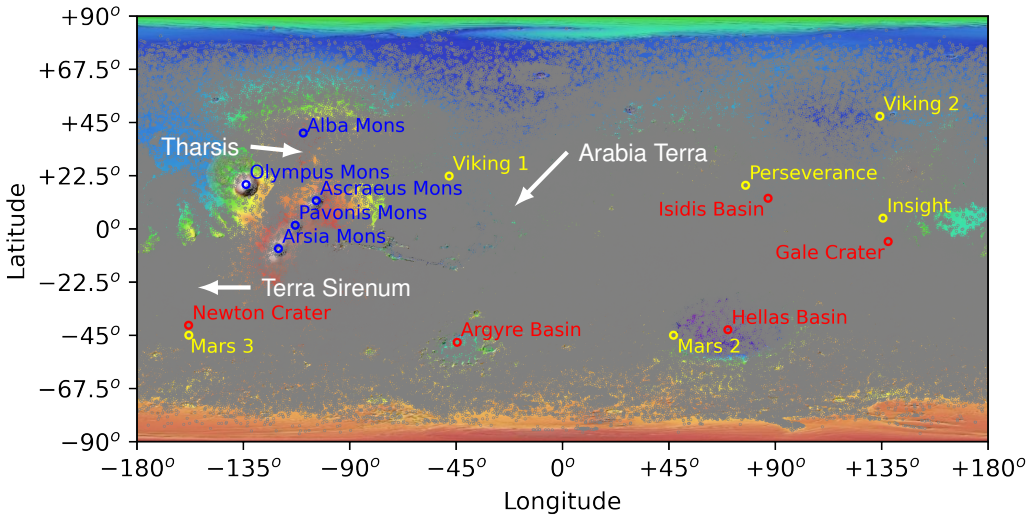

Figure 1.9: Recent database of Martian craters (grey dots) compiled by Robbins and Hynek [96] filtered to contain only craters possessing both a confidence and degradation level. The crater population overlies a MOLA heightmap [60, 97] providing a visual representation of location on the surface of Mars. Additionally, selected volcanic features (blue), large impact features (red), and mission landing sites (yellow) are labelled.

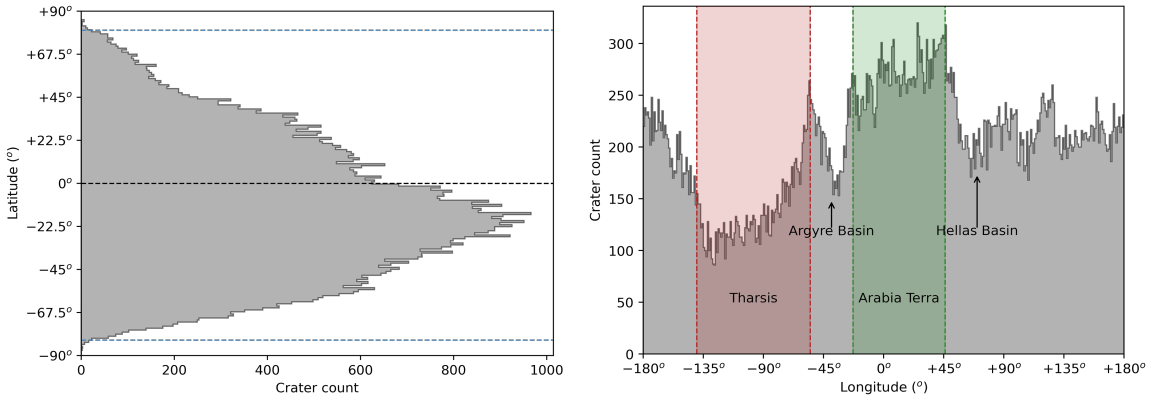

Figure 1.10: Latitudinal (left) and longitudinal (right) distributions of crater density after filtering of the crater database compiled by Robbins and Hynek [96]. Within the longitudinal distribution the regions of Tharsis and Arabia Terra are highlighted (by the red and green regions respectively) along with the Argyre and Hellas impact basins. The relatively low count rate in the Tharsis region is associated with volcanic resurfacing, and the high rate in Arabia Terra presumed to be related to its old age.

distributions for the filtered crater database. Latitudinal trends show a clear preference for craters to be identified within the southern hemisphere of Mars, with a sharp increase seen at $\approx 0°$, and the highest density being seen at $16°$ S. Within both hemispheres, crater density decreases as the latitude increases, with very few craters being seen at latitudes $> 80°$ N or $> 82°$ S (represented by the two blue dashed lines in Figure 1.10). To explain this observed scarcity of identified impact features within the extreme latitude region on Mars, several explanations can be posited. The reduced crater density may simply be an observational bias; with the majority of orbiter missions focusing on regions

close to the equator; a lack of observations at high latitudes may make craters increasingly difficulty to identify. Enhanced shadows (due to a higher Sun-surface angle), however, would aid somewhat in the detection of topographic relief features (e.g. crater rims and pedestal craters). As such, there are likely processes occurring within these high-latitude regions leading to the enhanced removal/degradation of craters. Observations of Mars have shown extensive deposits of polar-ice at both the north and south poles; the extent of which are known to vary over the year. Impacts into this ice layer or a temporarily exposed underlying surface, followed by the subsequent retreat of an ice layer, would lead to the removal of a crater; whilst the advancement of an ice layer over a crater formed within the underlying layer would substantially erode any recognisable topographic features. Thus, the seasonal variation observed in the Martian polar ice deposits is the likely explanation behind the almost complete lack of craters at extreme latitudes in both hemispheres.

Figure 1.10 also shows clear longitudinal crater distribution trends. As stated, reduced crater densities can be seen corresponding to large impact basins on the Martian surface (for example, the Hellas and Argyre impact basins as highlighted in Figure 1.10). By far the largest reduction in crater density for the longitudinal trends, however, corresponds to the Tharsis volcanic region, which is thus likely one of the youngest surfaces on Mars. Contrasting with Tharsis and the large impact features, an increase in crater density can be seen in the Terra Sirenum (located to the south-west of Tharsis) and the Arabia Terra regions. These regions are thought to be some of the oldest on the Martian surface, and therefore the most cratered regions of Mars. However, whilst the crater density on the Martian surface can provide substantial information, highlighting overall trends found on Mars, further categorisation of the Martian crater population can aid in the identification of more nuanced patterns displayed.

1.6.1 Crater Degradation States

The categorisation of the Martian crater population by the assigned degradation state (a description of how this was done can be found in Robbins and Hynek [96]) is shown in Figures 1.11, 1.12, and 1.13. In general, as the level of degradation increases, so does the number of identified craters - with $28,834$ craters being classed as 'most degraded', $17,364$ being classed as 'less degraded', $21,314$ being classed as 'less pristine', and only $6,283$ being classed as 'most pristine'. The number of craters falling into the 'less pristine' category goes against the general trend. Contrasting the identified global trend, the Tharsis region on Mars appears to possess mostly 'less pristine' craters, further supporting this region being one of the youngest on the Martian surface. Additionally, as the degradation level of the craters increases, Figures 1.11 and 1.12 show the extent of the Martian surface covered by the population to increase. Craters classed as being 'most pristine' are found to be located largely in equatorial regions - around the dichotomy boundary; craters classed as 'most degraded', however, cover a substantially larger portion of the Martian surface. This enhanced extent covered by increasingly degraded craters is mostly due to surface age, by may also reflect some enhanced degradation processes occurring within some areas.

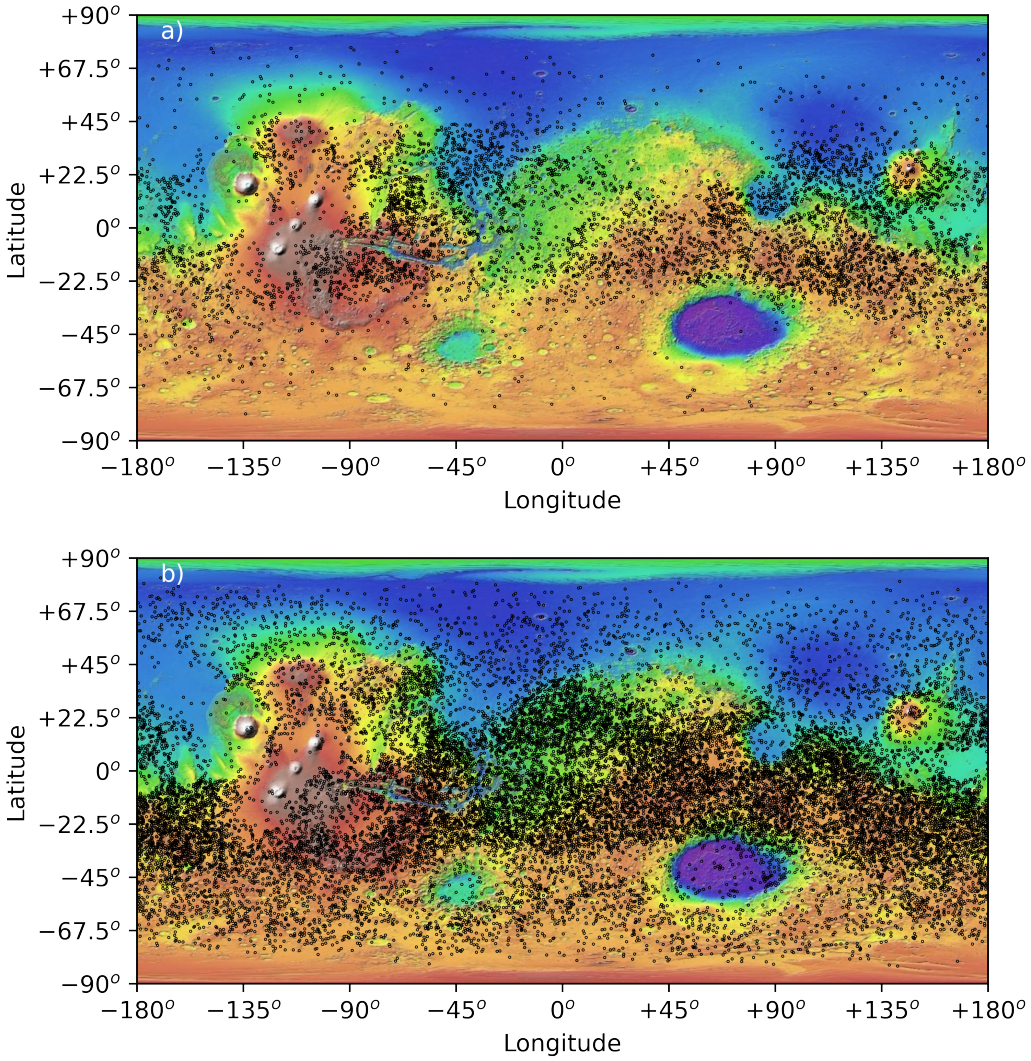

Figure 1.11: Population of Martian craters compiled by Robbins and Hynek [96] categorised by assigned degradation state. a) Craters identified within the database as being the 'most pristine' or freshest craters on the Martian surface, often assumed to be the youngest craters and surfaces. b) Craters identified as being 'less pristine', showing some level of degradation, erosion, or relaxation processes. Continued in Figure 1.12.

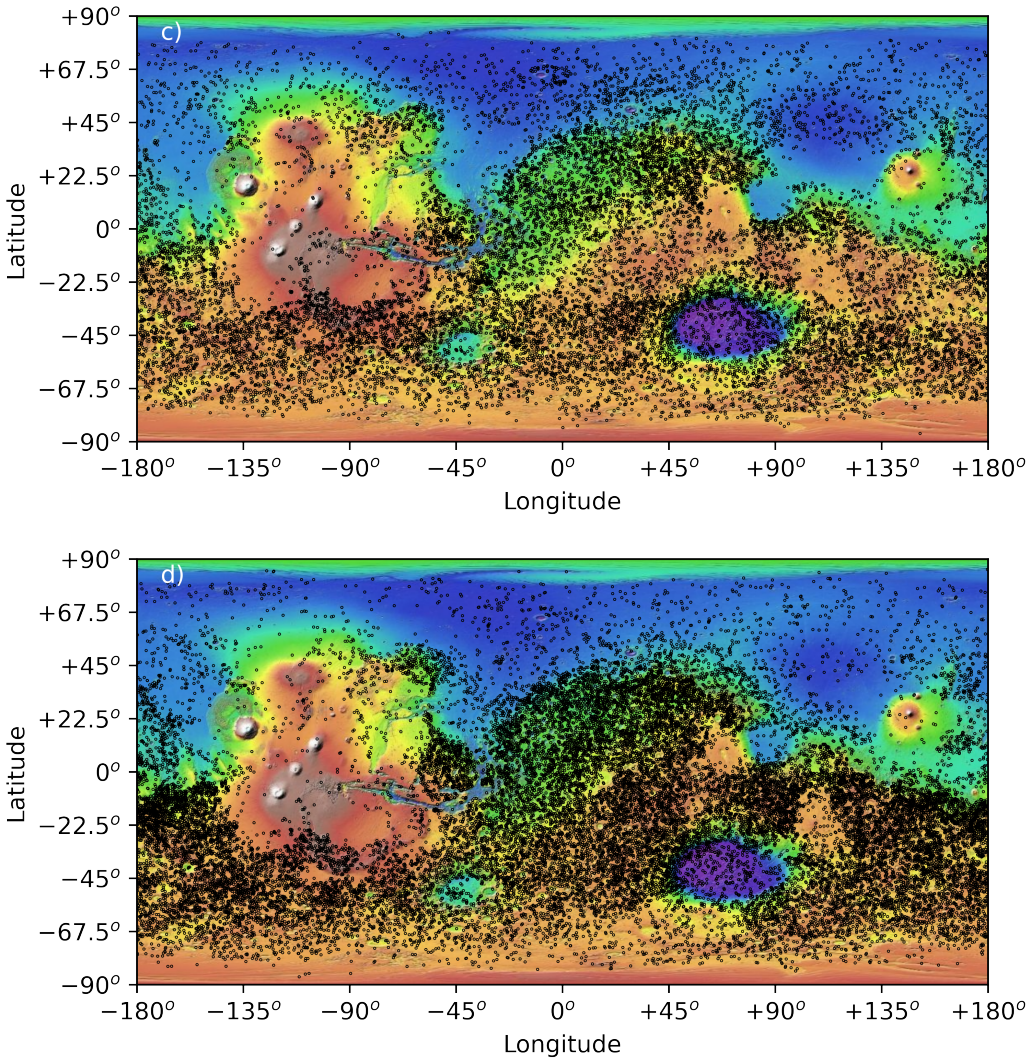

Figure 1.12: Continued from Figure 1.11. Population of Martian craters compiled by Robbins and Hynek [96] categorised by assigned degradation state. c) Craters identified as being 'less degraded'. d) Craters identified as being the 'most degraded', having undergone extensive degradation and/or relaxation processes, often assumed to be the oldest craters and surfaces on Mars

There are, however, some differences in the causes of crater densities and degradation status that are not age related. As stated, the crater population within the Tharsis region, shows an area of Mars with not only very few craters, but a substantial percentage of its crater population is found to be classified as 'most pristine' and 'less pristine'. Consideration must be made, however, when introducing the crater degradation level into estimations of the relative surface age of erosion and relaxation processes occurring on the surface of Mars. Whilst Tharsis is said to be one of the youngest surfaces on Mars, the same arguments can also be applied to the Northern Lowland region. In addition, the numerous volcanoes within the Tharsis region lead to the assumption that throughout this area, the surface of Mars is composed of extensive lava flows, providing a coherent rocky target surface. In comparison, the near-surface region of the Northern Lowland region is thought to be composed largely of permafrost-like material. Hence, the weaker material present in this northern region is likely

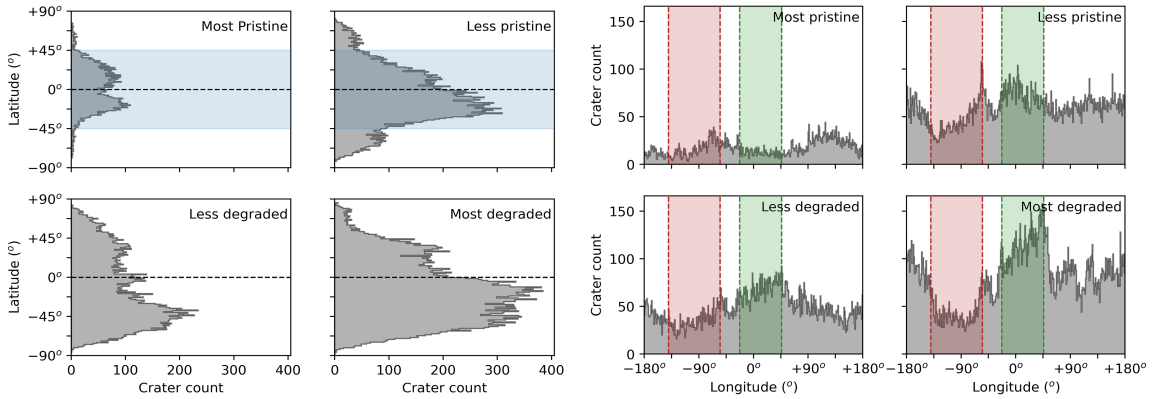

Figure 1.13: Latitudinal (left) and longitudinal (right) distributions of crater density separated by assigned crater degradation state. For most and less pristine craters, they are found to be heavily focused within the mid-latitude region of Mars (the blue shaded region within the figure). Outside of this region, both populations show a sharp decrease in occurrence. The Tharsis (red) and Arabia (green) Terra regions are identified within the longitudinal distributions. The relatively low count rate in the Tharsis region is associated with volcanic resurfacing, and the high rate in Arabia Terra is presumed to be related to its old age.

to enhance degradation processes subjected to formed craters. The lifetime, during which craters are able to be identified within this region, is thus likely to be considerably less than those in other rocky regions. Additionally, the lowland nature of the Northern Plains forms a dust trap for wind-blown material transported across the Martian surface [17]. As such, craters formed throughout this region may become buried by dust or other material at an increased rate.

1.6.2 Abrupt Terminus Ejecta (ATE) Craters

Further categorisation of the Martian crater database allows for the distribution of craters possessing ATE-appearing ejecta deposits to be analysed. From the $73,650$ craters included in the filtered database shown in Figure 1.9, $18,969$ were found to possess ATE-appearing ejecta (the exact breakdown of which - between SL, DL, and ML craters - is given in table 1.1). When considering the distribution of Martian ATE craters, those possessing a higher number of ejecta layers (22%) are noticeably rarer than those possessing only a single layer (78%). Within the population of Martian ATE craters, 90 craters are found to possess four ejecta layers, whilst only five are found to possess five distinguishable layers within their ejecta deposit. Currently accepted formation models for ATE craters require that, for the formation of a DL or ML ATE crater, the impactor must penetrate further into the target surface than for a SL ATE crater. However, if volatile material (thought to be key to the formation of Martian ATE-appearing craters) exists close to the planet surface, DL or even ML ATE craters may form as a result of much smaller impacts - penetrating to a substantially shallower depth. Thus the distribution of ATE-appearing craters on the Martian surface may potentially be used as a observational proxy to indirectly investigate the distribution of volatile materials throughout the

near-surface region of Mars (see Figure 1.15).

Table 1.1: Number of SL, DL, and ML craters within the database compiled by Robbins and Hynek [96].

Ejecta layers	Number of craters
Single layer (SL) craters	$14,577\ (78\%)$
Double layer (DL) craters	$3,290\ (18\%)$
Multiple layer (ML) craters	$829\ (4\%)$

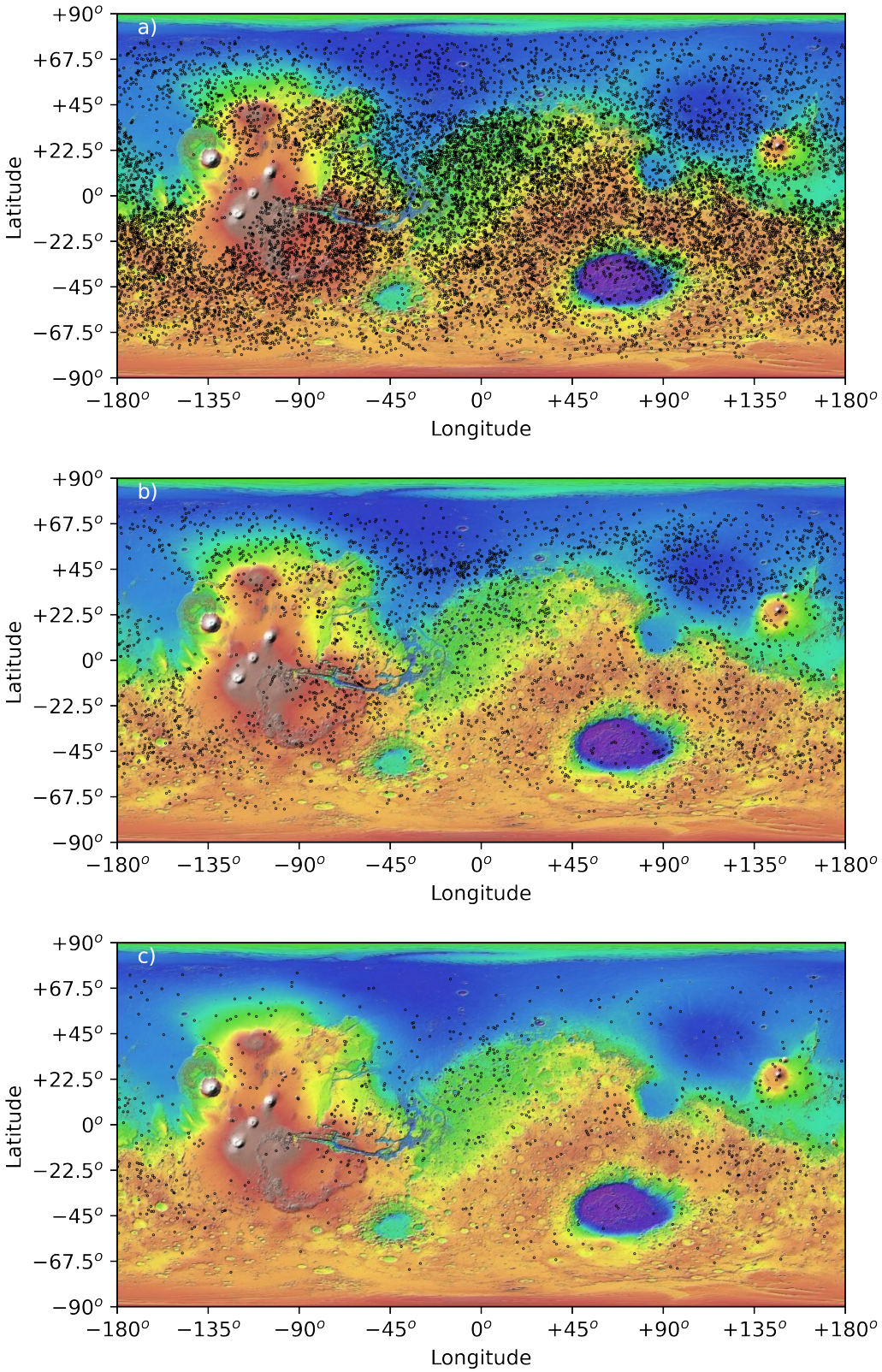

Figure 1.14: Martian crater population separated by distinguishable layers within ejecta deposits. a) Craters identified as having a single layer in their ejecta deposit (SL craters). b) Craters identified as having two layers within their ejecta deposits (DL craters). c) Craters identified as having three or more layers within their ejecta deposits (ML craters).

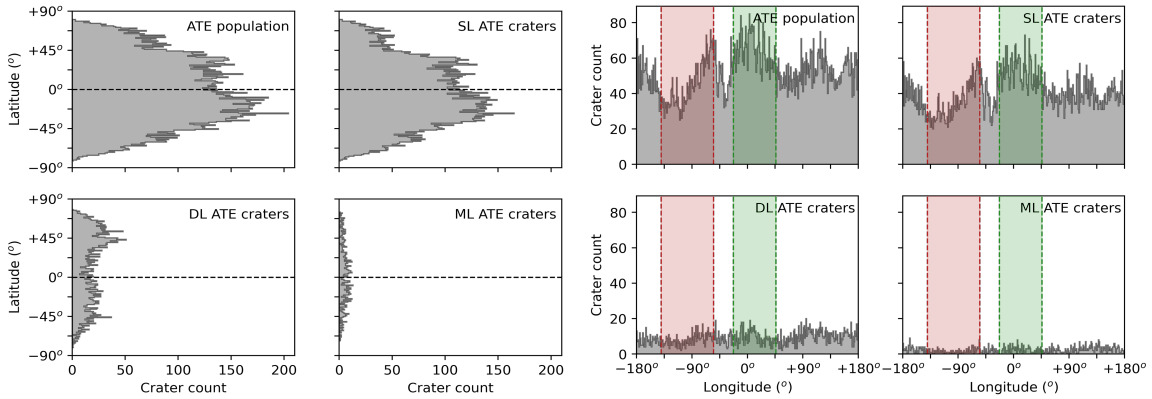

Figure 1.15: Latitudinal (left) and longitudinal (right) distributions of crater density separated by the number of distinguishable layers within ejecta deposits. The Tharsis (red) and Arabia (green) Terra regions are identified in the longitudinal distributions.

1.6.3 Central Pit Craters

From the population shown in Figure 1.9, 2512 craters are identified as possessing central pit features on the surface of Mars (Figure 1.16), with the crater density distribution being shown in Figure 1.17. The majority of these craters are found to be concentrated in equatorial regions (with a dip in concentration at the equator itself). The observed dip in this population along the equator, however, may indicate the presence of two central pit crater populations with the overall population presenting a bimodal distribution. Outside of the equatorial region ($\approx 30^\circ$ N/S), there appears to be a substantial decrease in the central pit crater population in both hemispheres. The majority of current mechanisms suggested for the formation of central pit craters (discussed in section 3.4) require the presence of volatiles within the target material. These suggested formation mechanisms would imply that most central pit craters therefore would be located in the Northern Lowland region; this region, however, shows a considerable lack of central pit craters, with the majority of them appearing to lie to the south of the dichotomy boundary. Such a distribution may indicate factors other than the presence of volatiles being necessary for the formation of central pit features. When looking at the latitudinal density distribution for central pit craters (shown in Figure 1.17), the distribution in the southern hemipshere shows a rather abrupt drop off in central pit crater numbers at a latitude of 38° S. In the northern hemisphere, however, whilst the distribution again shows a considerable decrease, the drop-off is much less abrupt, showing a more gradual decrease.

1.7 Conclusions

The surface and near-surface region of Mars supplies information about the geological past of the planet. When combined with the information obtained from analysis of the Martian crater population this can provide a robust means to infer properties about the near-surface composition and structure. The distribution of craters across the Martian surface aids understanding of the relative surface ages,

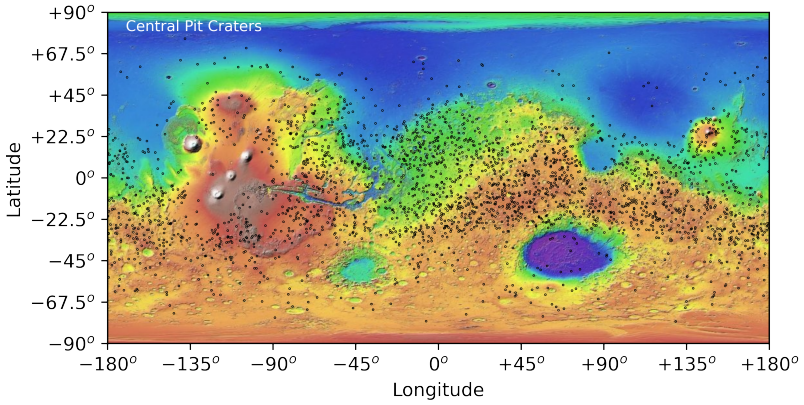

Figure 1.16: Population of Martian craters identified as having central pit features within database compiled by Robbis and Hynek [96]. From the filtered population shown in Figure 1.9 2512 craters are identified as having a central pit with the majority of them concentrated in the mid-latitudes.

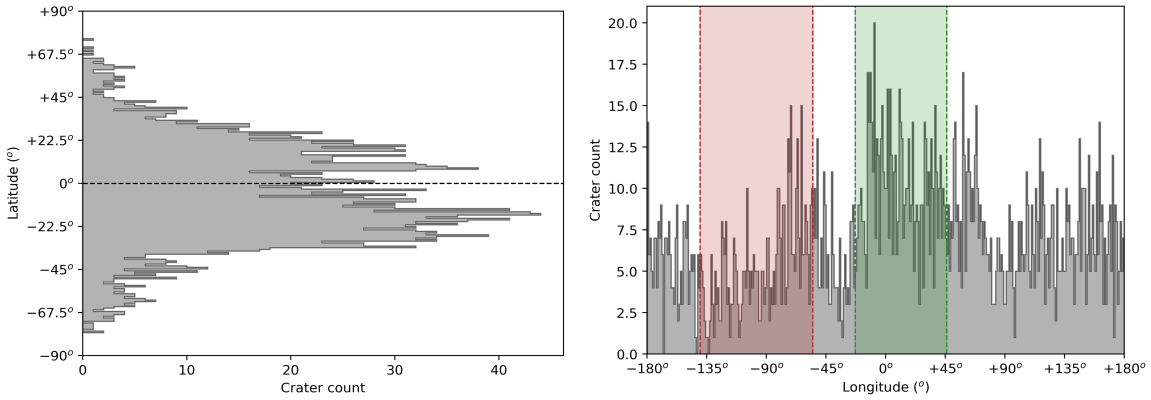

Figure 1.17: Latitudinal (left) and longitudinal (right) distributions of crater density for central pit craters. The latitudinal distribution shows a sharp drop-off in both hemispheres close to $\pm 45°$. Longitudinal trends show no clear distribution outside of the Tharsis (red) and Arabia (green) Terra regions highlighted in the figure. The reduced crater count is thought to be due to volcanic resurfacing whilst the increased count in Arabia Terra is thought to be due to its old age.

in particular when considering the degradation state of craters. Areas possessing a significant lack of degraded craters are younger than those possessing predominantly fresh craters. This may be due to either the resurfacing of the crust within this region (as is thought to be the case within Tharsis) or because of enhanced degradation rates due to the surface properties (a potential process occurring within the Northern Lowlands). The discussion presented within this chapter provides the information required for the following chapters within this thesis to be understood in the context of the Mars system. In the next chapters we look at how impact features form and are studied along with the morphological features typically thought to be related to the presence of ice throughout the broader Solar System.

Chapter 2

Impact Craters in the Solar System

"Follow the thread of this ancient tapestry"

The Voice of Tomorrow

2.1 Deciphering the Impact Crater

Impact craters are one of the most widely used groups of geological features in comparative planetology studies in recent decades [2, 10, 23, 27, 67, 71, 91, 99–120]. They are recognised as one of the most abundant geological features throughout the solar system [121], with their presence being observed extensively on the surfaces of the rocky terrestrial planets, and those of the icy satellites (and other small bodies) throughout the outer solar system [121, 122]. An impact crater is formed as the result of a hypervelocity impact between a projectile and target. There are numerous definitions of hypervelocity within the literature (the point at which shock waves traverse through a target and projectile at a speed higher than its sound speed [3] or impacts occurring at speeds higher than $\approx 1\ \mathrm{km/s}$ [1]). For the work within this thesis, it is taken as the point from where the resulting impact feature transitions between having a diameter approximately equal to the impactor to one considerably larger. Despite the established importance of impact structures, their study has only been recognised for a relatively short time [3] (mostly since the impact origin was suggested for Meteor Crater by Barringer in the early 20th century) - only coming to the forefront of scientific focus during the 1960's to 1970's, with the birth of the space age [3, 121]. Since the rise of this research field, robotic spacecraft have provided a substantial quantity of data regarding the populations of impact craters present throughout the solar system. Such data, combined with an increasing number of interdisciplinary investigations, has led to an ever expanding deepening understanding of impact structures and the mechanisms behind their formation.

2.1.1 The Origin of Crater Investigations

The modern understanding of impact cratering evolved from initially separate areas of study, each being incorporated at considerably different times over the last four centuries [3, 121]. The first discussions of impact craters emerged during the 17th century [3,121], with the observation of circular depressions on the lunar surface being documented by Galileo [123] in 1609. Observations carried out by Galileo went considerably farther than simply identifying depression features on the lunar surface. Features were preferentially identified along the lunar terminator (the dividing line marking the edge between day and night on the moon), which allowed for the recognition of raised rim features surrounding many of the craters [3, 123] - as shown in Figure 2.1. Despite the extensive recording of lunar craters undertaken by Galileo, he made no suggestions as to their origin [3, 124]. Speculation regarding an origin for the lunar features was first documented by Hooke [3,124,125], in 1665. Small-scale experiments undertaken by Hooke considered an impact origin for the lunar features. Similarity was noted between pits formed from dropping pellets into clay mixtures and the features seen on the lunar surface [125]. The lack of a fundamental understanding regarding the existence of asteroid populations [3, 121], however, led to volcanic or internal heating processes being favoured; further supported by the noted resemblance of a boiled alabaster surface to that of the Moon [123, 124].

It is only since the work of Gilbert [3, 121, 126] in 1893 that the study of an impact-based origin

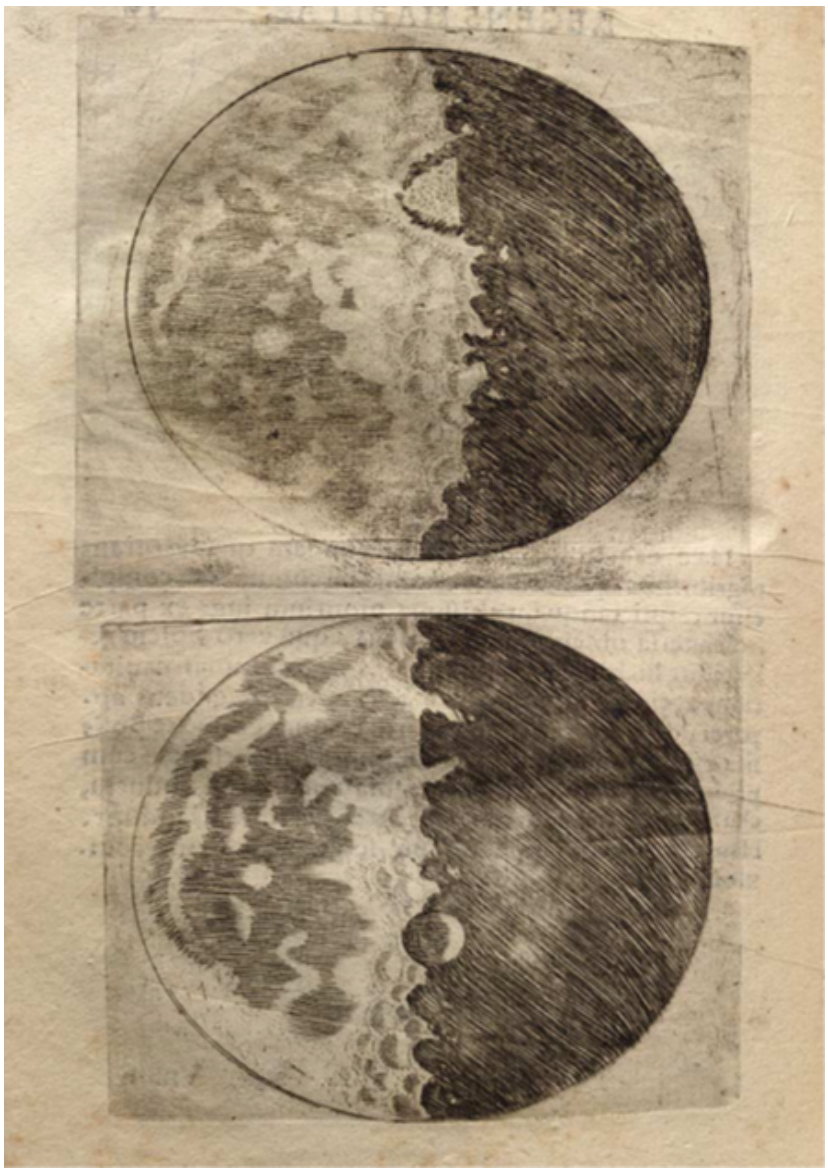

Figure 2.1: Sketches of lunar surface features by Galileo in 1609 based on observations made of the lunar surface [123].

for lunar craters gained momentum. Analysis of these features led not only to the identification of a size morphology relation (expanded upon in section 3.2), but further led Gilbert to propose an impact-based origin to be the only process capable of explaining the characteristics of the observed features [3]. This proposition was further supported with the identification of Meteor Crater, Arizona (Figure 2.2) as an impact crater in 1903 [3, 121], having been formed as the result of an impacting iron meteorite. Despite this, the geological and physical importance of the impact process remained largely ignored by much of the scientific community. The identification of shock metamorphic effects at both terrestrial and lunar impact sites highlighted the significance of impacts on the evolution of planetary systems, leading to a more substantial appreciation of their formation process [121]. Additionally, the identification of the Chicxulub impact structure in current day Yucatan, Mexico - thought to be heavily linked to the Cretaceous-Palaeogene boundary extinction event [121, 122] - cemented the idea within the scientific community that impact events not only have a substantial role

in the evolution of planetary systems, their influence continues to this day [122].



Figure 2.2: The 1.2 km diameter Meteor Crater, Arizona [127]. The first confirmed impact crater on Earth, proposed as an impact structure in 1903. Geological investigations into the crater aided the understanding of the crater formation process [3, 128]. Its 'squarish' shape is thought to be due to pre-existing faults within the Earth allowing preferential excavation along those axes [3, 7, 129].

2.1.2 Explosive Cratering and Underlying Mechanisms

One major theoretical issue dominated the field for a substantial time when considering the impact origin of lunar features. Small-scale, low-velocity experimental data initially indicated that, whilst craters could be formed as the result of meteorite impacts, only vertical impacts were thought to lead to the production of a circular crater feature [3]. Very few impact events, however, are thought to be vertical with the average impact being at an angle of 45° [3, 130]; hence, elliptical craters were initially assumed to be far more common (if an impact origin were true) than analyses found them to be. Observations have found that within the crater populations on Venus, Mars, and the Moon, only 5% are elliptical [131]. It was found in experimental investigations and numerical simulations, however, that all but the most oblique impacts produced a circular crater (see Burchell and Mackay [132] and references within). This solves an apparent discrepancy between the small population of elliptical craters and the frequent oblique impacts.

As the recognition of explosive craters increased following the onset of World War One, it became increasingly recognised that the energy release from impact events mirrored that from chemical explosive events [3, 133]. This led to an initial increase in large-scale explosive cratering studies, attempting to gain understanding regarding the mechanisms governing the crater formation process - particularly following the cessation of the Second World War, where high-explosive and nuclear craters underwent significant study [133–136]. Despite being substantially smaller than the simple craters (Figure 2.2) identified on Earth (which typically possess a diameter of ≥ 1 km), the production

of nuclear craters (Figure 2.3) allowed investigations into the crater formation process to be carried out under 'controlled' conditions; enhancing the identified link between explosive craters and those produced by meteorites including that of shock features in minerals at the relevant sites. Following the nuclear testing ban in 1963 [137], however, large-scale explosive testing came to an abrupt end.



Figure 2.3: Sedan Nuclear Crater, Nevada [138]. With a diameter of 390 m, it is the largest nuclear crater produced. Due to the similarities of impact craters to those generated by nuclear detonations nuclear testing was a primary focus of previous impact crater studies.

The interest in space flight following the end of the Second World War, led to an increasing number of studies investigating the effects of high-velocity impacts on spacecraft [3] - which continues today with specific interest in damage mitigation from these events [139–141]. In parallel, the large number of investigations looking at explosive cratering processes allowed for the development of the first scaling laws for crater dimensions as a function of impact conditions [3]; further studies have allowed for the advancement of these scaling laws (allowing dimensionless crater parameter relations to be scaled to different size ranges for comparison purposes), with their use for a range of different crater

parameters and materials [117]. Whilst explosive cratering studies reduced in their frequency, it is a method still being employed today using non-nuclear detonations, with a variety of explosive parameters (depth of burial, mass of explosive, type of explosive, etc.) being investigated due to their application to a large number of accidental and/or intentional explosive events [133, 135, 142–144]. Whilst not the main focus of this research, deductions can still be made with regard to the impact cratering process. In particular, investigations probing the effect of explosive events above the target surface [134, 136, 145], may provide considerable experimental insight into air-burst events (a considerably more common occurrence on Earth than that of crater formation [146]).

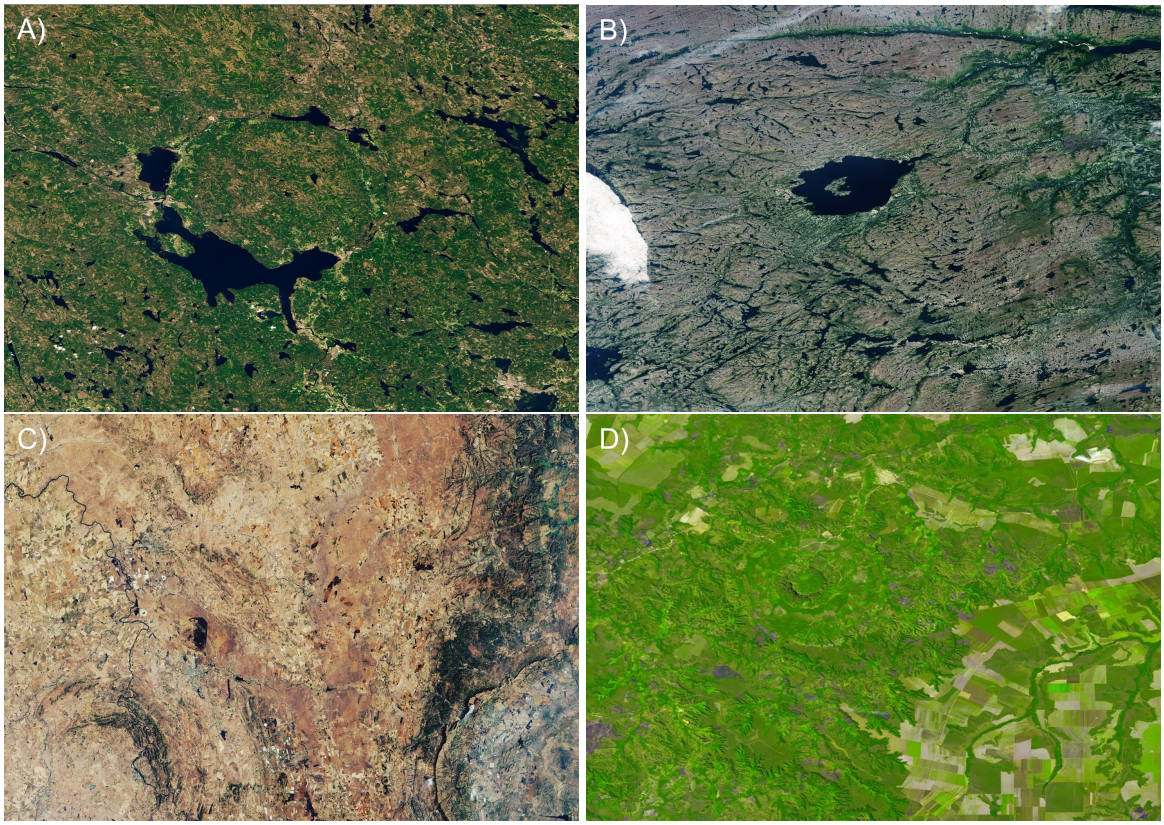

Figure 2.4: Heavily degraded terrestrial craters. A) $52\ \mathrm{km}$ diameter Siljan Ring, Sweden [147]. B) Mistatin Crater, Canada [148]. The crater is thought to have initially been $28\ \mathrm{km}$ in diameter with the lake today being $16\ \mathrm{km}$ across. C) Vredefort Crater, South Africa [149]. Originally $170 - 300\ \mathrm{km}$ in diameter. D) The $12 - 13\ \mathrm{km}$ diameter Serra da Cangalha Crater, Brazil [150]. As can be seen, often the level of degradation and erosion craters on Earth become subjected to following their formation makes their identification and subsequent study difficult.

Understanding of the crater formation process - typically divided as stated into: contact and compression; excavation; *and* modification [2, 3, 121, 122] - has increased substantially in recent decades [2, 121, 122]. Such advancements have supported the notion that, despite the extreme and apparent chaotic nature of crater formation, the physics governing the underlying mechanisms remain constant throughout the solar system [2, 3, 121]. Nevertheless, the study of such a process is still hindered by the generally unusual nature surrounding impact features [121, 122]. The extreme physical conditions associated with impact events, combined with their almost instantaneous nature and the

rarity of terrestrial impact events makes in situ investigations of planetary-scale craters exceedingly difficult to undertake [121, 128, 151]. In particular it is difficult to probe fresh structures even on Earth where we have access, due to their relative paucity [115, 121, 130]. Characteristic features produced during the cratering process (e.g. shock-metamorphic effects [2, 152], large-scale faults [7, 129], impactites [3, 153], etc.) are commonly used to identify the presence of a crater [4, 121, 154], even where one no longer remains clearly visible (such as the terrestrial impact features shown in figure 2.4). However, as such shock features require extensive field work to obtain evidence for, only those associated with terrestrial impact features can be easily studied [2, 4, 121].

2.1.3 The Crater Formation Process

Mechanisms governing the impact crater formation process are initiated upon the first contact of a projectile and target body. Whilst the process occurs as a continuous sequence of events governed by the propagation of shock waves [3, 122], a deeper insight can be obtained through the splitting of the event into three stages [2, 3, 121, 122]; each covering a somewhat distinct sequence of events. Between such stages, a gradual transition leads to the grading of each into the subsequent set of events. Traditional models of impact crater formation thus typically separate the process into the stages of: contact and compression; excavation; and modification [3, 121, 122]. In cases where substantial quantities of volatile materials may play a role in the crater formation process, an additional stage of chemical and hydrological alteration may be included, occurring both during and after the standard modification stage [121, 155]. Observed impact craters show a wide range of morphological features (discussed in chapter 3 in detail) due to their formation under different conditions (e.g: target/projectile composition, impacts speeds, etc) [2]. The drastic changes in both pressure and temperature during an impact lead to extreme strain rates and stresses, resulting in impact craters being unique from a geological perspective, presenting features unlike any other known geological feature on a planetary surface [2, 3, 121].

2.2 Contact and Compression

At the time when an incident projectile contacts a target surface, the first stage (contact and compression, Figure 2.5) of the impact cratering process begins [2, 3, 121, 122]. Often the briefest stage of this complex process [2, 3, 156], it lasts approximately the time it takes the projectile to traverse a distance equal to its own diameter into the target [156]. During this time, the initial kinetic energy of the projectile is partitioned between both the projectile and target in the forms of internal and kinetic energies [2, 122, 156, 157]. The partitioning of this energy is controlled by induced shock waves that propagate from the point of impact into the target and back into the projectile [2, 3, 122, 156, 157], The passage of these shock waves decelerates and compresses the projectile whilst simultaneously accelerating and compressing the target. As the shock wave passes, material is typically compressed to pressures on the order of hundreds of GPa (this is variable depending on the projectile mass

and velocity) [3, 121, 122]; a shock pressure much higher than known material yield strengths [3]. The propagation of the shock wave through the projectile and target occurs at a speed much higher than the standard sound speed of geological materials [122]. Hence, the change in pressure and temperature along the shock front is near discontinuous [2].

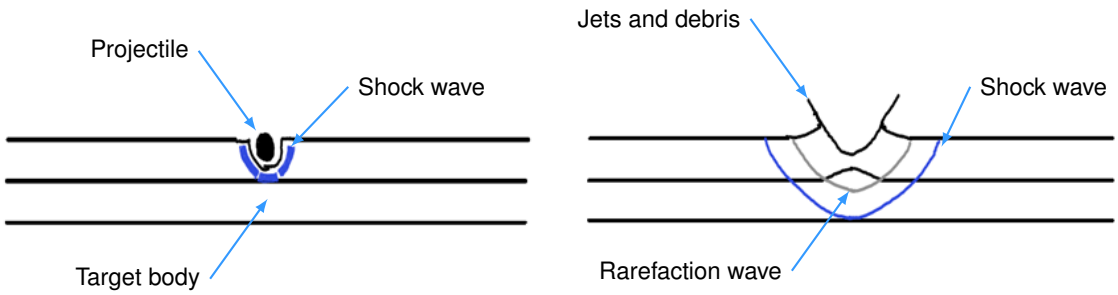

Figure 2.5: Schematic diagrams of the start (left) and end (right) of the contact and compression stage, adapted from [122]. Upon first contact, a shock wave - shown in blue - propagates through the target material. This is followed by the rarefaction wave - shown in grey - reflecting from the free-surfaces of the projectile and target. At the end of contact and compression the projectile no longer plays a role in the crater formation process having been largely melted/vaporised.

A short time after the initial contact, the shock wave propagating through the projectile reaches its rear free surface. Interaction of the shock wave with this surface causes a reflected rarefaction wave to begin propagating back through the compressed projectile, towards the target [3, 156]. Upon this reaching the projectile-target interface, contact and compression is said to have ended [3, 121, 122, 156]. These rarefaction waves travel at a speed faster than the generated shock waves [156] and as such, eventually catch up (covered in more detail in section 2.3.2). As the rarefaction front passes through the compressed projectile material, it causes it to unload from the high-pressure state. This unloading of the projectile material further decelerates it and reduces the shock pressure within the projectile to near-zero [3, 156]. As a direct result of the unloading process, projectile material is commonly melted or vaporised [122, 156]; thus, following the cessation of the contact and compression stage of impact cratering, the projectile plays no further role in the formation of the impact crater [3, 122]. While the projectile is undergoing shock compression and release, the generated shock wave continues to propagate through the target. This propagation begins the initial formation of the crater cavity [3], causing the target material proximal to the impact site to undergo shock metamorphism processes [121].

2.2.1 Impact Jetting (Ejecta Transport 1)

Impact jetting, during the initial contact and compression stage of crater formation, occurs as one of the first processes to launch ejecta material from the impact site [156, 158]. During this process, streams of very highly shocked, melted, or even vaporised material throw ejecta from the impact site

at speeds commonly faster than that initially possessed by the impactor [3, 158, 159]. Whilst the process of impact jetting was first understood through the development of armour piercing weaponry [3]. Application of the process to planetary impacts has undergone an increase [156, 158–160], having been initially thought a negligible process in all but the most oblique impact events [3]. This early neglection of the phenomena was largely due to the limited mass thought to be involved in the process [3, 158]; however, Melosh [3] has suggested that jetting plays a more important role in the crater formation process. Jetting is thought to be responsible for the production of many melts and chondrules [158, 159], as well as having a role in the ejection of material from a planetary body or system [159]. When considering a two-dimensional impact, as the projectile penetrates the target, two high-pressure regions develop on either side of the projectile [156] - at the points where its surface converges with that of the target [3, 158]. Material within these regions is subjected to a large unconstrained pressure gradient, leading to it experiencing an acceleration away from the impact site [156].

Investigations into the jetting phenomena initially modelled the process as a purely hydrodynamical effect through the thin-plate theory [158, 159, 161, 162], in which two material plates collide at an oblique angle. Analysis of the jetting process through the thin-plate theory led to the development of two criteria for when a jet will or will not form. Firstly, shocks present within the converging stream are required to be detached from the collision point [159, 161, 162], a jet may also form in the case where no shocks are present in the converging streams [159]. As the convergence angle between the two plates decreases, the jet velocity increases towards infinity [161, 162]. Along with this, a shock present within the converging steam moves towards the collision point [161]. At a critical angle, dependent on plate velocity and the material equation of state, the shock attaches to the collision point and the jet formation process ceases [159, 161, 162]. This material dependent critical angle provides the second criterion for jetting to occur during an impact event.

The simplest geometry when considering the impact jetting process is shown in Figure 2.6. In this geometry, two thin material plates collide with a collapse angle (α) between them [3, 159]. If this collapse angle is greater than a material-dependent critical angle (α_{cr}), a high-speed jet will emerge along the bisector [3, 158, 159] resulting form the geothermal leveraging generated from oblique collisions [159]. The jet has a velocity of v_j in the standard reference frame that may exceed that of the initial impactor [3, 156, 158]. As the collapse angle between two plates decreases, v_j increases as the jet mass decreases. Hence, the conservation of momentum means that, an opposing high-mass, low-velocity stream must form [3, 156, 158, 159]; this stream is termed the 'slug'. Figure 2.6 shows the thin plate theory in two distinct reference frames [158]. The collisional reference frame is defined such that the stagnation point in Figure 2.6 remains stationary [3, 158]. In this frame, the plate velocity vectors (v_{p0}) are parallel to their faces and the jet velocity (v_{j0}) can be found as a fraction ($f = v_{j0}/v_{p0}$) of this [3].

The maximum pressure of the material within the jet can be found through the application of Bernoulli's equations [3, 158, 159]. The sum of the specific enthalpy and kinetic energy is constant

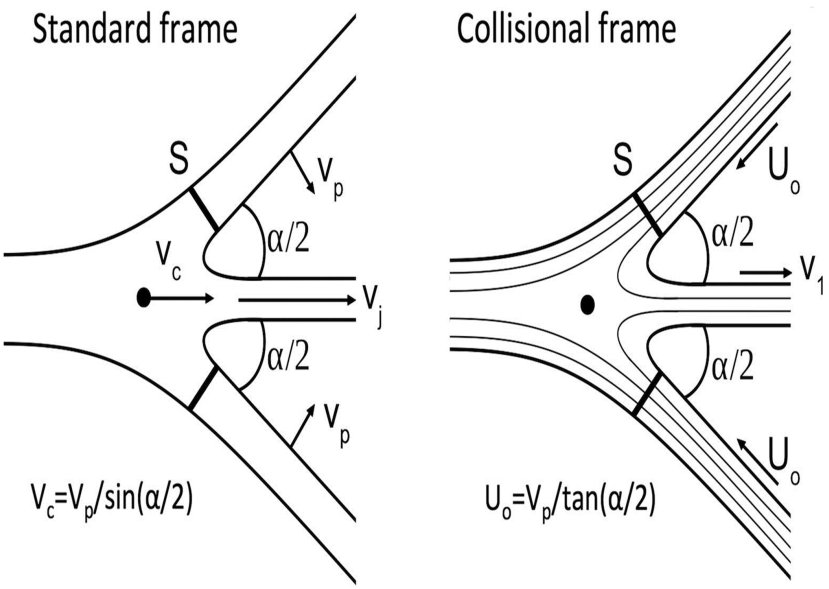

Figure 2.6: The thin plate theory of impact jetting [158] showing both reference frames. This illustrates the process of two plates collapsing at a speed v_p with a convergence angle α between them. The point of collision has a velocity of v_c. A jet is formed along the bisector with a velocity of v_j. In the collisional frame, the collision point is stationary with v_p and v_j undergoing geometric transformations. The lines marked S within the figure represent shock waves in the colliding plates.

along streamlines within the flow [3]. Whilst the material within the jet is some of the most highly shocked ejecta resulting from the impact process [3, 156], calculating the exact shock pressure is not a simple task as it is strongly linked to the equation of state for the material within the jet [3]. Pressures within the jet, however, are found to be highest when $\alpha \approx \alpha_{cr}$ [3,158]. When the geometry of jetting is extended to consider the impact of a spherical projectile into a planar target (such as that shown in Figure 2.7, and the basic geometry for a planetary impact event), the collapse angle between the projectile and target material changes. In this geometry, α ranges from $0 - 90°$; hence, at a time during the impact process, the critical angle will be passed and a jet will form [158]. To probe the jetting process further, a much deeper understanding of the mathematics governing this process would be required. This is, however, far beyond the scope of the work presented here.

2.2.2 Projectile Unloading

Upon completion of the contact and compression stage, the entire projectile has been shocked and subsequently unloaded from the high pressure state [3,122,156]. Similarly to the initial compression of the projectile, it unloads from its high pressure state differentially [3]; the rear of the projectile is decompressed much earlier than the front of the projectile. The decrease in pressure within the projectile material causes it to undergo a considerable expansion [3,156]. For sufficiently high shock pressures, this expansion occurs at a rate approximately equal to the thermal expansion velocity for the material within the projectile [156]. This results in the complete disruption of the projectile, and may lead to large portions of it becoming entirely vaporised [3, 122, 156]. The front of the projectile

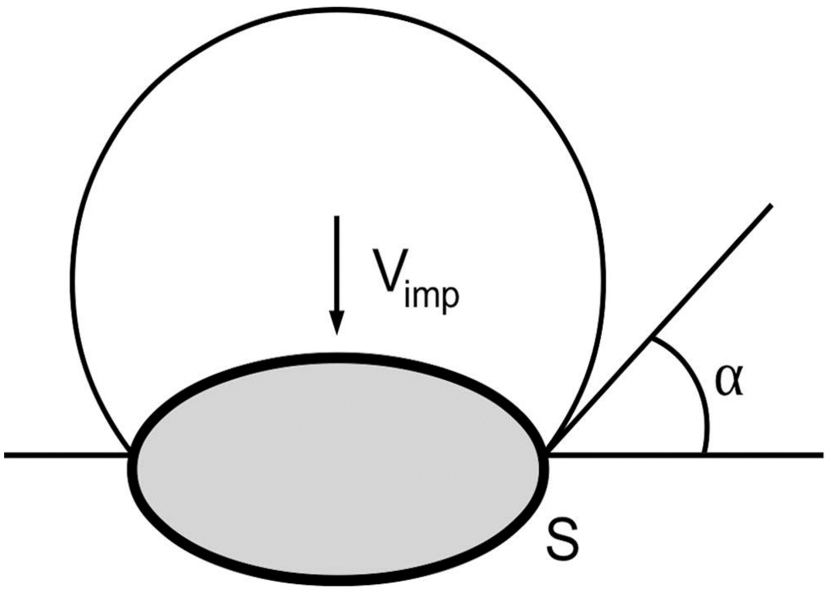

Figure 2.7: The spherical impact theory of impact jetting [158]. The projectile impacts the target surface at a speed v_{imp}. When moving to this geometry for the theory of impact jetting the collapse angle α between the two colliding surfaces moves through the range of $0 - 90°$. This means a jet will always be formed. In this figure, the shaded area and line labelled S represent the region that has been shocked and the shock front along which the jet will emerge, respectively.

sustains the projectile-target interface at high pressure [156]. As such, the decompression of projectile material induces an upward motion [3, 156] driven by the significant pressure gradient through the projectile [156]. This can lead to parts of projectile expanding out of the crater as a vapour plume [3], potentially allowing projectile material to escape the target planet - this process is distinct from the jetting phenomena already discussed. At this point through the crater formation process, the disruption and potential vaporisation of the projectile means that it no longer plays a role in excavating and modifying the crater. Remaining fragments, however, may provide valuable insights into emplacement processes and the intiail parameters of the impact event [5].

2.3 Excavation

The second stage of impact crater formation (excavation, Figure 2.8) is typically defined as beginning at the point the projectile has fully unloaded, starting immediately after the contact and compression stage [3]. During this phase, the crater opens up, forming a transient cavity [2, 7, 121, 122], the diameter of which is several times larger than the projectile itself [3]. The opening of this cavity is governed by two main processes [3, 122] shock wave expansion and excavation flow. An initial hemispherical, supersonic shock wave [3] expands into the target [2, 3, 7, 121, 122] weakening as it covers more material and eventually decaying into a sub-sonic stress wave [3, 7]. Resulting from the penetration of the target by the projectile, the shock wave is centred on a point below the target surface [3, 121, 122], typically about one projectile radii below the original surface [121]. As this

propagates through the target, it shock compresses the material [3], irreversibly changing it. Upwardly propagating portions of the shock wave then begin to interact with the free-surface of the target [7, 121]. Upon reaching this surface, the shock wave becomes reflected back into the target in the form of a rarefaction wave. The rapid nature of this process, relative to the time when the impact occurred, generates a Near-Surface Interference Zone (NSIZ) [7, 122].

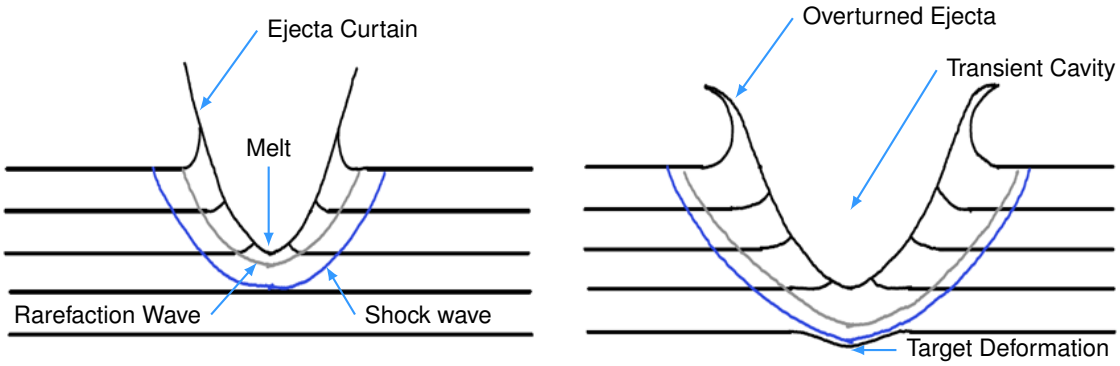

Figure 2.8: Schematic diagrams showing the start (left) and end (right) of the excavation stage of crater formation adapted from [122]. At the start of this stage, the shock wave propagates through the target material compressing it and accelerating it to high speeds. The rarefaction wave, releases this material from the shocked state and imparts an upward momentum to its movement - forming the excavation flow. This flow of material removes it from the crater forming an ejecta curtain. At the end of this stage, the transient cavity has been formed.

Shock and rarefaction wave interaction in the NSIZ leads to large-scale fracturing and a reduced shock pressure [7, 121]. As such, material ejected from this location (both in the form of large spall plates [7, 122] and smaller material) present a rather unique characteristic; becoming removed from the crater at a relatively high speed but also at a relatively low shock pressure [7, 122]. Once the target material has been shocked and fractured by the passage of the shock and rarefaction waves respectively [121], the second process governing excavation begins to dominate. The excavation flow is the process responsible for opening up the transient cavity [3, 7]. A sub-sonic flow of target material begins to remove and displace broken material from the cavity leaving an approximately hemispherical depression in the target [3, 121]. It is generally accepted that all of the material removed from the forming crater comes from the upper $1/3 - 1/2$ of the transient cavity [2, 121], whilst the lower material remains within the crater after being displaced downwards [2, 3, 121, 122]. The overall shape and size of this formed transient cavity is largely determined by the mechanical strength of the target material and the gravity of the planetary body [3, 7, 122]. Despite this stage of crater formation often being studied as two separate process (i.e. shock wave expansion followed by the NSIZ and spallation), both are intimately linked [3].

2.3.1 Shock Wave Propagation

A full analysis of the propagation and interaction of shock and rarefaction waves within a target is far beyond the scope of the work presented here. However, to investigate the process of spallation, it is useful to discuss the structure of these waves and some of their basic properties. Shock waves propagate at supersonic speeds through a target material as a single pulse, capable of quickly overtaking other slower propagating waves and adding their energy to its own [3]. The conditions caused by the passage of the shock wave through the target material are extreme; with materials becoming shocked to pressures of many 10's to 100's of GPa (far beyond their mechanical strengths) [2, 3, 7, 122]. Despite them often being represented as a physical discontinuity [3, 136, 145], the jumps in pressure and particle velocity are not instantaneous [3, 163]. The intense pulse is led by a short elastic precursor [163], after which the particle velocity and pressure of the target material rapidly rise to their maximum values [3, 163]. Following the passage of the shock wave, the pressure drops to near zero. Particle velocity, however, decreases to only one fifth of the peak value [3, 7, 163]. The time taken for the maximum pressure and particle velocity to be reached after the arrival of the shock wave is referred to as the rise time, whilst the time taken for these values to fall after the front's passage is termed the decay time [163].

The rise time τ_r for the pulse is calculated as

$$\tau_r = \frac{L}{2v_i} \tag{2.1}$$

where L is the projectile diameter and v_i its impact velocity [3]; with the decay time being a factor of β longer, giving $\tau_d = \beta\tau_r$ [3, 163]. The factor β is larger than one, leading to $\tau_d > \tau_r$ always being satisfied. This can be influenced by rate dependent processes occurring within the target as the shock wave passes (pore collapse, material strength limits being exceeded, etc.) and the propagation of fractures or faults [3]. The region of maximum pressure and particle velocity within the shock wave structure is referred to as the detached shock [163]. This difference between τ_r and τ_d induces an asymmetry in the shape of the detached shock, changing its shape depending upon the conditions of the impact. This asymmetry and shape is key in determining the distribution of ejected fragment size during spallation processes [163]. This distribution, however, varies for every crater due to the dependence on the initial conditions of the impact [3]. Hence, a generalised model for the fragments ejected during spallation cannot be obtained. As the shock wave continues to propagate, its energy is spread over an increasing area of target material. This leads to it weakening as it expands, eventually morphing from a supersonic shock wave to a sub sonic elastic wave [3]. Whilst still important for the excavation of an impact crater, once the shock wave has propagated beyond the region immediately adjacent to the point of impact, it is no longer important for the spallation process.

2.3.2 The NSIZ and Spallation (Ejecta Transport 2)

As the impact-generated shock wave propagates outward from the impact centre in all directions (including upwards) it begins to approach and interact with the free-surface of the target body [3, 156,

163] - leading to its reflection and the generation of a rarefaction wave. The rarefaction wave travels back downwards into the target body [3, 163] (see Figure 2.8). Due to the rise time associated with the detached shock front [163], in the near-surface region, the rarefaction wave arrives before the maximum shock pressure has been reached [3, 156, 163, 164]. This leads to a region of material which is shocked to a much lower pressure than deeper lying material at the same radius from the impact centre [163]; defining the NSIZ. The depth to which the NSIZ reaches within a target is given by:

$$z_s = \Lambda \sqrt{1 + \left(\frac{s^2}{\left(d_{eq}^2 + \Lambda^2\right)} \right)} \tag{2.2}$$

in which s is the horizontal distance form the crater centre and $\Lambda = U_t \tau_r / 2$ where $U_t \tau_r$ is the width of the rising shock wave [3] with U_t being the velocity of the shock and τ_r being defined in Equation 2.1. In this region, large fragments of target material (spall plates) are able to become ejected at both relatively high velocities and relatively low shock pressures [163] - a process termed spallation. Whilst a full understanding of spallation processes requires a numerical analysis of an individual impact event, it is the process by which the HED (howardite-eucrite-diogenite thought to have originated from Vesta) and SNC (shergottite-nakhlite-chassignite thought to have originated from Mars [165]) meteorite families are thought to have been liberated from their parent bodies [163, 164].

2.4 Modification

The final phase (modification) of the traditional three-stage formation model [121] begins once the excavation stage has ended. Typically said to start at the point in time when the excavation flow has stopped [2, 3, 122, 129], the flow of material during this stage is effectively reversed [2, 129]; with the formed transient crater undergoing collapse processes [3, 122]. It is at this stage of the crater formation process that a clear differentiation between the different crater types can be seen; with smaller cavities undergoing relatively little collapse when compared to their larger counterparts [2, 121, 129], who are often completely destroyed by the collapse process [3, 129]. This difference results in the formation of smaller ‘simple’ craters and larger ‘complex’ craters [121, 129, 166]. The size at which this transition occurs varies across solar system bodies (Table 2.1), scaling with the material strength and the inverse of the gravitational acceleration [121, 129, 166, 167]. The transition, however, is not a discontinuity - with so called ‘transitional’ craters forming over the transition diameter range [129, 167, 168]. For the smallest craters, the modification stage is a simple process, with the only change occurring being the back-falling of loose ejecta from the crater walls and rim region [3, 121, 129, 166, 168], forming talus deposits on the floor of the crater.

As the transient cavity grows in size, the level of modification begins to increase. Larger simple craters start to become filled with melt and breccia deposits [3, 166], forming a lens covering the floor of the crater. As the diameter of the cavity continues to increase, transitional craters begin to exhibit features of both simple and complex craters [166–168]. Populations of transitional craters are, as of yet, relatively understudied, having only recently been recognised as a distinct category

Table 2.1: Diameter range over which the simple-to-complex transition occurs on several bodies in the solar system.

Body	Transition Range (km)
Mercury	7 [3]
Earth	2-4 [3]
The Moon	15-20 [169]
Mars	5-8 [170]
Galilean Satellites	2-3 [100]
Pluto	11-12.5 [167]
Charon	13.5-16 [167]

when analysing crater populations [167, 168]. Throughout the transition diameter range, the size progression is thought to follow the sequence of floor failure, followed by the collapse of the rim region [168], leading to flat crater floors and terraced rims respectively. The last feature associated with complex craters during the transitional range is the central peak [3, 168] (the formation of these features is discussed in Sections 2.4.1.2 and 3.2.1). The primary forces driving the collapse of the transient cavity are the material strength and the gravitational acceleration of the target body, with transient cavities undergoing complete collapse once the negative buoyancy force overcomes the mechanical strength of the target material [3, 122]. Both of these forces act to close the transient cavity [2, 129], attempting to equalise the formed mass deficit [3]. As such, the modification stage is often said to have no true end [3,121,122]. However, it is commonly accepted that upon the cessation of large scale mass movements, modification processes have ended [2, 129].

2.4.1 Transitional and Complex Craters

The extent to which a transient crater becomes modified at the end of the formation process is heavily dependent upon the cavity diameter at the cessation of the excavation flow [3,122,129]. As the forming crater grows in size, a transition occurs from small-scale collapse to large-scale movement and deformation. Typical craterforms of either side of this transition are shown in figure 2.9. At sizes below which this transition occurs, simple craters form, undergoing only slight deviations from the transient cavity. Above the transition diameter, complex craters are formed. Complex craters themselves can be further sub-divided into: central peak, central pit, peak ring, and multi-ring basins [2, 3, 122, 129]. As the cavity becomes increasingly modified/degraded, its gravitational stability increases. The process through which this happens varies on differing planetary bodies, with cavities approaching gravitational stability termed palimpsests [3].

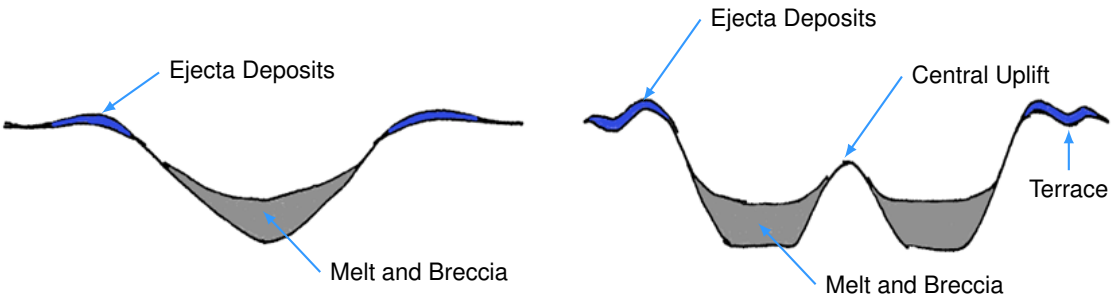

Figure 2.9: Typical simple (left) and complex (right) final crater cross sections. Melt/breccia deposits are marked in grey and ejecta deposits are marked in blue. Simple craters are typically bowl-shaped with the only variation from the transient cavity often being the formation of a melt/breccia lens. Complex craters are subjected to a much stronger level of modification. The underlying region of the crater becomes uplifted, and the rim region undergoes terracing.

2.4.1.1 Transitional Craters

Whilst simple and complex crater populations have been extensively studied on bodies across the solar system, there exists a largely unstudied crater population lying between the two. As a result of the simple-to-complex transition being continuous, a diameter range of transitional craters exits between the two extremes [167, 169, 171], presenting morphological features of both simple and complex craters [129]. As stated, the precise diameter at which the transition occurs varies throughout the solar system, depending primarily on surface gravity and the mechanical strength of the target material [166, 169, 171, 172]. To distinguish between simple and complex crater morphologies, past studies have typically used the depth-to-diameter ratio (δ) [167] - with simple craters often possessing a ratio of 0.2 [3], whilst complex craters possess δ values in the range of $0.1 - 0.05$ [129]. Despite the δ values beginning to change at the extremes of the transitional range [171], previous analysis has shown it does not significantly alter the overall trends presented in the δ values for each crater type [167]. Further, relying solely on the δ value for distinction in this transitional diameter range means that, much of the morphological nuance defining this crater type is lost. As such, when considering craters within the simple-to-complex transition on a planetary surface, morphometric analyses are often used [167, 169, 171].

The currently accepted sequence of morphological changes within a transitional crater is that as the bowl-shaped cavity increases in diameter, it undergoes: floor fracturing, then rim collapse, and finally central uplift [167, 169]. Examples of the two extremes of transitional craters can be seen in Figure 2.10. The transition occurs as the cavity becomes increasingly unstable, succumbing to gravitational collapse [3, 129]. As the transient cavity increases in diameter, the instability of the underlying region against the negative buoyancy force causes large-scale fracturing, leading to a flat floor crater [167, 169]; with a reduced depth-to-diameter ratio. As the size of the cavity continues

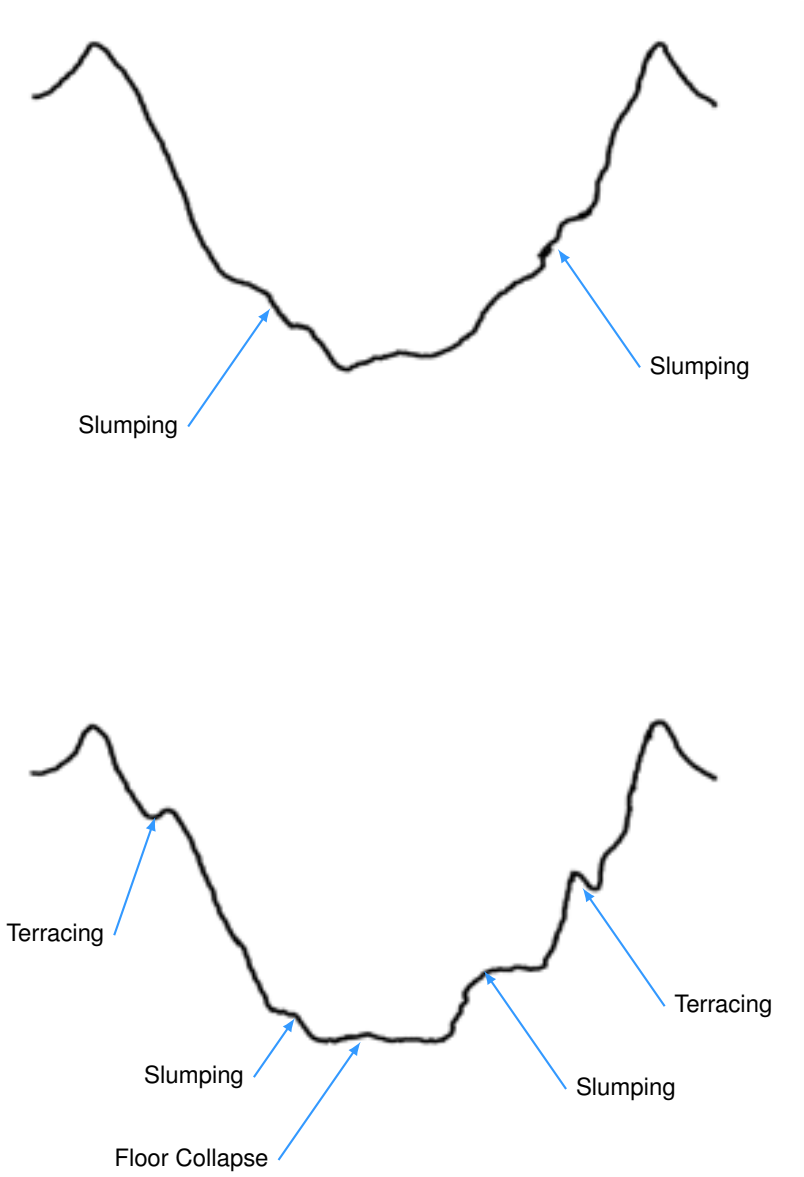

Figure 2.10: Example profiles across transitional craters, adapted from [169].The top profile shows a crater close to what would be referred to as 'simple', exhibiting some localised slumping close to the bottom of the crater. The bottom profile presents a larger crater close to what would be classed as 'complex'. This crater presents more drastic slumping and terracing in the crater rim region. As the crater moves closer to a characteristic complex crater, the floor region begins to undergo collapse and the crater profile changes from a typical bowl-shape to present a flat-floor shape.

to grow further, excess mass concentrating in the crater rim region starts becoming gravitationally unstable [167, 169, 172]. This leads to the production of localised faults and terraces in parts of the crater rim region. Another result of this increased instability in the crater rim region is that substantially more slumping and back-falling of material can occur as the transient cavity increases in diameter [169, 172]. This can lead to a much more chaotic and asymmetric appearance, particularly in the central region across the crater profile [169]. Once central uplift processes have started to occur within the central region of the crater, it is considered to have passed through the transition

point and is then considered a complex crater [167, 169].

2.4.1.2 Complex Craters

The mechanisms governing the process by which the central region of a crater becomes uplifted are multiple and inter-related. Due to the displacement of material within the crater cavity, the central region begins to move in an upward direction attempting to return to a gravitational equilibrium [2, 129]. In sufficiently large craters, this material can overshoot the equilibrium point resulting in the formation of a central peak/mountain feature within the impact crater [3,129,166]. Despite this central peak typically being defined as the feature distinguishing a complex crater [166], it does not signify the end of the crater size evolution progression [3, 129]. The height of the central peak increases with an increasing crater diameter [3], becoming increasingly unstable as it does so [2, 3, 129]. At a certain size, the mechanical strength of this central peak is unable to overcome the gravity of the target, leading to its collapse [2]. This induces a downward and outward flow of material [3]. Following the collapse of the central peak, a ring of mountain-like peaks forms within the central region of the crater [3, 166]; the diameter of which appears to scale with the overall crater diameter [3]. Example profiles of both a central peak and peak ring crater are shown in Figure 2.11. Subsequent to this, the largest craters on a planet's surface may present multiple ring features (both interior and anterior to the crater rim) [3]. This is discussed in section 3.2.1 where the influence of volatiles on the crater formation process is covered in more detail.

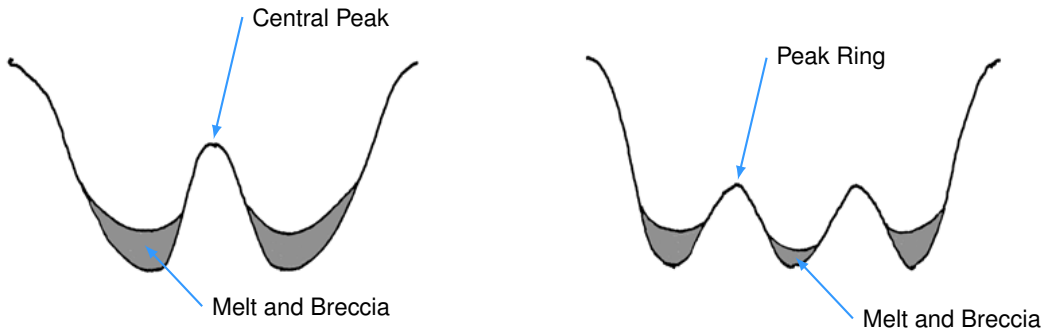

Figure 2.11: Example profiles of a central peak (left) and peak ring (right) crater. Melt and breccia deposits are shown in grey. As the central uplift increases in height, it becomes unstable eventually collapsing under its own weight. Once this occurs, it forms a ring of peaks within the crater.

2.4.2 Target Composition and Stratigraphy

The model of crater formation often assumes the target to be a homogeneous, crystalline rock target [129]. The presence of inhomogeneity (such as stratigraphic layers, faults, or changes in mechanical properties) within a target surface influences the outcome of the cratering process. As an example, the presence of ice is often a contributing factor to surface inhomogeneity, with consequen-

tial variations as discussed in chapter 3. Observed variations differ, depending on whether vertical or lateral inhomogeneity exists within the target [3, 129]. The most common vertical heterogeneity within the target is the presence of layering [129]. This typically takes the form of transitions from sedimentary surface materials to crystalline and basement rocks, however, it can also be due to the presence of a loose regolith layer covering the target surface [106, 129, 173]. The thickness of the uppermost layers has an influencing role over the final morphology of the formed crater. Surface layers are typically weaker than those deeper within the target [117, 129]. Thicker surface layers lead to enhanced crater diameters whereas thinner layers can lead to an increase in structural uplift during the modification stage [129]. If a significant difference in strengths is present between the target layers, as would be the case for an overlying regolith layer, the differences in final crater morphology can be used to estimate the depth of the regolith layer [173].

2.5 Crater Relaxation

Following the completion of modification, the crater formation process is said to have ended. This, however, does not signify the end of material movement within or around the crater. Once the crater has formed, it undergoes relaxation processes - until the cavity has achieved gravitational equilibrium. These processes can occur over millions of years following the end of crater formation [129], however, the end of crater relaxation may be reached much sooner on active planetary surfaces [122]. Once the large-scale material movements have stopped, the long-term relaxation processes are driven by the plastic flow of the crustal material underlying the impact crater [3,129]. The end result of the crater relaxation process is the complete removal of morphological impact features from the planetary surface. Whilst almost impossible to study within a laboratory investigation, for the research presented in the following chapters, consideration of the factors and processes affecting the crater relaxation process must be made. Despite many of the processes of interest commonly being influenced by the presence of volatiles within the target (as they are considered to be part of the crater formation process rather than a morphological feature resulting from the presence of volatiles), it makes sense to consider them here.

On planetary surfaces considered active, impact craters are also subjected to numerous erosion processes, removing any visual and geological traces of them long before they undergo crater relaxation. For large impact craters, relaxation processes occur on a much shorter timescale [3]; the longer time scale erosion processes, however, are far more important when considering populations of smaller craters. Of the solar system planets: Venus, Earth, and Mars possess the surfaces that present the highest levels of activity [98,174,175]. On Earth, formed craters are subjected to: aeolian, fluvial, and tectonic erosion, due to the highly active nature of the Earth's environment [3,4,115,121]. Whilst Venus and Mars present significantly lower levels of activity than the Earth, visual features of craters may still be removed by volcanic and aeolian activity, respectively [175–177]. High levels of volcanic activity on a planetary surface may lead to the complete infilling and covering of crater

cavities - as seen on Venus [175, 177]. Aeolian erosional processes lead to the large-scale muting of features; a processes observed extensively throughout the Northern Lowland Plains on Mars [174]. If the surface is tectonically active, however, the motion and recycling of crustal material can lead to the complete removal of all features relating to impact crater formation [3, 121, 129].

2.5.1 Effects of Target Viscosity

The viscosity profile of a target body influences the time taken for a crater to undergo relaxation. For many planetary lithologies throughout the solar system, viscosity can be modelled - due to the typically linear increase in temperature with depth. This follows the exponential law:

$$\eta\left(\mathrm{z}\right) = \eta_0 \exp\left[\pm\frac{\mathrm{z}}{\mathrm{d}}\right] \tag{2.3}$$

in which η_0 and $\eta\left(\mathrm{z}\right)$ represent the material viscosity at the surface and at a depth z respectively, and d represents the distance over which the viscosity varies by a factor of e (the exponential) [3]. Whilst initial assumptions meant that Equation 2.3 provided a good approximation in the crustal region of many (particularly rocky) planetary bodies, further studies into the rheological properties of ice and permafrost materials show them to exhibit more complicated behaviour [178]. Hence, the accurate modelling of the viscosity of a permafrost or permafrost-like material requires a much deeper understanding; specifically the ice content at which viscous creep begins under the conditions on the planetary body of interest [179]. Experimental investigations into terrestrial permafrost creep have been carried out [179, 180], however, their application to extraterrestrial permafrost regions remains dubious [178, 179]. Whilst a full analysis of shock wave propagation and crater formation processes within permafrost materials are beyond the scope of the work presented in this thesis, it is important to acknowledge their influence for the work presented deeper within the thesis.

2.6 Conclusions

This chapter has covered the crater formation process as currently understood. For the work presented within this thesis, the important stages are those of excavation and modification. During these stages the properties of the target material have the highest level of influence on the final morphology produced. Despite this, much of the work investigating the process has focused on rocky, crystalline targets. This thesis, however, investigates impacts into a presumed permafrost material and regolith layer (the surfaces of northern Mars and Phobos respectively). Whilst a regolith layer provides only a slight variation covered by the target viscosity, the presence of volatiles within a planetary surface can have a substantial level of influence over a significant proportion of the morphological features associated with a crater. Having considered the standard formation process for an impact feature, we can now look at how this changes in the presence of ice material. The next chapter in this thesis thus covers the morphological features typically associated with the presence of volatiles and how they change throughout the solar system.

Chapter 3

Crater Morphology and Volatiles

"Follow this river of letters,

and write your own magnificent chapters"

The Voice of Tomorrow

3.1 Crater Morphology

The presence of traditional (nitrogen, water, carbon dioxide, etc.) and non-traditional (potassium, sulphur, ammonia, etc.) volatiles within a target can have a strong influence over the cratering process and the final morphological features of a formed crater [20,27,63,67,100,101,181–187]. Morphological investigations analysing crater populations throughout the Solar System have identified several features surrounding and within craters that are thought to be highly indicative of the presence of volatile elements within the target surface [16, 21, 63, 67, 100, 120, 183, 185, 187, 188]. These features are thought to originate due to the differences in response of rocky and icy materials to high shock pressures [3,122,129]. Identified features become more distinctive during the modification and post-modification phases [2, 129]. At smaller crater diameters, there presents very little difference in morphology within the crater due to the presence of volatiles [100]; at larger diameters, however, differences become more prominent [120, 187] often replacing features observed on volatile-poor surfaces [100]. The portion of the crater often presenting the largest variation due to the presence of volatiles is the central region [2,90,185,187–189]. The extensive modification this region is subjected to during the final stages of the crater formation process can be heavily influenced by both the initial conditions of the impact and the properties of the target and/or impactor [3, 129].

3.2 Crater Classifications

Within the standard size progression morphology of impact craters, morphological observations [16, 21,23,67,182,183,185,187,190] and numerical/experimental [20,100–102,181,184,191] investigations find that differing target properties can influence the morphological features formed; indicating a more nuanced dependence than previously thought. At all sizes, differences can be seen surrounding the crater in the form of fluidised ejecta [71, 190, 192] and spallation zones [181, 184, 191]. Due to the more brittle nature of icy surfaces, particularly when compared to their rocky counterparts, the area surrounding the forming crater is more susceptible to fracturing and the removal of large fragments of material [163], particularly in strength-dominated smaller craters. This causes an apparent widening of the crater cavity potentially contributing to the shallower than expected nature of icy craters [100, 193]. The biggest differences, however, are that the simple-to-complex transition typically occurs at a smaller crater diameter in ice rich targets, and over a much narrower range of diameters (see Table 2.1), than on ice-poor target surfaces [100,187,194]. Further, a second transition is identified within numerical studies linked to the rheological properties of ice [100]. As the crater increases in diameter, the variations between ice-poor and ice-rich targets increases, beginning as stated with changes to the central region, and ending with entirely different structures for multi-ring basins [3, 100, 187, 194].

On ice-poor target surfaces, the distinguishing feature of a complex crater is the central peak [3, 129]; on ice-rich targets, however, these features are rare [187]. In the diameter range where cen-

tral peaks are expected to first appear, they are often replaced with a rimmed depression, forming a central pit [185, 187]. Central pit features are not only seen on icy target surfaces, they have been observed on the surfaces of Mars, Ceres, Mercury, and the Moon. Despite the somewhat extensive study of these features, however, mechanisms governing their origin still remain poorly understood and are likely to be different on rocky and icy bodies [90, 189]. At even larger crater diameters, on icy targets the central pit feature appears to develop into a central dome [188]. These domes are currently found almost exclusively on the surfaces of icy bodies - in particular the Galilean moons [185, 187]. At the largest sizes, the differences seen in crater morphology due to the presence of volatiles is extensive [3]. Multi-ring basins are observed to form with a completely different structure. The formation of this class of crater is thought to be significantly different for the Galilean moons than for rocky bodies (discussed more in section 3.2.2). Hence, interactions with this different structure would lead to a substantially different craterform (see Figure 3.1) [3].

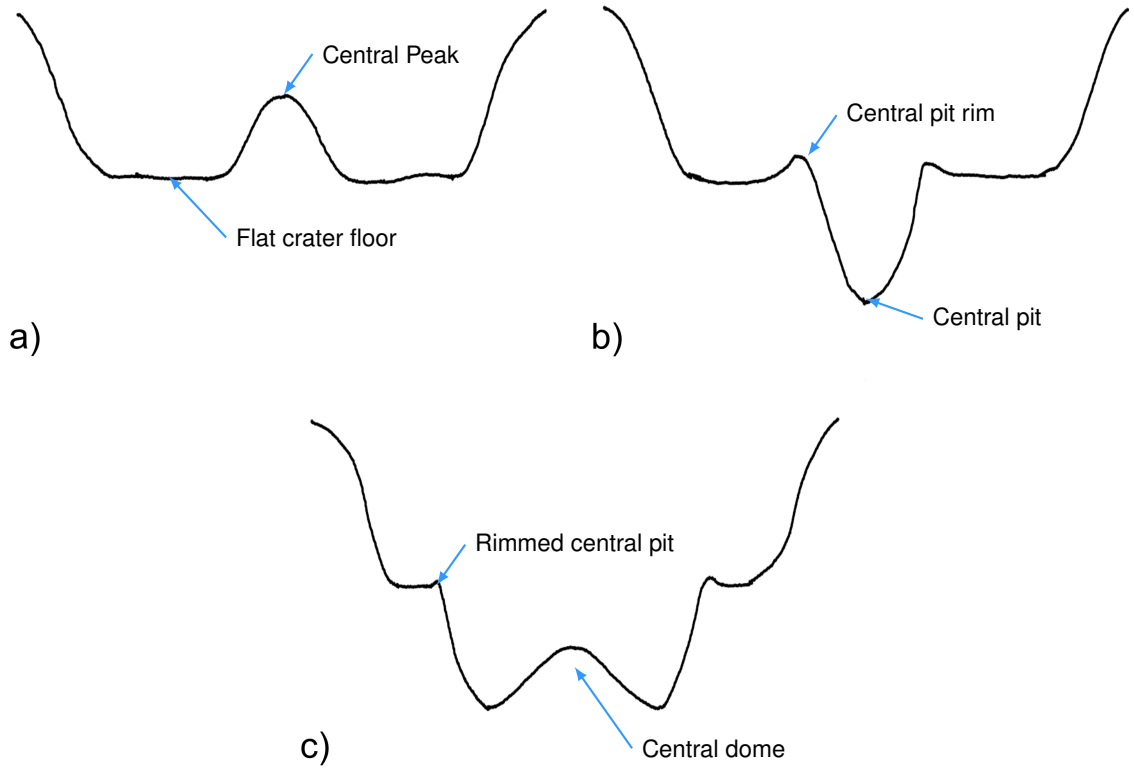

Figure 3.1: Examples of central morphology features. Panel a) shows a typical central peak morphology. Panel b) shows a typical central pit. Panel c) shows a typical central dome.

3.2.1 Transitional and Complex Craters

The smaller transition size for forming complex craters on icy bodies is due to both the weaker nature of ice compared to rock under shock processing [2, 3, 100], and the brittle-to-ductile transition of ice (occurring at ≈ 26 km on Ganymede and Callisto and at ≈ 8 km on Europa) [100]. The simple-to-complex transition is known to scale with the gravitational acceleration of the target body [2,3,122]. As

such, the smaller diameters at which complex craters form are most visible on the Galilean satellites. Their similar size and gravitational acceleration to Earth's Moon means that observed differences (the different diameters at which the simple-to-complex transition occurs (Table 2.1)) are due to the composition of the surfaces and not the local gravity. The response of ice to shock processing is also thought to lead to complex craters on icy bodies being substantially shallower than their rocky counterparts [100, 185, 187]. This shallower depth has led to complications when considering the formation of several complex crater features, as many formation mechanisms within icy target surfaces require the host crater to have penetrated a substantial depth through the crust [100].

Once the transition to complex crater has completed, morphological differences due to ice become substantially more pronounced. As already stated, on rocky bodies, the feature distinguishing a complex crater is the central peak [3, 121, 187], but on icy surfaces, however, central peaks are rare [100, 185, 187]; with central peak features often replaced with the appearance of a central pit [185, 187]. These form a depression in the central portion of the crater and are observed on both volatile-dominated and volatile-enhanced surfaces (e.g. Mars [90, 189] and Ceres [188]). Be that as it may, the precise morphology of these features is seen to differ slightly from body to body [187]. This has led to differing formation mechanisms being proposed for each body, with volatile explosion processes currently being favoured for Martian pits [189], impact-induced cryovolcanism being favoured for pits on Ceres [188], and melt drainage being favoured for icy satellites [120]. At larger sizes, on icy satellites, pits are seen to take on anomalous forms. Observations have identified degraded features [195] with pits appearing to take up larger fractions of the crater floor [195, 196]. Differences are also seen to form on volatile-enhanced target surfaces with Martian pits have also been seen to possess several apparent levels of degradation (shown in figure 3.2).

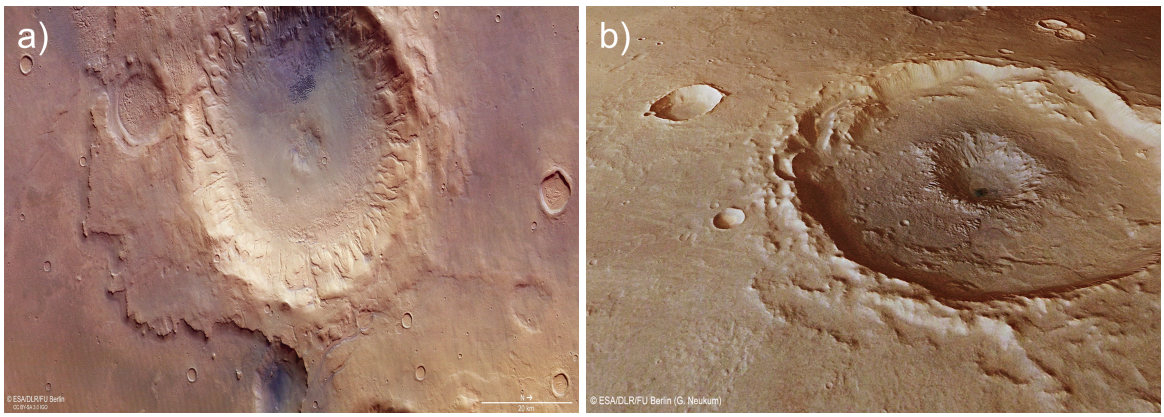

Figure 3.2: Central pits within Martian craters possessing a range of varying degradation states. Panel a) shows a heavily degraded central pit within a 50 km diameter crater located close to Mare Serpentis on Mars [197]. Panel b) shows a well preserved central pit feature within a 50 km diameter crater located within Thaumasia Planum. Image source: ESA/DLR/FU Berlin.

As the crater diameter continues to grow, observed central pits are seen to possess formed domes on surfaces possessing substantial quantities of ice. [120, 195]. These features are currently found to dominate on icy surfaces [120, 187, 195], becoming increasingly rare as the silicate contamination

of the icy surface is thought to increase (discussed more in section 3.5) [195]. Whilst the features, thought to be indicative to the presence of volatiles (specifically water-ice) within a target surface, are not universally observed across both ice-dominated and enhanced targets [100]. The variations in distribution and morphology are likely to provide an observational proxy to probe to the ice content of a surface based on the crater morphology. Despite the features observed within complex crater morphology being the most widely distributed, differences in crater morphology due to the presence of volatiles are also seen at even the largest crater sizes [3]. The largest complex craters undergo a transition to an impact basin. This scale of crater is usually surrounded by multiple rims, and are thought to form through a different process to either simple or complex craters, with the interior structure of the target body being thought to play a much more significant role [3, 121]. This is discussed further in the next section.

3.2.2 Multi-ring Basins

Previously misidentified as a continuation of the size-evolution of impact craters, multi-ring basins lie outside this continuum as their own distinct class with still somewhat unclear conditions determining their formation. These basins are commonly the largest impact-related features found on a planetary surface [3, 121, 122, 198], possessing multiple rings beyond the extent of the original crater rim [3, 121, 122]. The formation of these larger features is found not to scale with the inverse of gravity [3], differentiating them from other classes of impact craters with substantial differences seen between those identified on 'rocky' bodies and those on 'icy' bodies [3, 122]. Hence, multi-ring basins can be classified into two types: Orientale (rocky body) type or Valhalla (icy body) type [3, 121, 122]; respectively named after the Orientale Basin on the Moon and the Valhalla Basin on Callisto with significantly less surface relief in the Valhalla-type basins (examples of both are shown in figure 3.3). These very large-scale features are found to be exceedingly rare with their existence only being currently confirmed on Callisto, Ganymede, and the Moon [3, 121]. Some are, however, additionally suggested to be present on the surfaces of Mercury, Mars, and the Earth [3, 122] but their existence is still somewhat disputed as large basins on these bodies typically lack the external rings required [122].

Orientale (rocky body) type basins possess multiple, outward facing scarps beyond the original crater rim, with the distance between consecutive rings typically satisfying an approximate relationship of $1 : \sqrt{2}$ [3]. Contrastingly, Valhalla (icy body) type basins have been seen to possess a significant number (up to hundreds) of inward facing scarps beyond the crater rim, with no relation yet identified for the distance between consecutive rings [3]. Whilst variation in the ring morphology for each type of multi-ring feature may indicate a slight variation in formation mechanism, currently accepted formation models rely on the ring tectonic theory of formation [121, 198, 201]. This theory allocates a controlling role in multi-ring basin formation to the thickness and structure of a target's internal layering [121, 122], with more current numerical modelling of Orientale type basin formation on the lunar surface additionally highlighting the role played by the thermophysical properties of the

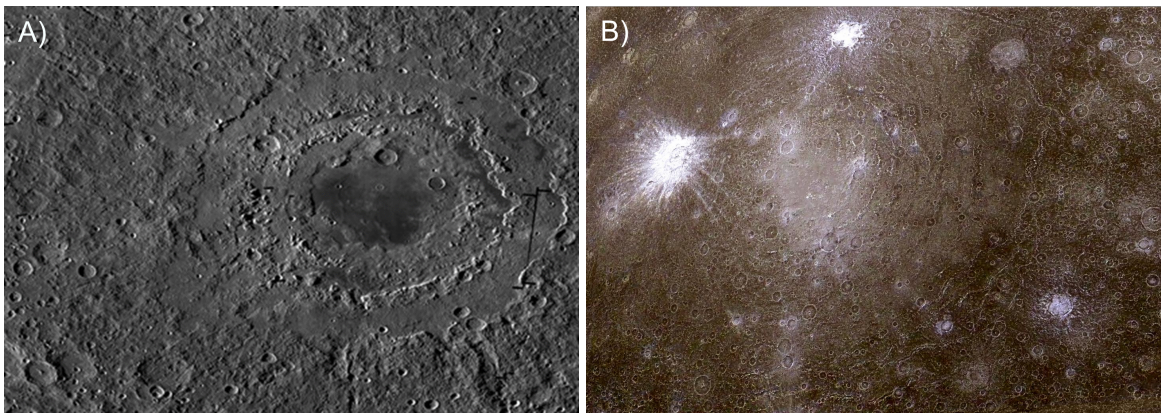

Figure 3.3: A) 950 km diameter Orientale-type, Orientale Basin on the lunar surface [199]. B) 1600 km diameter Valhalla-type, Asgard Basin on Callisto [200].

target material [198, 201]. Such dependencies would explain both the variation seen between icy and rocky target body multi-ring basins, as well as why similarly sized (or even larger) impact features have been identified on both Callisto and the lunar surfaces without falling into the class of a multi-ring basin [122].

3.3 Crater Ejecta Deposits

The region surrounding a fresh impact crater presents a typically large deposit of material (termed ejecta) removed from within the crater during the formation process [2, 3, 7, 122]. Ejecta proximal to the crater rim almost always presents as a thick continuous blanket having obscured the underlying topography [3, 7]; whereas more distal ejecta is typically found to become thin and discontinuous, grading into the surrounding terrain [3]. The continuous ejecta deposits surrounding some craters, however, are seen to extend much further from the crater rim than for others [3,7,71,99,190,202,203]. Such ejecta deposits (commonly referred to as fluidised ejecta deposits [71]) are thought to be due to the influence of volatile materials on the crater formation and ejecta deposition processes [7, 71, 99, 190]. Further observations have additionally posited that such morphologies can form due to interactions between an advancing ejecta curtain and atmospheric vortices [3,7,91,203]. Identification of apparent fluidised ejecta deposits on bodies possessing only a tenuous exosphere [99, 190, 204], however, have further enhanced the link between such deposits and the presence of volatile materials in the impact cratering process. As such, this apparent correlation, has allowed for fluidised ejecta to be used as a proxy for the inference of volatiles within the target surface.

3.3.1 Abrupt Terminus Ejecta (ATE) Deposits

Since having first been identified on the Martian surface [71, 99], craters possessing potentially fluidised deposits have been identified on the surface of all major bodies within the inner Solar System [190, 202–204]. Additionally, fluidised deposits are suspected to have been present surrounding some terrestrial impact features [7], although the presence of active, short timescale erosional pro-

cesses make ejecta deposits surrounding terrestrial impact features increasingly difficult to identify or classify [7,99]. Whilst extensive analysis of inner Solar System bodies has shown that the Martian surface presents the most extensive collection of fluidised-appearing craters, this population shall not be covered here, having already been discussed in Section 1.6.2 in greater detail. Observation, and analysis of impact features (and their surrounding ejecta deposits) provides a way to probe the structure of both planetary interiors and crusts [1, 115]. Fluidised-appearing ejecta deposits are of particular importance for the work presented here, due to their common attribution to the presence of volatile materials within a planetary sub-surface region.

The extensive variation shown in environmental conditions that fluidised-appearing ejecta is seen within, mean a single formation mechanism cannot be agreed upon [3, 7, 99, 190]. Initial investigations undertaken by Barlow, *et al.* [71] proposed formation via either interaction with volatile material or atmospheric vortices during the crater formation process. However, as already stated the identification of such deposits on bodies possessing only a tenuous exosphere, diminishes the role of atmospheric interactions within the formation process [99,190,202,205]. Additionally, identification of fluidised ejecta on volatile-poor bodies (Mercury [202, 204], Venus [203], and the Moon [99]) induces doubts regarding the role of volatile materials within the formation process of such ejecta materials. Removing the implied attribution to volatile material or atmospheric interactions in previous naming conventions, Robbins, *et al.* [99] introduced the terminology of Abrupt Terminus Ejecta (ATE). This collates past separate terminologies for continuous ejecta blankets under a single umbrella, many of which are utilised to describe precise morphological features associated with this type of ejecta deposit [71, 99].

3.3.2 Formation Without Target Volatiles

The currently proposed formation mechanisms for ATE deposits are heavily focused on the role of volatiles within the target surface [71, 190, 202]. Identification of ATE-appearing deposits on the surfaces of both Mercury [202,204] and Venus [203,206], however, has introduced substantial doubt into whether target volatile formation mechanisms can be universally applied. Investigation of the deposits found on Mercury and Venus has increased the level of interest in formation mechanisms focusing on the presence of volatiles within the projectile [204] and atmospheric interactions [83,203]. Whilst both of these formation mechanisms were initially considered before the identification of ATE-appearing deposits on Mercury and Venus, these discoveries have provided continued support for the alternate formation processes. The surfaces of the two innermost planets are harsh environments, with Mercury possessing only a tenuous exosphere and a surface temperature range of $93 - 703$ K, whilst Venus has an atmospheric pressure of ≈ 91 atm and a mean surface temperature of 737 K [207]. Both provide extremely volatile-poor cratering environments (although there is some ice in permanently shadowed regions on Mercury [202,204,208–210]) [206,211]. Whilst the features identified on Mercury and Venus do posses some morphological variations from those seen on Mars and throughout the outer Solar System, they are similar enough to fall under the umbrella of ATE deposits.

3.3.2.1 Volatile-Rich Projectiles

Whilst the focus of many proposed ATE formation mechanisms are based on the presence of volatile materials within the target surface, the identification of ATE-appearing deposits surrounding Hokusai crater on Mercury has led some to consider how the presence of volatiles within an impacting projectile would influence the ejecta formation process [99, 202, 204]. Even though projectile volatiles are a formation mechanism requiring the presence of volatiles, this idea of their being in the projectile may explain the rare presence of ATE-appearing deposits on bodies known to be volatile-poor. Despite the projectile being largely vaporised during the initial contact and compression phase, it is known that fragments can become emplaced within the target [6, 212–214]. It has also been suggested that volatiles emplaced on the target surface originating within the projectile may then undergo migration processes [204], explaining the ice having been detected in permanently shadowed regions of both the lunar [109] and Mercurian [204] poles. It is not unreasonable, therefore, to investigate the assumption that these volatile materials could influence the ejecta emplacement process. Robbins, *et al.* [99], however, caution that the presence of volatiles within a projectile is unlikely to be a significant contributor to the formation of ATE craters due to their limited quantity and the extent of material fluidised during crater formation.

Projectile-based volatiles being a driving force behind the formation of ATE craters would lead to their preferential presence on outer Solar System surfaces [99]. Whilst ATE-appearing deposits are commonly observed on Pluto and numerous moon and small bodies in the outer Solar System, the largest population by far is currently found on the surface of Mars [94, 215]. Mars, however, is known to host a volatile-enhanced surface. Hence, this cannot rule out the potential influence of projectile-based volatiles within the formation of ATE deposits. The relative scarcity of volatile-rich projectiles impacting the surfaces of inner Solar System bodies may go some way to explaining the rarity of ATE-appearing deposits on surfaces known to be depleted in volatiles. The impact of a volatile-rich projectile is also the only mechanism currently known to sufficiently account for the quantities of ice observed on both the lunar and Mercurian surfaces [109, 204, 216]. This is particularly true for the deposits observed within the permanently shadowed regions at the north Mercurian pole. The ice detected within these regions is thought to be relatively pure (based on radio telescope observations of this region on Mercury [208]), indicative of deposition over a short period of time, likely by a single event [204], such as the impact of an ice-rich projectile.

3.3.2.2 Atmospheric Interactions

Some of the earliest formation mechanisms proposed for ATE deposits are based on interactions with an atmosphere [3, 71, 192, 217]. Due to deposits initially being identified on the surface of Mars, it was suggested that they formed due to aeolian erosion [71]. Their global distribution, and identification on Ceres [190] and outer Solar System moons (all known to be extremely volatile-rich), however, was a major problem for this proposed formation mechanism. Studies of these ejecta deposits on Mars has, nevertheless, still considered the potential influence of atmospheric interaction during the

emplacement process [192, 217]. It has been suggested that vortices within the atmosphere may interact with a propagating cloud of ejecta material [3, 203]. This is thought to lead to a down-surge of material causing it to be deposited as a smooth layer across the planet surface, rather than it being deposited radially as would be expected on airless bodies [3, 129, 206]. Aiding this suggested formation mechanism is the identification of ATE-appearing deposits on Venus [203, 206, 211]. The conditions on Venus provide a volatile-poor environment for impact cratering [203, 206]; even when considering the possibility of non-traditional volatiles.

Venus does, however, have a significantly high atmospheric pressure at the surface [203, 207], which is thought to efficiently constrain the ejecta material as it is removed from the crater, forcing it to flow along the surface rather than following a ballistic trajectory [203, 206]; forming ATE-appearing deposits. Despite being identified as ejecta deposits, these materials are seen to be rheologically similar to fresh lava flows on Earth [211]. Their morphology, however, is similar to that of the ATE deposits seen on Mars. The cratering environments on Mars and Venus, however, are very different. Therefore, despite the ATE-appearing deposits having morphological similarities, is is unlikely that their formation mechanism is the same. Whilst aeolian mechanisms have been considered, the global distribution makes these processes unlikely to be a driving factor. Further, not all craters on the surface of Mars are seen to have ATE deposits [16,20,22,71,77,83]. Thus, whilst it is possible that these interactions may have played a role, it is unlikely that interactions between an ejecta cloud and the Martian atmosphere would have provided a major contribution to the formation of ATE material in general.

3.4 Central Pit Craters

Central pit craters have been found across the Solar System (Table 3.1), being confirmed on: Mercury [187, 218]; the Moon [219]; Mars [83, 90, 185, 187, 189]; Ceres [183, 188]; the Galilean satellites of Callisto, and Ganymede [100, 120, 185, 187, 188]; and Pluto [187], with evidence additionally suggesting their presence on some Saturnian and Uranian satellites [187, 194]. Examples of central pit craters are shown in Figures 3.2 and 3.4. Pits are observed as irregular-to-circular depressions in the central regions of their host craters [83, 183, 185, 187, 218], being located either directly on the crater floor, or upon a central peak feature [185, 187, 218, 219]. Multiple formation mechanisms have been proposed for central pit craters [90, 100, 185]; all, however, fail to fully explain variations across bodies showing central pit craters (summit and floor pits on Mars [187], changes in pit-to-crater diameter ratios [195], etc.). Further, the relative abundance of central pits identified on volatile-enriched target bodies as opposed to the apparent deficit found upon volatile-poor targets, somewhat swayed the focus of many onto the role of volatiles within the formation process [83, 120, 185, 187, 189, 218, 219]. Notwithstanding this, subtle differences in pit morphology found throughout the Solar System indicate variations in pit formation from body to body, or a combined mechanism [185, 219] - analogous to that posed for the formation of ATE-appearing ejecta.

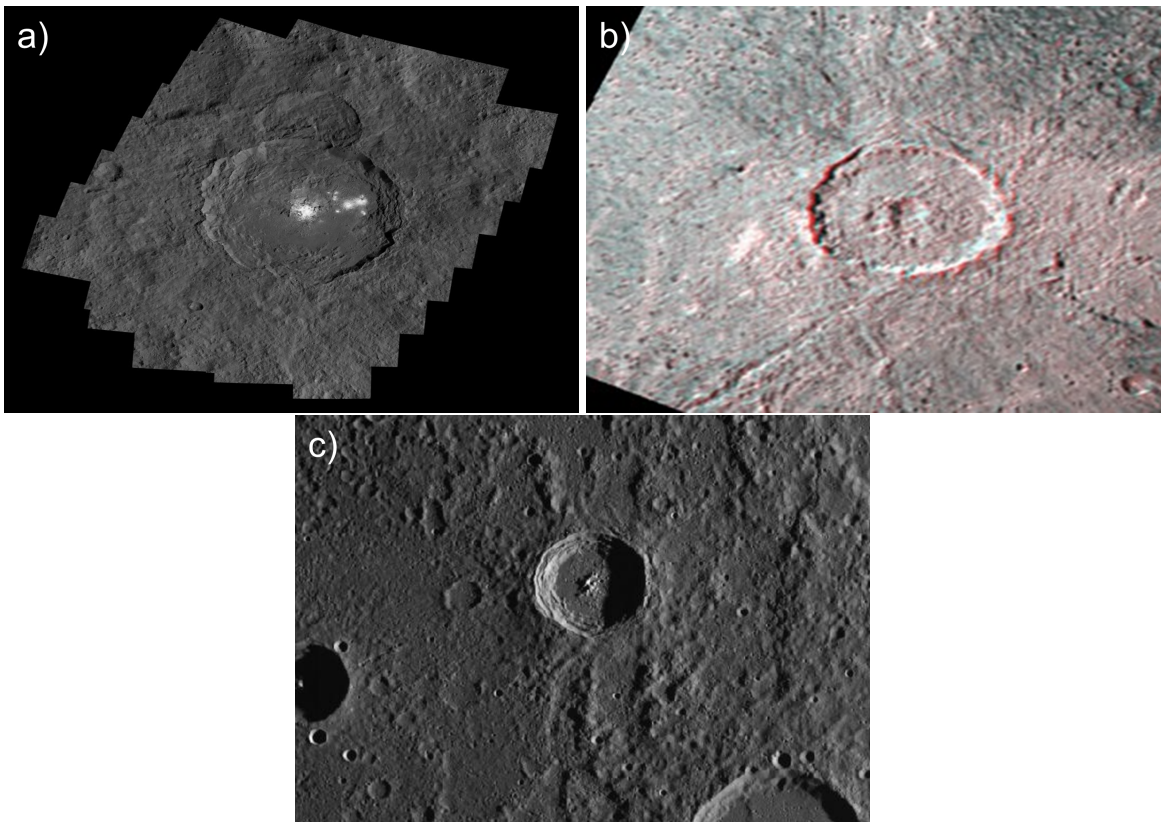

Figure 3.4: Central pit craters throughout the solar system. Panel a) shows a mosaic of the 92 km diameter Occator crater on Ceres imaged by the Dawn spacecraft [220]. Panel b) shows the 75 km diameter Isis crater imaged by voyager 2 on Ganymede [221]. Panel c) shows an unnamed summit pit within a 25 km diameter crater located on Mercury imaged by MESSENGER [222].

Table 3.1: Central pit crater characteristics for identified populations throughout the Solar System. In the table, Δ_{pit} denotes the pit-to-crater diameter ratio.

Body	Central pit population	Summit/floor pits	Crater diameter range (km)	Δ_{pit}
		Inner Solar System		
Mercury [218]	$27-32$	Summit	$16-33$	$0.12-0.26$
Moon [219]	56	Summit and floor	$9-57$	$0.05-0.29$
Mars [90]	1783	Summit and floor	$5-125$	$0.02-0.48$
Ceres [188]	11	Floor	$70-150$	$0.1-0.2$
		Outer Solar System		
Ganymede [120]	471	Floor	$12-144$	$0.11-0.38$
Callisto [120]	unspecified	Floor	$43-159$	$0.1-> 0.5$
Tethys [187]	2	Unspecified	≈ 450	$0.26-0.42$
Rhea [187]	2	Unspecified	Unspecified	0.24
Dione [187]	2	Unspecified	Unspecified	0.22

3.4.1 Volatile-Rich Targets

Voyager and Galileo spacecraft images revealed the crater populations of Ganymede and Callisto to be dominated by central pit craters, particularly within their populations of large impact craters [100, 120, 185, 187]. In the diameter range of $30 - 180$ km, almost all craters on Callisto are observed to possess a central pit morphology [120]; with an additional 471 central pit craters having been identified on the surface of Ganymede in the diameter range of $12 - 144$ km [187]. In contrast to Ganymede and Callisto, no central pit craters are observed on the surface of Europa [100] with the final Galilean moon of Io having a very small population of craters if any, as expected due to the extreme level of volcanic activity [223–225]. Central pit craters on the Galilean moons can typically be classified as either small or large pit craters, with smaller pits commonly being rimmed and large pits being partially or non-rimmed [120]. Craters are classified based on their pit-to-crater diameter ratio (Δ_{pit}), see Table 3.1. Small pit craters are observed to have Δ_{pit} values ranging between $0.1 - 0.45$, whilst large pit craters possess Δ_{pit} values > 0.5 [120]. Analysis of the surfaces of these bodies have found the largest difference between the pit classifications to be the relative age of the impact crater [120]. Additionally, both small and large pit craters commonly possess characteristic morphological features (see below), aiding in their classification [120, 185, 187].

Morphological features associated with small pit host craters are found to be fresh with their topography being well preserved. Large pit host craters on the other hand, are observed to be much more degraded with an often difficult to distinguish topography [120]. The distribution of central pit craters has been extensively investigated on the surface of Ganymede. Initial observations found that central pit craters appeared to be concentrated both closer toward the equator, and within the western hemisphere of the moon [185, 187]. However, these trends are thought to be at least partially representative of differing imaging resolutions across the Ganymedean surface, with the equatorial and leading hemisphere regions having been imaged at higher resolutions [185]. Additional contributions to the western-eastern hemisphere difference in central pit crater density may come from the apex-antapex asymmetry [185, 187], with the overall crater density in the western hemisphere being around four times that of the eastern [187]. Similar investigations into the central pit crater population of Callisto likewise found that no trends within the distribution were observed [120]. The host craters of almost all central pits on the icy satellites of Ganymede and Callisto are typically found to be upbowed [100, 120, 187], contrasting the typically flat floors found in complex impact crater features further reducing the crater depth (section 3.2.1).

Limited observations of the remaining outer Solar System icy body population has restricted possible classification of crater morphology on many bodies. Despite this, several Saturnian and Uranian satellites, along with Pluto, have been suggested to host central pit craters [120, 185, 187]. Around Saturn, the moons Dione, Tethys, and Rhea are thought to present central pit morphologies inside some craters [187]; with Tirawa crater on Rhea, and Odysseus crater on Tethys being the best examples [120]. Titania (a Uranian satellite) is additionally suggested to present central pit morphologies

within Gertrude and Ursula craters [120, 187], both displaying complex ring structure morphologies within the crater central regions [120]. Observations of other icy satellites around Saturn, Uranus, and Neptune reveal no obvious further central pit crater populations [187], with larger craters on other icy satellites being typically identified as central peak craters [120]. As central pit craters are complex crater features, the formation of which commonly occurs during gravitational collapse, it can be theorised that central pit morphologies would not be expected on smaller satellites due to their lower surface gravitational accelerations [185, 187]. However, when considering the Uranian and Neptunian satellite collections, image resolution severely limits the identification of surface features [120, 185, 187].

3.4.2 Volatile-Enhanced Targets (Mars and Ceres)

Images obtained during the Mariner 9 fly-bys, and subsequent spacecraft missions to Mars, have consistently allowed for the identification of a continually increasing number of central pit craters on the planet's surface [187]. Whilst the population of central pit craters found on Mars is larger than those found elsewhere [77,83,90,185,187–189], the morphology is by no means dominant within the host crater diameter range between which they are found [185, 188]. A population of ≈ 1783 central pit craters [187] is found between the diameters of $5 - 125$ km [77, 90, 185, 189] (of an approximate $43,000$ craters in that diameter range [96]); with the population being additionally split between floor or summit pits, based on the level of the pit floor relative to the surrounding crater floor [185]. Martian central pit craters are distributed between $\pm 70^{\circ}$ latitude [90, 189], with an apparent concentration for the mid to low latitude regions ($\pm 40^{\circ}$ [90]); with only minor correlations seen for both central pit types [90, 185, 187]. Central pits of both types are more common within older and non-volcanic regions of terrain on Mars, with a notable lack of central pit (and central peak) craters on younger volcanic plains, such as Tharsis and Elysium [90, 187]. Within regions presenting a paucity of central pit craters, floor pits are found to be more common than their summit pit counterparts [187].

The Cerean crater population spanning $70 - 150$ km in diameter, as observed within Dawn images, show central pits to be the dominant central morphological feature [183, 188]. The identification of central pits in craters over a range of preservation levels across the Cerean surface indicates the conditions required for their formation were present over much of Ceres' geological past [183]. Despite forming the dominant crater morphology within this size range, only eleven central pit craters are observed on the Cerean surface [188]. Similarly to Mars, Cerean central pit craters are suggested to present both floor and summit pit craters [183, 188]. However, similarly to Ganymede (as suggested by Alzate *et al.* [185]), Cerean summit pits appear to be morphologically similar to rimmed floor pits [188]. Many central pit rims appear to be asymmetric or incomplete, displaying features interpreted to be uplift massifs around regions of the central pit [183, 188], which in turn display amphitheater appearances orientated toward the central pit [188]. Smaller craters on the surface of Ceres (between $50 - 70$ km in diameter) are observed to have disrupted or partially collapsed central peak features, commonly assumed to be precursors to a central pit [188]. The Cerean central

pit population shares morphological features with both Mars, and the icy satellite bodies [183, 188], providing a bridge between the two regions of the Solar System.

3.4.3 Volatile-Poor Targets

Hypothesised formation mechanisms for central pit craters typically rely on the substantial presence of volatile materials within the target. As such, the identification of central pit craters on both the Mercurian and lunar surfaces [187, 218, 219] (with ≈ 37 on Mercury, and $59 - 91$ being identified on the Moon), provides considerable complications for studies into their formation. Whilst both summit and floor pits are observed on the Moon [219], only summit pits have been identified on Mercury [187, 218]. Summit pit craters, however, are considerably more dominant on the lunar surface compared to their floor pit counterparts [219]. This sway toward favouring summit pits over floor pits, presents a difference from central pit craters present in other regions of the Solar System. Similarly to other Solar System bodies, lunar central pit craters are observed within craters spanning multiple degradation stages. They are thus thought to have formed through several geological ages indicating formation conditions required for lunar central pits have existed for a substantial portion of the Moon's history [219]. Contradictorily, Mercurian central pit craters have been observed only as fresh craters (commonly observed to still possess extensive crater ray systems) [218, 219]; presenting a clear difference between Mercurian pits and those elsewhere.

Lunar central pit craters present multiple variations from the populations identified on other bodies [219]. Whilst central pits are almost exclusively a feature seen in complex impact features, several on the lunar surface are seen to have formed in simple craters. Additionally, the lunar pit population appears to show a slight geographical correlation particularly within the distribution of floor pit craters, with many being found on the ejecta deposits of larger, older craters. Central pits on Mercury are found to be heavily focused within the northern hemisphere [218]. They are, however, found to show no correlation with other Mercurian features thought to be associated with volatile processes [187] (hollows [218] and bright radar features in permanently shadowed craters thought to be water-ice [204]). This lack of correlation has led to the conclusions, contradicting those made for other central pit populations, that 1) Mercurian central pits are not formed through volatile interactions, and 2) they are a morphological feature distinctly outside of the typical crater size morphology evolution [187, 218]. Furthermore, many central pit craters on the surface of Mercury are observed to have formed on plains interpreted as being volcanic in nature, and are thus likely heavily depleted in volatile materials relative to the Mercurian surface [218].

3.4.4 Formation Mechanisms

As already stated, a range of formation processes have been hypothesised to explain the formation of central pit features within host craters [90, 100, 120, 185, 187–189, 218, 219]. Many of these rely on the presence of volatiles (e.g. melt-contact [189] and steam explosion [90, 189] models); some, however, have attempted to explain the formation of depressions without the use of volatile mate-

rials (e.g. peak collapse [100, 185, 189] and floor rebound [219] models). Currently, no model is capable of fully explaining all observed features [90, 100, 189]. As such, many speculate that central depression formation mechanisms may vary, both between bodies, and across the surface of the same body [90, 188, 219], or that pits are formed through a combination of several processes rather than having a single controlling factor [90]. Furthermore, it has been posited that the properties of the impact event (impactor composition, impact velocity, etc.) may present a non-negligible influence over the formation of central pit craters [120, 185, 187, 218]. Current proposed methods often lack observational/experimental evidence to support their propositions [100, 120, 187]. The remainder of this section provides a brief overview of the main hypotheses developed thus far, attempting to somewhat explain the underlying mechanisms for central pit formation.

3.4.4.1 Volatile-Based Formation

Initial observations and analyses of central pit features within some Martian craters led to the proposition of an explosive origin controlled by the presence of volatile materials throughout the near-surface region [90, 189, 218] within excavation depth of the formed craters [90, 185]. TES and THEMIS (Thermal Emission Spectrometer onboard Mars Global Surveyor and THermal EMission Imaging Spectrometer onboard the Mars Odyssey spacecraft respectively) thermal inertia measurements of material surrounding many Martian pits supported an explosive origin for central features [90, 188]. However, the lack of morphological rim features around some pits on Mars, and elsewhere in the Solar System, cannot be explained through an explosive volatile release formation method alone [189, 218]. Furthermore, analyses of central pits within icy satellite craters, find no evidence supporting the formation of central pits through the explosive release of near-surface volatile materials [188]. Providing additional complication to an explosive release formation method for central pits, current models struggle to retain sufficient vaporised/melted volatile material generated early in the crater formation process to allow for the explosive release to occur [185, 189, 218]. To solve this issue, Williams *et al.* [189] proposed a melt-contact model. In this model, volatile-rich material uplifted from below the crater floor comes into contact with impact-generated melt, leading to the build-up of 'steam' and the explosive release of volatiles during the later modification stage of crater formation.

A different model notes that material underlying the central region of the crater becomes heavily brecciated during the crater formation process [152, 154, 156]. This broken and fractured material may allow for the drainage of impact-generated melt or melted volatile material below the crater, or from within the central peak. This drainage produces a void below the crater, subsequently collapsing the crater floor and central peak, leading to the formation of a central pit feature [90, 185, 218, 219]. Whilst the presence of volatile material within the target near-surface is not necessarily required for melt-drainage formation processes [185], the inclusion of melted volatiles within target material may enhance the ability of impact melt to drain below the crater cavity [90, 219]. This allows a larger void space to form below the crater cavity, enabling the central regions to collapse, leading to the formation of central pit craters. Complexities arise when considering such a model, however, when

attempting to account for the existence of pit rim features [189]; typically, collapse processes are unable to form topographic relief rims [83, 120]. Hence, similarly to the proposed explosive volatile release mechanism, the melt-drainage formation process is unable to account for all characteristic morphological features associated with central pit craters [90].

Alongside the explosive volatile release and melt-drainage models, several other influencing factors (target rheology, surface temperature, thermal gradient, etc.) have been proposed to aid or hinder the formation of central pit features [185, 187, 188]. During a cratering event on an icy satellite, a central plug of shock-compressed material is thought to form at the bottom of the transient cavity [100, 185, 188, 218], particularly during impacts of cometary projectiles [100, 185]. Some speculate this plug plays a key role in the formation of central pit craters on outer Solar System icy satellites [188]. At sufficient temperatures, material within and around the icy plug likely undergoes melting over substantial periods of time, generating melt water that drains from the central region of the crater, inducing collapse [185]. This variation on the standard melt-drainage formation model relies on the unique mechanism behind the central plug seen within numerical modelling of crater formation in icy targets using multi-phase equations of state for water [100, 188]. There is currently no observational or experimental evidence for this process thus, it relies on typically poor equations of state for ice [100]. Despite this, and the extensive study invested into both the explosive release and melt-drainage models, observations of Saturnian and Uranian satellites, along with other icy bodies in the outer Solar System bring the role of volatiles within central pit formation into question [187]. The Saturnian satellites of Rhea, Dione, and Tethys present substantially fewer central pit craters than would be expected based on their compositions, with the Odysseus Crater pit on Tethys being the only central pit crater thought to be present [187, 188]. Additionally, when considering the onset diameter for pit formation to begin, central pits on Tethys and Titania are found to break the inverse-gravity scaling relationship followed by the vast majority of other crater morphology features [188].

3.4.4.2 Non-Volatile-Based Formation

The identification of central pits on the surfaces of Mercury and the Moon threw into contention ideas surrounding the requirement of a volatile-rich target for their formation [90, 185, 187, 218, 219]. Hypotheses considering the formation of such features in volatile-depleted targets focused heavily on the collapse of central peaks. Prior to, and during, the uplift process responsible for the formation of a central peak, the material may become heavily brecciated and fractured [2, 3, 129, 152]. Brecciation and/or fracturing is likely to reduce the effective strength of the target material forming the central peak reducing its ability to support its own weight as it is uplifted [90, 120, 185, 189], with the formation of floor/summit pits being attributed to the complete/lesser collapse of the peak structure respectively [90, 185]. Floor rebound based models have also been suggested to be key to the formation of central pit craters on both the Mercurian and lunar surfaces [120, 218, 219], a slight variation on the peak collapse model. Central peak structures are suggested to collapse due to the presence of a competent material layer overlying the brecciated core material. This competent layer is not

only uplifted at a slower rate but also to a lesser extent. The spilling out of the brecciated material produces only a weak peak which subsequently collapses [219]. This differs from the standard peak collapse model as peak collapse during the floor rebound model occurs at smaller peak sizes, relying on the material strength rather than the gravitational instability alone.

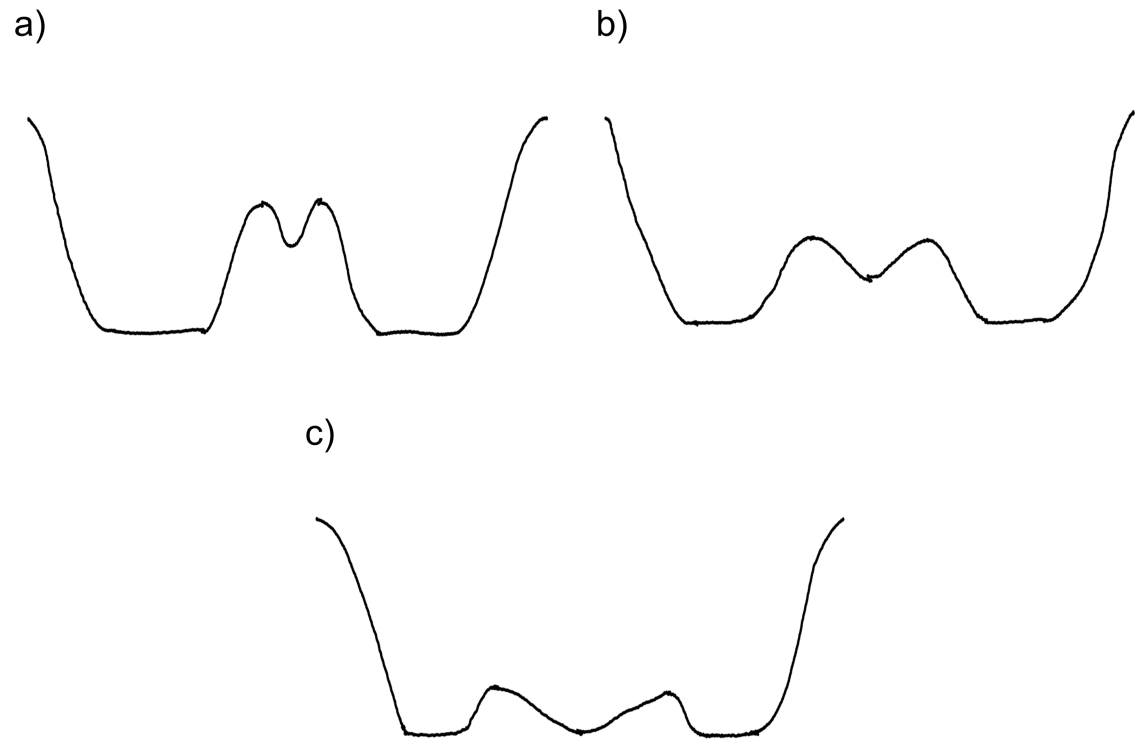

Figure 3.5: Stages of peak collapse for the formation of central pits without the presence of volatiles. Panel a) shows the initial collapse at the point where the peak becomes gravitationally unstable thought to lead to formation of summit pits. Panel b) shows the peak having undergone a partial level of collapse leading to the production of a larger summit pit. Panel c) shows the results of a complete peak collapse producing a floor pit.

Despite the extensive study and wide reaching support for the peak collapse model, it still fails to fully explain observed central pit features [90, 120, 188, 189, 219]. The considerable overlap, often possessed between the geographical distributions of central pit and peak craters, indicates collapse processes alone cannot be responsible for the formation of central pits within craters [189]. Hence, the idea of internal layering within the target has gained popularity over time [185, 187–189]. Layers possessing varying rheological properties within the target have been shown to aid in the formation of central pit features [185, 189]. The uplifting of layers within the central region of the forming crater leads to the preferential displacement of brittle material as more ductile layers interact with it [188], as was seen in numerical models applied to the crust of Ceres and outer solar system icy satellites. Such interactions may induce separation between the central peak and the crater floor [189], leaving a pit-like feature behind. Whilst internal layering of the target provides an explanation for pits observed to be considerably younger than their host crater (such as Occator pit [188]), layer-based pit formation

models have so far shown it to preferentially form central pits within smaller craters [185, 189] with the effect of internal layering on the crater formation process reducing as the crater size increases [3, 189]. As such, the applicability of layer-based pit formation models is uncertain at best on planetary scales [185, 188].

To provide a volatile-free variation on the melt-drainage pit formation model, it has been proposed that drainage of impact-generated melt from within/below the impact cavity can induce the collapse of the central region, forming pit-like features [185, 187, 188, 218, 219]. Melt produced during the impact event is proposed to drain through sub-surface fractures, generating a sub-crater void space. In contrast to the previously discussed drainage model, this volatile-free model relies solely on impact-generated melt rocks [185, 188, 219]. Such melt, however, is likely to cool and solidify before a substantial volume is able to escape through fractures before re-solidifying [188, 218, 219]. Thus, a volatile-free melt-drainage model is unlikely to lead to the generation of central pits. Higher energy impacts are thought to produce larger quantities of impact melt [1, 3]. This larger quantity of energy deposited within the target may allow the generated melt to remain liquid for a longer time; potentially allowing a significant quantity of melt to drain below the crater [218, 219]. Much of this work, however, has been observation based. As such, little has been done to quantify the increase in impact velocity required to allow a significant portion of melt to drain before re-solidification occurs.

In general, the lack of consensus regarding the formation model responsible for central pit formation, even after extensive study, implies a combination of formation mechanisms are likely to be behind the formation of central depressions.

3.5 Central Dome Craters

Having been observed on the surfaces of Ceres [188], and the icy satellites of Ganymede and Callisto [120, 195, 196], central dome craters are currently thought of as the next step in the size evolution for craters forming on ice-dominated surfaces [185, 195]. They possess an interior morphology similar to that of central pit craters [195], leading to the assumption that the two are linked [195, 196]. Within the pit, however, central dome craters posses a large steep-sided dome [120, 185, 196]; typically filling the majority of the pit floor [196]. Central dome craters are most common on Ganymede, being the dominant crater morphology in the $60 - 180$ km diameter range [185, 195]. This dominance is lost when moving to Callisto, with a relative paucity of central dome craters observed on this surface [196]. The population size drops even further on Ceres, with only a single dome being observed (within Occator crater [188]). This substantial decrease in population size, particularly between Ganymede and Callisto, has been suggested to link to the purity level of the icy surface [120, 196]. Ganymede is thought to possess an almost pure water-ice crust, whilst both Callisto and Ceres are thought to possess ice-silicate surfaces [188, 196]. Little work has been carried out to investigate the effects other properties (salinity, homogeneity of ice material, etc.) have on the production of central domes. Whilst this potential link provides little to enable a formation mechanism to be identified, it may provide an

insight into the quantity of ice within an ice-silicate mixture surface.



Figure 3.6: The $160\ \mathrm{km}$ diameter crater Neith on Ganymede. An example of a central dome crater, imaged by the Solid-State Imager onboard the Galileo spacecraft [226].

Proposed formation mechanisms for central domes heavily depend on the presence of water-ice within the target surface [120, 185, 195]. The most common proposed methods typically rely on impact-induced/enhanced processes (melt lake formation [120], cryovolcanism [196], etc.), or long-term responses of ice-dominated material to the impact process (isostatic upwarping [188], or topographic relaxation [195]). Whilst it has been suggested that a difference in formation mechanisms may be required to explain dome formation on Ceres due to the singular dome there [188, 195], it is still largely assumed that domes on Ganymede, Callisto, and Ceres form via the same mechanism [188, 195]. Thus, the lack of central dome craters observed on the Martian surface allows an approximate upper limit on the quantity of ice within the Northern Lowlands to be defined. Taking Ceres as the end-member state for suppressing the formation of domes, one can say that Mars should have an ice content of $< 25\ \mathrm{wt.}\%$ [183].

3.6 Conclusions

This chapter has presented a review of impact crater morphological features typically related to the presence of volatiles within the target surface. For many of these features, however, variations exist which are unable to be explained by volatile-based formation mechanisms alone (e.g. ATE deposits on Mercury and Venus and central pits on volatile-poor bodies). Hence, despite the heavy focus on the role of volatiles within previous formation mechanisms, many have investigated the potential formation of these features with no volatiles present. Currently, no single formation mechanism can explain all of the observations across the solar system, indicating that a variety of methods may be capable of producing similar features. This has particularly been the case with central pit features, which have been observed on a large number of planets and satellites presenting drastically different surface and cratering environments. Central dome craters, on the other hand, have so far only been observed on bodies possessing a significant quantity of ice, indicating it to be vital to their formation. Following this discussion, In this thesis we now investigate the crater process within Martian permafrost experimentally, with the formation mechanisms proposed here enabling insights to be made into the observed crater morphologies.

Chapter 4

Experimental Equipment

"Step boldly onto the path,
and let your adventures begin"
The Voice of Tomorrow

4.1 Light Gas Gun (LGG)

Initially having been developed following the end of the Second World War [3, 227, 228], multi-stage Light-Gas Guns (LGGs) (in particular two-stage LGGs (2S-LGGs) [229]) became the most common method of replicating hypervelocity impact (HVI) processes [229, 230]. They allow for high-speed phenomena to be investigated under laboratory conditions, accelerating typically $\mathrm{mm} - \mathrm{cm}$ sized projectiles to speeds of several $\mathrm{km\ s^{-1}}$ [227,229–231]. Whilst the precise muzzle velocity of the LGG depends on the complex relation between a considerable number of parameters (propellant type, piston mass, initial working gas pressure, etc.) [232], 2S-LGGs in use today reliably cover the $1 - 9\ \mathrm{km\ s^{-1}}$ velocity range [227, 233]. The lower end of this speed range has traditionally marked the definition for a HVI event [231, 234]; more recent analysis, however, has suggested that a collision might not be classed as an HVI until the speed reaches $\geq 3\ \mathrm{km\ s^{-1}}$ [227], a speed still comfortably covered by current-day 2S-LGGs. For the work presented here, the LGG at the University of Kent [231, 235] was used, both in the one stage (1S-LGG, which achieves lower speeds) and 2S-LGG configurations. This allows differing speed ranges and regimes to be covered dependent on the specific investigation.

4.1.1 One-Stage Operation

For investigations requiring a slow speed (see chapter 7), the 1S-LGG configuration is used - shown in figure 4.1. In this configuration, the projectile is loaded into the rear of the launch tube over which a two-layer bust disc (shown in figure 4.2) is secured. The launch tube is pressurised with either a nitrogen or hydrogen driver gas. The pressure within the pump tube is increased gradually by a hand controlled valve leading to a pressurised container, until the burst disc ruptures. At this point, the projectile is forced down the launch tube towards the target. The pressure at which the burst disc ruptures is primarily controlled through the thickness of the front foil disc layer, allowing the speed to be controlled. The fastest speed achievable in this configuration is $1\ \mathrm{km/s}$ (corresponding to an approximate $900\ \mathrm{kPa}$), the approximate speed of sound in hydrogen gas at room temperature [236]. When speeds slower than $1\ \mathrm{km/s}$ are required, the speed is controlled through changes to the burst disc, and changes to the driver gas composition. For the work presented in this thesis, a 0.22" ($5.56\ \mathrm{mm}$) smoothbore barrel was used firing a shell projectile. This meant that no sabot was discarded during the shot and that the target was required to be placed within the blast tank, to ensure that it was reached by the projectile.

Whilst control of the projectile speed using the 1S-LGG configuration is possible, projectile speeds substantially below $1\ \mathrm{km/s}$ are close to the lower limit of the possible speed range for the Kent LGG which is approximately $0.4\ \mathrm{km/s}$. To give more details, for 1S-LGG configurations, the burst disc used is formed of a foil disc (with a thickness of t) and a backing annulus (with an inner diameter of d). This provides three parameters capable of controlling the speed: driver gas pressure (P), the foil thickness (t), and the annulus inner diameter (d). For the Kent LGG, d is fixed, thus differences in both t and P are used to exert some control over the projectile speed. Primary control over the projectile speed is

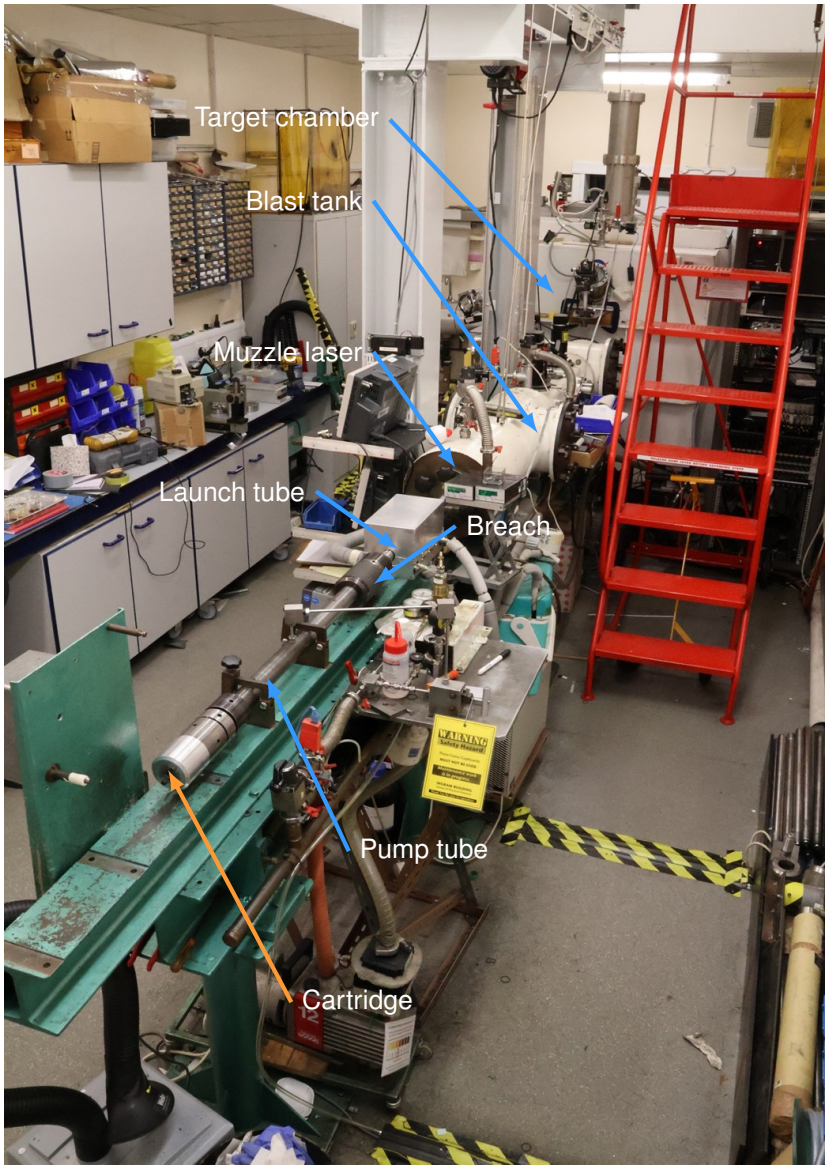

Figure 4.1: The LGG in the Kent impact facility. Blue arrows signify components used within both 1S-LGG and 2S-LGG configurations, whilst orange labels identify components only used within a 2S-LGG configuration.

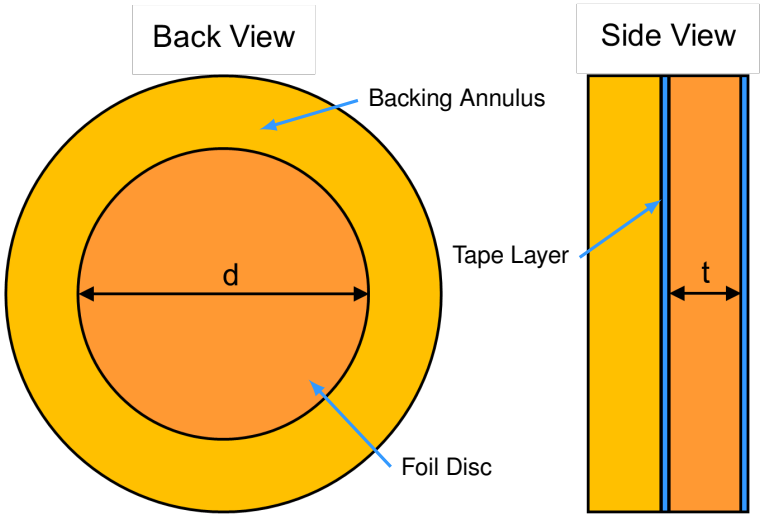

Figure 4.2: Schematic diagram of the two-layer burst disk for the Kent 1S-LGG. The foil thickness (t) goes between 40-100 microns depending on the required projectile speed and desired bursting pressure. The total diameter of the burst disk is ≈ 1.5 cm, with the inner diameter of the annulus (d) being 4.3 mm.

exerted through the choice of foil thickness, it ranges between 40 μm for the slowest speed shots to 100 μm for the highest speed shots. This changes the value of P required in the pump tube before the foil disc ruptures allowing the projectile to become accelerated. Typically the pressure used can be as much as 90 bar. It is found experimentally, that the ability to pre-set the desired speed is degraded as the speed gets significantly lower than 1 km/s, and the actual speed can vary significantly from that chosen pre-shot.

4.1.2 Two-Stage Operation

The two-stage configuration differs from that of the one-stage through the means of pressurising the pump tube via a special firing mechanism (shown in Figure 4.1). To allow higher speeds to be achieved, a substantially higher level of compression is required within the pump tube. To achieve this, during a two-stage shot, the rear of the pump tube is sealed with a single-use nylon piston (shown in figure 4.3) which, in turn, has a powder-loaded shotgun cartridge placed behind it. Similarly to a one-stage shot, the pump tube is then filled with a pressurised gas. When fired, a pendulum is released, allowing it to strike the firing pin. This detonates the primer in the shotgun cartridge, igniting the gunpowder load. The explosive force and release of hot, high pressure gas, forces the nylon piston (Figure 4.3) down the pump tube, rapidly decreasing the available volume for the gas to fill. This rapid compression of the gas significantly increases the pressure within the breech - generating pressures on the order of 10^7 atm. Under this pressure, the burst disc ruptures, causing the gas to accelerate the sabot at hypervelocity speeds. Whilst the speed regimes available in a two-stage configuration are significantly higher than those capable of being reached for a one-stage shot, the

use of gunpowder as an initial propellant can substantially increase the level of target contamination during a shot.



Figure 4.3: An example nylon piston before (left) and after (right) being fired. The piston is used in two-stage shots of the light gas gun at the University of Kent [231]. Combined with o-rings, it forms an air-tight seal at the rear of the pump tube allowing the gas inside to be compressed to substantially high pressures. The length of the piston pre-shot is 8.5 cm and its width is 1.27 cm. These dimensions allows the piston to just fit inside the pump tube ensuring a gas tight seal.

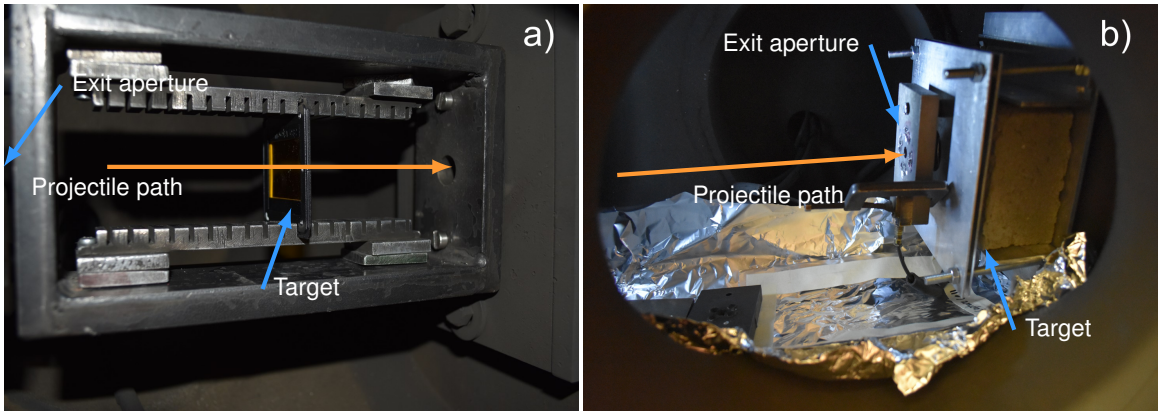

Figure 4.4: The two main blast tank target holders used within this thesis. Panel a) shows the standard target holder for the blast tank. Panel b) shows the target holder used for larger targets within the blast tank (such as those within Chapter 7). Attached to the leading face of both target holders is an 'exit' aperture, used to catch discarded sabot parts after leaving the launch tube.

4.1.3 Target Placement

Once fired, the operation of the light gas gun is almost identical for both a one- and two-stage shot; with differences for a shot now lying in the placement of the target. The experimental configuration

at the University of Kent allows for targets for both shot types to be placed in either the blast tank, or target chamber (both are labelled within Figure 4.1) which are evacuated to low pressures (typically < 1 mbar) pre-shot. Target location is typically selected based on the type of projectile and the analyses required during the shot itself - not the speed regime being investigated. For targets placed within the blast tank (which can hold targets up to 10 cm in size), only a few target holders can be used (the main two used for this work are shown in Figure 4.4).

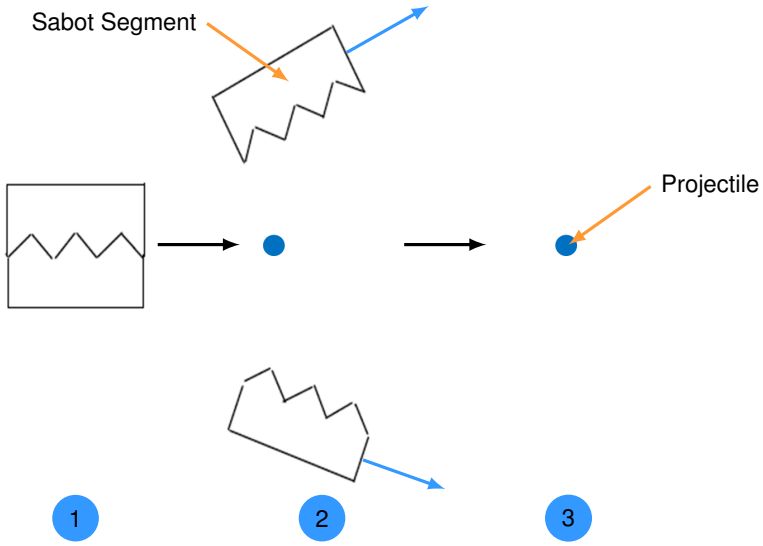

Figure 4.5: Schematic diagram showing the process of sabot segmentation during flight. Stage 1 shows the sabot travelling down the launch tube with the projectile housed in the interior. Rifling in the launch tube causes the sabot and projectile to spin. Stage 2 follows once the sabot leaves the launch tube. Once the sabot segments are no longer constrained by the launch tube, their spinning motion causes them to fly off-axis away from the projectile. Once the projectile is free from the sabot, it continues towards the target in stage 3. The spin of the projectile helps stabilise it on axis during flight. Note that whilst only two sabot segments are shown here (in side view), a typical sabot has four interlocking segments with the projectile carried in a central shaft between the sabot parts.

4.1.4 Projectile Speed calculations

The precise way through which the projectile speed can be calculated within the Kent LGG varies depending on the parameters of the shot. Within each shot, the projectile passes through at least the muzzle laser upon leaving the launch tube. For shots utilising a split sabot, discarded sabot segments (Figure 4.5) impact the blast tank exit aperture generating a vibration signal. If the target is located in the target chamber rather than the blast tank, the projectile then exits the rear of the blast tank and passes through two collimated laser light curtains mounted transverse to the direction of flight (forming a time of flight laser system). These can be seen in Figure 4.6. This provides several redundancies to measure the speed within varying shot parameters. The most precise way is for a shot in which the projectile passes through the time of flight laser system located down-range of the

blast tank. The known separation of these lasers, along with the time delay for the projectile to reach the second laser allows the speed to be calculated to an precision of $\pm 1\%$.

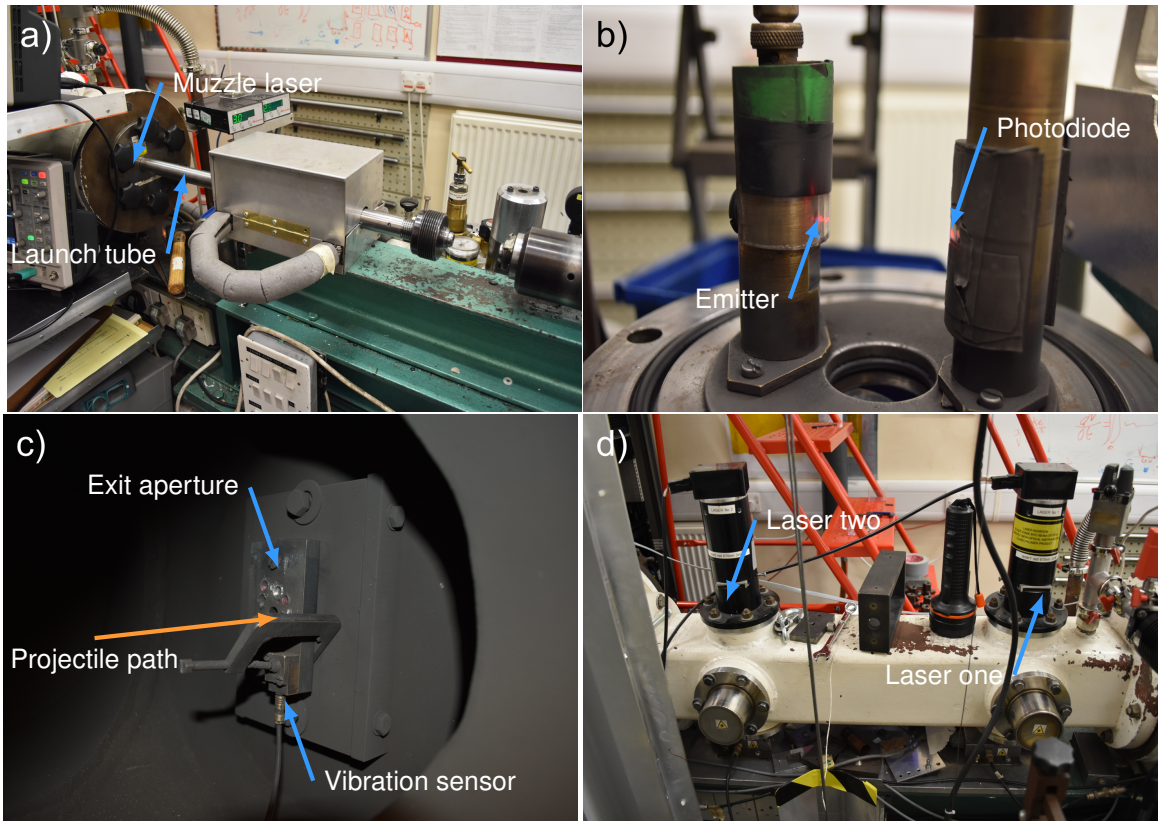

Figure 4.6: The equipment used to measure the speed of a projectile within the Kent LGG. Panel a) shows the muzzle laser situated immediately after the launch tube. Every projectile passes through this laser and the trace generated on the oscilloscope provides a method to ensure the projectile successfully survived the initial acceleration. For shots using a solid projectile with a target inside the blast tank the signal from this laser provides the only method to measure projectile speed. The time delay between the leading and trailing edge of the projectile provides the projectile speed to an accuracy of 5% providing the length of the projectile is known. Panel b) shows the emitter and photodiode used for the muzzle laser. Panel c) shows the standard set-up for targets placed further along the gun. It shows the exit aperture affixed to the blast tank with the vibration sensor attached to the plate. This sensor reads to a oscilloscope outside of the chamber The time delay between the vibration signal generated by impacting sabot segments and the muzzle laser signal allows the projectile velocity to be calculated to a precision of 5%. Panel d) shows the time of flight lasers located down range of the blast tank. The known separation and the time delay between the projectile passing through each laser allows the projectile speed to be calculated to an accuracy of $\pm 1\%$.

For shots in which the target has been placed within the blast tank, this method is not an option. The projectile only travels as far as the blast tank and thus does not pass through the time of flight laser system. In this situation, the method for calculating projectile velocity is dependent on the properties of the projectile. For split sabot shots, upon leaving the launch tube, the sabot segments are discarded prior to the projectile impacting the target. These segments impact the blast tank exit

aperture causing a detectable vibration. The time delay between this vibration signal and the signal from the muzzle laser can be used to calculate the projectile velocity to a precision of 5%. For this method, the distance between the rear face of the blast tank and the front face of the exit aperture must be measured. For solid sabot shots (such as those carried out for the work in Chapter 7), the process of calculated projectile velocity relies entirely on the signal detected by the muzzle laser. For solid sabot shots, no sabot segments are discarded, hence no vibration signal is detected by the blast tank exit aperture (providing the projectile remains on axis). In this situation, the time delay between the leading and trailing face of the projectile passing through the mizzle laser allows the projectile velocity to be calculated to a precision of 5%, provided the length of the projectile is known.

4.2 Material Characterisation Techniques

In this thesis, projectile and target materials sometimes need to be characterised. Induced interactions between an incident source of electromagnetic radiation and a sample material fall under the umbrella of spectroscopic techniques. Whilst all falling under the same family of analysis, the methods used vary drastically (both sample preparation and analysis) for each technique. The interactions are characteristic to the structure and composition of the sample. Hence, spectroscopic analysis can be used to identify elements and compounds within a sample or to quantify the composition. Methods can be both non-destructive (XRF, Raman, X-Ray Diffraction (XRD), etc.) and destructive (Atomic Emission Spectroscopy (AES), Laser Ablation Mass Spectrometery (LA-MS), etc.), depending on sample preparation and the methods by which it is analysed. For the work presented here, a range of methods are used. Their use is primarily focused on the work covered in Chapter 7 to aid in the identification of post-shot projectile material. The following sections will discuss the underlying physics of the selected processes, XRF and scanning electron microscopy, and the methods required for sample preparation.

4.2.1 X-Ray Fluorescence (XRF)

XRF spectroscopy is used to determine the elemental concentrations within a sample. The technique relies on the production of secondary electrons due to the excitation of atoms within the sample; the measured energy of these secondary x-rays allows for the precise identification of the elements within a sample. When exposed to high energy incident x-rays, inner shell electrons may become ejected from atoms within a sample ionising the atom leaving it in an unstable state. The result of this is an atomic relaxation cascade, during which electrons from outer shells fall to lower energy levels within the atomic structure (Figure 4.7). These transitions fall within defined series (Figure 4.8), denoting transitions between electron shells and are dependent on the vacancy that is being filled within the atomic structure. As this occurs the reduction in energy generates photons (typically secondary x-rays), the energy of which is equal to the well defined energy difference between electron orbitals. These energy levels of the x-rays produced from this cascade are characteristic for each element.

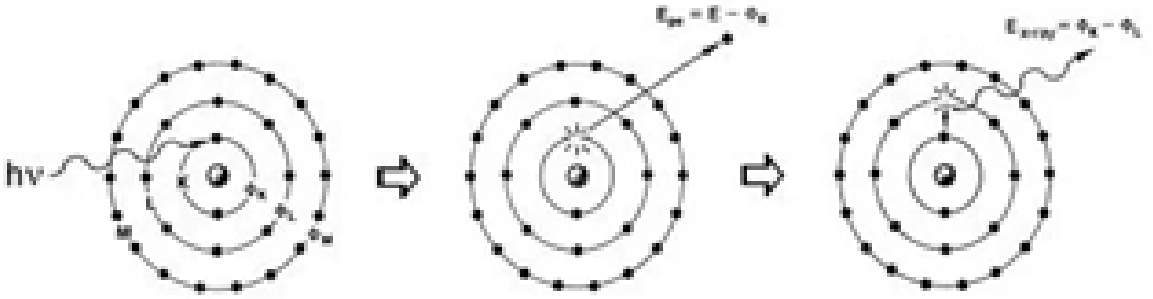

Figure 4.7: The process by which characteristic x-rays are produced within an atom. Image from [237].

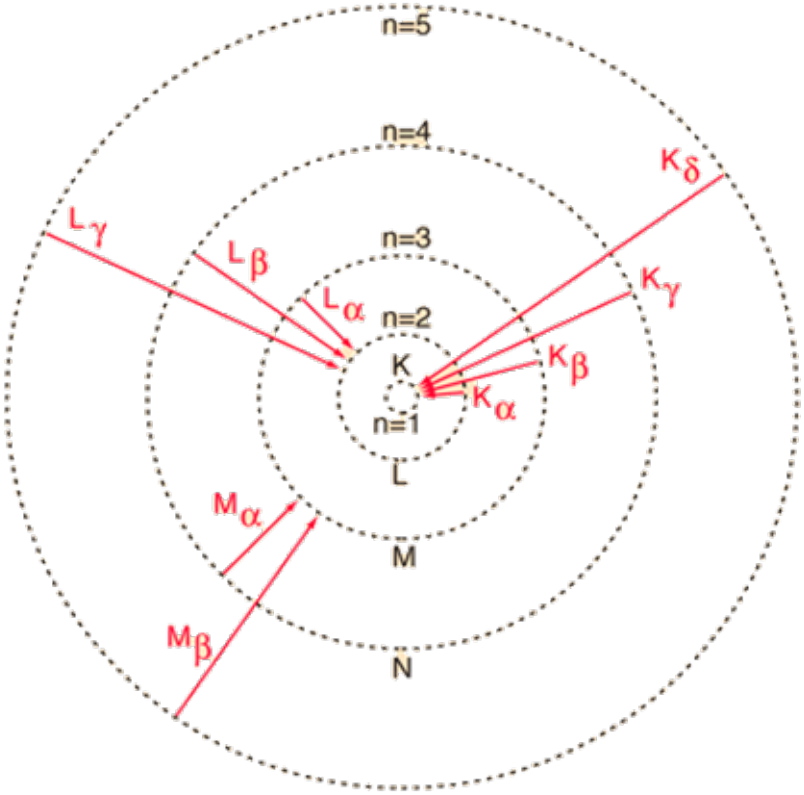

Figure 4.8: Electron transition series available within the structure of an atom. Image from [238].

For the analyses presented in this thesis, XRF spectroscopy was undertaken using the Malvern PANanalytical Epsilon3 Energy Dispersive XRF (EDXRF) spectrometer (shown in figure 4.9) at the University of Kent. The spectrometer is capable of measuring elemental abundances between carbon and americium. Whilst there is no theoretical limit to the quantity of sample that can undergo analysis within the spectrometer - other than that dictated by the size of the sample container (a cylinder of 28.22 mm diameter and 28.65 mm height) - EDXRF analysis works best in cases where the sample size forms a thin (of a few mm) layer over the base of the sample holder. The spectrometer is fitted with an automated sample changer allowing ten individual samples to be analysed before changing is required. When setting up the analysis, samples can be set to spin to reduce the influence of inhomogeneities during the x-ray bombardment. Each sample takes 75 minutes per

analysis, composing five individual runs of 15 minutes to provide an average result. Under the 'standard' running conditions, the space between the x-ray tube, sample window, and the x-ray detector is filled with He gas. Four measurements are taken with the Rh x-ray tube at the voltages of 30.0 kV, 20.0 kV, 12.0 kV, and 5.0 kV. In combination with the Ag diffraction grating, a 200 μm Al filter, 50 μm Al filter, and no filter are used. Measurements are carried out for the durations of 120 s, 120 s, 300 s, and 300 s respectively. The combined results spectrum is obtained after the overall measurement time of 15 minutes, spectra are then analysed using Malvern PANanalytical software for standardless XRF analysis.

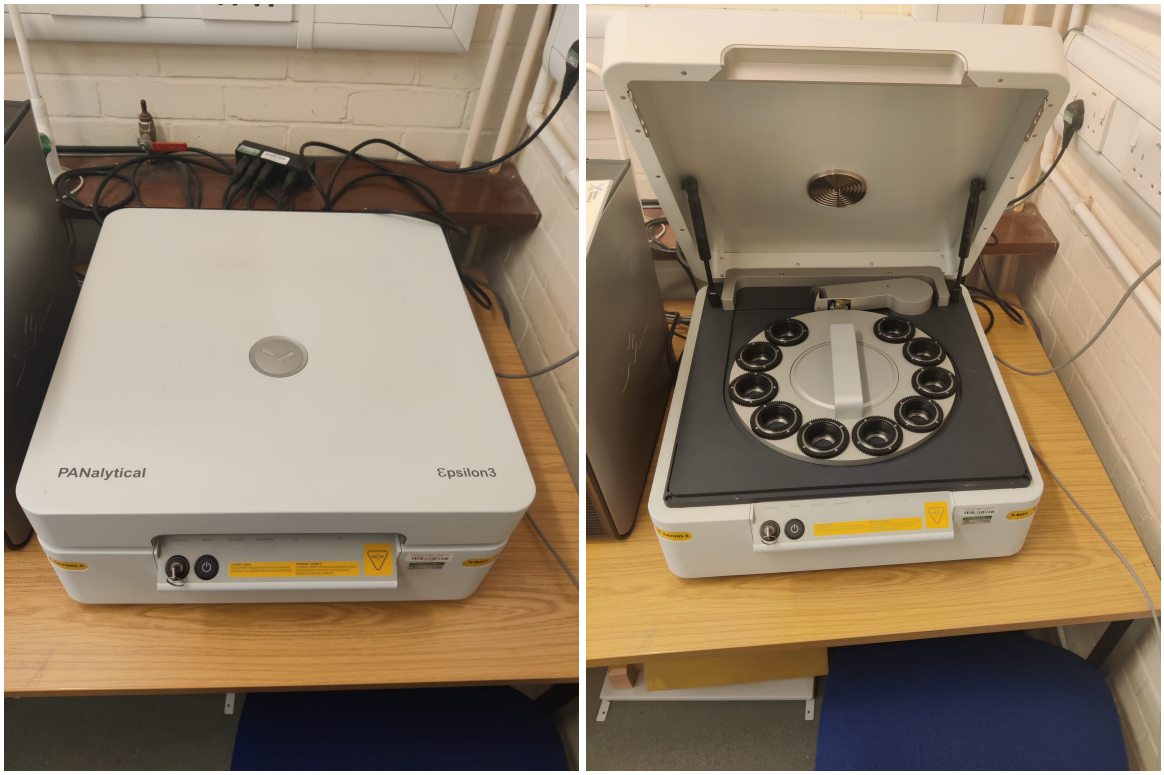

Figure 4.9: The PANalaytical Epsilon3 EDXRF spectrometer at the University of Kent. Left shows the machine exterior with the lead shielding and right shows the interior sample holder and rotating wheel capable of holding up to ten samples.

Sample holders (shown in figure 4.10) for the XRF spectrometer consisted of four components: two plastic cylinder walls (forming the inner and outer walls), a plastic lid, and a thin (3.6 μm) mylar film base. Containers are built such that the thin mylar film is trapped between the inner and outer walls which fit together tightly; this holds the film securely in place forming a thin, tight base of the container. Mylar is used for the base of the container as this material is relatively transparent to x-rays, thus allowing the sample to be analysed with no contamination. To ensure the sample and container present a plane surface to the incident x-rays, it is important to ensure that no creases are formed in the film when constructing the container. The plastic lid of the container is used to both protect the film base during moving of the sample, and to prevent spilling of the sample during analysis. For some analyses presented in this thesis, a europium mineral standard was used to calibrate the

spectrometer. The size of this standard was mm in diameter, thus it could not be held in a standard sample holder. To analyse the standard, it was simply wrapped in a thin mylar film, allowing easy insertion and removal of the standard. Following the analysis, the results were provided in the form of a table with the percentage weights of each component being given to three decimal places. These values could then be averaged for each sample providing the standard deviation and standard error.



Figure 4.10: The samples holders used for analysis within the XRF spectrometer. Left shows the outside of the sample holder with the lid attached whilst the image on the right shows the interior of the sample holder with the clear mylar film visible at the base of the holder. The holders were 28.22 mm in diameter.

4.2.2 Scanning Electron Microscope (SEM)

Within this thesis, SEM analysis was used to provide high-magnification (beyond those achievable with an optical microscope) of the silicate samples used. The Hitachi SN4000 at the University of Kent was used with an Oxford Instruments $80\ mm^2$ X-max Energy Dispersive X-ray Spectrometer (shown in Figure 4.11). Within the machine a voltage is applied across a tungsten filament to generate electrons. These are then directed towards the sample, where they interact with the material. This interactions generates secondary electrons through ionisation interactions and through inelastic backscattering interactions. The machine has two possible modes of operation, utilising either a complete vacuum (SEM mode) or variable pressure (VP) mode. Whilst each have different pros and cons, for the work within this thesis, VP mode was required due to the nature of the sample.

This both prevented charging of the sample (an issue with some grains within the samples consisting of materials known to charge) and the dislocation of samples during analysis. A result of this was that during analysis, backscatter electron (BSE) mode was needed for the detector, as secondary electrons (an alternative detector mode) would not possess high enough energies to be detected due to the presence of the residual atmosphere within the sample chamber. During analysis, the sample chamber was held at a pressure of 25 Pa. Within the SEM, analysis via secondary electrons follows a process similar to that described in Section 4.2.1. Electrons contained in atoms within the sample are dislodged by the incident beam and become ejected from the atom with a defined energy level. These secondary electrons are characteristic of the element they are ejected from. Back scatter electrons, however, are produced via the deflection of incident electrons from the sample. Backscattered electrons provide no information on the surface morphology of the target. They can, however, provide information on the relative densities of the materials within the sample. Denser materials appear brighter within the produced images due to the increased number of backscattered electrons, whilst lighter materials appear darker. Whilst secondary electrons can provide information of the surface morphology of the sample, their energies are much too low to be used within the VP mode selected for this analysis. For this analysis the pressure within the SEM was set to 25 Pa and the voltage across the filament was 20 Kv.



Figure 4.11: The scanning electron microscope at the University of Kent. Panel b) shows the inside of the sample chamber which is sealed during analysis.

For this work, the image of the sample was formed through the detection of electrons being elastically scattered by the target. To produce an image, electrons are accelerated from an electron

gun. All electrons reach the target with the same energy. These electrons then interact with the sample and are elastically scattered. When incident upon the detector, the measured energy of scattered electrons provides information about the density of the sample material; with higher density materials appearing brighter (whiter) in the image. SEM analysis is a minimally destructive technique. However, whilst the process involved within the SEM is itself non-destructive, the sample mounting required during preparation means that the sample often cannot be reused. To prepare the sample for analysis, it is mounted on a metallic stub (Figure 4.12) with adhesive to hold it in place within the sample chamber. The use of BSE limited the topographical information able to be obtained about the sample, but provided a sufficient level of detail to draw conclusions regarding grain morphology and size distributions.

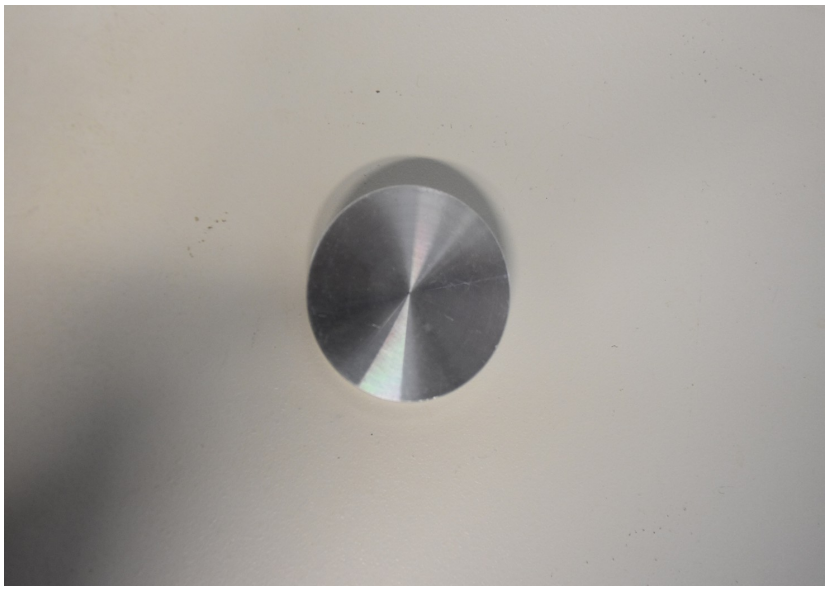

Figure 4.12: Mounting stub (top view) used for the standard analysis carried out within this thesis. The stub is 2.5 cm in diameter.

Attempts were made for the work presented in Chapter 7 to the use SEM Electron Diffraction Spectrometry (EDS) to identify emplaced projectile material. For this, samples required a unique mounting system (shown in Figure 4.13) due to their large size. SEM EDS works due to inelastic scattering of electrons leading to a change in their energy. This change is characteristic of the elements within the sample allowing the composition to be analysed (this process is similar to that of XRF). Difficulties encountered during the sample preparation and time constraints, however, meant that no results for this analysis were obtained.

4.3 conclusions

This chapter has described the primary equipment used for the experiments performed within this thesis along with the standard operating procedures and a brief look at the physics behind their operation. In the next chapters, the details and results of a series of experimental investigations are

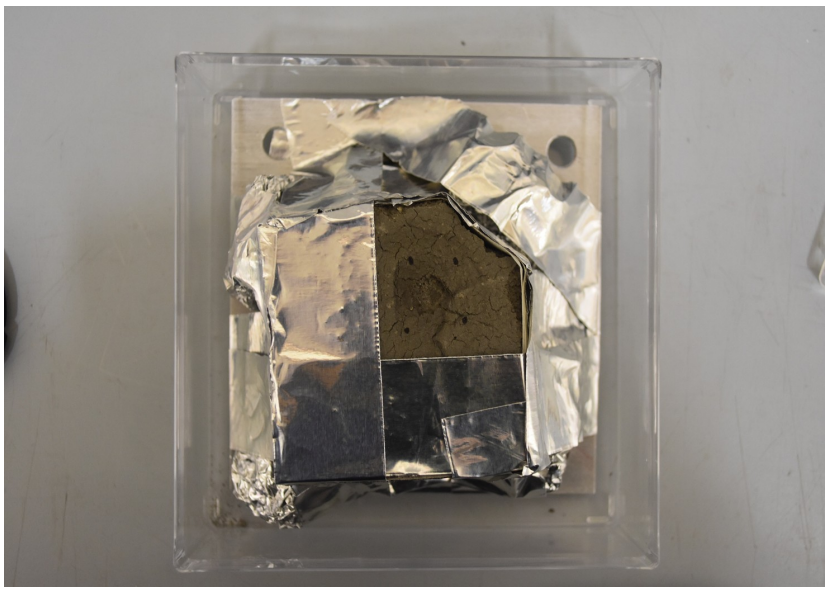

Figure 4.13: Method used for mounting Phobos simulant targets for analysis. Due to their large size the blocks were affixed to a metallic plate for support by aluminium tape. This tape was to prevent excessive charging of the sample as well as to hold it in place. This plate was then mounted on a standard stub allowing the sample to be mounted within the SEM. The metal plate has a side length of 8 cm.

given. Within these chapters, investigation specific methods are given featuring additional details related to those chapters in regards to a variety of equipment.

Chapter 5

Planetary Simulant Materials

"We are but notes in the cosmic score,

forever connected by the universal melody of life"

The Voice of Tomorrow

5.1 Mars and Phobos Simulant Materials

When selecting a planetary simulant for use within a study, there are a wide range of available materials. These materials possess a variety of physical properties with each typically being engineered for a specific purpose [239]. Despite simulant materials often having undergone development for a specific use case, the limited availability and limitations often associated with experimental investigations typically means that they are used far beyond their intended applications. This is likewise the case for the simulants used within the work presented in this thesis. Therefore, it is of high importance that analyses of these materials are undertaken to allow for meaningful comparisons to be made during investigations. An in-depth review of all available planetary simulants is beyond the necessary scope of the work presented in this thesis (an in-depth review of the available Martian and lunar simulants can be found in [239] and [240] respectively). It is useful, however, to look at the planetary analogues used within this thesis that focus on the Mars system, with simulants being used to replicate both the Martian and Phobosian surfaces.

Use of the simulant materials falls within two investigations in this thesis, the first focusing on the surface of Mars utilising JSC Mars-1 (JSC-M) [241], and MGS-1 [239] (both of which are compared to a kiln dried sand (KDS) material). The second investigation focuses on the transfer of material from Mars to Phobos using doped MGS-1 simulants and PCA-1 [242] to replicate the predicted regolith composition of Phobos. The work presented in this chapter only scratches the surface of possible testing that these simulants can be subjected to in order to classify them. However, these analyses form a key step in interpreting the data collected within subsequent chapters. The testing carried out additionally allows comparisons between vastly different silicate materials (e.g. the Martian simulants and KDS used in Chapter 6) to provide further insights into the cratering processes within sand-based target materials. Further, analyses examining the chemical compositions can be used to guide the methodology undertaken and interpretations made in the geological analysis undertaken in Chapter 7.

Due to the time constraints of this project the testing and analysis each simulant material was subjected to varied, based on the requirements of the subsequent investigation in which it was used. A more complete comparison of some of the simulant materials used can be found in [**?**]. For the first investigation focusing on the differing crater morphology in a variety of Martian permafrost analogue materials, the geotechnical properties (the properties of natural ground minerals) of the simulants are of primary interest. This testing primarily focused on the grain morphology for each simulant, the size distribution of each simulant, and how these influenced other geotechnical properties (such as coefficient of static friction, etc.) and potentially their response to the impact process. For the second investigation, the primary focus was the chemical composition of MGS-1 and PCA-1 and the identification of post-impact mixed simulant projectile material. This heavily depended on the use of XRF techniques to identify unique components within the projectile and target materials. Whilst this process is a common method of characterising planetary simulant materials [239, 242–244], it would

prove difficult to employ for in-situ measurements onboard spacecraft.

Of the simulant materials used within this investigation, they fall into three categories. The first is that consisting of the kiln dried sand, this was a building sand purchased from the local hardware shop with little to no information provided by the supplier regarding its composition or size distribution. The composition of kiln dried sand is, in general, typically 99.7% SiO_2, with traces of other materials such as $Al_2)_3$, and Fe_2O_3 for example. The exact composition to an accuracy better than this is not critical for the purpose of which it is used in this work, so was not pursued in greater detail. The grain size distribution and coefficient of static friction was, however, measured where relevant. The second group for these simulant materials is the spectral simulant JSC Mars-1 (produced by NASA at Johnson Space Centre [241]). This simulant was sourced from the Pu'u Nene cinder cone in Hawaii with additional components included to provide a closer spectral match the the IR reflectance spectra obtained from bright regions on Mars. The mineralogy, elemental composition, and size distribution of this simulant can be found in Allen, *et al.* [243]. Whilst a size distribution is also provided by Allen, *et al.*, [243], due to the age of this simulant and its prior use within the impact laboratory, this was re-measured for the simulant used for the work presented within this thesis. Whilst this simulant has components added to it, primarily it is sourced from exposed environments on Earth. As such it will have been subjected to alteration and natural weathering. The final group of simulants used within this thesis are those sourced from SRT (Space Resource Technologies based at the University of Central Florida [239, 242]. The first of these, MGS-1, was produced as a chemical match to x-ray diffraction results obtained from the Rocknest sample site on the surface of Mars [239]. This analysis was carried out by the Curiosity rover [55]. To simulate the Phobosian surface, however, SRT produced the PCA-1 simulant to spectrally match the Orgueil meteorite [242] (a meteorite thought to have a similar composition to that of Phobos if it was found to be a captured asteroid). To construct these simulants, minerals were sourced from mines by SRT. These were then combined to provide a simulant of a known size range and mineralogy. These values are given in the safety data sheets for the simulants (found on the SRT website) and within the initial papers regarding these simulants [239,242]. Between sample batches, however, these parameters can change slightly depending on the source of the mineral and the precise mineral included in the simulant. As such, it is useful for the work here to analyse the size distribution of the simulants and the elemental composition.

5.2 Experimental Protocol

Testing was undertaken with samples of KDS, JSC-M, and MGS-1 to measure grain size, specific gravity (both bulk and grain densities), and static friction. For comparisons between MGS-1 and PCA-1, testing was focused on the composition of these simulants rather than their geotechnical properties, as this was key to the investigation involving these materials. They were subjected to XRF analysis (see Section 4.2.1) investigating elemental concentrations, aiding in post-shot identifi-

cation (discussed more in Chapter 7). All of the simulants presented in this chapter were additionally analysed through optical microscopy and SEM (see Section 4.2.2) to allow investigations into their morphology and microscopic features.

5.2.1 Sample Preparation

Minimal preparation of the sample was required for the majority of analyses. To examine the grain size distribution of the Martian simulants used, a set of sieves were used (information provided in Table 5.1), with each sieve weighed prior to use. 200 g of simulant was added to the stack and sieved for three minutes with varying direction of agitation, allowing grains to move past each other and effectively separate into their respective sized sieve. At the end of the sieving period (samples were sieved for a period of three minutes), the mass of simulant retained in each sieve (m) was determined. Estimating the number of grains retained during the sieving (N) was possible through the equation:

$$N = \frac{V\rho_g}{m} \tag{5.1}$$

where ρ_g is the measured grain density of the simulant. This requires the assumption that each grain is a sphere with a diameter equal to the midpoint of each represented range (both the size range of each gradation and midpoints are given in Table 5.1), allowing the volume (V) to be calculated. In Equation 5.1, the density is the calculated grain density of each simulant. To calculate this, a mass of each simulant was added to a known quantity of water inside a measuring cylinder. This ensures that the pore space between grains is filled with water. Hence, the increase in both volume and mass due to the added silicate then provides the grain density. Bulk densities of the simulants can be measured through the standard means of adding a quantity of the material to a measuring cylinder.

Table 5.1: Parameters of the sieve stack used to analyse the grain size distribution for the Martian simulant materials [245]. Average particle volumes were calculated using the mid-point size for each sieve mesh.

Sieve	Mesh (μm)	Size Range (μm)	Mid - point (μm)	Average volume (μm^3)
10	2000	>2000	2000.0	4.19×10^9
20	841	2000-841	1420.5	1.5×10^9
40	420	841-420	630.5	1.31×10^8
60	250	420-250	335.0	1.97×10^7
80	177	250-177	213.5	5.10×10^6
120	125	177-125	151.0	1.80×10^6
250	58	125-58	91.5	4.01×10^5
Base	n/a	58-0	29.0	1.28×10^4

The coefficient of static friction for the Martian simulants was measured via the tilting box method. Approximately 100 g of the simulant was added to a glass beaker. This was then slowly tilted until the

material on the upper surface began to slide. The angle at which slipping started (the angle of repose θ) was measured using an inclinometer, with the coefficient of static friction (μs) (given in Table 5.2) being calculated through:

$$\mu\mathrm{s} = \tan(\theta) \tag{5.2}$$

Similarly, minimal preparation was required for the X-Ray Fluorescence (XRF) analysis of PCA-1 and MGS-1. Samples were contained in holders described in Section 4.2.1, with enough of the sample added to ensure the base was covered during analysis. The analytical conditions for the sample scans were kept at standard (see Section 4.2.1). For each sample, five scans were taken allowing the scatter and standard error to be calculated for each constituent.

Two samples of each simulant were used to assess the natural variation in grains. Due to the nature of construction for both MGS-1 and PCA-1 (discussed in detail in [239,242]), samples presented as extremely inhomogeneous for chemical and spectral analysis. Ball milling methods were therefore employed to increase the homogeneity of the samples for microscopic analysis.

5.2.2 Ball Milling

To increase the homogeneity of simulant samples during analyses, samples underwent a standardised ball milling procedure. Samples (5 g of simulant) were ball milled using a mixer mill (figure 5.1) for a period of five minutes at a frequency of 15 Hz. Milling was carried out using 3×11 mm stainless steel ball bearings within the milling jar (the container in which the sample is held during milling - highlighted in figure 5.1). The sample filled this milling jar to approximately one-third of its capacity. A small quantity of ethanol ($2 - 3$ ml) was added to samples to act as a lubricant during the milling. The ball milling process subjects the simulant materials to pulverisation and grinding via impact friction. This is induced through the side-to-side motion of the milling jar. Repeated contact between the sample and the side of the jar, along with the ball bearings, rapidly homogenises the sample. Hence, further analyses of the simulant compositions allows a less diverse composition to be obtained whereas this was previously limited by the granular nature of the synthetic simulants. Due to the change in grain size and the potential introduction of chemical processes, however, ball milled samples are not ideal for both grain size distribution studies or analytical techniques dependent on crystal structure (e.g. x-ray diffraction analysis).

5.3 Geotechnical Properties of Martian Simulants

Within the investigations presented later in this thesis, a range of silicate based materials are used to simulate impacts onto the surface of Mars. The nature of these materials influences how the target materials used respond to the impact process and in turn, the morphology of the produced craters. Of the parameters measured through the geotechnical testing performed here, the two base features are grain morphology and grain size distribution. Whilst other parameters can provide information of specific responses, they are all somewhat dependent on these two features. Figure 5.2 shows

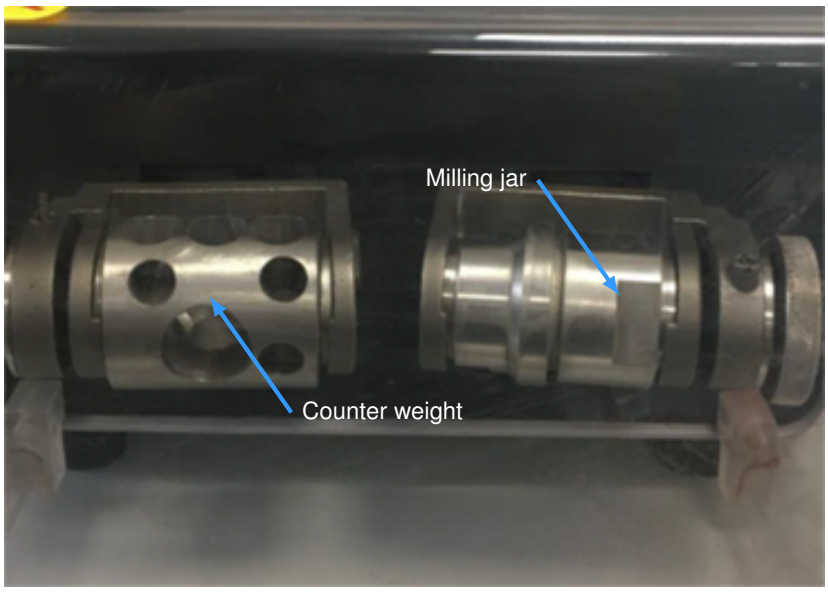

Figure 5.1: The Retsch MM301 mixer mill used for the ball milling processes within this Chapter. Within the figure the milling jar (the container in which the sample is held) and the counter weight are highlighted. During milling, both are shaken from side to side (horizontally) to induce crushing within the sample.

optical and SEM images of each simulant. When comparing the silicate materials used, a stark difference can be seen between the KDS and the Martian simulants (JSC-M and MGS-1). Grains within the Martian simulants appear irregular in shape whilst those in the KDS materials are seen to be much smoother. This increases the force required to induce motion in the Martian simulant materials when compared to the KDS. This can be seen when looking at the values for the coefficient of friction for each material in Table 5.2. Despite the coefficients of friction being similar for KDS and JSC-M samples, the irregularity and wider range in grain sizes observed within JSC-M simulant acts to increase the required force to induce motion. The large jump seen between JSC-M and MGS-1, however, is likely due to JSC-M grains having undergone weathering prior to collection whereas grains within MGS-1 will not have undergone this process. SEM images of each simulant again shows the same differences in grain morphology, with grains from MGS-1 appearing to be the most irregular. These images further allow the population of sub-micron grains included within both the MGS-1 and JSC Mars-1 simulants to be seen clearly, and the morphology of these grains to be analysed.

Table 5.2: The measured geotechnical properties of the used materials.

Material	Sample mass (g)	Bulk Density (g/cm^3)	Grain Density (g/cm^3)	Angle of repose ($^\circ$)	Coefficient of friction
MGS-1	200.46	1.49	1.91	46.2	1.04
JSC-M	200.34	1.07	1.91	34.2	0.68
KDS	200.71	1.71	2.65	31.8	0.62

From both the optical and SEM images of the simulants, qualitative information can be obtained

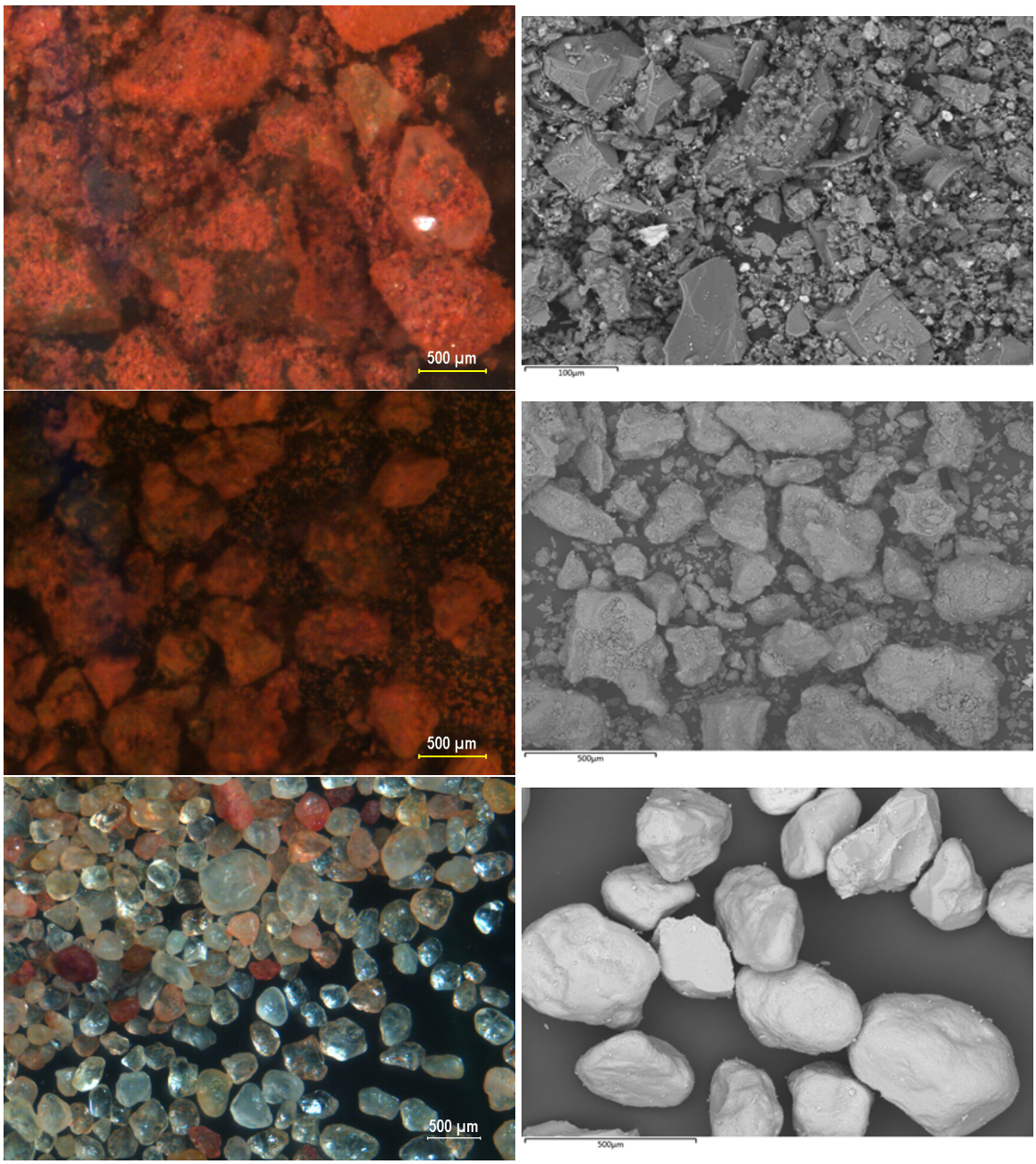

Figure 5.2: Optical and electron microscopy images of the silicate materials used to represent the Martian surface. The top images show MGS-1 Martian simulant [239], the middle row shows the JSC Mars-1 simulant [241], and the bottom row shows the kiln dried sand (KDS) material. SEM images obtained curtsey of Jessica Wills

about the size distribution of grains. Each of the silicate materials shows a unique size distribution. The KDS appears to have an almost unimodal distribution. Both JSC-M and MGS-1 are seen in optical images to have both large and small grains which will increase the packing fraction of the material, consequently increasing the force required to induce motion. As well as this, in SEM images, both Martian simulants are seen to have very fine grains coating the larger ones, in particular within the MGS-1 material. Large grains are seen to be heavily coated with sub-micron dust grains. Whilst still present, the number of sub-micron grains seen within JSC-M is substantially lower than those seen

within MGS-1. This likely explains the sudden jump in Table 5.2 seen when looking at the coefficients of friction for the silicate materials. To gain further quantitative insights into the grain size distribution, the results of the sieving methods are shown in Table 5.3 and Figure 5.3.

For KDS, the material remaining within each sieve rapidly increases, peaking between $420 - 177$ μm, it then decreases almost as rapidly as the increase before almost disappearing completely. MGS-1 follows a very similar trend to the KDS material. For MGS-1, a broader mass distribution is seen in Figure 5.3 than for either KDS or JSC-M. The mass distribution peaks at an average size of 630.5 μm before slowly decreasing. The trend then rapidly decreases after an average grain size of 213.5 μm. The observed trend for the number of grains, however, shows an almost normal distribution, with the peak number of grains estimated for grains with an average diameter of 213.5 μm. For JSC-M, the trend differs from those seen for the previous simulant materials, especially for the estimated number of grains. For JSC-M, the estimated number of grains increases for each sieve with the largest number being estimated for the base. For the mass distribution, JSC-M shows a normal distribution peaking at an average grain size of 335 μm. Due to the significantly higher measured grain density for KDS (2.65 g/cm^3) when compared to the Martian simulants (1.91 g/cm^3), the overall estimated number of grains within the sample is considerably lower than for both Martian simulant materials. This is likely due to the KDS being composed of largely low porosity quartz grains whereas the simulants are basalt based, possessing a higher grain porosity.

Table 5.3: Distribution of simulant mass and estimated number of grains within each sieve for all three simulants. The assumed mass of a single grain within each sieve (based on the measured average grain density) is also shown.

Sieve	MGS-1			JSC-M			KDS		
size	Mass (g)	Single grain (g)	Number	Mass (g)	Single grain (g)	Number	Mass (g)	Single grain (g)	Number
10	0.64	8.00×10^{-3}	80	0.16	8.00×10^{-3}	20	0.01	1.11×10^{-2}	1
20	5.84	2.87×10^{-3}	2037	0.93	2.87×10^{-3}	324	0.03	3.98×10^{-3}	8
40	44.77	2.51×10^{-4}	178608	72.89	2.51×10^{-4}	290791	9.35	3.48×10^{-4}	26885
60	97.79	3.76×10^{-5}	2600926	53.95	3.76×10^{-5}	1434911	139.99	5.22×10^{-5}	2683602
80	43.79	9.73×10^{-6}	4499345	49.57	9.73×10^{-5}	5093230	45.50	1.35×10^{-5}	3369561
120	6.95	3.44×10^{-6}	2018468	15.87	3.44×10^{-6}	4609078	5.31	4.78×10^{-6}	1111525
250	0.63	7.66×10^{-7}	822328	6.53	7.66×10^{-7}	8523499	0.43	1.06×10^{-6}	404539
Base	0.02	2.44×10^{-8}	819981	0.31	2.44×10^{-8}	12709712	0.09	3.38×10^{-8}	2659525

5.4 Compositional Properties of MGS-1 and PCA-1 Simulants

Table 5.4 gives the compositions of both MGS-1 and PCA-1 from XRF analysis. As stated, samples were analysed five times, to assess the measured uncertainties. Whilst these compositions vary slightly from those given in the literature for MGS-1 [239] and PCA-1 [242], this can be accounted for due to differences in the spectrometer used to perform the analysis and changes to the simulant recipe by suppliers. For example, the listed composition for MGS-1 within Cannon, *et al.* [239] gives a

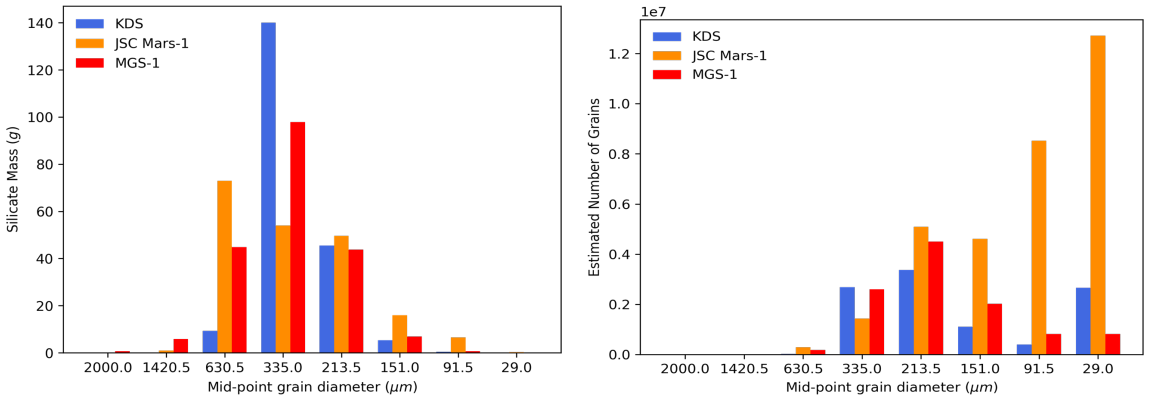

Figure 5.3: Distribution of mass (left) and estimated number of grains (right) in each sieve following processing for each material.

value of 3.4 wt.% of Na_2O within the simulant. Within the analysis carried out here, however, no value for sodium was identified due to it being close to the limit of detection for the spectrometer (discussed in Section 4.2.1). The literature measurements show Na_2O to be the only unique listed constituent within the MGS-1 material when compared to the published composition for PCA-1 [239, 242]. As such, identifying post-impact MGS-1 material would simply require the identification of Na within the collected ejecta or target. The results in Table 5.4 show that very little difference can be identified between both PCA-1 and MGS-1 through XRF analysis. Hence, to aid in the investigations presented in Chapter 7, an alternative approach was required when considering the projectile material analysis.

Table 5.4: Elemental concentrations of MGS-1 and PCA-1 measured by XRF analysis. All values are given in units of wt.% with errors calculated as the standard error of the average over five scans per sample. Analysis was performed using the spectrometer described in Section 4.2.1.

	MgO	Al_2O_3	SiO_2	P_2O_5	SO_3	Cl	K_2O	CaO	Ti
MGS-1	9.546 ± 0.025	14.525 ± 0.022	43.890 ± 0.013	0.175 ± 0.001	1.317 ± 0.011	0.045 ± 0.001	0.464 ± 0.001	9.402 ± 0.007	0.283 ± 0.008
PCA-1	10.231 ± 0.076	5.992 ± 0.147	34.503 ± 0.200	0.221 ± 0.007	5.189 ± 0.106	0.034 ± 0.003	3.409 ± 0.067	9.222 ± 0.163	0.346 ± 0.021
	Cr	Mn	Fe_2O_3	Ni	Zn	Sr	In	Eu_2O_3	Trace
MGS-1	0.173 ± 0.001	0.091 ± 0.001	19.614 ± 0.050	0.138 ± 0.001	0.011 ± 0.001	0.042 ± 0.001	0.197 ± 0.007	0.069 ± 0.003	0.038
PCA-1	0.053 ± 0.002	0.099 ± 0.009	30.015 ± 0.232	0.053 ± 0.001	0.024 ± 0.001	0.167 ± 0.002	0.177 ± 0.006	0.096 ± 0.002	0.161

5.5 MGS-1 Geopolymer Reactions

During attempts to produce a permafrost analogue target (the process of which is covered in detail in section 6.2.1) using the MGS-1 Martian simulant material, it was noted that in the presence of hard water, a 'pozzolanic'-like reaction [246] occurred producing a cement-like substance. Closer inspection of this 'cemented' target, however, showed the cementing to be limited to only the upper millimetres of the target; warranting further study. Due to the thin nature of this 'crust' material, it presented as a very brittle substance with low material strength. Additionally, the top and bottom surface of the initial cement produced show drastically different textures, with the top being relatively

smooth whilst the bottom was much rougher. The properties of the cement crust are shown in Figure 5.4. Further, if the presence of hard water is required for the MGS-1 simulant to 'naturally' cement, the closed nature of the initial container (those used for target construction discussed in Section 6.2.1) may contribute to the relatively thin nature of the crust produced, as well as the uneven nature of the bottom layer of this material. The oven during the target preparation heated samples from their base, thus the closed nature of the container forced the evaporating water within the target upwards. This process exposed the upper surface of the target to a substantially higher level of ion-rich hard water.

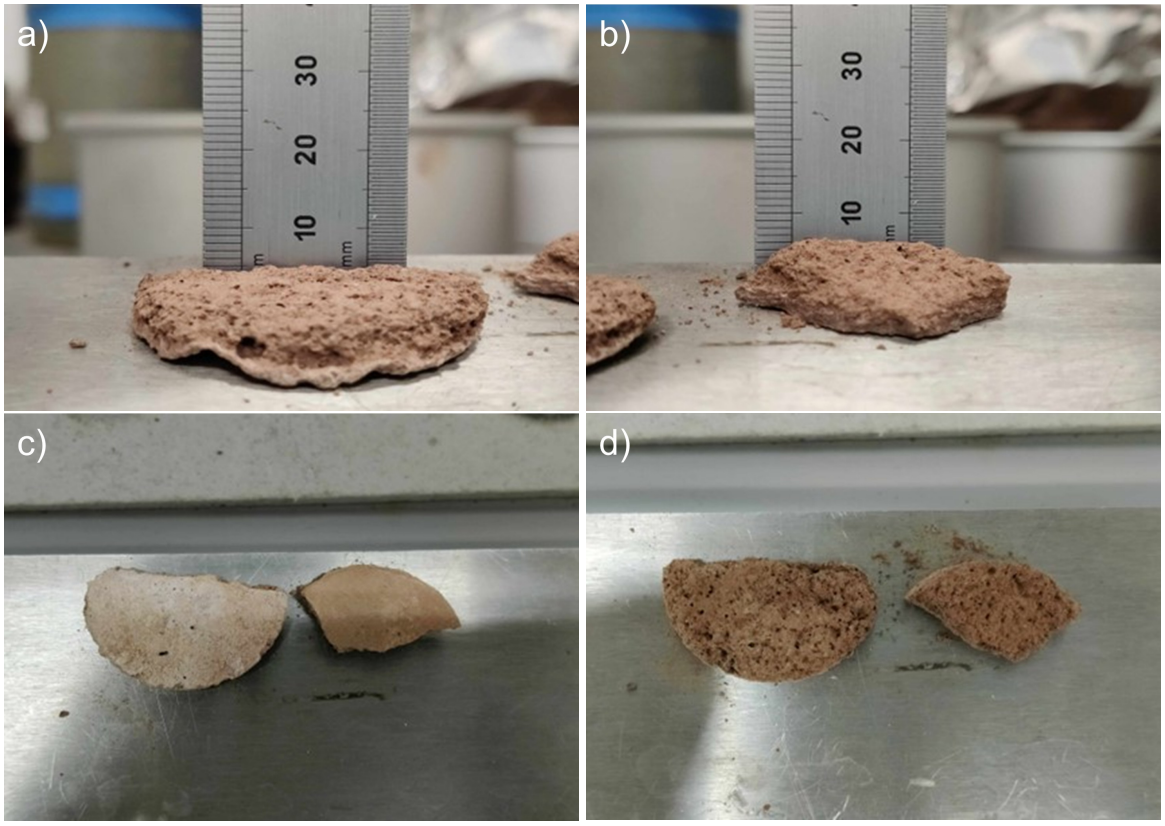

Figure 5.4: Images of the initial cement crust formed through the combination of MGS-1 and hard water. Panels a) and b) show the thickness of the 'crust' layer whilst panel c) shows the upper surface and panel d) shows the bottom surface. The target underwent freezing at -20° C for a period of 48 hours, and was then heated to a temperature of 90° C for a period of 24 hours to remove residual water-ice from the target. After heating, core samples were removed from the target to investigate the extent of cementation.

In order to fully understand the cementitious nature of this material, an extensive study of the cementing reaction and process would be required. This is, however, far beyond the scope of the study presented here. However, to fully exploit the cementitious nature of the MGS-1 simulant, attempts were made to enhance the pozzolanic nature of the material. Samples were made from 5 g of MGS-1 simulant, 0.45 ml of deionised water, and 0.5 ml of calcium hydroxide ($Ca(OH)_2$). This allowed a known quantity of calcium hydroxide to be added to the mixture compared to the unknown quantity contained within the standard tap water. 0.5, 1.0, or 2.0 g of orthosilicilic acid was additionally

added to the solution to act as a binding agent. The mixture was heated to a temperature of 80° C for a period of 72 hours to induce the pozzolanic reaction, forming a 'cement' material. As shown in figure 5.5, however, testing of this reaction failed to produce a homogeneously cemented material; instead forming a solid 'plug' surrounded by loose material. XRF analysis of the pre-cemented MGS-1 simulant identified it as being similar to a fly ash with a mid-CaO content [246]. Thus, rather than attempting to enhance the pozzolanic reaction occurring within the MGS-1 material, a chemical activator was added to form a geopolymer cement. Potassium hydroxide was chosen as the chemical activator (several others are possible), with the justification and precise process detailed in Chapter 7.2.1.1.

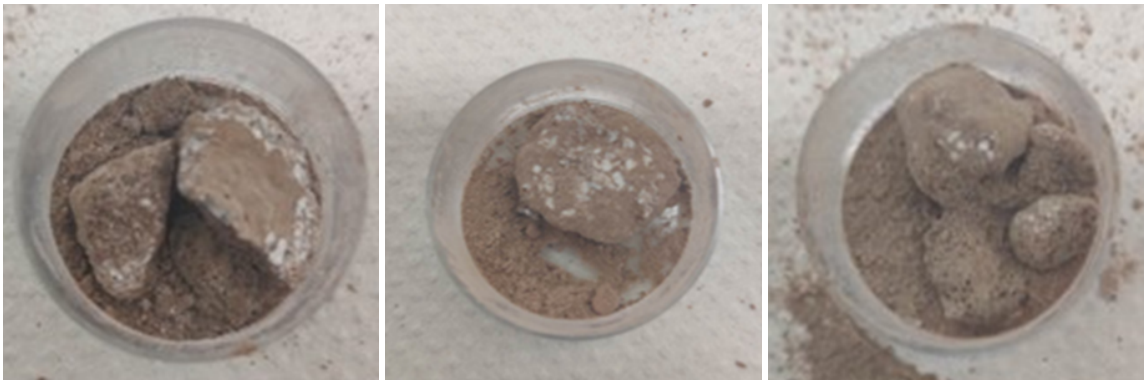

(a) 0.5 g orthosilicic acid (b) 1 g orthosilicic acid (c) 2 g orthosilicic acid

Figure 5.5: Pozzolanic cement samples formed with an increasing quantity of orthosilicilic acid (from left to right). In each sample the cement 'plug' can be identified along with lose material from the reaction. Sample holders had a diamter of 2.5 cm.

5.5.1 MGS-1 Ball Milling

Whilst not discussed in detail here, it is useful to introduce the projectile recipe utilised within Chapter 7 (see Section 7.2.1.1 for a full discussion) and the influence of ball milling on the projectile production process. The elemental tracer (or taggant) of choice within this mixture is europium acetate hydrate ($Eu\,(CH_3COO)_3 \cdot xH_2O$) existing as either a sesquihydrate or tetrahydrate. This material was added for the investigation undertaken within Chapter 7 to assist in the identification of post-impact emplaced or ejected projectile material. A europium-based material was chosen due to the extremely limited presence of europium in the analysis of both the MGS-1 and PCA-1 simulant materials, and the availability of europium compounds when compared to other rare-Earth metals. The chemical activator and elemental tracer were both added to the MGS-1 simulant before ball milling was carried out. Specifically, 5 g of MGS-1, 0.9 g of KOH, and 0.5 g of $Eu\,(CH_3COO)_3 \cdot xH_2O$ were subjected to the standard ball milling process described in Section 5.2.2. Unlike previously milled samples of MGS-1, when combined with the KOH and elemental tracer, milling resulted in a paste-like mixture, as shown in Figure 5.6. As the formation of the paste mixture was unexpected, it is useful to investigate the milling process with each element added to the MGS-1 separately, providing an insight into

potential processes occurring.



Figure 5.6: Paste material produced by milling MGS-1 with KOH and $Eu\,(CH_3COO)_3 \cdot xH_2O$.

Table 5.5: Sample component matrix for the milling performed in Section 5.5.1.

	MGS-1 (g)	KOH (g)	$Eu\,(CH_3COO)_3 \cdot xH_2O$ (g)
Sample 1	5	0.9	-
Sample 2	5	-	0.5
Sample 3	5	0.9	0.5

The same proportions were used, with the milling jar containing one of the mixtures shown in Table 5.5. Milling was carried out with the same parameters and under standard atmospheric conditions, meaning that samples were somewhat susceptible to changes induced by variations in humidity and temperature. Whilst the samples from Table 5.5 underwent milling on a different day to that shown in Figure 5.6, they were all milled within 24 hours to minimise variation and allowing comparisons between the three mixtures. The mixtures adhered to the inside of the milling jar, which was similarly seen in samples of individual simulants, likely due to compaction rather than from chemical processes induced during the milling procedure. Figure 5.7 (panels a, d, and g) shows the result of the milling process for Sample 1. Visual inspection of the mixture shows that, when compared to milled samples of MGS-1 alone, the colour is substantially lighter for much of the sample. Close to the rim of the milling jar, however, a much darker layer can be seen.

This colour change may be artificially induced, resulting from the lighter coloured smaller dust grains settling closer to the centre of the milling jar. However, this difference was not observed in other milled samples of the MGS-1 simulant. This implies that the change occurred due to the presence of the chemical activator within the sample. After removal from the milling jar, the dichotomy appears to even out across the sample, appearing approximately uniform in colour. Whilst some chemical changes may have occurred to account for the observed darkening within the milling jar for the

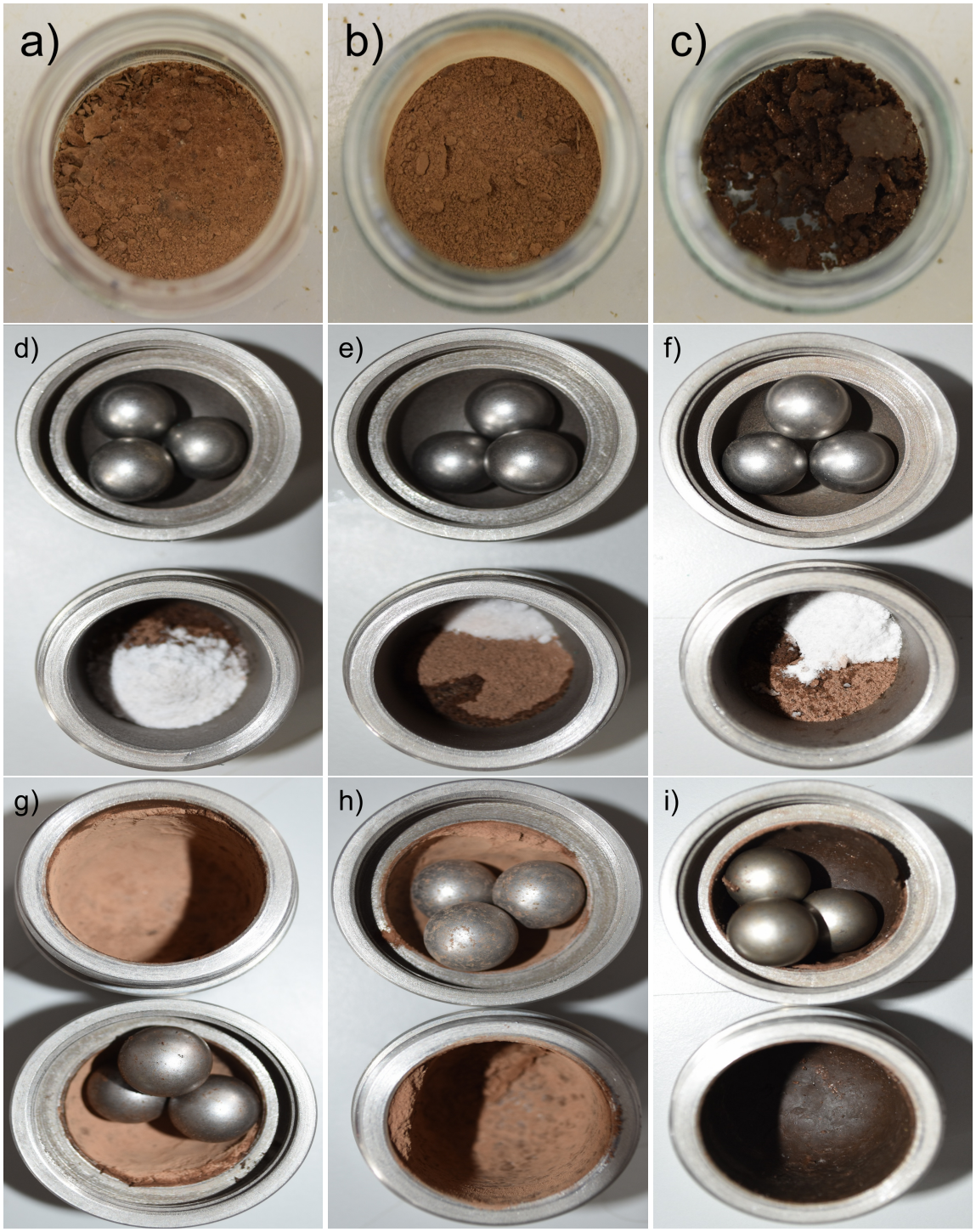

Figure 5.7: The results of milling the sample mixtures in Table 5.5. Panels a), b), and c) show close up images of post-milled samples 1, 2, and 3 respectively. Panels d) and e) show the pre and post milled state of sample 1. Panels f) and g) show the pre and post milled state of sample 2. Panels h) and i) show the pre and post milled state of sample 3.

sample, this change appears to have been on a smaller scale. After removal from the milling jar, the sample exhibited a level of clumping. A flake morphology (irregular with significant size in only two dimensions) was observed indicative of them being formed through compressive forces.

The results of milling sample 2 are shown in Figure 5.7 (panels b, e, and h). Comparisons show

the level of clumping are higher than for sample 1, with the coating of the milling jar observed to be much more irregular. Material appears to have preferentially coalesced during the milling process, indicating that the elemental tracer has more control over the level of clumping seen than the chemical activator. This suggests that an increased level of atmospheric water is being consumed during the milling process in the presence of $Eu\,(CH_3COO)_3 \cdot xH_2O$ than with KOH alone. The increased level of clumping observed within the milling jar can also be seen once the sample was removed. Whilst it again possess flake morphologies, small 'rubble' pile morphologies (irregular with significant size in three dimensions) can be seen within the sample. Unlike sample 1, however, no colour change was observed throughout this sample.

Figure 5.7 (panels c, f, and i) shows the results of milling with sample 3 and shows considerable differences to samples 1 and 2. Post-milling, the colour of the entire sample appears darker, with a slightly lighter coloured ring of material present against the outside of the milling jar. Following the removal of the sample, however, this colour difference was no longer visible. Additionally, the level of clumping seen within sample 3 is higher, with the sample consisting of large and small clumps rather than a fine powder. The inclusion of both the chemical activator and elemental tracer was therefore required to form the unusual texture for the post-milling sample. Differences, however, can be seen when comparing sample 3 to that shown in Figure 5.6. The material in Figure 5.6 appears to have a more paste-like texture than that seen in panel c within Figure 5.7. This difference is thought to be indicative of the sensitivity of the process on the ambient humidity. Changes may have additionally been introduced to the milling process through changes to the quantity of ethanol used within the milling jar.

5.6 MGS-1 Martian Permafrosts

The cementing nature of MGS-1 caused a substantial issue for the work presented in Chapter 6. That work focusses on the impact of projectiles into ice-silicate mixtures and how variations in the type of silicate material used affected the outcome of the crater formation process. In order to complete this with MGS-1 based targets, a new method of target construction required development. For this, the method of vapour diffusion was selected. Whilst this method presents a substantial increase in difficulty compared to that described in Section 6.2.1, it minimised the contact between the MGS-1 target and any liquid water. This prevented as much of the cementation as possible. For this method, a cryogenic vacuum chamber system (using a closed cycle CH-202 SHI Cryogenic cooling system with a HC-4E helium compressor for cooling and an Edwards E2M5 Two Stage Rotary Vane Vacuum Pump) was developed (shown in Figure 5.8) in which a $10 \times 10 \times 2$ cm (width x depth x height) high-porosity block of consolidated MGS-1 was placed. These blocks were constructed by SRT at the University of Central Florida. The system is designed to, once under vacuum, release a mixture of water vapour and nitrogen gas (as a carrier gas) into the chamber. This mixture was subsequently drawn through and past the cooled MGS-1 block at which point the water vapour begins to freeze.

The final aim is to produce an MGS-1 permafrost-like block which can then be impacted within the Kent LGG.

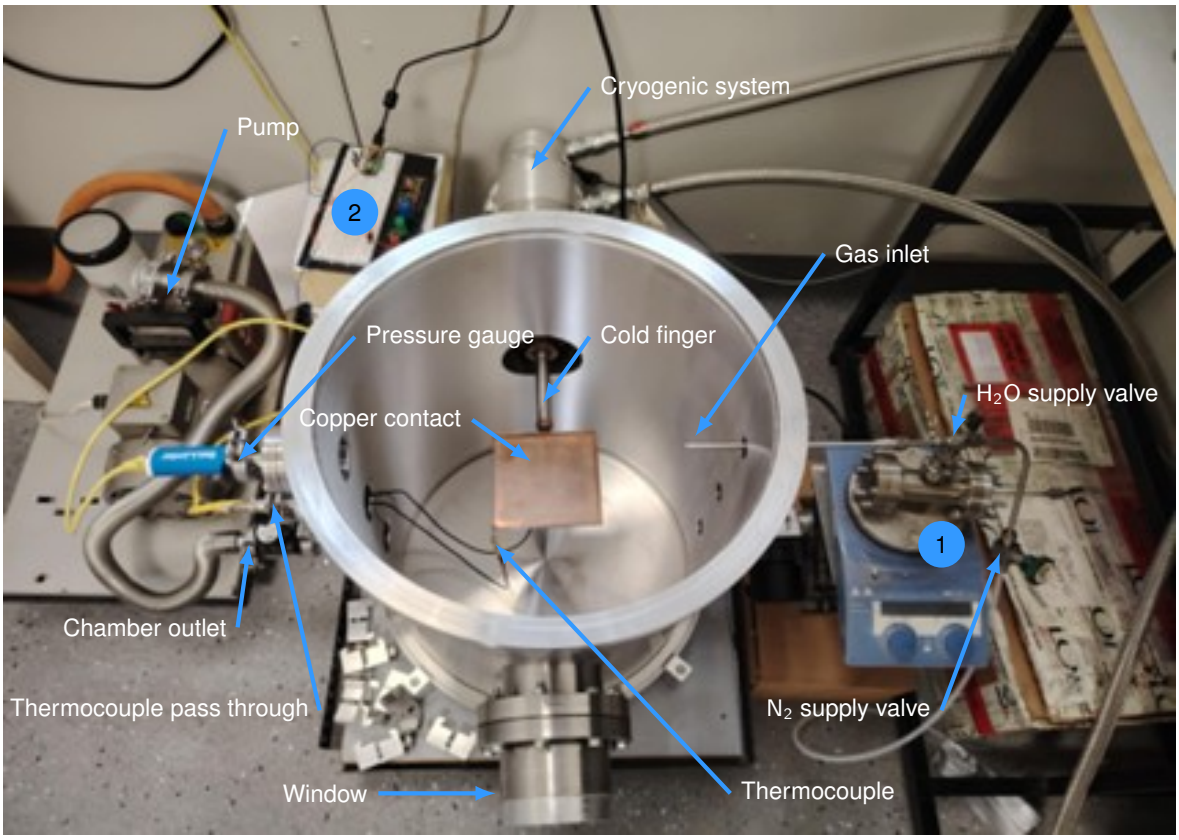

Figure 5.8: The cryogenic vacuum chamber system developed to form MGS-1 and water ice targets. A target block was placed on the copper contact plate to regulate the temperature. Once under vacuum, a mixture of water and nitrogen (as a carrier gas) was introduced to the chamber. To increase the level of water carried into the chamber it was heated to $40°$. This mixture was drawn through and around the block allowing it to freeze forming a permafrost-like material. Key components of the system are labelled within the figure. The areas numbered one and two represent the water reservoir system and the thermocouple circuitry respectively and are shown in Figure 5.9. The internal diameter of the chamber was ≈ 45 cm and the internal height was ≈ 60 cm tall.

Whilst the cryogenic system shown in Figure 5.8 was capable of cooling the copper contact plate to a temperature of $-30°$ C, it proved insufficient to additionally cool a room temperature block to a similar temperature (due to the high porosity limiting conductive cooling and the high thermal inertia of the simulant material limiting the rate of possible cooling). As such, the MGS-1 blocks required pre-cooling allowing the cryogenic system to simply hold them at a sub-zero temperature rather than actively cooling them. The MGS-1 blocks were thus pre-cooled within a $-120°$ C freezer for a period of 24 hours. In preparation for this, blocks were placed into a plastic bag into which nitrogen was inserted to reduce the residual atmosphere within the bag. This prevented the build up of ice from atmospheric water as much as possible whilst blocks were pre cooled. Blocks were then placed onto a copper plate and into a polystyrene insulation box before being placed into the freezer. This

storage method provided two benefits for the process. Whilst stored in the freezer the polystyrene box provided some level of protection from damage. Before removing the block from the freezer, the chamber system was evacuated and the cryogenic cold finger was turned on to cool the copper contact plate. The temperature of the copper contact plate was continually monitored during the process through a thermocouple. Once the copper contact plate was sufficiently cooled (reaching a temperature of at least -30° C), the chamber was brought back to atmospheric pressure and the pre-cooled block was placed on the contact plate. The second benefit of the block storage system whilst pre-cooling the block was its nature as an insulator during transport between the freezer and the chamber. This extended the time for which the block could be outside of the freezer without the temperature increasing substantially. The chamber was then evacuated again. This procedure was carried out as quickly as possible (to prevent build-up of ice on the cryogenic cold finger) whilst taking care to ensure the block was secure inside the chamber.

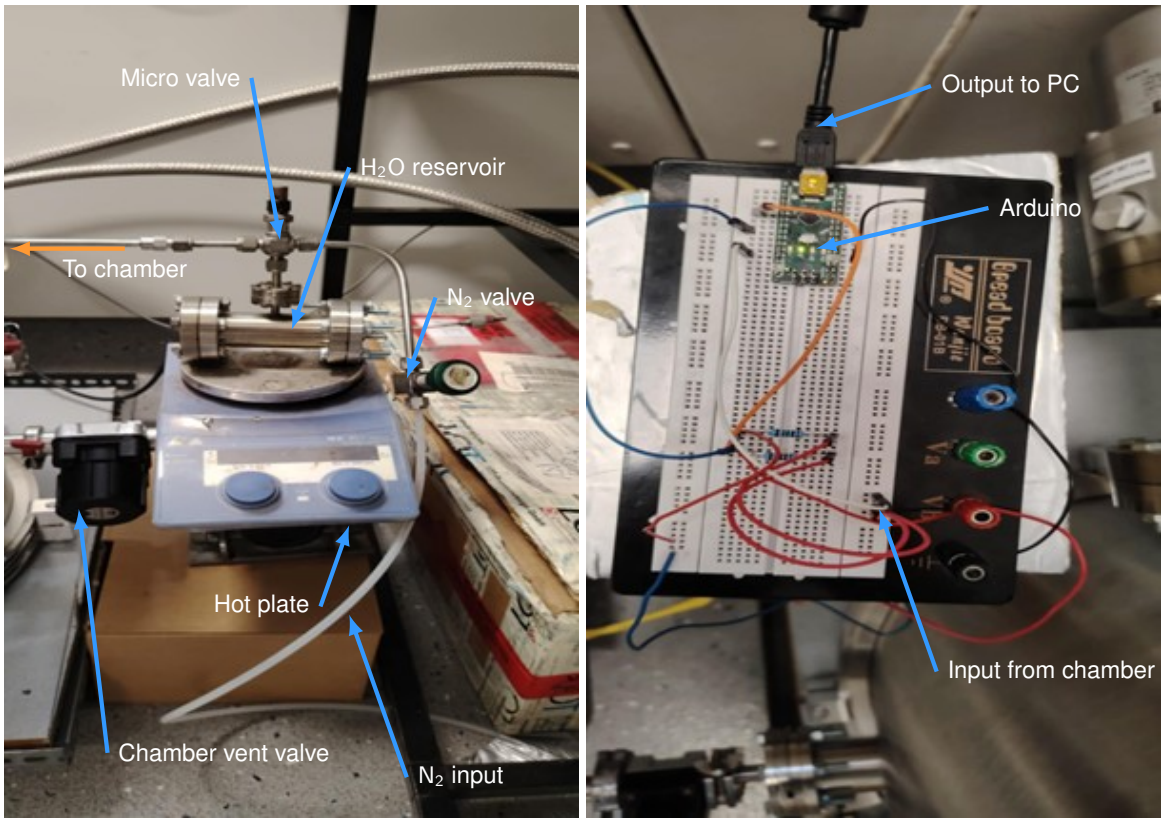

Figure 5.9: Close up images of the water reservoir system and thermocouple circuitry for the cryogenic vacuum chamber system (areas labelled one and two in Figure 5.8 respectively).

Once the chamber had reached a pressure of ≈ 1 mbar, the flow of N_2 was introduced. This increased the pressure within the chamber to the working pressure of 6 mbar. Due to the manual design of the experimental set-up, a precise control of this pressure proved difficult meaning that during the experiment, the nitrogen flow was increased allowing the pressure in the chamber to increase above the working pressure and then subsequently decreased allowing the internal pressure to fall. This meant that during the experiment the internal pressure in the chamber would consistently change. This is not thought to have caused any issues, however, as at all times the internal pressure

remained above the vapour pressure (the point at which ice would begin to sublimate). At a temperature of $-30°C$ this is approximately ≈ 0.5 mbar. Once the flow of nitrogen into the chamber was established, the tapered micro-valve to the water reservoir could be opened. The design of this valve meant that even when fully closed, nitrogen was able to flow into the chamber. As it was opened, the flow of nitrogen ensured the water vapour travelled into the chamber and past the MGS-1 block. The idea of this was that water vapour passing through the sub-zero block would begin to freeze forming a permafrost analogue material suitable of being impacted within the Kent LGG. The most recent result from this method can be seen in Figure 5.10.



Figure 5.10: The surface and interior of a block having been exposed within the cryogenic vacuum chamber system for a period of six hours. Very little evidence can be seen for the presence of water-ice on either the exterior or interior of the block. It was noted, however, that the upper surface of the block appeared almost desiccated, an appearance not noted during previous tests.

Within Figure 5.10, a block is shown after having been removed from the vacuum chamber system. It was exposed to the water vapour for a period of six hours. Visual inspection of the block interior shows very little evidence for the presence of ice. This is supported by the lack of ice present on the block surfaces (in particular the face orientated towards the gas inlet). The small pore size within the block, however, would make the visual identification of pore ice difficult. Further, upon removal of the block from the chamber, it was noted that ice was only visibly present on the cold finger component of the cryogenic system. The time constraints of the work presented in this thesis meant that shots into these targets could not be carried out, as the presence of ice within the block could not be guaranteed. Further, the quantity present could not be reliably measured. Despite this, the method shows promise as a way to produce a Martian permafrost analogue, with similar processes having been used to embed CO_2-ice within Martian analogue targets [247].

5.7 Chapter Summary

The work presented in this chapter has shown that, whilst the materials used within the further studies of this thesis replicate similar surfaces and have similar compositions, they possess different properties. This furthers the discussion started by Cannon, et al, [239] in regard to the use case of each simulant material and their application in experimental investigations far outside of these intended cases. Whilst this may present an issue for some investigations, acknowledgement of these differences and consideration of how they may be overcome will enable the use of simulant materials in methods beyond those for which they are designed. The use of chemically matched simulants provides a much closer approximation to a planetary body than the use of a single mineral simulant (which have been previously used within numerous impact studies) Whilst not an ideal solution, it presents a far more practical solution to the development of bespoke simulant materials for each investigation.

The geotechnical characterisation carried out allows the target materials used within Chapter 6 to be compared, enabling a greater understanding of the role of the simulant during the process of crater formation within these materials, in particular the morphology of the produced craters. Understanding the differences between the silicate materials in this chapter highlights variations in the target materials to be investigated. In particular, MGS-1 was found to behave in a drastically different way from either KDS or JSC-M, leading to the requirement of a new method of target construction in a cryogenic vacuum chamber. Whilst the development of this new method has shown only limited results currently, its development has allowed for the large-scale production of permafrost analogues through means more analogous to planetary surfaces. In particular, the method of vapour diffusion ensures a homogeneous distribution of ice and would prevent the inclusion of large fragments of ice within the sample.

Analysis of the chemical composition of the simulant materials used helped guide the methodology and analysis presented in Chapter 7. Whilst the literature compositions of these materials show some distinguishing components, performing this characterisation and analysis in-house ensures that differences in equipment and analysis techniques are capable of identifying constituents of interest within the simulants. For the work presented in this thesis, this was found to be an issue with NaO_2 being close to the limit of detection for the XRF spectrometer used. Reliance on literature values would have ensured that no projectile materials would have been identified within the ejecta collected during Chapter 7.

Chapter 6

A Changing Silicate Material

"As long as we dream, write, and explore,

this world will never cease to grow"

The Voice of Tomorrow

6.1 Ice-Silicate Mixtures in the Laboratory

Continuing observations of Solar System bodies show that, on almost all rocky surfaces, impact craters are the most commonly observed geological feature [67, 115, 130]. The widespread presence of both ice and ice-silicate mixtures on the surfaces of moons and planetary bodies, particularly in the outer Solar System [99, 107, 114, 120, 190, 194, 248–253], has led to many studies of the impact process in these materials via laboratory experiments [101–105, 111, 112, 184, 191, 254, 255], and modelling [20, 100, 114, 181]. Not only do the impact parameters (e.g. velocity, angle, etc.) and projectile characteristics (e.g. size, density, etc.) control the size and final morphology of the impact crater [101, 191], but the crater is also strongly influenced by the target type. In ice, cratering can be significantly affected by the type and temperature of the ice and, if not pure ice, then by the ratio of material forming an ice-'contaminant' mixture [102, 254, 256].

Table 6.1 provides a summary of the ranges of target parameters considered to date in prior studies of ice-silicate targets. Initial results, reported by Lange and Ahrens [255], found that decreasing ice temperature (along with the addition of a silicate material) increased the tensile strength of the target, leading to a decrease in the crater diameter. Grey and Burchell [254] further investigated, in more detail, the dependence of the cratering process on the temperature of the water-ice. They confirmed that, as the temperature decreases, the crater volume similarly decreases. Following this, Koschny, *et al.*, [256], investigated crater formation within porous ice targets, finding that as the porosity was increased, the crater volume increased although the mass of ejected material remained similar for all porosities. This finding was confirmed through modelling and similar experiments, Burchell, *et al.*, [257] and Burchell and Johnson [101], also investigated the effect of varying porosity; confirming that, as target porosity increases, so does the crater depth (which had previously been stated by Koschny, *et al.*, [256]). Additionally, over a large range of target porosity values, the crater volume was found to increase whilst the excavated mass of ice remained constant, again, similar at all porosities.

Hiraoka, *et al.* [102] probed the impact cratering process in ice-silicate mixture targets (in which the silicate component consisted of a serpentine powder possessing a grain diameter of several microns), confirming the presence of a decreasing crater diameter as the silicate content of the target was increased; the addition of which led to an increase in the target tensile strength. Crater morphology was also observed to change as the quantity of silicate material was increased, with less spallation being found to occur in targets as the silicate content increased. In a subsequent paper, Hiraoka, *et al.* [108], confirmed that crater volume scales with the tensile strength of the target following an inverse relation; with the tensile strength in turn, scaling directly with the increasing silicate content of the target. However, at a silicate content of $50\ \mathrm{wt}\%$ (the maximum used during their investigation), the tensile strength of the target mixture was found to depend on the properties of the silicate component (composition, density, grain size, etc.), suggesting the cratering process within such mixtures to have a more nuanced dependence on the silicate component than previously

Table 6.1: Examples of past investigations that have studied the influence of target properties (composition, porosity, temperature, and contaminant content) on the crater formation and target disruption processes. Targets studied have ranged from pure water-ice to pure silicate material, including a range of ice compositions and contaminant (silicate or otherwise). Other than those investigations impacting pure silicate targets, no contaminant concentration exceeded 50 wt$\%$.

Target type	Ice material	Contaminant	Porosity	Temperature	Reference
Ice-silicate	Water-ice	$35-40$ wt$\%$	not reported	81 K and 257 K	[255]
Ice	CO_2-ice	0 wt$\%$	not reported	not reported	[258]
Ice	Water-ice	0 wt$\%$	$40-50\%$	$218-258$ K	[256]
Ice-silicate	Water-ice	$5-20$ wt$\%$	not reported	not reported	[105]
Ice and ice-silicate	Water-ice	50 wt$\%$	$0-55\%$ (for ice targets) $0-39\%$ (for ice-silicate targets)	not reported	[103]
Ice	Water-ice	0 wt$\%$	not reported	255 K	[191]
Ice	Water-ice	0 wt$\%$	not reported	$100-253$ K	[254]
Ice-silicate	Water-ice	$0-50$ wt$\%$	$0-37\%$	not reported	[104]
Ice-contaminant	Water-ice and ammonia ice	$0-50$ wt$\%$ (ammonia ice)	not reported	not reported	[184]
Ice	Water-ice	0 wt$\%$	$\leq 70\%$	not reported	[101]
Sand	n/a	100 wt$\%$	not reported	not reported	[112]
Ice-silicate	Water-ice	0, 12.5, 25, 37.5, 50, and 100 wt$\%$	not reported	not reported	[102]

assumed.

Increasing interest in the outer Solar System, and the ice-dominated ice-silicate mixtures identified in that region, has led to an ever increasing gap between the knowledge of the cratering process occurring in the outer regions of the Solar System (where it is assumed that ice dominates the present ice-silicate mixtures, as seen within the past investigations listed in Table 6.1), and within the inner Solar System (for example, Mars) where the presumed ice-silicate mixtures are thought to be silicate dominated. In an attempt to bridge this gap, comparisons are often made between the crater morphology on Jovian and Saturnian satellites, and the Cerean and Martian surfaces [99, 100, 182, 190, 248]. The findings reported by Hiraoka, *et al.* [108] however, suggest that such comparisons and assumptions may be invalid, due to the differing silicate content within the ice and ice-silicate surfaces present on all of these previously compared bodies.

In this chapter, an initial study into the influence of varying the silicate component of such ice-silicate mixtures on the cratering process is described, using two target types (JSC-M simulant or KDS). KDS targets contained a silicate content of 50 wt$\%$ whilst JSC-M targets contained either 50 wt$\%$ or 80 wt$\%$ silicate content, with the remaining target mass being composed of water-ice. Targets utilised for this initial study were impacted with either 1.50 ± 0.03 mm diameter copper or 1.5 ± 0.05 mm diameter basalt spheres over a velocity range of 1.98 ± 0.02 kms^{-1} to 4.74 ± 0.05 kms^{-1} using the two-stage light-gas gun at the University of Kent (see section 4.1);

6.2 Experimental Protocol

6.2.1 Target Construction

Targets were constructed such that they contained a 50 wt.$\%$ silicate content for KDS targets and either a 50 wt.$\%$ or 80 wt.$\%$ silicate content for JSC-M targets. The required masses for each component were calculated based on the density (0.92 g/cm^3 for water-ice, 1.07 g/cm^3 for JSC-M, and 1.36 g/cm^3 for KDS). Constituent masses for each target type are given in Table 6.2. Targets were cylindrical with a diameter of 20 cm and a depth of 9 cm. Construction was carried out using a method based on the one described by Hiraoka, *et al.* [102]. Water-ice was crushed with an electric mixer, forming a fine powder. This powder was then combined by hand with the silicate material to form a homogeneous mixture. Once combined the mixture was then pressed into the target container forming the target. Targets containers had a volume of 3112.04 cm^3. Due to the conditions within the laboratory (the lack of a cold room) work had to be completed quickly meaning little control over the porosity was possible. After being formed, the target was stored in an upright (-18°C) freezer for a period of at least 24 hours prior to use. Again, due to the experimental limitations of the laboratory, targets were unable to be kept outside of the freezer for an extended time without melting. This meant that the construction method was not always the same leading to observed variations in target porosities. The target masses given in Table 6.2 assumed a 0% porosity, thus the ratio of this compared to the measured mass of the pre-impact targets gives a measure of the porosity. Despite these difficulties, the average porosity was found to be $25 \pm 4\%$ for KDS targets, $16 \pm 2\%$ for JSC-M targets with a 50 wt$\%$ silicate content, and $25 \pm 2\%$ for JSC-M targets with a 80 wt$\%$ silicate content.

Table 6.2: Constituent masses for each target type using in this investigation. Mixture densities were calculated assuming a 0% target porosity.

Silicate type	Mass of silicate material (g)	Mass of water-ice (g)	0% porosity mass (g)	Average target mass (g)	mixture density (g/cm^3)
		50 wt.$\%$			
Kiln Dried Sand	1887.3	1887.6	3774.9	2838 ± 188	1.21
JSC Mars-1	1539.4	1539.5	3078.9	2582 ± 119	0.99
		80 wt.$\%$			
JSC Mars-1	2579.7	645.0	3224.7	2420 ± 26	1.04

6.2.2 Target Analyses

Following each shot, targets were removed from the LGG for analysis. Initial visual inspection allowed for the identification of both anomalies occurring during the cratering process (i.e. chunks of ice being exposed close to the surface) and significant morphological features (e.g. central pits, spallation regions, etc.). After visual inspection, targets were placed in the freezer to re-freeze. For in-depth analysis of the formed crater morphology, depth profiles were taken across the crater. Two profiles were taken across each crater in orthogonal directions using a depth gauge (the set-up for this can be seen in Figure 6.1). Measurements were taken at increments of 5 mm outside of the crater region,

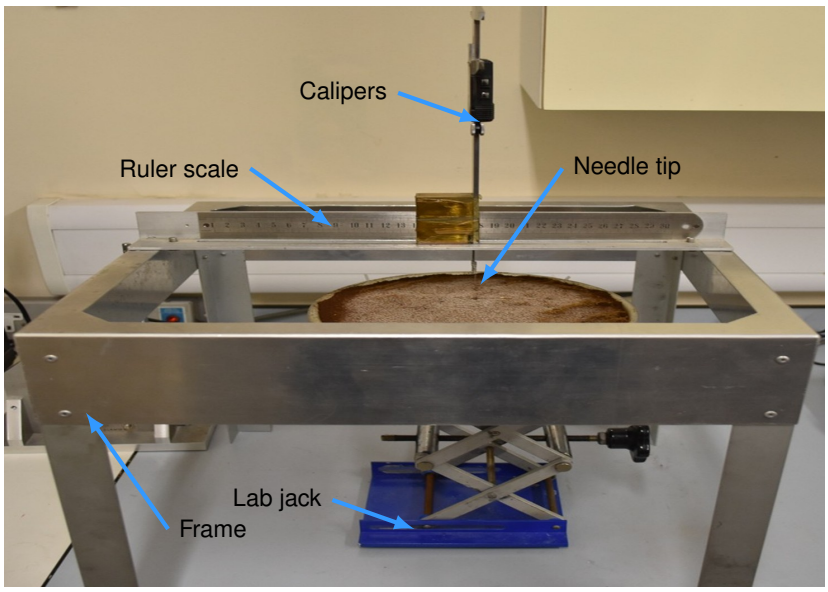

Figure 6.1: Depth gauge set-up used to obtain depth profiles across the formed craters. A zero depth was set to the target surface surrounding the crater and measurements of the depth across the crater were taken at 1 mm intervals.

reducing to increments of $1\ mm$ close to and inside of the crater. These measurements were relative to the depth of the target surface from the depth gauge frame outside of the crater. In-between each profile, the target was re-frozen to prevent changes occurring to the crater shape as it thawed. Due to the cryogenic nature of the targets, long-term storage for subsequent analysis was unfeasible, and the obtained depth profiles allowed analysis to be performed without the need to retain the target. Therefore, the crater diameters, depths, and volumes given in Table 6.3 are all taken from the depth profiles.

6.2.2.1 Depth Profile Processing

Measured 'raw' depth profiles (e.g. Figure 6.2, left panel) were processed to centre them on the deepest point and to correct for any slope in the surrounding surface. This was accomplished using Python and was carried out prior to measurements of the crater parameters being made. Centring the profile on the deepest point was a trivial process of shifting the entire profile horizontally by an amount equal to the horizontal position of the deepest point (typically close to the crater centre). Accounting for the slope of the surrounding surface was more complex, requiring a rotational transformation of the profile. This was accomplished by defining the outermost points of the craterform (the radial positions of the crater rim or edge). These two points allowed for a straight line to be defined across the 'top' of the crater. From this, a simple transformation of

$$d_{corr} = d_i - (mx_i + c) \tag{6.1}$$

could be applied to the depth profile where m is the gradient of the straight line and c is the intercept of the y-axis. From the corrected profile (e.g. Figure 6.2, right panel), the depth and diameter of the crater could then be obtained. For most craters in this chapter the corrections applied were

minor. In some cases, however, significant corrections had to be applied to account for deformities in the target (e.g.: excess ice, severely sloped targets, etc.). These target deformities would alter the apparent volume of the target with excess ice on the surface (being removed prior to the shot being undertaken) and sloped target surfaces leading to a lower crater volume.

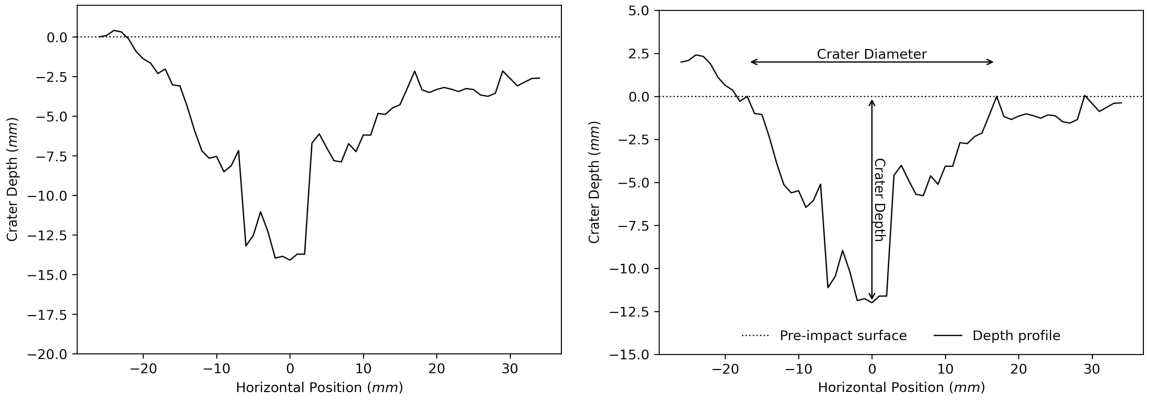

Figure 6.2: An example of a depth profile obtained across the crater formed during shot 8. Left shows the raw profile measured from the target whilst right shows the post-processed profile having undergone a rotational transformation to acount for the sloped surface of the target.

6.2.2.2 Crater Volumes

Crater volumes were calculated through a numerical volume of revolution method, using the measured depth profiles. Whilst typically crater volumes are measured by filling the crater with a fine-grained sand or glass, the cryogenic and sand-based nature of the targets make this an unrealistic method. For each profile, a parabola of best-fit was generated from the depth profiles by defining a series of anchor points across the profile. This formed a smoothed profile from which the area between consecutive anchor points could be calculated. The area was calculated using the equation:

$$A_s = \sum_{i=1}^{n} \left[(x_i - x_{i+1}) \left(\frac{y_i + y_{i+1}}{2} \right) \right] \tag{6.2}$$

where A_s is the segment area, x is the horizontal position of the anchor point, and y is the associated depth of the profile at the anchor point. n corresponds to the maximum index of the listed anchor points. This generates a summed area of the smoothed parabolic profile from which the volume can be calculated by rotating through a complete circle:

$$V_t = \frac{3}{4}\pi \left(\frac{x_{-1} - x_1}{2} \right) A_s \tag{6.3}$$

where V_t is the estimated volume and x_{-1} and x_1 correspond to the right most and left most anchor point respectively.

Figure 6.3 shows an example of this process for a measured depth profile with the anchor points and smoothed parabola shown. Typically, the anchor points correspond to abrupt changes in the depth profile (crater rim, edge of the central depression, etc.). Due to the nature of the smoothing process, the fitted parabola frequently over and under estimates the depth of the crater in areas,

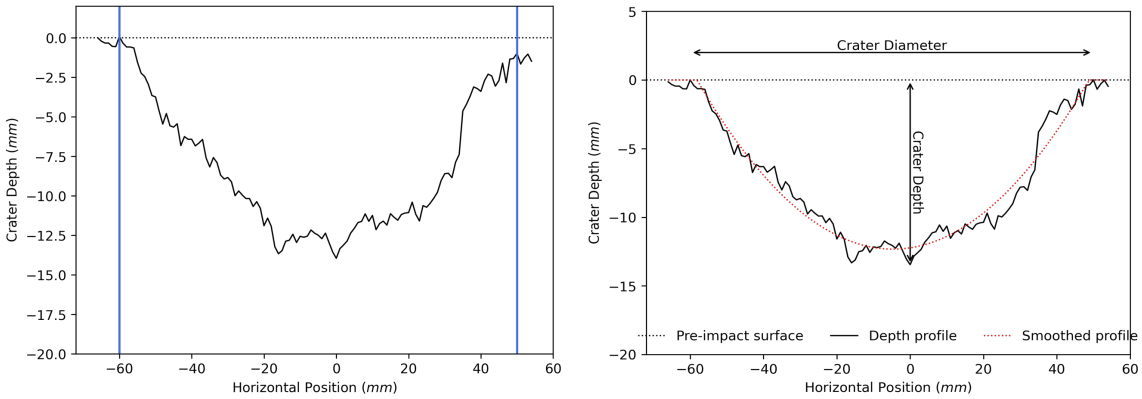

Figure 6.3: Left shows the pre-processed depth profile centred at the deepest point with the anchor points for this crater shown by the two blue vertical lines in the plot. Right shows the profile post-processing with the surrounding surface levelled and the smoothed parabolic profile shown in red. The profiles shown correspond to data collected from Shot 4 in Table 6.3

as shown in Figure 6.3. This was particularly true within the central depressions due to the often substantial and rapid increase in depth and their narrow nature. Often, these would cancel out with over and under estimations across the same profile. For profiles where this was not the case, however, the volumes given in Table 6.3 are the average of the volume measured from both profiles with the errors being the experimental error. This calculated error was substantially larger than those associated with the revolution method, or those induced by substantial deviations from the profile. Unbalanced deviations typically occurred at the very centre of the crater resulting from the numerical fitting method and could often be reduced or removed by the tweaking of an anchor point (moving the anchor point one position left or right within the profile).

6.3 Results

The results from the shot programme carried out within this chapter are shown in Table 6.3. In total 26 shots were carried out into both KDS and JSC-M based targets. Parameters of the shot programme were varied allowing a variety of scenarios to be considered. Whilst copper is not a material typically found in large quantities within asteroids or comets, it is a high density material commonly used within impact experiments and allows for high impact energies to be achieved within an experimental setting. Shot speeds are calculated via the method discussed in Section 4.1.2 with the errors being $\pm 1\%$ of the calculated value. Energies are the calculated kinetic energy of the projectile given by the equation:

$$E = \frac{2}{3}\pi\rho v^2 \left(\frac{d}{2}\right)^3 \tag{6.4}$$

where d is the projectile diameter (given in Table 6.3) and ρ is the projectile density ($8930\ \mathrm{kg/m^3}$ for copper [101] and $2900\ \mathrm{kg/m^3}$ for basalt [259]). Two depth profiles were taken in orthogonal directions allowing averaged parameters to be given in Table 6.3 for all but shot 1, where during analysis the target underwent significant melting, and thus morphological change, prior to a second depth

profile being taken. For the results associated with shot 4, the errors are taken to be the average percentage errors of the remaining dataset rather than the unknown actual experimental error. Shot 9, whilst included in Table 6.3, was excluded from further analysis due to the anomalously small crater diameter. The average diameter gave this crater a depth-to-diameter ratio of 0.83 ± 0.22 whilst other craters within the same data series had an average of 0.31 ± 0.02. Whilst key depth profiles are discussed in depth within this chapter, depth profiles for all craters can be seen in Chapter A.

Table 6.3: Shot and crater parameters for the shot programme undertaken within this chapter.

Shot	Speed (km/s)	Proj. Diam. (mm)	Proj. Mat.	Energy (J)	Silicate	Silicate Content (wt%)	Diameter (mm)	Depth (mm)	Volume (cm^3)
1	2.22 ± 0.02	1.5	Cu	39 ± 3	KDS	50	45.0 ± 1.4	11.24 ± 0.04	8.73 ± 0.07
2	2.97 ± 0.03	1.5	Cu	69 ± 5	KDS	50	67.5 ± 0.5	11.01 ± 0.38	30.91 ± 3.08
3	4.12 ± 0.04	1.5	Cu	134 ± 9	KDS	50	89.0 ± 5.0	14.73 ± 1.02	65.66 ± 11.63
4	4.74 ± 0.05	1.5	Cu	177 ± 12	KDS	50	112.0 ± 2.0	13.58 ± 0.13	112.60 ± 1.17
5	1.98 ± 0.02	1.5	Cu	31 ± 2	JSC-M	50	32.5 ± 10.5	11.57 ± 1.30	7.05 ± 4.71
6	2.13 ± 0.02	1.5	Cu	36 ± 3	JSC-M	50	30.0 ± 1.0	9.66 ± 2.64	4.60 ± 0.60
7	3.32 ± 0.03	1.5	Cu	87 ± 6	JSC-M	50	48.0 ± 6.0	12.55 ± 1.01	12.87 ± 1.81
8	3.67 ± 0.04	1.5	Cu	106 ± 7	JSC-M	50	37.5 ± 3.5	12.90 ± 0.90	10.46 ± 2.55
9	4.30 ± 0.04	1.5	Cu	146 ± 10	JSC-M	50	21.5 ± 5.5	17.82 ± 0.83	5.26 ± 2.35
10	4.47 ± 0.04	1.5	Cu	158 ± 11	JSC-M	50	45.0 ± 3.0	13.30 ± 0.36	12.91 ± 1.95
11	4.60 ± 0.05	1.5	Cu	167 ± 12	JSC-M	50	51.5 ± 8.5	12.95 ± 0.98	21.16 ± 8.57
12	1.83 ± 0.02	1.46	Basalt	8 ± 1	JSC-M	50	21.5 ± 2.5	8.62 ± 0.42	1.21 ± 0.11
13	2.11 ± 0.02	1.51	Basalt	12 ± 1	JSC-M	50	22.5 ± 4.5	6.43 ± 0.33	1.22 ± 0.57
14	3.25 ± 0.03	1.48	Basalt	26 ± 1	JSC-M	50	31.0 ± 1.0	8.73 ± 0.94	3.35 ± 0.57
15	3.53 ± 0.04	1.51	Basalt	33 ± 1	JSC-M	50	38.0 ± 1.0	7.03 ± 0.37	5.40 ± 0.93
16	3.67 ± 0.04	1.53	Basalt	37 ± 1	JSC-M	50	38.0 ± 1.0	7.22 ± 0.31	4.80 ± 0.93
17	4.89 ± 0.05	1.53	Basalt	65 ± 2	JSC-M	50	32.0 ± 3.0	11.15 ± 0.14	5.51 ± 1.01
18	4.97 ± 0.05	1.50	Basalt	63 ± 2	JSC-M	50	47.5 ± 2.5	8.83 ± 0.14	10.75 ± 0.72
19	0.95 ± 0.01	1.5	Cu	7.1 ± 1	JSC-M	80	10.5 ± 0.5	13.09 ± 0.76	0.44 ± 0.02
20	1.80 ± 0.02	1.5	Cu	25 ± 2	JSC-M	80	42.0 ± 7.0	19.39 ± 0.56	10.63 ± 2.54
21	2.04 ± 0.02	1.5	Cu	33 ± 2	JSC-M	80	35.5 ± 4.5	17.17 ± 0.27	6.46 ± 1.34
22	2.46 ± 0.02	1.5	Cu	48 ± 3	JSC-M	80	24.5 ± 0.5	18.57 ± 1.28	3.34 ± 0.65
23	2.89 ± 0.03	1.5	Cu	66 ± 5	JSC-M	80	54.0 ± 0.0	9.91 ± 0.20	19.99 ± 0.66
24	3.72 ± 0.04	1.5	Cu	109 ± 8	JSC-M	80	34.0 ± 2.0	14.99 ± 0.17	7.38 ± 1.18
25	3.86 ± 0.04	1.5	Cu	117 ± 8	JSC-M	80	42.0 ± 0.0	15.81 ± 0.08	15.96 ± 0.28
26	4.95 ± 0.05	1.5	Cu	194 ± 14	JSC-M	80	47.5 ± 1.5	15.95 ± 0.18	17.09 ± 1.12

6.4 Influences of Silicate Type

To provide a meaningful comparison to the investigation carried out within this chapter, crater properties were compared to those of Hiraoka, *et al.* [102] who impacted ice:silicate mixtures of the same ratio over a similar energy range. Their simulant mixtures were composed of coarse- or fine-grained serpentine powder mixed with powdered ice. In contrast to the targets prepared for this study, however, the targets produced by Hiraoka, *et al.* [102] underwent pressure sintering prior to impact providing a high level of control over the target porosity. This process was not possible for the targets constructed at the University of Kent due to the lack of a cold-room environment. For comparison purposes, the data provided by Hiraoka, *et al.* [102] was analysed and put through the same fitting process as the data collected from this work (as the parametrisation of their fits was not

provided in the published article); this fitting was carried out for their 50 wt.$\%$ silicate content targets only. Providing a further comparison to previously collected data, the data from this chapter was additionally compared to data from Burchell and Johnson [101] presenting impacts into pure water-ice. The results from Burchell and Johnson [101] follow the power law relations provided in their article.

6.4.1 Crater Dimensions

The crater dimensions are presented here as a function of the impact energy. This allows for varying projectile materials and impact speeds to be easily compared due to the energy dependencies of the variations in both projectile density and speed. Thus, considering the results as a function of the impact energy provides a simple way to compare the crater dimensions for differing target types and projectile materials. Figures 6.4 and 6.5 respectively show the crater diameters and depths as a function of the increasing impactor energy for the 50 wt$\%$ silicate content targets impacted with copper projectiles. As to be expected, crater diameters and depths increase with an increasing impactor energy. However, whilst the crater diameters increase at a differing rate for each target type, their depths increase at the same rate. The relations plotted in the figures within this chapter can be plotted as power-law relations. For the equations subsequently presented within this chapter the subscripts on the left-hand sides provide information on the silicate type, silicate quantity, and projectile material. Further, in order to provide a comparison to past literature, datasets from Burchell and Johnson [101] (impacts using copper projectiles into pure water-ice) and Hiraoka, *et al.* [102] (impacts using nylon projectiles into serpentine and 50 wt.$\%$ water-ice targets) are included within the analysis in this section.

In Figure 6.4, crater diameters follow the relation:

$$\mathrm{D_{KDS-50-Cu}} = (5.734 \pm 1.617)\,\mathrm{E}^{(0.570 \pm 0.058)}, \quad \mathrm{R}^2 = 0.984 \tag{6.5}$$

for KDS targets and:

$$\mathrm{D_{JSC-50-Cu}} = (12.840 \pm 5.107)\,\mathrm{E}^{(0.260 \pm 0.086)}, \quad \mathrm{R}^2 = 0.721 \tag{6.6}$$

for JSC-M targets where the diameters D are in mm, the impactor energy E is in J, and R^2 is the regression coefficient of the fit. The diameters within KDS-bearing targets increase at a substantially higher rate than those for JSC-M targets. The largest differences can be seen at higher impact energies. Whilst JSC-M targets appear to follow a similar trend to that of the Hiraoka, *et al.* [102] data (where the diameters follow the power law relation of $\mathrm{D_H} = 16.170\mathrm{E}^{0.223}$). The trend for craters formed within pure water-ice can be found in both Burchell and Johnson [101] and within Table 2 of Shrine, *et al.*, [191] ($\mathrm{D} = 19\mathrm{E}^{0.36}$). Within KDS targets, the slope of the trend is significantly larger than those for the comparison datasets. Indeed, the KDS crater diameters increase at such a rate that over the energy range considered here their diameters transition from approximating those formed within JSC-M and the trend found by Hiraoka, *et al.*, [102] to approaching those for craters formed in pure water-ice.

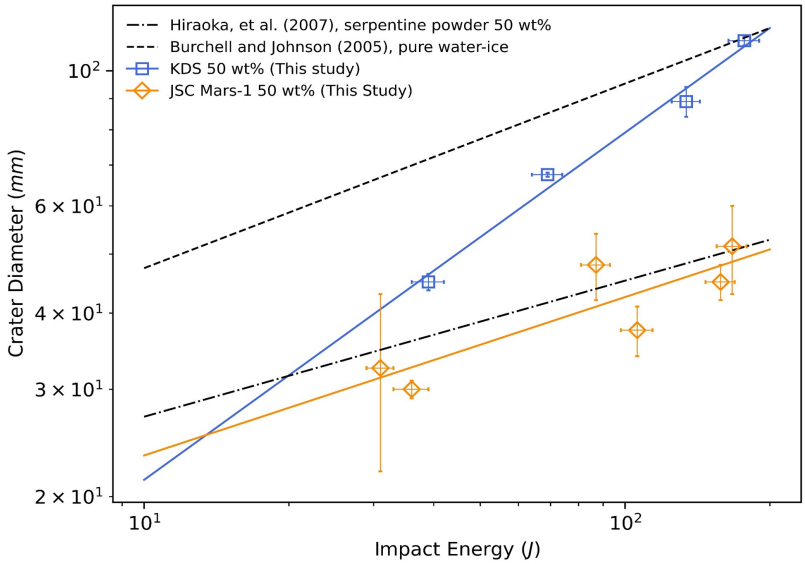

Figure 6.4: Logarithmic crater diameter against impactor energy. Diameters for craters formed in KDS and JSC-M based targets follow the power law relations given in Equations 6.5 and 6.6 respectively. For comparison purposes data from Burchell and Johnson [101] (dashed line) and Hiraoka, *et al.*, [102] (dash and dot line) are shown representing impacts into pure water-ice and a serpentine-ice mixture respectively.

When comparing this to the analysed depths, however, the combined trend of

$$d_{cmb-50-Cu} = (6.312 \pm 1.078)\, E^{(0.150 \pm 0.037)}, \quad R^2 = 0.682 \tag{6.7}$$

for both JSC-M and KDS targets with depth d being in mm differs from either of the past literature trends. The data for the crater depths in the KDS and JSC-M targets was combined for analysis due to the high level of similarity, individual trends were indistinguishable. The combined dataset is intermediate in magnitude between that of Hiraoka, *et al.*, [102] who found a relation of $d = 4.70E^{0.118}$ and Burchell and Johnson [101] who reported a trend of $d = 4.4E^{0.24}$.

The variation observed in the crater diameters are thought to be due to differences seen within the silicate materials within the impacted targets. As discussed in Section 5.3, grains within the KDS are regular and smooth contrasting the irregular, jagged grains seen in JSC-M. This change in morphology can be seen to significantly influence the coefficients of static friction for each material (Table 5.2), with a substantially higher level of force being required to induce motion in JSC-M samples than KDS.

This increased coefficient of friction means that the energy delivered to the target by the projectile is far more effective at opening up the crater within KDS-based targets than those containing JSC-M. For crater depths, however, the results show that much of the control resided in the projectile properties rather than the properties of the target. Equation 6.7 shows the depth to increase with energy at a rate similar to that found for the Hiraoka, *et al.* [102] data (following a relation of $d_H = 4.704E^{0.118}$). This is likely due to the increased material strength of copper compared to nylon (the projectile material utilised by Hiraoka, *et al.* [102]) providing it with a significantly higher pene-

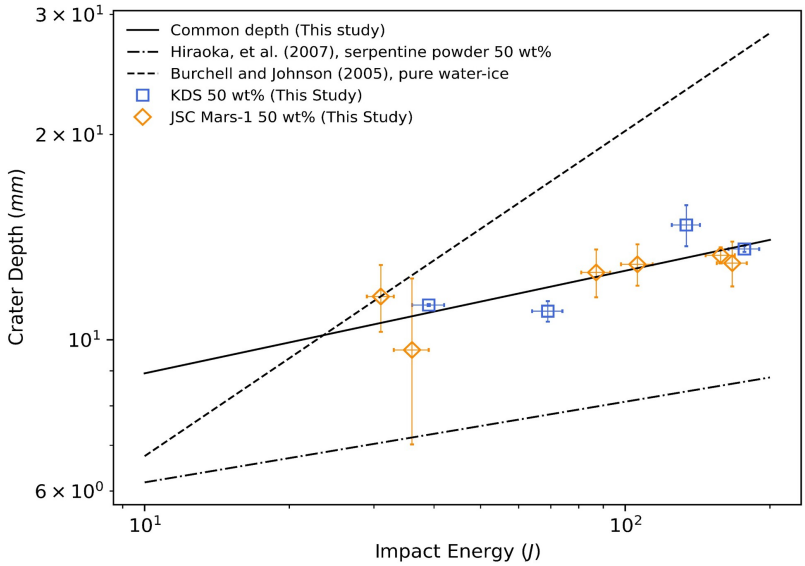

Figure 6.5: Logarithmic crater depth against impactor energy. Crater depths for both target types in this study were found to increase at the same rate following the power law relation in Equation 6.7. For comparison purposes data from Burchell and Johnson [101] (dashed line) and Hiraoka, *et al.*, [102] (dash and dot line) are shown representing impacts into pure water-ice and a serpentine-ice mixture respectively.

tration power. The reduced strength of nylon compared to copper significantly increases the level of disruption experienced by the projectile upon impact with the target surface. A projectile remaining coherent for an increased time during the initial impact process will penetrate further through the target than one which becomes disrupted upon contact with the target surface. In contrast to this, however, the results from Burchell and Johnson [101] show that some level of control over the crater depth is exerted by the target. The measured depths for craters formed within pure water-ice increase at a significantly higher rate than the combined relation in Equation 6.7, despite them having used a copper projectile. This difference is likely due to the nature of the response from the target material to the impact process. Pure water-ice responds as a brittle material to the shock processing of an impact, with the material fracturing and splintering rather than flowing [3, 7, 100].

Ice-silicate mixtures, in contrast, present an increased ductility to pure water-ice due to the inclusion of silicate grains. As the material flows and displaces rather than fractures, it is more effective at absorbing the energy from the impact resulting in a smaller final crater being produced [3]. It is interesting to note, however, that due to the occasionally inhomogeneous inclusion of water-ice within the targets some fracturing is still present in cases where the alignment of the ice allowed fractures to propagate through the target. This will be discussed in more detail in the next section.

Figure 6.6 shows the changes in the volumes of the final craters for the $50\ \mathrm{wt}\%$ silicate content targets hit by a copper projectile as the impact energy increased. It is found that the volume follows a linear relationship with impactor energy being

$$V_{KDS-50-Cu} = (0.717 \pm 0.078)\,E + (-20.672 \pm 9.190)\,, \quad R^2 = 0.977 \tag{6.8}$$

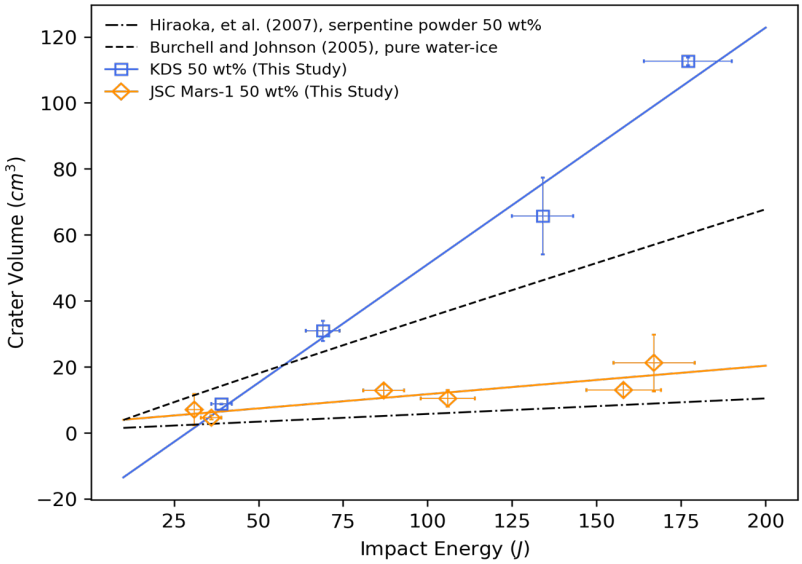

Figure 6.6: Crater volume against impactor energy. Crater volumes for KDS and JSC-M based targets follow the linear relations in Equations 6.8 and 6.9 respectively. For comparison purposes data from Burchell and Johnson [101] (dashed line) and Hiraoka, *et al.*, [102] (dash and dot line) are shown representing impact into pure water-ice and a serpentine-ice mixture respectively.

for KDS-based targets and

$$V_{JSC-50-Cu} = (0.086 \pm 0.024)\,E + (3.110 \pm 2.717)\,, \quad R^2 = 0.756 \tag{6.9}$$

for targets containing JSC-M where the volume V has the units of mm^3. Also shows are the results of Hiraoka, *et al.*, [102] ($V = 0.047E + 1.038$) and Burchell and Johnson [101] ($V = 0.008E + 63.372$). Of particular interest within Figure 6.6 is the comparison between the trend shown by Equation 6.8 for KDS-ice and that found by Burchell and Johnson [101] for pure water-ice. Figure 6.5 shows that the depths of craters within KDS-based targets are lower than those in pure water-ice, whilst Figure 6.4 shows that, at all but the highest energies within this investigation, the diameters are smaller. Figure 6.6, however, shows their volumes to be significantly higher at all but the lowest impact energies.

This result is likely again an effect of the brittle nature of pure water-ice and its influence on the morphology of the produced crater. During the crater formation process, water-ice targets undergo spallation [100], forming a shallow 'terrace' close to the surface of the target surrounding the much deeper central crater. This drastically increases the diameter of the final crater whilst only contributing minimally to the final volume. Little to no spallation was observed around the craters formed within KDS-based targets, with them being observed to posses the typical bowl-shaped morphology - particularly at higher impact energies. This means that, even with the smaller diameters and depths, their volumes would be expected to be significantly larger than those found by Burchell and Johnson. As the analysed results indicate, the volumes found for craters within JSC-M targets are significantly smaller than those for craters in KDS-based targets, appearing to increase at a very slow rate (similar to the results found for the Hiraoka, *et al.*, [102] data). Whilst the dimensions of the final crater do have an influence over the crater volume, the largest contributing factor to this measurement is the

interior morphology of the final crater produced.

6.4.2 Morphological Comparisons

Figure 6.7 shows the averaged radial profiles across six craters, three KDS and three JSC-M. Profiles are centred at the deepest point measured, providing four radial profiles for each crater. Averaging these allows for the interior morphology of the crater to be compared minimising the influence of extreme morphological features. Cases of severe deviation from the average morphology will be discussed individually. Within Figure 6.7, the craters are grouped by impact speed, with the speed increasing for each successive pair. In the figure, the black circle at the origin represents the size of the projectile compared to the formed crater. Figure 6.7 shows that the interior morphology differs between each target type, particularly at higher speeds. For the craters formed in JSC-M targets, the morphology of the central region appears to be similar at all speeds, presenting an irregular convex cone with a sharp downturn in the very centre - a region similar in size to the initial projectile diameter. As the speed increases, the morphology outside of this region appears to differ. At the slowest speeds, the crater is formed from only this central region, being simply an irregular convex cone. As the speed then increases, a shallower outer region appears surrounding the inner cone, with an approximately smooth transition between the two regions.

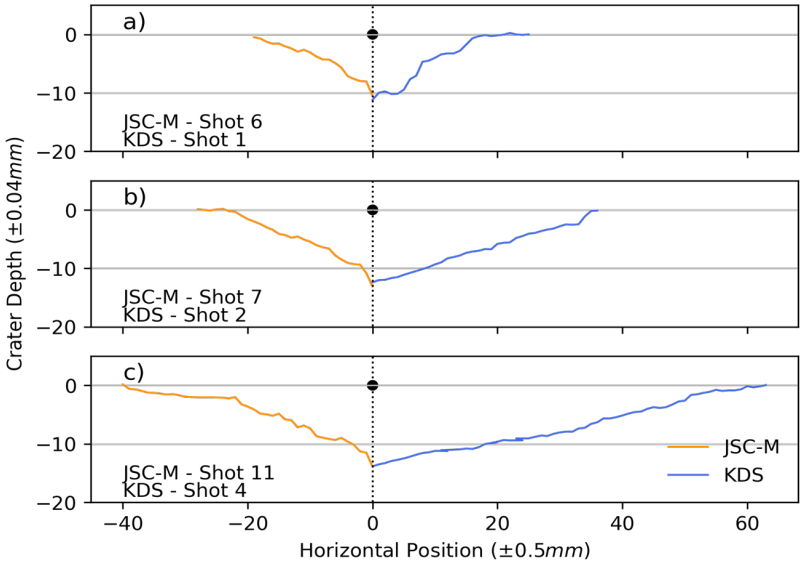

Figure 6.7: Average radial profiles for craters formed in KSD and JSC-M targets. Radial profiles are formed from the measured depth profiles for each crater with the left and right half of the profile (with the centre at the deepest point) being averaged. Depths are relative to the pre-impact surface of the target surrounding the crater. Profiles are grouped by impact speed (shown in Table 6.3), being ≈ 2 km/s in the top panel, ≈ 3 km/s in the middle panel, and ≈ 5 km/s in the bottom panel. Within each panel, the black circle located at the origin represents the projectile.

As the speed increases further still, this outer region transitions from a shallow and irregular region to an almost bowl-shaped depression - appearing almost as a crater-in-crater morphology.

Contrasting this morphological progression, craters formed in KDS-based targets show a changing morphology for each impact speed. At the slowest speeds, the interior morphology appears morphologically similar to that of JSC-M, with the middle portion of the crater appearing irregular with both profiles showing the presence of a central pit feature. Contrastingly, however, the crater formed within the JSC-M target appears to almost bowl-shaped with a central depression whilst that formed within the KDS target appears almost terraced. The profile shown in panel a) of Figure 6.7 additionally shows that, for the slowest speed, craters formed in KDS-based targets appear to show a broad central depression region contrasting the narrow central pit observed in JSC-M targets. This is then surrounded by an irregular shallow region - forming a crater-in-crater appearance. Unlike craters formed within JSC-M targets, the central depression is only seen at the slowest speeds for KDS-based targets. The interior morphology appears much more linear at medium velocities. This appears to change as the edge of the crater is approached with a sudden jump being seen taking the profile back to a pre-impact surface level. At the highest impact energies, craters within KDS-based targets appear to possess an almost bowl-shaped morphology, substantially contrasting that seen for craters within JSC-M targets.

6.4.3 Unusual Crater Morphologies

6.4.3.1 Shot 2

Figure 6.8 shows the crater formed during shot 2 (KDS-based target impacted at 2.22 ± 0.02 km/s), with the measured depth profiles being shown in Figure 6.9. Within the profiles, interior terraces can be seen in one direction, whilst the other shows an approximate bowl morphology. This irregularity in the depth profiles is likely the result of the excessive ice observed in Figure 6.8. Whilst stored within the freezer, ice within the target appeared to melt and rise to the surface. This formed a layer of solid ice covering the target (which can be seen around the edge of the target in Figure 6.8). Prior to the shot being carried out, this had to be removed leading to the pre-impact surface being somewhat irregular. Additionally, this apparent redistribution of ice during target storage may have led to inhomogeneities forming within the target. During some shots, this was a known occurrence with ice clumps allowing the propagation of fractures through the target. The observed shocked ice present within the centre of the target supports this. Despite the excessive ice being present on the target surface, and the inhomogeneous distribution, the measured crater parameters closely follow the trends observed for KDS-based targets.

6.4.3.2 Shot 5

The crater in Figure 6.10 was formed during shot 5 (JSC-M based target impacted at 1.98 ± 0.02 km/s) with the obtained orthogonal depth profiles being shown in Figure 6.11. The profiles shown in Figure 6.11 show the crater to be substantially irregular and asymmetrical. The profile shown on the left-hand side of Figure 6.11 possesses a crater diameter approximately half of that shown on the



Figure 6.8: The post-impact target for shot 2 (KDS-based target impacted at 2.22 ± 0.02 km/s) with the formed impact feature located in the centre of the target. The target is 20 cm in diameter.

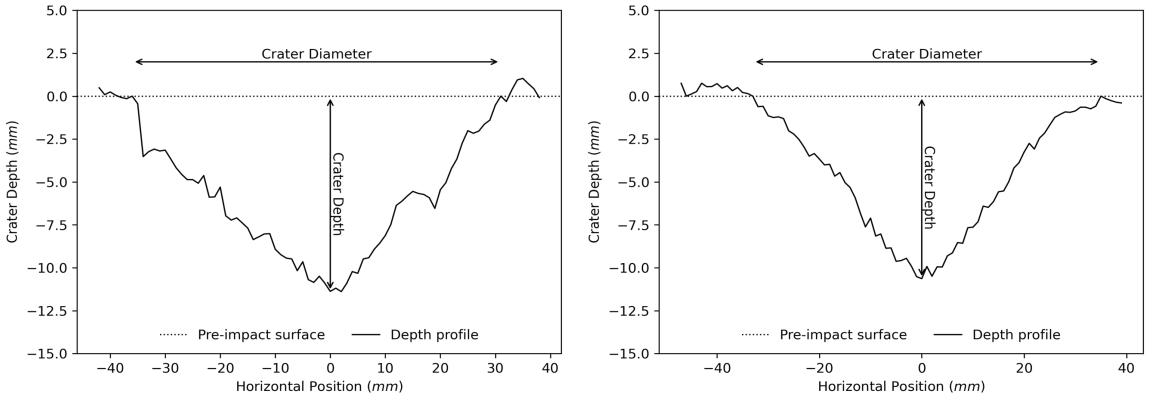

Figure 6.9: Depth profiles measured across the crater formed during shot 2. Profiles are taken in orthogonal (longest and shortest diameter) directions across the target.

right-hand side with the formed crater being a narrow, cone-shaped feature. In contrast, the profile shown in the right-hand panel of Figure 6.11 is that of a wide bowl-shaped feature with a deep central depression - as typical for craters formed in JSC-M based targets. An explanation for this irregularity can be found within Figure 6.10. The surface of the target for shot 5 is seen to be uneven and undulating. This can also be seen within the obtained depth profiles with the surface surrounding the formed crater seen to be highly uneven with crevices present surrounding the formed crater. These features are unlikely to have formed as a result of the impact process. Hence, the irregularity of this surface may have led to the crater becoming preferentially larger.

6.4.3.3 Shot 11

Figure 6.12 shows the crater formed during shot 11 (JSC-M based target impacted at 4.60 ± 0.05 km/s) with the measured depth profiles being shown in Figure 6.13. In Figure 6.12 the crater can be seen



Figure 6.10: The post-impact target for shot 5 (JSC-M based target impacted at 1.98 ± 0.02 km/s) with the formed impact feature located in the centre of the target. The target is 20 cm in diameter.

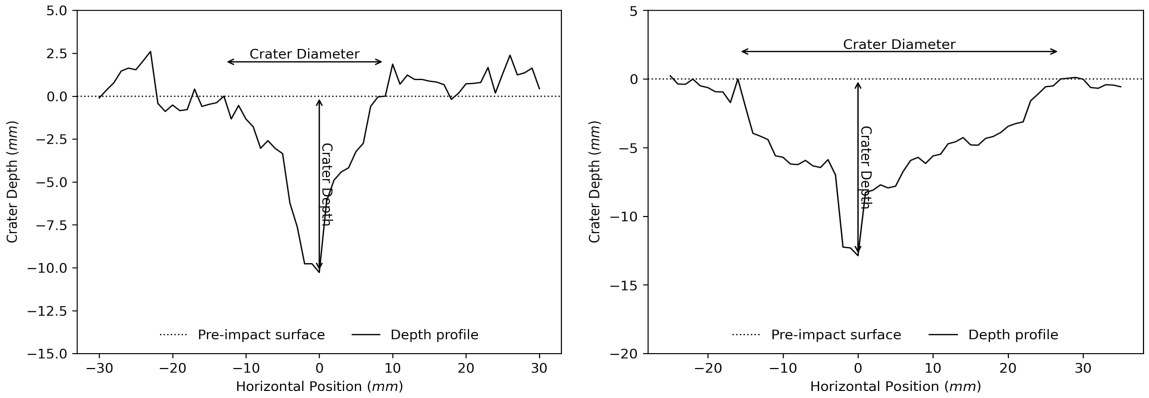

Figure 6.11: Depth profiles measured across the crater formed during shot 5. Profiles are taken in orthogonal (longest and shortest diameter) directions across the target.

to be highly irregular with the presence of damaged ice around the central depression feature. This irregularity is also visible in the depth profiles shown in Figure 6.13. Both profiles are highly irregular showing a jagged, asymmetrical crater. In particular, the profile shown on the left-hand side of Figure 6.13 shows an extensive, almost bowl-shaped feature to the left of the central depression. This high level of irregularity is thought to be the result of irregular spallation processes and inhomogeneous ice distribution within the target. This led to the large-scale removal of material plates during the formation of the crater. When looking at the parameters in Table 6.3 for shot 11, diameter and depth are seen to closely follow the trends observed for JSC-M targets. When looking at the volume, however, it is seen to be substantially higher than any other target containing JSC-M simulant. This is likely due to the observed asymmetry and irregularity within the crater.



Figure 6.12: The post-impact target for shot 11 (JSC-M based target impacted at 4.60 ± 0.05 km/s) with the formed impact feature located in the centre of the target. The target is 20 cm in diameter.

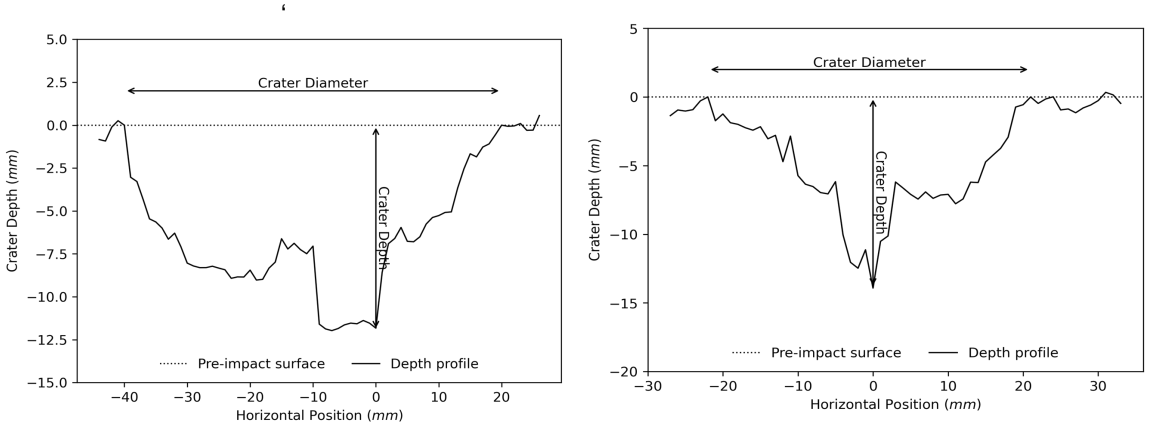

Figure 6.13: Depth profiles measured across the crater formed during shot 11. Profiles are taken in orthogonal (longest and shortest diameter) directions across the target.

6.4.4 Copper or Basalt Projectiles

A potential cause of the apparent central pits inside the craters formed within JSC-M targets is the impedance miss-match between the primarily basaltic target and the copper projectile used (resulting from the large differences in their densities with the density of JSC-M and KDS targets being 0.99 g/cm^3 and 1.21 g/cm^3 respectively and the density of the copper projectile being 8.93 g/cm^3). Thus, to further investigate this observed morphology, a series of shots into 50 wt% silicate content JSC-M targets was undertaken using 1.5 mm spherical basalt projectiles - possessing a density approximately equal to that of the target. The outcome of these experiments can be seen in figures 6.14, 6.15, and 6.16. Whilst the shots with each projectile type covered the same velocity range ($2 - 5$ km/s), the difference in projectile density means that the respective impact energies are substantially lower for the basalt projectiles than for the copper ones. Figure 6.14 shows the relationship

between the impact energy and crater diameter for both projectile types. Both follow power law relations with basalt projectiles following the relation:

$$D_{JSC-50-Bas} = (12.019 \pm 4.478)\, E^{(0.296 \pm 0.102)}, \quad R^2 = 0.675 \tag{6.10}$$

and the copper projectiles following Equation 6.6. As to be expected, the diameters of craters formed by basalt projectiles are considerably smaller than those formed by the copper projectiles at similar impact speeds.

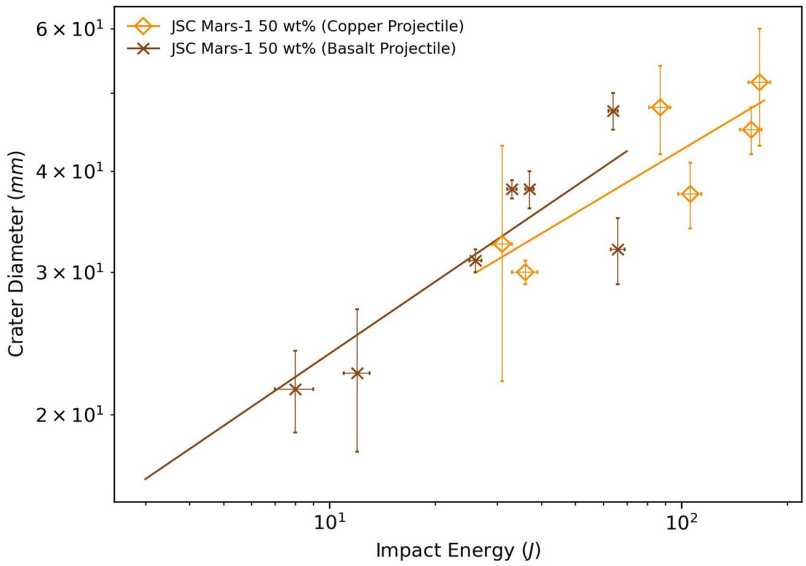

Figure 6.14: Logarithmic crater diameter against impactor energy. Crater diameters resulting from the impact of a basalt projectile follow the power law relation in Equation 6.10. The significant overlap within the central region of the plot however indicates that diameters may follow the combined power-law relation given in Equation 6.11.

Of note, however, is the similarity between these trends, particularly in the region of overlap between the two datasets. Plotting a power law relation for the combined data presented here, we find that within JSC-M targets, the diameter follows the relation of:

$$D_{JSC-50-Comb} = (13.988 \pm 2.840)\, E^{(0.246 \pm 0.048)} \quad R^2 = 0.731 \tag{6.11}$$

This substantial overlap indicates that whilst the projectile material holds some influence over the crater diameter (through its control over the impactor energy), it presents no direct affect on the final crater diameter.

When looking at the crater depths, however, differences begin to emerge between the two datasets. In Figure 6.15, the measured depth for craters formed via the impact of a basalt projectile show a general trend of increasing with increasing impact energy. They are, however, found to be lower than those for craters formed from the impact of a copper projectile, even at similar impact energies. There is, however, a substantial increase in the scatter of these results. The fitting value for the power law relation is only $R^2 = 0.239$ (hence the line of best fit not being included on the graph presented here),

showing that whilst a general increase in depth can be seen as the impact energy increases, this is only a very loose trend.

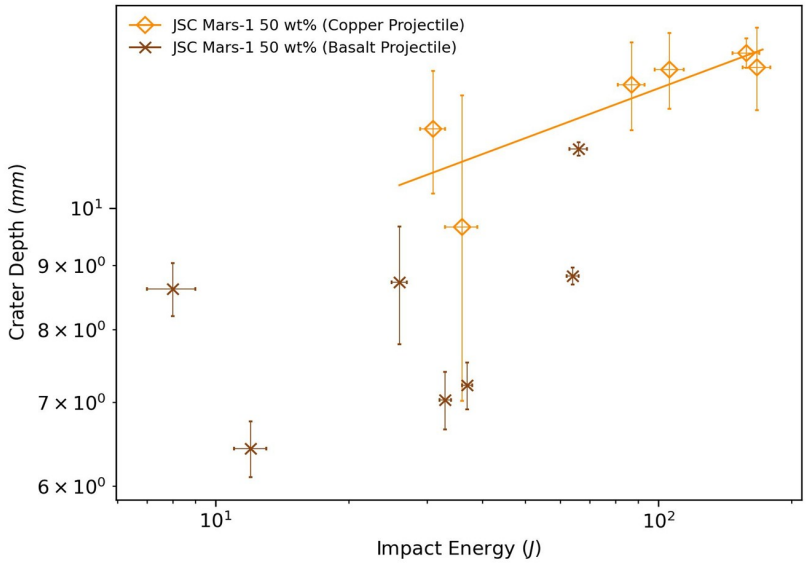

Figure 6.15: Logarithmic crater depth against impactor energy. The depths of craters formed by the impact of a basalt projectile show a significant scatter with the regression value for the power law relation found as $R^2 = 0.239$. The very low regression coefficient is why the trend line has not been included within this figure. Craters formed within 50 wt% silicate component targets follow the power-law relation of $d_{JCS-50-Cu} = (6.788 \pm 1.336)\, E^{(0.132 \pm 0.043)}$, $R^2 = 0.710$

As the targets for these datasets remained the same, the increase in scatter is thought to be due to changes in the projectile material. When targets are impacted by the copper projectile, it is thought that after first contact with the target, the projectile continues travelling deeper into the target at a reduced speed but still relatively intact. This is likely the largest contributor to the apparent central pit features seen in Figure 6.7. This process is thought to occur due to the large difference in density between the ice-silicate target and the copper projectile. A basalt projectile is much more comparable in density to the target material, however. Hence, following the impact of the basalt projectile, it likely undergoes disruption limiting the level of penetration capable. Disruption of the projectile explains both the shallower crater depth achieved with basalt projectiles and the increased scatter. Whilst each projectile will undergo disruption, heterogeneities within the target and projectile will influence this and alter the dimensions of the produced final crater. Figure 6.16 shows the calculated volume for each crater as a function of the impact energy.

As the impact energy increase, the final crater volume increases linearly; similarly to the trend observed with copper projectiles. The trend for craters formed by basalt projectiles follows the relation of

$$V_{JSC-50-Bas} = (0.123 \pm 0.032)\, E + (0.299 \pm 1.330) \quad R^2 = 0.741 \tag{6.12}$$

whilst the trend for copper projectile formed craters follows Equation 6.9. the smaller volumes are to be expected given both the smaller crater diameters and depths. The volume for basalt formed

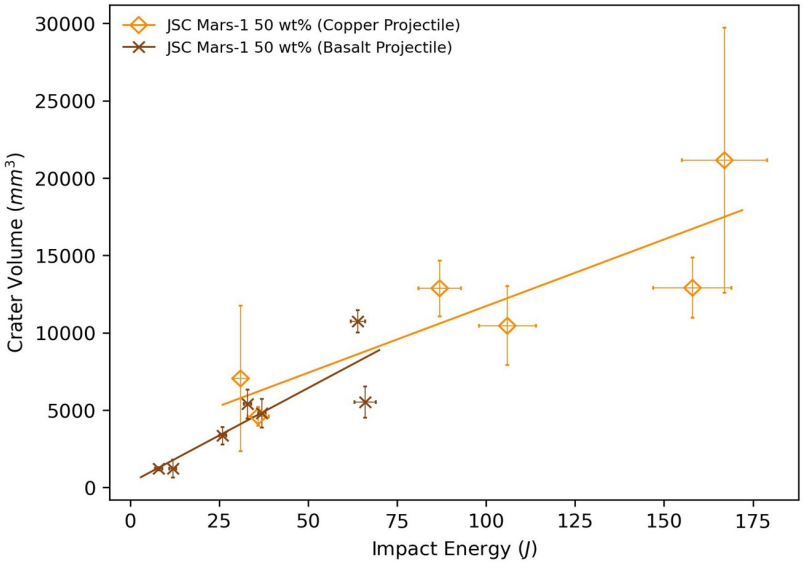

Figure 6.16: Linear crater volume against impactor energy. The volumes of craters formed by the impact of a basalt projectile follow the linear relation in Equation 6.16. Similarly to the diameters shown in Figure 6.14 a significant level of overlap is seen with the data in this figure following the combined linear trend given in Equation 6.13.

craters, however, appears to increase at a rate slightly higher than that for copper projectile formed craters. Despite this, the results shown in Figure 6.16 show a similar level of overlap as those seen in Figure 6.14. When plotting a combined volume trend, it is found that the crater volume increases following the linear trend of

$$V_{JSC-50-comb} = (0.099 \pm 0.013)\,E + (1.455 \pm 1.078) \qquad R^2 = 0.835 \tag{6.13}$$

Equations 6.11 and 6.13 possess regression coefficients higher than those for trends shown by basalt or copper projectiles alone. This suggests that when comparing crater parameters as a function of the impactor energy, much of the control lies with the target material rather than with the projectile - particularly for diameter and volume.

Figure 6.17 shows differences can be seen when comparing the interior morphology of craters formed by the impact of a basalt vs. copper projectile. The biggest differences seen within the interior morphology for craters formed by basalt projectiles are the increased linearity of the radial profiles. Those formed by the impact of a copper projectile show at least one distinct transition in the central region with craters formed at higher impact energies showing additional transitions close to the pre-impact surface with the formation of what appears to be a very shallow spallation region. A similar profile is only seen within panel a) of Figure 6.17 when considering those formed by basalt projectiles. This profile appears to show a sudden drop approximately halfway towards the centre. This is then followed by a very slight down-turn within the very centre. As the velocity of the impactor increases, however, this morphology changes completely to an almost linear profile deviating slightly close to the crater edge. At the highest impact velocity in Figure 6.17 the profile formed by the impact of a basalt projectile shows an almost perfectly linear profile with depth appearing to increase smoothly

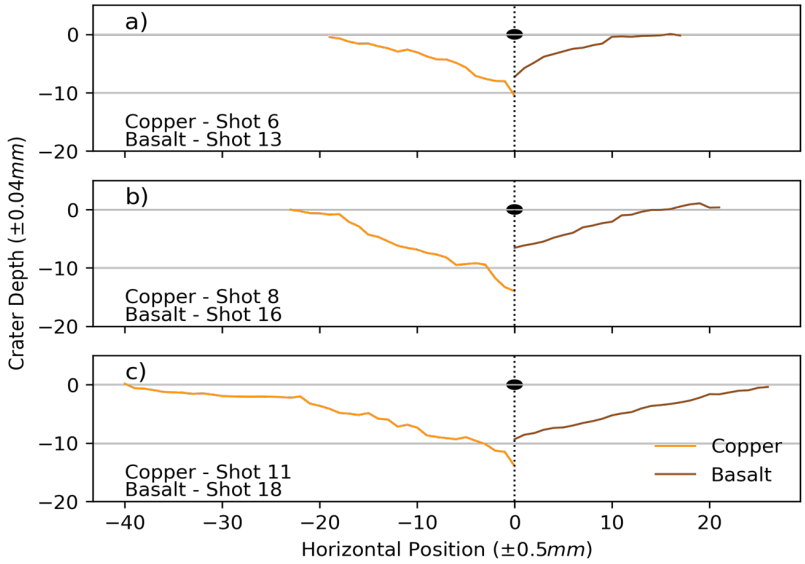

Figure 6.17: Average radial profiles for craters formed in JSC-M targets by the impact of either a copper of basalt projectile. Radial profiles are formed from the measured depth profiles for each crater with the left and right half of the profile (with the centre at the deepest point) being averaged. Depths are relative to the pre-impact surface of the target surrounding the crater. Profiles are grouped by impact speed (shown in Table 6.3), being ≈ 2.1 km/s in the top panel, ≈ 3.7 km/s in the middle panel, and $4.6 - 5$ km/s in the bottom panel. Within each panel, the black circle located at the origin represents the projectile.

as distance from the crater edge increases. These differences in interior morphology are indicative of the central depressions seen in targets impacted by copper projectiles resulting from the impactor properties.

It is thought that upon impacting with the target surface, the copper projectile remains largely intact and continues travelling into the target at a now reduced speed. The result of this is a secondary impact on the floor of the formed impact feature at which time the projectile remnants tunnel into the target forming the central depression seen; a process similar to the mechanism governing early armour piercing weaponry [3]. This mechanism is thought to occur due to the substantial differences in densities between the impacting projectile and target material. It does, however, not explain why the depressions are primarily observed within JSC-M based targets - disappearing from KDS-based targets at impact velocities above ≈ 2 km/s. Similar depressions are commonly observed within pure water-ice targets impacted with their formation due to spallation processes. The localisation of this feature to only the central region of the formed crater and the secondary transition observed at larger radii closer to the target surface, however, indicate the central depressions observed here are formed by mechanisms other than spallation. This mechanism, however, is as of yet unknown.

6.5 Silicate-Dominated Mixtures

Whilst 50 wt.% silicate content targets allow for comparisons to past data-sets, they are inaccurate when considering the cratering process on Mars. Current estimates for the ice content within the near-surface region of Mars predict between a $10 - 30$ wt.% ice content [23, 67]. Due to the time constraints of this work, the value of 20 wt.% ice (80 wt% silicate) was chosen as the mid-point for this range, and used in this initial study into cratering in silicate-dominated mixtures. Silicate-dominated targets were impacted over the same energy range and with the same projectiles as targets with a 50 wt% silicate content. The results of these impacts can be seen in Figures 6.18, 6.19 and 6.20. Figure 6.18 shows the change in crater diameter with an increasing impact energy. These diameters are found to follow a power-law relation:

$$D_{JSC-80-Cu} = (13.949 \pm 7.883)\, E^{(0.237 \pm 0.129)} \quad R^2 = 0.434 \tag{6.14}$$

The data from silicate-dominated targets, however, shows an almost complete overlap with those from targets with a 50 wt% silicate content, having a combined trend described by the power law:

$$D_{JSC-Comb-Cu} = (13.547 \pm 4.815)\, E^{(0.246 \pm 0.079)} \quad R^2 = 0.516 \tag{6.15}$$

Of note for the combined trend is the lower regression coefficient when compared to the trend for target containing a 50 wt% silicate content in Equation 6.6, which has a regression value of $R^2 = 0.721$. This is a result of the increased scatter present within silicate-dominated targets. This is seen in particular within the results for crater depth in Figure 6.19.

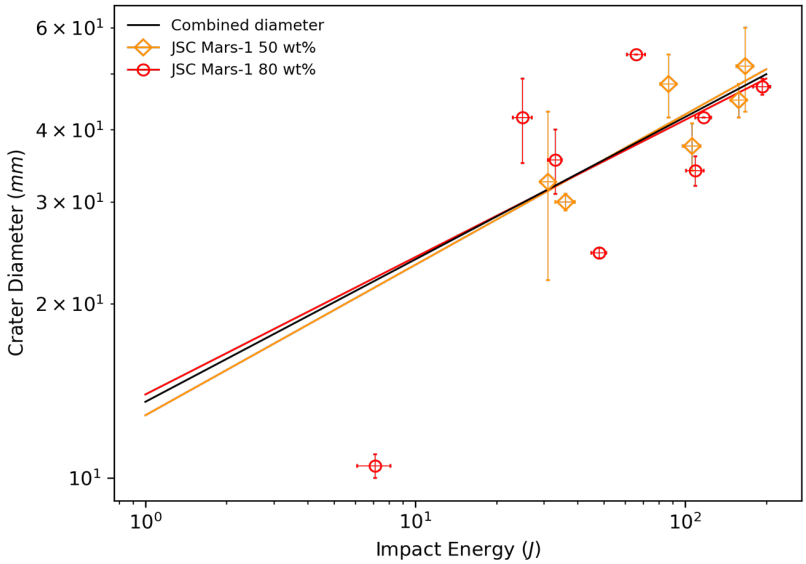

Figure 6.18: Logarithmic crater diameter against impactor energy. Diameters of craters within silicate-dominated targets show an almost complete overlap with those from 50 wt% content targets despite the increased scatter of the results. The silicate-dominated crater diameters follow the power-law relation in Equation 6.14.

For silicate-dominated targets, measured crater depths show no clear trend with an increasing

impactor energy. The fitting line for this data set is not shown for this relation due to the extremely low regression coefficient ($R^2 = 0.000$). This result is unexpected as previously discussed results indicate that a significant portion of the control over formed crater depth is held by the projectile rather than the target material (Figure 6.5). The results shown in Figure 6.19, however, indicate that some control over the crater depth is still exerted by the target material. There are several potential factors contributing to the scatter in the data. One is the combination of analytical techniques and the nature of the target material. The reduced ice quantity within the $80\text{wt}\%$ silicate content targets leads to a much more granular target material, which presents less resistance to the needle tip used to form the depth profiles. This increases the difficulty in identifying the true surface particularly within the narrow central pit region.

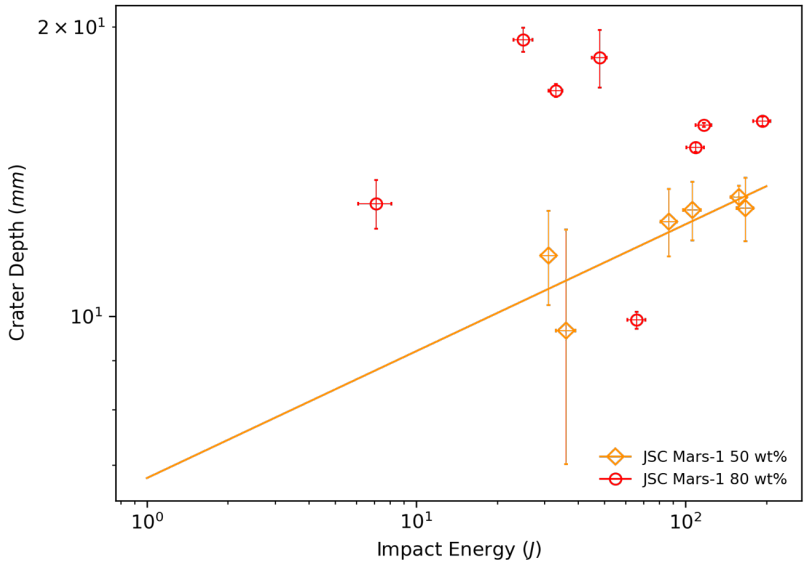

Figure 6.19: Logarithmic crater depth against impactor energy. Depths of craters within silicate-dominated targets show an extreme scatter with no discernable trend. Craters formed within $50\ \text{wt}\%$ silicate component targets follow the power-law relation of $d_{JCS-50-Cu} = (6.788 \pm 1.336)\, E^{(0.132 \pm 0.043)}, R^2 = 0.710$

Additionally, the narrow nature of the central pit may further increase this difficulty by restricting the access of the depth gauge to this region. Another potential reason for this increased and approximately constant depth when compared is the weaker target material. In Figure 6.19, all but one of the data points representing silicate-dominated craters lie above the trend for those within $50\text{wt}\%$ silicate content targets. As the impact energy increases, however, the gap between the two trends closes. Both trends follow power-law relations meaning that as the energy of the impactor increases they tend towards an approximately constant maximum depth. Thus, within a weaker target material this maximum depth will be achieved much quicker than within a stronger material. This is suggested to occur here due to the changes observed in crater depth differences. The increased level of scatter and the lack of low energy impacts within the dataset presented here, however, limit the level to which this trend can be assessed.

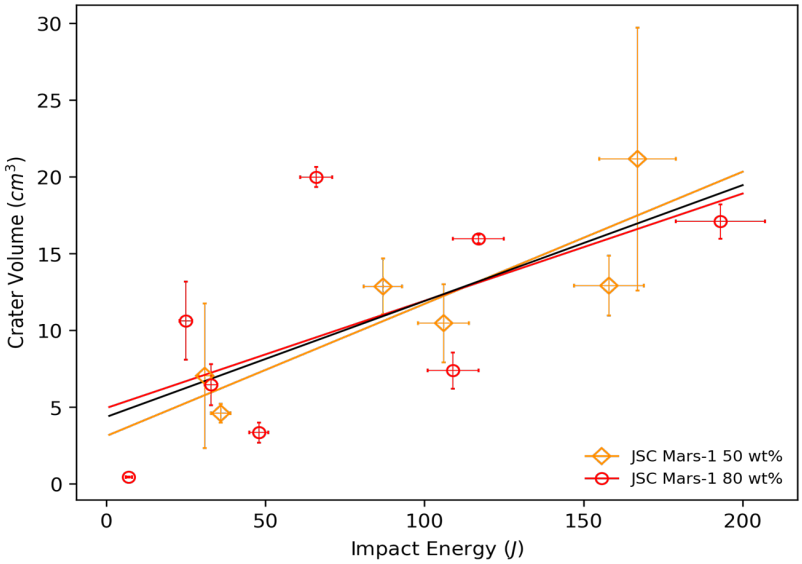

Figure 6.20: Linear crater volume against impactor energy. The volumes of crater formed in silicate dominated targets follow the linear relation of Equation 6.16 shown here as the red line (Equation 6.16). Despite the large level of scatter observed within silicate dominated crater volumes, a considerable level of overlap is seen between the two data sets with them following the combined linear relation of Equation 6.17 shown here in black with the orange line being the fit for 50 wt$\%$ silicate content targets (Equation 6.9).

Figure 6.20 shows the changes in crater volume as the impact energy increases. Within Figure 6.20 it can be seen that errors in crater volume for craters formed in silicate-dominated targets are significantly lower than those for 50wt$\%$ silicate content targets. The errors in crater volume within Figure 6.20 can be taken as a proxy of asymmetry in interior morphology. Hence, this reduced level of error seen is suggestive of craters formed within silicate-dominated mixtures having a higher level of symmetry when compared to craters formed within targets containing a higher proportion of ice. Craters formed within 50 wt.$\%$ silicate content targets follow the linear relation shown in Equation 6.9. Craters formed in silicate-dominated targets follow the linear relation of

$$V_{JSC-80-Cu} = (0.070 \pm 0.036)\,E + (4.935 \pm 3.438) \quad R^2 = 0.380 \tag{6.16}$$

The trend for both target types are highly similar, with them following a combined relation of

$$V_{JSC-Comb-Cu} = (0.076 \pm 0.022)\,E + (4.354 \pm 2.208) \quad R^2 = 0.503 \tag{6.17}$$

As the impact energy increases, however, the trends begin to diverge. A large portion of the control over the trends seen in crater volume of the final crater produced is given to the interior morphology. A comparison of the interior morphology for silicate-dominated targets and those formed in targets containing a 50 wt.$\%$ silicate level are shown in Figure 6.21. Whilst the morphological progression seen for targets containing a 50 wt.$\%$ silicate content follows the same progression discussed in Section 6.4.2, the morphology of craters in silicate-dominated targets is seen to vary drastically as the impactor energy increases.

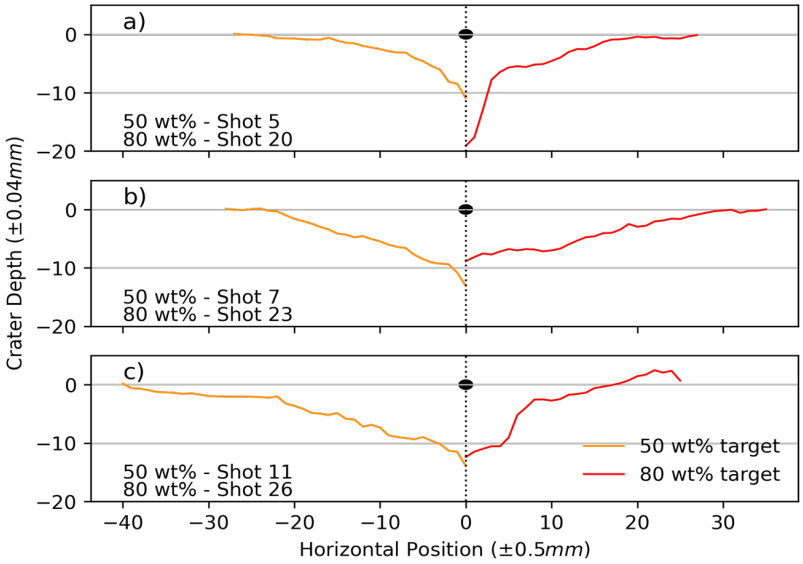

Figure 6.21: Average radial profiles for craters formed in JSC-M targets with either a $50\ \mathrm{wt}\%$ or $80\ \mathrm{wt}\%$ silicate content. Radial profiles are formed from the measured depth profiles for each crater with the left and right half of the profile (with the centre at the deepest point) being averaged. Depths are relative to the pre-impact surface of the target surrounding the crater. Profiles are grouped by impact speed (shown in Table 6.3), being $1.8 - 2\ \mathrm{km/s}$ in the top panel, $2.9 - 3.3\ \mathrm{km/s}$ in the middle panel, and $4.6 - 5\ \mathrm{km/s}$ in the bottom panel. Within each panel, the black circle located at the origin represents the projectile.

At the lowest impact energies, within the average radial profiles, the profile appears to follow a similar trend to that for craters in equal component craters. This, however, is only true outside of the very central region. Whilst in targets containing $50\ \mathrm{wt.}\%$ silicate material presented a sharp downturn in the very central region, this is limited to approximately the size of the projectile. Within silicate-dominated targets, the central region presents a much deeper and much wider pit-like region. As the energy increases, however, this morphology appears to change for the crater profiles shown in panel b) of Figure 6.21. At middle impact energies, profiles appear largely similar in both target types, both presenting a much flatter morphology. This again changes as the impact energy increases again. At the highest impact energy, the central pit feature is again observed. Contrasting the profiles seen within panel a), however, the pit takes up a significant portion of the profile. The increased prominence of the pit feature seen in Figure 6.21 suggests a potential difference in formation mechanism compared to those within $50\ \mathrm{wt.}\%$ silicate content targets.

6.6 Conclusions

The results in this chapter have shown how the crater dimensions and interior morphology of craters within ice-silicate mixtures vary as the silicate material, projectile material and target ice quantity are changed. The change in grain morphology and size distribution between target types appeared

to have considerable influence over the crater diameter and interior morphology, thus providing an influence over the total volume of the formed crater. The crater depth, however, was found to increase at the same rate regardless of the silicate type within a target. As other parameters were altered it was found that both crater diameter and volume followed highly similar trends to those observed for targets constructed with a $50\text{wt}\%$ content of JSC-M. Contrasting this, crater depths were seen to differ considerably. For craters formed by a basalt projectile or those formed in silicate-dominated targets, no discernible trend was seen in crater depths due to the large amount of scatter. This scatter was seen to be substantially larger for craters formed in silicate-dominated targets than for those formed by the impact of a basalt projectile.

When considering the internal morphology of the produced craters, all features formed by the impact of a copper projectile within a JSC-M based target possessed a central depression. This feature was only seen in KDS-based targets at the lowest impact speed with craters at progressively higher speeds showing the expected bowl-shaped morphology. Whilst it is thought that the formation of these central depressions is due to the density difference between the copper projectile and target material, the rapid nature of crater formation makes the study of this phenomena difficult. Without further investigation into the formation of these features, the mechanism behind their formation remains unconfirmed. For craters formed by the impact of a basalt projectile, no central depression features were seen. Additionally, the craters resulting form these impacts showed an almost linear interior morphology as opposed to the expected bowl-shape exhibited by simple craters across the Solar System. Craters formed within the laboratory are formed entirely within the strength dominated regime of crater formation. Hence, spallation processes can occur altering crater sizes and profiles. For larger craters in the solar system, however, their growth is gravitationally controlled. The transition between these regimes for the surface of Mars is thought to occur at crater diameters of $3 - 8$ km [3]. Thus, smaller Martian craters should form entirely within the strength regime. The differences shown in morphology are thus likely to have implications for the interpretation of the smaller impact features within the Northern Lowlands region of Mars (discussed in Section 8.3).

The work presented within this chapter has potential implications for both our understanding of the Northern Lowlands region of Mars and potential in-situ resource utilisation of future crewed missions to Mars. More work is required to confirm the trends observed within this chapter. However, the increased scatter observed as the level of simulant within the target increases indicates that within silicate-dominated permafrost mixtures the use of crater morphology to infer subsurface properties may become increasingly difficult as the quantity of ice within the near surface region decreases. This further applies to the potential future use of ice within the near surface to support the crewed exploration of Mars. Future missions would require access to water on the Martian surface. The permafrost regions within the Northern Lowlands region may present the easiest access to this resource for future exploration. For this, however, it is vital to quantity the level of ice within this region to ensure it can support a future mission. The work presented within this chapter shows that when considering this factor, crater morphology may not provide the answers required.

Chapter 7

The Mysterious Martian Potato

"Every flutter of paper whispers

secrets from worlds unseen"

The Voice of Tomorrow

N.B. **A note on terminology**: In impact studies, it is common to use the term sabot when referring to the stabilising portion of the overall projectile (see section 4.1.2). Sabot, however, inherently implies some level of disposability. Whilst this term has long been used in the impact cratering field, to prevent confusion, a different terminology is used in the chapter presented here when describing the custom projectiles - as no part of the projectile is discarded during flight. When referring to the 3D printed projectiles, the overall manufactured object is referred to as a shell. A shell is comprised of a casing (the lower 'cup'-shaped portion) and a lid (used to seal the shell). Then during sample preparation, the casing is filled with an effective projectile mass - the projectile material of interest.

7.1 Presenting the Problem

The origin of the Martian satellites has been a topic of long lasting debate [260–265]. From this, either a captured asteroidal or re-accretion in orbit hypothesis remain prevalent as the most popular mechanisms to explain the existence of both Phobos and Deimos. In this chapter, the origin of Phobos (Figure 7.1) is considered. Whilst numerical studies have largely favoured an in-situ re-accretion scenario (see [260, 265] and references within), observational measurements of the Phobosian surface and physical properties indicate the moon is more likely to be a captured asteroid (see [263, 264] and references within). Despite the extensive study of proposed mechanisms, neither are without flaws; resulting in a considerable lack of consensus within the scientific community on a likely origin for the Martian satellites. Spectral measurements of the Martian moons show them to possess spectra in poor agreement with the primitive, carbon-rich material commonly attributed to C-type carbonaceous chondrite asteroids [260, 266] (some agreement can be found however between the spectra of Phobos and those of some space-weathered C-type asteroids [264]). They have been proposed however, to have spectra similar to D-type asteroids, but D-type asteroids are thought to be very dense [261,263,264,266]. Conversely the estimated bulk density ($1.87\ \mathrm{g/cm^3}$ [260,262]) and porosity (ranging between $25 - 35\%$ [260]) are, however, thought to differ from typical C-type asteroids (e.g. higher density and lower porosity than most C-type asteroids) [260]. Further issues arise surrounding captured asteroidal origins for Phobos, when the orbital characteristics are considered. The orbit of the Martian satellite is found to be extremely circular [264, 265], and close to the Martian ecliptic [265]; atypical for a captured body [260, 264]. Whilst some propose the orbit of Phobos to have undergone circularisation through tidal perturbations [260], the suggested geological age of $4\ Ga$ for the Martian satellites [264] indicates this to be unlikely.

The in-orbit re-accretion of Phobos, however, is able to account for the orbital characteristics of the Martian satellite [260,261,265], as well as the relatively low density measured through spacecraft flybys [262,265,268]. Within the re-accretion hypothesis there are two primary mechanisms proposed: co-accretion with a primordial Mars [264], and re-accretion of ejecta launched into circum-Mars orbit by a large impact event [260, 265]. Due to its location inside the Martian synchronous altitude, Phobos' orbit is decaying over time. Such decay, accelerating as it gets closer to Mars due to the

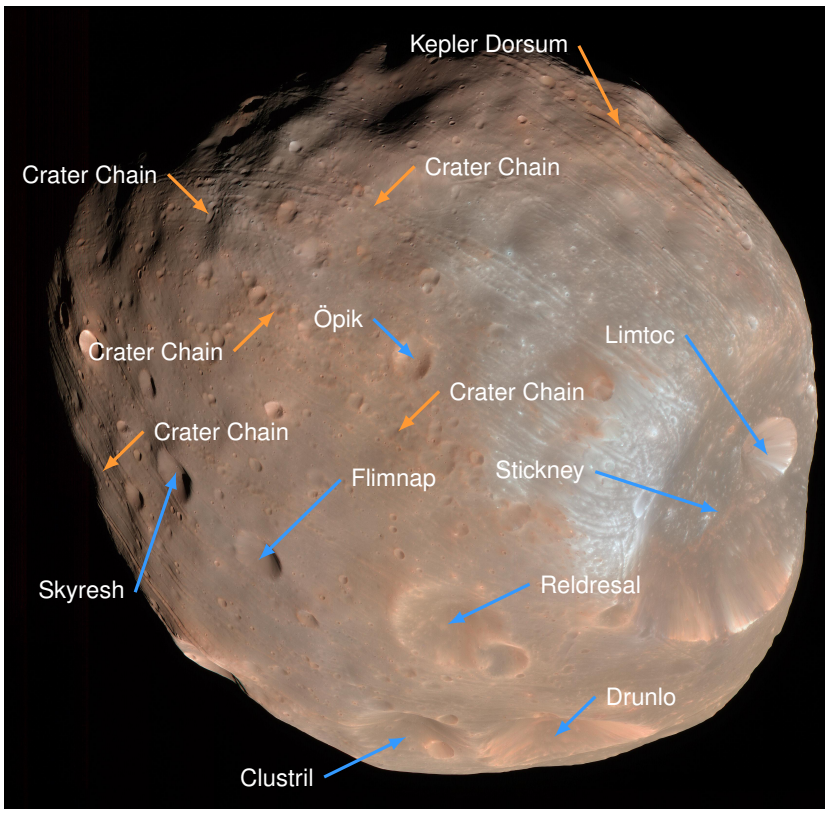

Figure 7.1: An image of Phobos captured by HiRISE onboard the Mars Reconnaissance Orbiter (MRO) spacecraft during a fly-by of the moon [267]. In the image, a selection of named craters are identified (blue) along with a selection of geological features (orange). The naming convention for Phobos dictates that features are named after either scientists who have contributed to the understanding of the moon or characters/locations within Gulliver's Travels. Phobos is triaxial in shape, being approximately $26 \times 23 \times 18$ km in size.

increasing tidal force, would rule out co-accretion alongside Mars. Furthermore, whilst the currently analysed reflectance spectra show no features associated with H_2O or OH-bearing mineral species in the near surface of Phobos, Fobos-Grunt images have shown what are interpreted to be evidence of past outgassing [263, 269, 270]. Such evidence suggests the presence of water-ice within the near surface of Phobos; with the presence of water-ice within the deeper 'mantle' region of Phobos being suggested by some to account for the lower measured density [263]. The heat induced by a large enough impact event, able to launch a sufficient quantity of ejecta to form the Martian satellites, would remove almost all H_2O and OH species from the ejecta disk [264]. Perhaps, the primary issue with the re-accretion of ejecta model however, is that a sufficiently large enough impact feature is yet to be identified on the Martian surface. Some have suggested the Northern Lowland Plains region (Borealis Basin) to be the impact feature responsible [260, 265]. However, evidence for the 7700 km diameter depression having an impact origin however is at best, tenuous.

7.1.1 Projectile Emplacement

To complicate studies of the origin of Phobos, it is possible for Martian surface material to be present, even on a captured asteroid, as a result of capture of ejecta from impacts on Mars. This material will become emplaced on Phobos, contaminating the Phobosian regolith. Projectile emplacement processes have previously been investigated for many Solar System bodies (the lunar surface [212,213], Ceres [214], Solar System asteroids [6], and even within the Mars system [165,271]), as well as the identification of projectile material within impact features [5]. Despite the many differences presented throughout the Solar System, the underlying principle behind projectile emplacement processes are thought to remain constant [6]. Alongside these investigations, the identification of the SNC [165,272] meteorite family (identified as originating from Mars), along with the Kaidun meteorite (hypothesised to have originated from Phobos, although this is disputed and not yet widely accepted [272, 273]), provide nuanced evidence for the transfer of material between major Solar System bodies and potentially Solar System moons. The transfer of Phobosian meteorites to the Earth, whilst possible, is currently not thought to be very likely despite the debate about the Kaidun meteorite [272]. By contrast, extensive numerical investigations have considered the transfer of Martian material from the surface of Mars to the surface of Phobos and find it plausible [165, 271, 274]. Ramsley, *et al.* [271], for example, predicted that within the upper layers of Phobosian regolith, Martian material should be detected in the range of $20 - 1250$ ppm as a result of such transfers. Impact speeds onto Phobos for Martian impact ejecta have been estimated to have a minimum speed of 0.58 km/s, with a typical range of $1.1 - 3.2$ km/s or more dependant on the initial launch speed of the ejecta from Mars [275]. Whilst Martian material will initially become emplaced at the point of impact, the vast majority of ejecta launched from impacts into the Phobosian surface itself eventually returns to Phobos [271,276]. Thus, subsequent impacts from both additional Martian ejecta and other Solar System projectiles will redistribute the emplaced Martian material over the entire Phobosian surface [276]. Gardening (through micrometeorite/ejecta bombardment [3]) of the upper layer of Phobosian regolith tends towards a hypothesised even distribution of Martian material within the upper layer of Phobos, predicted to present a detectable mean concentration of $255\ ppm$ [271, 276].

7.2 Method Development

The work presented in this chapter focuses on the post-impact identification of potential Martian material within the regolith and near-surface of Phobos. For this, a series of six shots were carried out, using the Kent light-gas gun in both the 1S-LGG and 2S-LGG configurations (see sections 4.1.1 and 4.1.2), covering both relatively low and high speed impacts. To ensure a significantly large enough quantity of projectile material reached the target, to enable post-shot analysis of both collected ejecta and the formed impact feature, projectiles (formed of an Eu-doped MGS-1 mixture contained within a UV resin 3D-printed shell) were designed for this investigation to fit the 0.22" (5.56 mm) diameter smoothbore barrel. The projectiles were fired over a speed range of 651.7 m/s

to $1620.1\ \mathrm{m/s}$ crossing from the high-speed physics regime to the hypervelocity regime at speeds of $\approx 900 - 1000\ \mathrm{m/s}$ (if the distinction is defined as the point at which impact features change from having diameters approximately equal to that of the projectile to diameters much larger). This speed range was selected as it covers the lower end of speeds predicted for the impact of Martian ejecta onto the Phobosian surface [165, 274]. Within this chapter, the speed over which projectiles could be fired was limited due to the significant decrease in projectile survivability at higher speeds. That is, as the speed approached $1500\ \mathrm{m/s}$, in some shots the projectiles began to break-up upon acceleration. This is an important consideration due to the nature of the investigation and the supply of materials. The quantity of PCA-1 was limited and targets from an unsuccessful shot could not be reused due to potential contamination by projectile material.

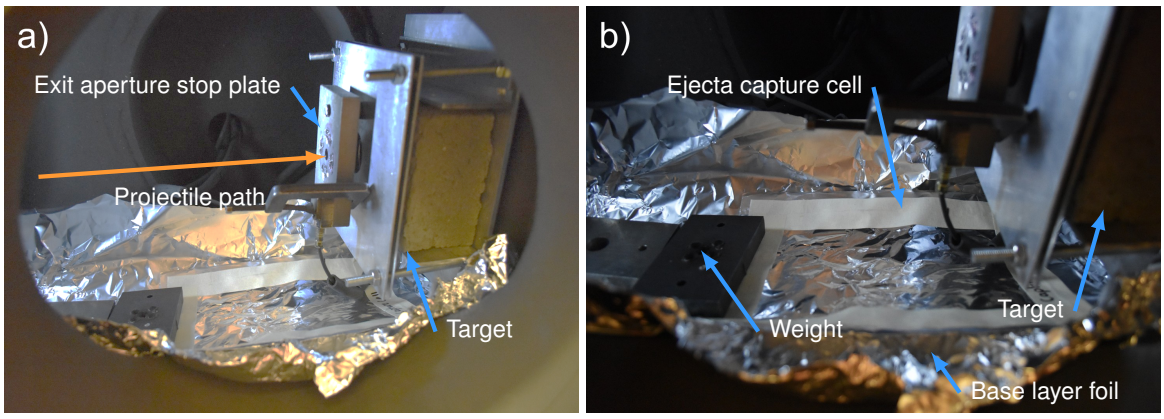

Figure 7.2: The experimental set-up used for the shots presented in this chapter. Panel a) shows an overview with the target shown on the right of the panel. The projectile passes from left to right once fired. Panel b) shows a close-up of the ejecta capture cell system located on the base of the blast tank during the shot. This is weighed down to prevent movement and the loss of ejecta material when venting the chamber after the shot. For scale, the target blocks are $5.8\ \mathrm{cm}$ thick.

In order to replicate the upper surface of Phobos, targets were formed of 'cemented' PCA-1 simulant [242] blocks. These blocks were constructed at the University of Kent, formed from a mixture of PCA-1, methanol, and de-ionised water (with each block being formed from a mixture of $630 \pm 1\ \mathrm{g}$ of PCA-1, $315 \pm 1\ \mathrm{g}$ of methanol, and $105 \pm 1\ \mathrm{g}$ of de-ionised water). This is an approximate ratio of $60 : 30 : 10\ \mathrm{wt.\%}$ for each component (more details of the blocks and their construction are given in Section 7.2.2). For each shot, the targets were placed within the LGG, being located within the blast tank. The set-up for each shot is shown in Figure 7.2. On the base of the blast tank during each shot was a foil lining and ejecta capture cell. The weight visible in Figure 7.2 held the capture system in place preventing the loss of material during venting to atmosphere following the shot. Once fired, the projectile follows the orange arrow in the left side of Figure 7.2. It passes through the exit aperture stop plate impacting the target. The stop plate is required to prevent damage to the target holder in the case of the projectile missing the target. The capture system was designed to both reduce the potential level of contamination from the blast tank itself, and to capture material ejected from the

target during the impact. The foil lining formed a barrier between the 'clean' capture and the inner surface of the gas gun. Whilst this did not prevent any potential contamination resulting from the barrel and gun powder charge, it substantially reduced the influence of any residual material left over from previous shots in the gun (which may have been present despite cleaning attempts between shots).

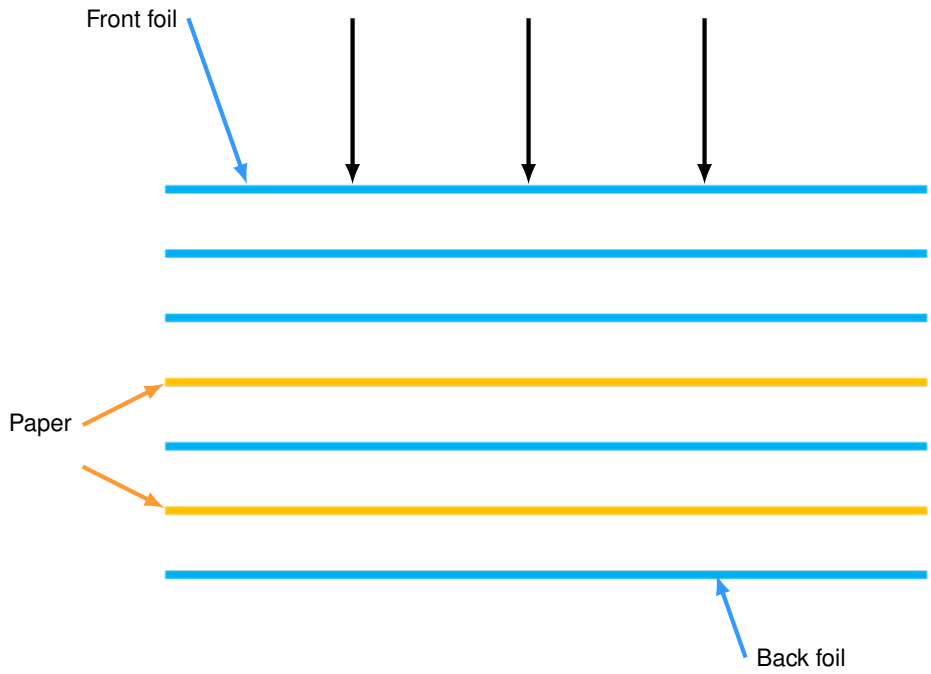

Figure 7.3: A schematic diagram of the ejecta capture cell used. Blue lines represent foil layers and orange lines represent paper layers, black arrows represent ejecta.

The capture cell (a schematic of which is shown in Figure 7.3) was designed with multiple layers. The three upper foil layers are used to slow and capture finer or slower moving ejecta, with the two lower paper layers present to disrupt, slow, and capture medium to large fragments. The aluminium foil had a thickness of 16 μm and the paper was cut from typical photocopier paper sheets. Following each shot, the capture cell was removed from the blast tank and any material lying on top collected. Upon dismantling the cell and separation of the layers, material contained within the cell was collected as additional ejecta from the shot. Due to the very small quantity of ejecta collected from each individual layer, it was impossible to perform any meaningful analysis of the material as a function of the layer from which it was collected. Thus, the analysis of the ejecta material was conducted on the sample collected from each shot as a whole. Analysis was carried out in order to both initially identify and subsequently quantify the level of projectile material (if any) contained within the ejecta, this was performed through XRF. All samples were put through the standard analysis processes for each technique as laid out in Chapters 4 and 5.

7.2.1 Projectile Design Iteration

In order to experimentally investigate the emplacement of Martian material onto the surface of Phobos, an appropriate projectile required development. Whilst it would have been largely appropriate to replicate Martian debris through the use of a basalt sphere projectile, a key component of the investigation presented in this chapter was the attempted identification of a geologically complex projectile material within a geologically complex target. As such, MGS-1 Martian simulant [239] was selected as the projectile material. There were, however, issues still needing a resolution. The first was substantial inhomogeneity in the simulant. This was often related to grain size effects and the mixing of minerals during simulant construction. To solve this, the simulant was ball milled to produce a more uniform size and a better mixing of materials. The second issue was how to deliver the material to the target. Loose material could be poured into the shell, but a solid projectile was initially preferred because it would add to the rigidity of the shell (essential to prevent the shell breaking up during initial acceleration), permitting thinner shell walls and thus an increased volume for the simulant. A solid simulant could be formed by adding a binding resin, but this introduces an extra organic material. Instead, the cementitious nature of the simulant was taken advantage of. As shown earlier, when hard water (with a strong lime content) was mixed with the simulant, it formed a cement. This permitted a solid simulant to be obtained.

7.2.1.1 Shell Filling Methods

Accordingly, shells were initially designed to exploit the cementitious nature of the MGS-1 simulant discussed in Chapter 5. To allow for the use of a cement material within the gas gun, a 3D-printed resin shell was produced. The shell was designed with a cylindrical $5.06\ \text{mm}$ diameter by $5\ \text{mm}$ tall internal (central) cavity to be filled with the geopolymer cement mixture. This shell was formed of a $1\ \text{mm}$ thick base and thin ($0.25\ \text{mm}$) walls, to provide support during the curing process and initial acceleration within the gun. The purpose of the shell was to preventing damage occurring to the barrel as a result of the solid cement rubbing the barrel walls and causing scarring during launch. One issue when forming these projectiles, however, was ensuring that the shell was entirely filled with the cement. First attempts were made to fill the shell with a single dose of the mixture injected from a pipette. However, This led to a substantial cavity forming underneath a cement cap, because when injected, the surface tension of the cement prevented it from reaching the floor of the central cavity (shown in Figure 7.4). After this, filling was done by adding a small amount of the cement mixture at a time and partially setting it, gradually building the projectile material up layer by layer. This, however, had difficulties in ensuring that no small gaps or fractures formed between layers during the proving time of the cement (Figure 7.5).

In addition to the issues with the shell filling methods, issues also began to arise regarding the strength of the cement material formed. Even with the presence of minimal inhomogeneities within the cemented projectile, it was found that the set material was highly friable. Once set, even the

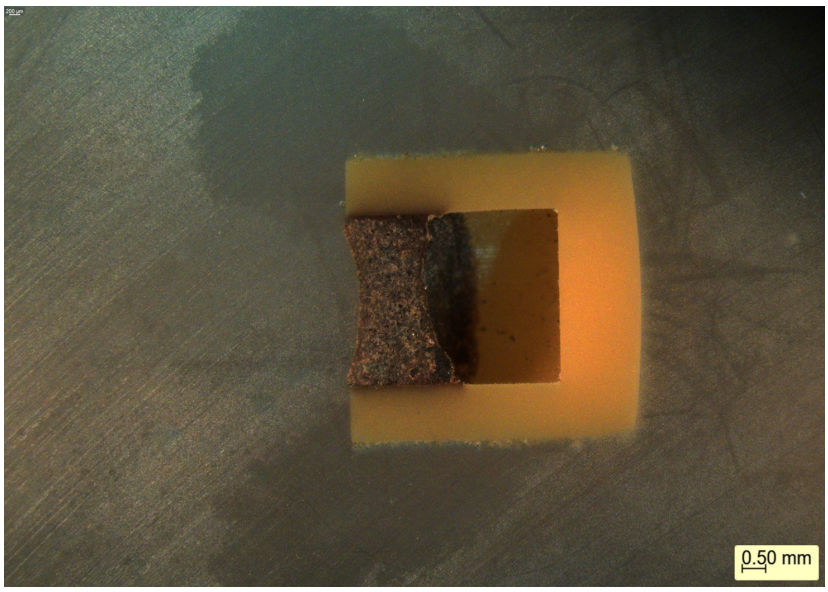

Figure 7.4: First filling attempt of 3D printed shell. Once the shell was filled with a cement mixture and set, it was embedded in resin allowing a slice to be taken through the shell. This allowed the interior to be observed. A large trapped air bubble can be seen taking up the lower half of the shell. This was caused due to the single stage filling of the shell and the surface tension of the cement holding it at the upper surface of the cavity.

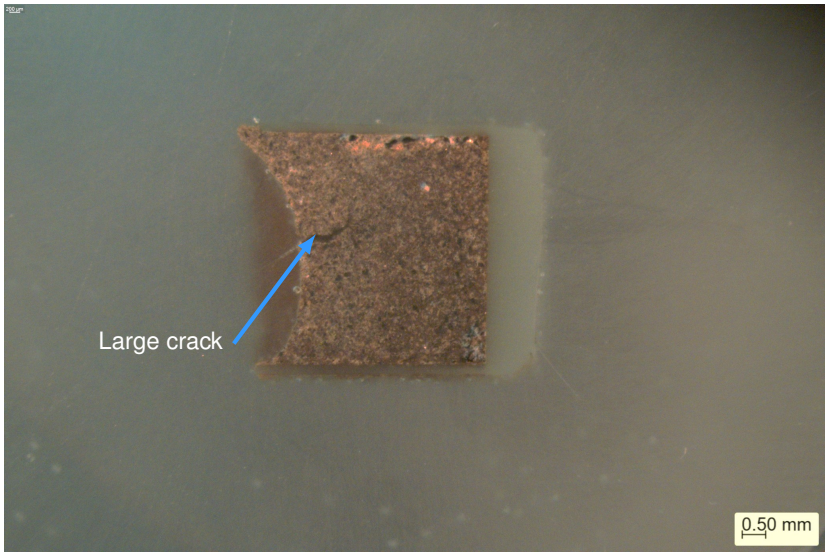

Figure 7.5: Second filling attempt of 3D printed shell. Shells were filled in two steps to prevent the formation of a large trapped air bubble at the bottom of the shell. Once the cement material has set, the projectile was embedded within resin enabling a slice to be taken through the projectile. This allowed the interior to be observed. A concave cavity can be seen at the top of the shell in which cracks form into the cement. A large crack is indicated by the blue arrow.

slightest shock led to the whole sample of cemented material crumbling and falling out of the shell. This is thought to be due to the method used for mixing the simulant, chemical activator and elemental tracer and then pipetting the sample into the empty or partially full shells. This favoured the

liquid and fine-grained components of the mixture, leaving the large-grained material behind which is traditionally required to increase the strength of cement materials. In an attempt to improve this, two methods were used. The first was to increase the quantity of chemical activator used and then the second was to combine the materials before ball-milling the simulant. The effects of this led to the discovery of the MGS-1 paste discussed in Section 5.5.1. When setting this mixture in the resin shells, however, the strong alkali nature of the potassium hydroxide used as the chemical activator, led to the redin dissolving. This rendered the projectiles unusable within the Kent LGG. The damage caused to the 3D-printed shells can be seen in Figure 7.6. Whilst the cementing nature of the MGS-1 simulant may have applications for use within the LGG as a projectile material in the long term (providing the issues highlighted here are addressed), the time constraint of the work presented in this chapter required a new form of projectile to be developed.

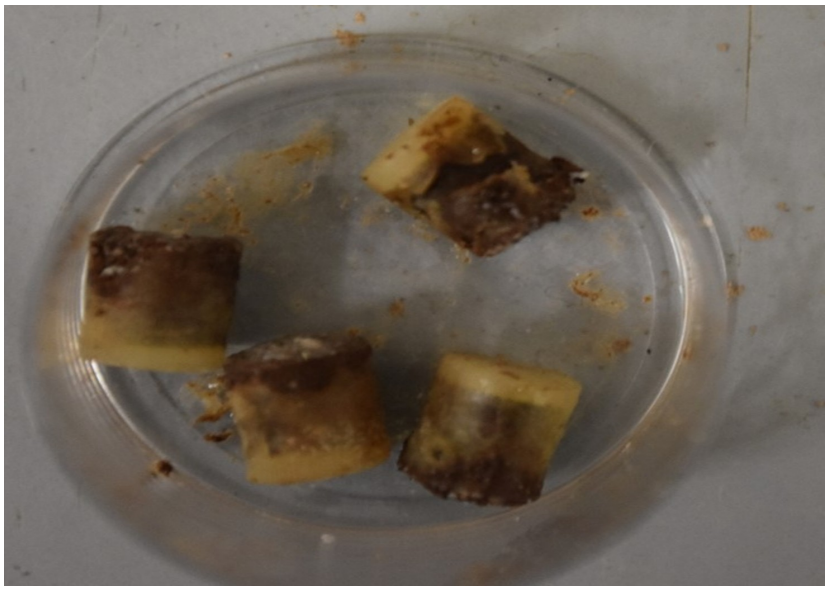

Figure 7.6: High alkalinity cement led to the shells dissolving during the curing period leading to them being unusable within the Kent LGG. The shells shows are 6 mm in length.

7.2.1.2 Shell Lids

Due to issues surrounding the setting of an MGS-1 simulant cement within the 3D-printed resin shells, a redesign was required. Development work led to a slight increase in the wall thickness - from 0.25 mm to 0.375 mm - and the leading edge to be countersunk. The thicker walls aided in the shell rigidity, whilst the countersunk top allowed for the placement of a resin lid to the front of the shell. The purpose of this is to allow for the use of a granular material within the printed shell. Due to the fragile nature of the resin material, particularly the thin shell walls, care had to be taken when both filling the shells and emplacing the lids. Initial designs for the lidded shell included a 1 mm thick lid. Such a design increased the ease of handling when working with the shells, and allowed the affixing of the lid (by pressing it into place) without the use of adhesive materials when using a granular material. It, however, substantially increased the mass of the shell, reducing the relative mass of the

projectile material. A single test shot was carried out using the lidded shell, firing at a speed of $1\ \mathrm{km/s}$ into a $50\ \mathrm{mm}$ diameter aluminium plate target (Figure 7.7). Whilst this showed the lidded shell was able to contain the majority of the material most of the way down the barrel, damage to the plate in some locations caused by the impact of the projectile was substantial. This is primarily thought to be due to thinner thickness of the target in this region (the central region contained a threaded hole for target mounting).

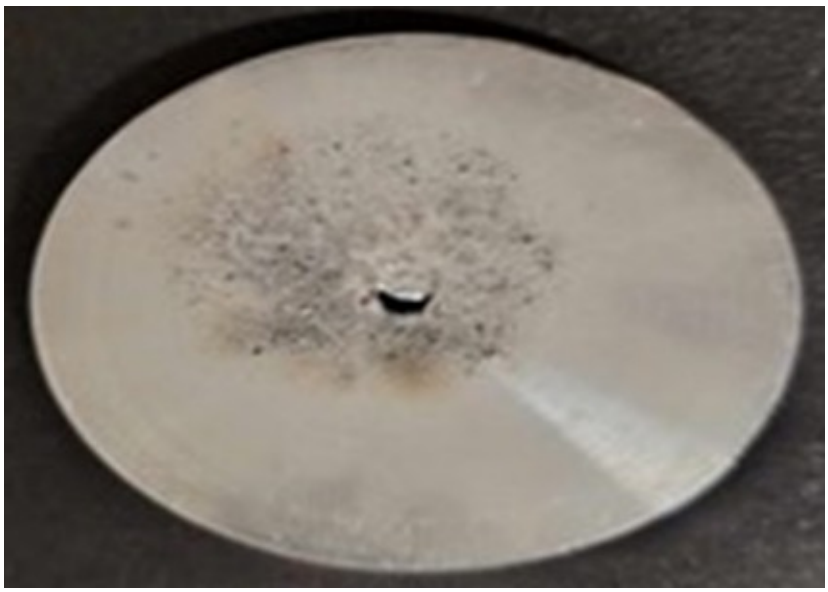

Figure 7.7: The results of an impacting lidded shell into a $50\ \mathrm{mm}$ diameter aluminium target. The projectile was fired at $1\ \mathrm{km/s}$ and impacted close to the centre of the target. The heavy damage within the very centre of the target is due to the thinner nature of the target in this region. Surrounding this, several marks can be seen indicating the projectile broke-up upon impact with the target. Additionally, the lower half shows some level of orange staining indicating the simulant material to have been emplaced on the surface.

Other than the central region of the target shown in Figure 7.7, where the shell body is thought to have impacted, a large population of smaller impact craters can be seen resulting from what is thought to be the impact of sand grains. Despite this, however, the relatively concentrated location of these - as opposed to them having occurred over the entire target surface - suggests that the sand material was contained for some distance down the barrel. For this shot, the lidded shell was placed into the barrel with the lid facing backwards, towards the launch tube of the light-gas gun. This configuration caused the expanding gas to force the lid into the shell, preventing it becoming dislodged during the initial acceleration. Despite this, the lack of adhesive securing the lid in place led to the opening of the shell before impact with the target. This is thought to have occurred due to the uneven fitting of some shell lids; a flaw that was overcome for the remainder of the shots through careful selection of the projectile. The extensive damage close to the centre of the target, however, led to a further redesign to decrease the mass of the empty shell.

The design of the shell should permit a sealed shell to reach the target prior to the release of

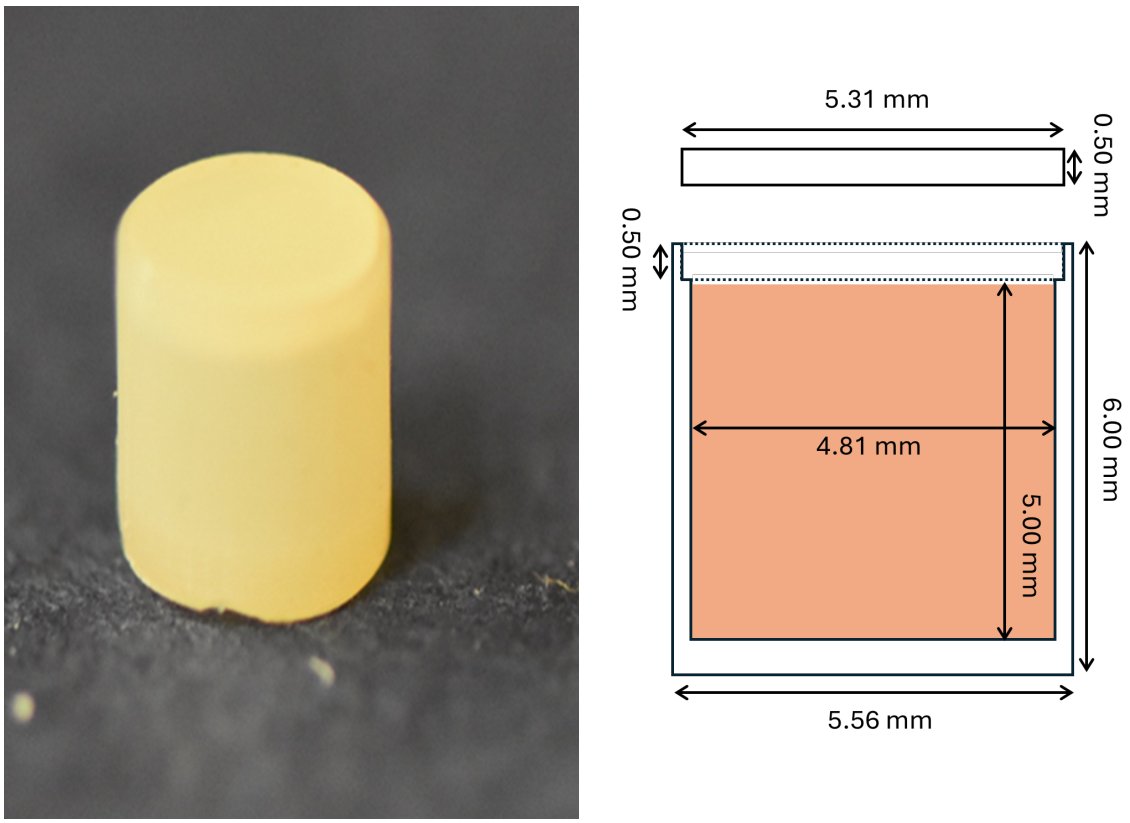

Figure 7.8: The projectile casings developed for the work presented in this chapter. Panel a) shows a close up image of a shell with the front lid in place. Panel b) shows the schematic design of the shell with the orange area representing the projectile material.

material. Along with this, the fraction of the shell filled by simulant material had to be optimised. In the shell designs at this stage, when filled with crushed MGS-1 simulant, the shell possessed a mass of ≈ 0.18 g, with the empty mass being measured to be ≈ 0.09 g, this gave an effective projectile material mass of ≈ 0.09 g ($\approx 50\%$ of the impacting mass was simulant material). Due to the similarity in masses between the projectile material and the resin shell, it would be difficult to distinguish processes resulting from the projectile material and resin shell respectively. Thus, it was deemed vital to increase the effective projectile mass, reducing the influence of the resin shell on the crater formation process. This was done through substantially reducing the thickness of the lid to 0.5 mm, and increasing the wall thickness to 0.375 mm (Figure 7.8). Whilst this increased the difficulty in handling shells during filling and preparation, it changed the mass distribution of the shell, reducing the overall effect it had on the impact process. When filling the new iteration of lidded shell, care was taken to tap the base of the casing between each addition of projectile material. This allowed the loose granular material to settle, reducing the porosity and minimising the possibility of air bubbles existing within the sample. Casings were filled as much as possible before the lid was put in place, reducing the possibility of blow-out when under vacuum. This brought the mass of a filled shell to the range of $0.16 - 0.19$ g. The mass of simulant material was retained at $\approx 50\%$ of the impactor mass, but the decrease in lid thickness ensured that the resin shell played as minimal a part as possible in the cratering process. To ensure that the lid was held in place during each shot, projectiles were

again fired with the lid facing away from the muzzle.

7.2.2 Target Construction

The initial targets intended for this investigation were produced by Space Resource Technologies (SRT) in Florida [277]. They were produced from a PCA-1 mixture and formed into a block shape with an average depth of $2\ \mathrm{cm}$. This was done by the company prior to shipping using the method described by Landsman, *et al.* [242]. During initial shot testing, however, the weak strength of these sourced blocks was found to be unsuited to the desired purpose (with the blocks being completely broken apart due to fractures at speeds as low as $\approx 300\ \mathrm{m/s}$). As such, an alternative target production method was required. It was decided to attempt to reproduce the SRT blocks ourselves following a similar method to that of SRT. The raw PCA-1, methanol, and de-ionised water (in the ratio of $60 : 30 : 10\ \mathrm{wt.\%}$) mixture from which the solid targets were formed was combined into a slurry, which was then poured into a $10\ \mathrm{cm}$ cube silicone mould. The inclusion of the methanol within this mixture allowed for the porosity of the blocks to be increased.

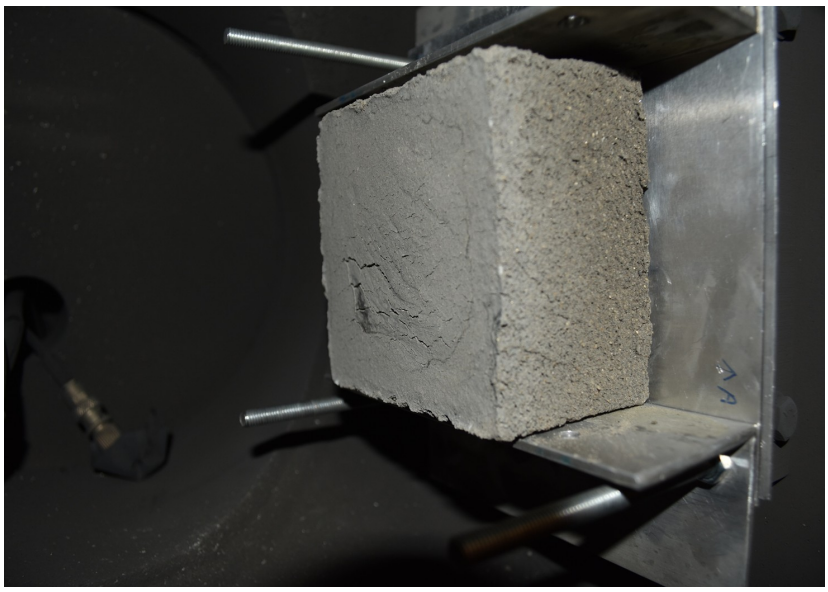

Figure 7.9: The pre-impact surface of a target block. The block has a side length of $8.5\ \mathrm{cm}$ and a depth of $5.8\ \mathrm{cm}$. Blocks had an average porosity of 9.6%.

This was then heated in a vacuum oven at a temperature of $80^\circ\ \mathrm{C}$ for a period of $24\ \mathrm{h}$ causing them to set. During the heating process the oven remained at atmospheric pressure, with the air only being removed towards the end of the heating period removing any remaining methanol vapours prior to opening. Once removed from the oven, the now set block was left to cool and rest for a period of $48\ \mathrm{h}$ allowing the residual volatile water and methanol to evaporate away before use. This ensured as little mass loss as possible whilst under vacuum throughout the shot. On average blocks had a side length of $8.5 \pm 0.2\ \mathrm{cm}$ with a depth of $5.8 \pm 0.2\ \mathrm{cm}$ and a porosity of 9.6% (see Figure 7.9). The blocks were notably thicker than those produced by SRT (Figure 7.10). All other aspects of the method were kept the same as that carried out by SRT. Despite this, the blocks produced at Kent appeared

to show some level on internal horizontal layering. This is not thought to have impacted the cratering process, however.



Figure 7.10: A block produced at the University of Kent (left) and one produced by SRT (right). Both blocks have been sectioned providing a view of the internal structure. Blocks produced at Kent were notably thicker than those produced at SRT. Note for the block produced at Kent, the smooth appearance close to the edge of the block was due to the cutting method. Despite following the same method, the blocks produced at Kent show some level of internal layering whilst those produced by SRT do not.

7.3 Results

The results of the shot programme carried out within this chapter are given in Table 7.1. Six shots were carried out over a speed range of $650 - 1620\ \mathrm{m/s}$. Targets were weighed before and after each shot to find the mass lost during the impact. The design of the ejecta capture system meant that only a fraction of the ejecta was able to be captured, with the size of the capture system limited by the size of the blast tank. After each shot, targets were removed from the gun to undergo detailed analysis. To aid in post-shot identification, shells were filled with a mixture of MGS-1 and a europium elemental tracer ($\mathrm{Eu\,(CH_3COO)\cdot xH_2O}$).

7.4 Crater Analysis

Figure 7.11 shows the results of the shots carried out for the investigation presented in this chapter, with the speed and shot number increasing in each panel (the shown scale is in cm). It shows a clear morphological progression as the impactor velocity increases. For the impact features formed here, diameters and depths were not physically measured to prevent any potential contamination to emplaced projectile material. Crater diameters can be approximated from images and relative

Table 7.1: The parameters and results of the shot programme carried out within this chapter. For shots 2 and 3, the quantity of ejecta collected was too small to be measured.

shot	Speed (m/s)	Projectile mass (g)	Target mass (g)	Target mass loss (g)	Collected ejecta mass (g)
1	652 ± 33	0.16 ± 0.01	581.9 ± 0.1	1.5 ± 0.1	0.0026 ± 0.0002
2	720 ± 36	0.17 ± 0.01	586.8 ± 0.1	8.8 ± 0.1	n/a
3	858 ± 43	0.16 ± 0.01	584.4 ± 0.1	7.0 ± 0.1	n/a
4	995 ± 50	0.19 ± 0.01	624.6 ± 0.1	43.2 ± 0.1	0.0386 ± 0.0002
5	1581 ± 79	0.17 ± 0.01	618.2 ± 0.1	36.0 ± 0.1	0.2838 ± 0.0002
6	1620 ± 81	0.17 ± 0.01	635.1 ± 0.1	20.5 ± 0.1	0.0670 ± 0.0002

depths can be used to investigate the morphological progression. Hence, for the investigation presented in this chapter, analysis of the post-impact targets was limited to a semi-quantitative visual interpretation. For the slowest impact speed (panel a), the formed feature is approximately the same diameter as the projectile (5.56 mm), with the depth being extremely shallow. In this regime, due to the extremely shallow impact feature, it is thought that the projectile simply rebounded from the target leaving only the slightest indication of an impact having occurred. As the speed increased, the level of damage occurring to the target increased.

Panels b and c in Figure 7.11 show the resulting features from shots 2 and 3 respectively. At these speeds it is thought that the entire or majority of the projectile became embedded within the target. In panel b and highlighted in Figure 7.12, what appears to be fragments of projectile material can be seen on the target surface. At higher impact energies, whilst fragments of projectile could be identified they appeared to be smaller and less frequent. As the impactor speed increases, a central pit begins to appear (being clearly visible in panels d and e in Figure 7.11), indicating that projectile material may have become emplaced deeper within the target. This trend changed, however, for the highest impact speed (panel f). In this shot, it is thought that the acceleration to the higher speed caused the shell to break-up in-flight substantially increasing the surface contamination of the target. This can be seen in Figure 7.13 where projectile material on the surface is highlighted. This pre-impact break-up further accounts for the distinctive change observed in crater morphology. Rather than a single projectile impacting the target, a cluster of smaller fragments formed a wide shallow impact feature.

For analysis beyond visual inspection of the target, it was required to reduce the size of the blocks after the impact so that they could fit into various instruments. For this, cuts were made through the blocks around the crater taking care to ensure minimal disruption was made to the crater. However, the size to which the blocks could be cut was limited due to the formation of fractures and the semi-friable nature of blocks once cut. Despite reducing the size of the target blocks (to an approximate side length of 5 cm and height of 2 cm), the limitations of the equipment design meant that Raman analysis of the post impact target was impossible. The height of the reduced targets proved to be a significant issue leaving insufficient room for the instrument to focus. This is because the friable

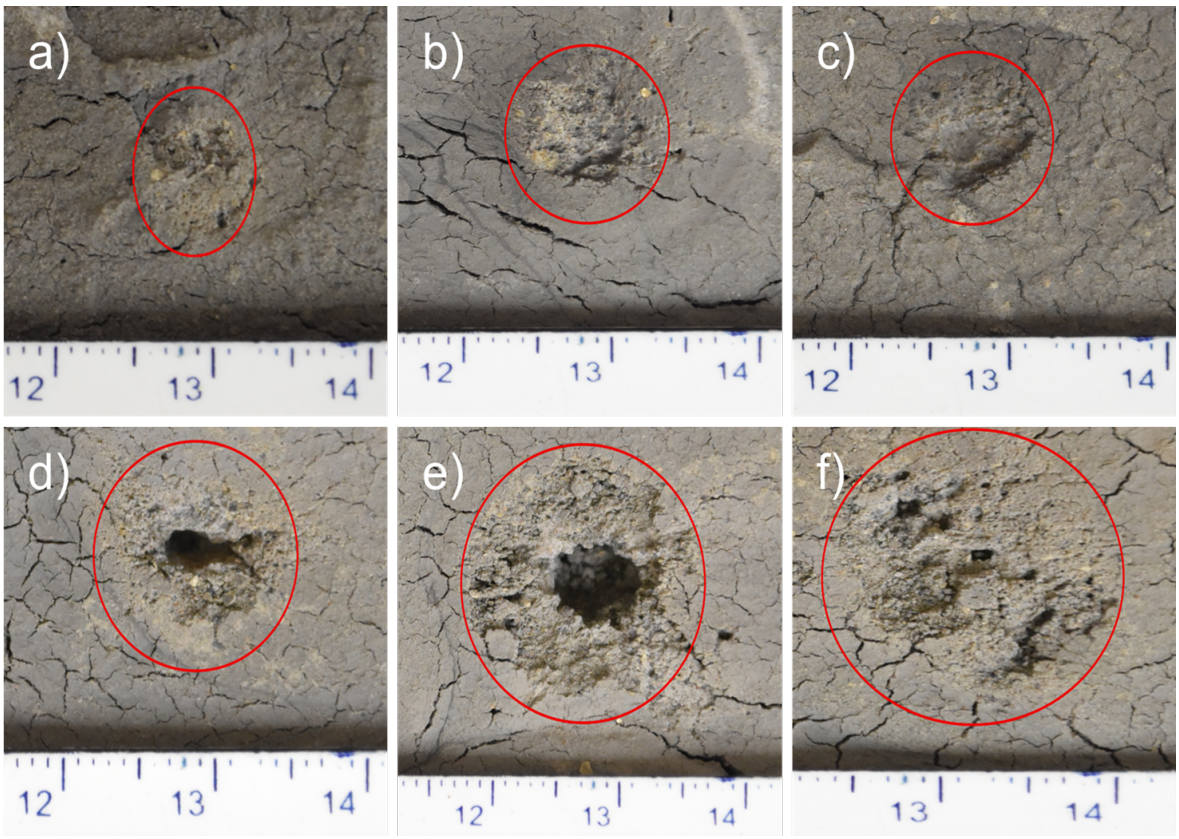

Figure 7.11: Images of the impact features formed during the shots carried out for this chapter. Within each panel, the red circle provides an approximate outline of the formed feature. The parameters for each shot can be found in Table 7.1. Panels a) to f) show the craters formed during shots 1-6 respectively. Crater diameters were approximately 0.5 cm, 1 cm, 1 cm, 1.5 cm, 2 cm, and 1.5 cm respectively.

nature of the target blocks (in particular when making lateral cuts) severely limited the height to which blocks could be cut before the impact feature would undergo damage. As such, SEM-EDS analysis was considered instead. Due to the time limitations surrounding this part of the work presented within this thesis, however, analysis of the Phobos simulant targets was limited to purely visual analysis. Nevertheless, despite these issues, the targets have been preserved for future analysis of the impact sites, with detailed crater morphology to be analysed along with further attempts to section the targets to repeat analyses searching for emplaced projectile material.

7.5 Ejecta Analysis

Attention then turned to the ejecta collected from each shot which was subjected to analysis to identify post-impact projectile material. The quantity of collected ejecta (given in Table 7.1) varied considerably for each of the shots but were sufficient for XRF anaylsis. The results of the XRF analysis are shown in Table 7.2 (with the errors given being the standard error for the sample runs - see Section 4.2.1) and a comparison for the key elements are shown graphically in Figure 7.14,

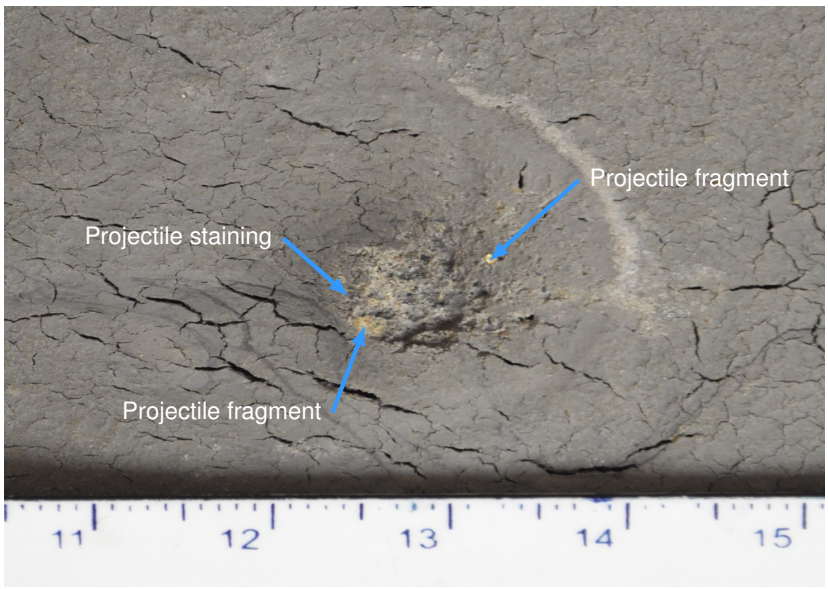

Figure 7.12: An image of the feature produced during shot 2 (speed 720 m/s). Details given in Table 7.1. Potential projectile material is highlighted within the figure. Additionally, close inspection of the target shows what appears to be some orange staining on the left hand side of the impact feature. The shown scale is in cm.

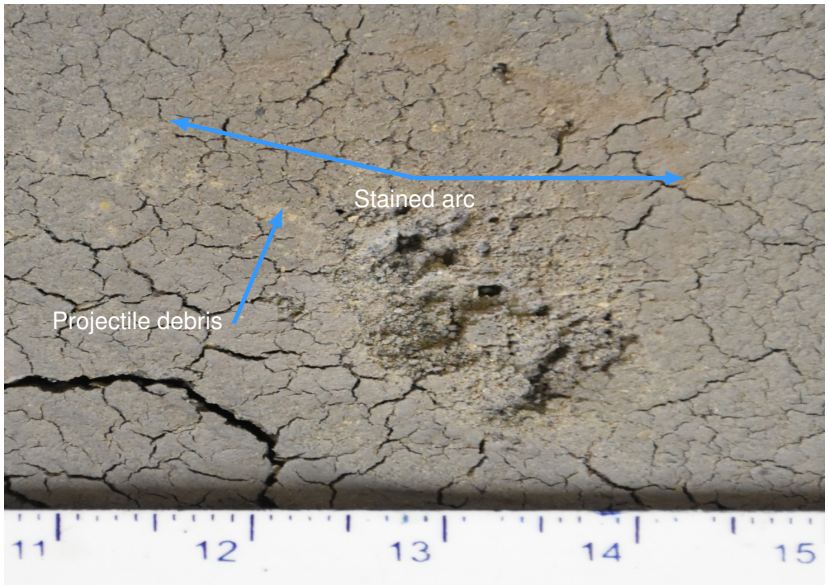

Figure 7.13: An image of the crater formed during shot 6 (speed 1620 m/s). Details given in Table 7.1. Possible projectile debris is marked, along with the extent of what appears to be a large quantity of projectile material staining the target surface. The shown scale is in cm.

normalised to the values for PCA-1. Within Figure 7.14, the results for the europium levels are not shown due to the influence of the projectile material and the large quantity of the europium compound. The results in Figure 7.14 shown that, despite their similar chemical compositions, distinctions can be made between the projectile and target materials with differences being present between PCA-1 and MGS-1. When looking at the collected ejecta material, it appears that they somewhat follow the trend set by the analysed projectile material (Eu-doped MGS-1) with some influence of the PCA-1 target

Table 7.2: Raw XRF results of the components used for comparison within this chapter. All values are given in the units of wt% with the standard errors being given for each value.

Oxide	PCA-1	MGS-1	Doped Projectile	Capture Cell 5 Shot 1	Capture cell 6 Shot 4	Capture cell 7 Shot 5	Capture Cell 8 Shot 6
MgO	10.231 ± 0.076	9.546 ± 0.025	6.085 ± 0.043	3.215 ± 0.945	11.342 ± 0.046	9.732 ± 0.053	11.450 ± 0.203
SiO_2	34.503 ± 0.200	43.869 ± 0.013	25.604 ± 0.077	27.583 ± 0.403	41.851 ± 0.143	34.220 ± 0.044	41.741 ± 0.668
SO_3	5.189 ± 0.106	1.317 ± 0.011	4.355 ± 0.014	0.000 ± 0.000	3.795 ± 0.126	3.704 ± 0.035	4.225 ± 0.160
K_2O	3.409 ± 0.067	0.464 ± 0.001	0.616 ± 0.002	1.829 ± 0.077	2.900 ± 0.042	3.415 ± 0.008	3.607 ± 0.048
CaO	9.222 ± 0.163	9.402 ± 0.007	8.001 ± 0.023	12.682 ± 0.161	9.130 ± 0.059	10.033 ± 0.056	9.756 ± 0.385
TiO_2	0.346 ± 0.021	0.283 ± 0.008	0.370 ± 0.002	0.475 ± 0.020	0.342 ± 0.011	0.311 ± 0.007	0.334 ± 0.012
Cr_2O_3	0.053 ± 0.002	0.173 ± 0.001	0.157 ± 0.001	0.062 ± 0.005	0.040 ± 0.003	0.052 ± 0.002	0.043 ± 0.001
MnO	0.099 ± 0.009	0.091 ± 0.001	0.000 ± 0.000	0.051 ± 0.003	0.059 ± 0.001	0.085 ± 0.002	0.065 ± 0.001
Fe_2O_3	30.015 ± 0.323	19.614 ± 0.050	18.949 ± 0.045	16.830 ± 0.325	15.682 ± 0.075	31.455 ± 0.064	19.409 ± 0.844
NiO	0.053 ± 0.001	0.138 ± 0.001	0.175 ± 0.003	0.042 ± 0.021	0.018 ± 0.002	0.044 ± 0.001	0.023 ± 0.002
Eu_2O_3	0.096 ± 0.005	0.068 ± 0.006	27.646 ± 0.110	0.308 ± 0.087	0.103 ± 0.008	0.130 ± 0.005	0.134 ± 0.010

composition. In general, however, they lack the expected PCA-1 concentrations of Cr_2O_3 and NiO. What is clearer, however, is that all of the ejecta samples contained elevated amounts of europium compared to the raw MGS-1 and PCA-1 materials.

Using the europium values given in Table 7.2, the quantity of projectile material within the ejecta can be calculated. To calculate this, the background level of europium within the PCA-1 has to be subtracted to isolate the projectile material. This value can then be multiplied by the reciprocal of the analysed value for the europium content within the projectile material (wt.%). The calculated percentage weights of projectile material within the collected ejecta can then be multiplied by 10,000 to convert to parts per million (ppm). The level of projectile material within the collected ejecta from each shot can be calculated to be 7833 ± 1594 ppm for capture cell 5 (shot 1), 260 ± 166 ppm for capture cell 6 (shot 4), 1259 ± 105 ppm for capture cell 7(shot 5), and 1407 ± 199 for capture cell 8 (shot 6). The wide range in the weights of collected ejecta and the calculated values of projectile concentration are indicative of the shot series having transitioned through a range of projectile emplacement regimes, starting with the projectile rebounding from the target with minimal shock processing or contamination, and ending with the pre-impact break-up of the impactor and transfer of the projectile material to the ejecta, as described below.

Discussing this in more detail, shot 1 is in the rebound regime with the ejecta sample size being the smallest collected sample and the analysis finding the highest level of projectile material. As the sample size for this shot was, however, only a few grains of sand, the variability if the shot was redone here is likely to be very high and the shell itself was not found in a post-shot inspection of the inside of the blast tank. For shots 2 and 3, the projectile is thought to have become emplaced within the target with very little to no ejecta being found despite capture cells being present. Shot 4 appears to be on the border between emplacement of the projectile and the standard crater formation process. The final two stages are covered by shots 5 and 6. Shot 5 represents the standard crater formation stage with an approximately bowl-shaped crater being produced and ejecta being formed

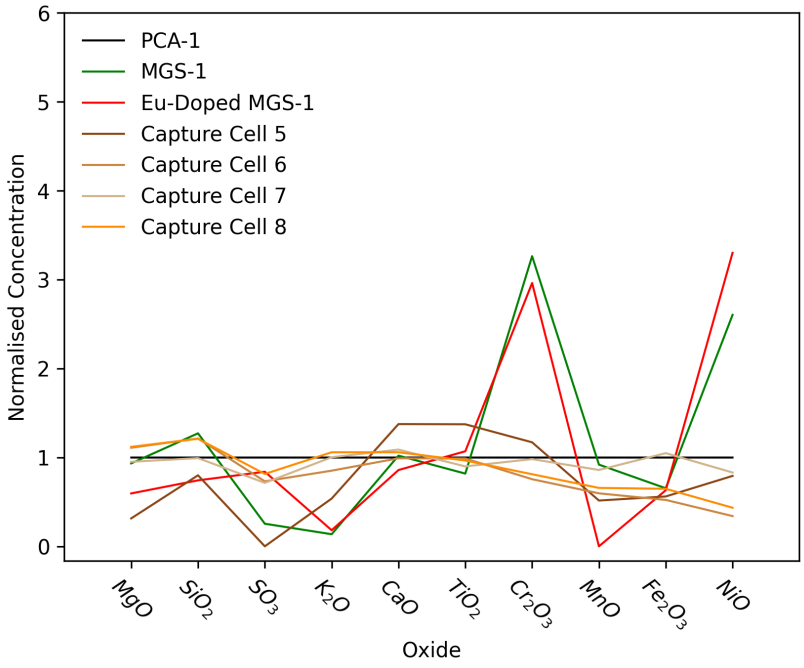

Figure 7.14: XRF data from Table 7.2 normalised to the values for PCA-1. Note that measured values for europium are excluded from this figure.

as normal. The analysed ejecta from this shot represents a mixture of both target and projectile materials. During shot 6, it is thought that the shell broke-up prior to impact with the target surface. In this shot therefore, the projectile material impacted the target as multiple fragments leading to the production of a cluster of smaller craters and the coating of the target surface by projectile material. More work would be required to further test this, however, to reproduce this and see if the potential break-up was due to a flaw within the shell used for this shot, or due to the speed being close to the upper limit of the shell design. The quantity of ejecta produced within in shot 6 is reduced below that expected from the other shots. This is likely associated with the enhanced contamination of the target surface (shown in Figure 7.13) and the smaller size of the craters, formed within the cluster.

7.6 Conclusions

The work presented in this chapter focuses on the transfer of material from the surface of Mars to Phobos. For this, a custom projectile required development for use within the Kent LGG, enabling a Martian 'meteorite' analogue to be fired. This involved the repeated redesign of a 3D-printed resin shell capable of containing a projectile until it impacts onto the target. Development of a suitable target was additionally required to prevent their break-up during the impact. A series of six shots was carried out for this investigation over the speed range of $260 - 1620$ m/s with a measurable quantity of ejecta being collected from four of these.

Whilst projectile material could be visually identified in the initial post-shot analysis of the formed impact features, subsequent initial analysis of the craters within analytical equipment failed to locate

this material. Hence, whilst the transfer of projectile material to the formed ejecta could be successfully demonstrated, at this stage the level of projectile material transferred to the target cannot be quantified.

Analysis of the collected ejecta identified the presence of projectile material with a concentration between $652 - 7833$ ppm (which overlaps with the lower end of the range of Martian impact ejecta striking Phobos). Whilst this range is large, it is thought that the impacts passed through a variety of projectile emplacement stages. These range from the projectile almost entirely rebounding from the target at the lowest speeds (despite no intact shell fragments being recovered) producing the highest level of projectile material within the ejecta, to the brink of hypervelocity with much of the projectile being emplaced leading to lower detected concentrations within collected ejecta. At higher speeds, 'normal' crater formation processes occurred leading to an ejecta formed of primarily target material with a projectile component on the order of ≈ 1000 ppm.

The transfer of projectile material to the ejecta formed during an impact event is a known phenomenon in general [278]. Here it is shown that this can happen in processes specific to Phobos, and thus, this is the first experimental step into the investigation of Phobos' origin. More detail regarding the implications of this work and the potential further steps are discussed in Chapter 8. However, we can already say that this it is fairly clear that material ejected from Mars can become emplaced on the surface of Phobos, both within the crater formed when it strikes Phobos, and via ejected material which is subsequently re-accumulated elsewhere on Phobos.

Based on the ejecta analysis results obtained here, it is suggested that Martian material (that arrived as ejecta from impacts on Mars) is highly likely to be identified within the Phobosian regolith. By contrast, it is not possible (based on the results so far) to quantify how much Martian material is likely to be found by the MMX mission within, and underlying impact craters on the Phobosian surface. More work is needed on this point. What can be said about the presence of Martian material in the crater, is that, if the three impact regimes identified within this work (projectile rebound, projectile emplacement, and the standard impact cratering regime) are found to occur on the Phobosian surface, it can be reasoned that a subset of the Phobosian crater population will lie within the emplacement regime. From the work presented here, it can be inferred that ejecta from these craters is likely to be formed of material originating from Phobos, with MMX likely to find concentrations of Martian material underlying this subset of craters. Therefore, when analysing results from the mission, the influence of where samples were obtained on the Phobosian surface should be borne in mind.

Chapter 8

Conclusions

"We honour our past, celebrate this moment,

and dream of the future yet to come"

The Voice of Tomorrow

8.1 Introduction to the Thesis

This thesis was motivated by the desire to better understand Mars and its moons. The intention was to do this by considering impact processes. Accordingly, various simulants were obtained and studied. Martian simulants were used to investigate impacts in ice-silicate targets (to represent the surface of Mars) and to impact asteroid simulant targets to try to better understand the processes to which Phobos is subjected. In this conclusion, the results and implications of this work are considered alongside possible future work.

8.2 Simulant Materials

The results presented in this thesis have shown that the responses of planetary simulants to conditions and the introduction of volatiles varies considerably, despite their similarity in chemical compositions. At times, this led to unexpected outcomes such as the cementation of MGS-1 based targets, when combined with tap-water in what had been an attempt to form a permafrost target. This response was a drastic deviation from the behaviour of both kiln dried sand and the JSC Mars-1 simulant under similar conditions. Whilst the differing mineralogy in the various simulants (independent of the chemical composition determined by XRF) is thought to contribute to the drastically different response to the introduction of water, the primary cause is thought to be the lack of weathering exposure experienced by the newer generation of 'synthetic' simulants. In contrast to the older JSC generation, which were sourced from exposed weathered minerals, the newer SRT era of simulants are sourced from mined minerals. As such, when exposed to volatiles, the minerals within the newer generation of simulants may be more prone to chemical reactions due to more active grain surfaces. This is supported by the examination of the older JSC Mars-1 and newer MGS-1 simulants within this thesis. This unexpected result advances further the discussion started in the paper by Cannon. *et al.*, [239]. Each simulant is produced with a specific use-case in mind and utilisation outside of this may have unintended outcomes.

Whilst a full comparison of the simulant materials is beyond the work presented in this thesis, the identification of the cementitious properties associated with MGS-1 highlights the often unknown properties of simulant materials, which can control how they respond to experimental investigations. Although, some level of prior research has been undertaken into the response of simulant materials to varying conditions [**?**, 239, 242, 279] there is, as of yet, no large-scale publicly available source for cataloguing these properties. As a result, simulants may continue to be used far outside their intended use cases. This is somewhat accounted for within the investigations carried out in the preceding chapters through comparing different silicate materials to each other and to past results. The known influences of the simulant materials on experimental results are often accepted by the scientific community, however, issues arise when these influences are unknown. The wide array of investigations utilising simulant materials mean that the intended use cases will always be exceeded.

The only way to prevent this is the production of a bespoke simulant for each investigation, a costly and time consuming process. Hence, variations in simulant responses must be accounted for and documented to prevent unrealised influences on the results of future investigations. The examples considered in this thesis are described next.

8.3 Impacts into Varying Simulants

Chapter 6 shows the results from impacts into ice-silicate mixture targets. These targets were designed to replicate the permafrost surfaces of Mars thought to be present in the northern polar regions. Both the silicate type and quantity within the constructed targets were varied to investigate how variations in the grain composition, morphology and the quantity of ice would influence the cratering process. The results in Chapter 6 have shown that whilst the dimensions of the crater depend on both the type of silicate and the quantity within the target, crater depth is more sensitive to just the quantity of silicate within the target. Craters formed in targets of varying silicate types possessed crater depths that increased at approximately the same rate whilst diameters increased significantly faster for targets formed of larger, smoother KDS grains than those containing JSC Mars-1. The significant results from this chapter, however, lie in the impacts into targets containing 80 wt.$\%$ JSC Mars-1 and the craters formed by the impact of a basalt projectile. When these changes were introduced to the shot programme, the experimental scatter of measured crater parameters increased dramatically.

Whilst this increased scatter meant that for several parameters accurate trends could not be identified, it is indicative of a substantial change having occurred in the cratering process. The increased scatter is observed within almost all of the presented results. It is, however, seen to be most prominent within the measured crater depths, particularly for those associated with craters formed in silicate-dominated targets. This may simply be due to the nature of analysis used for obtaining the crater depths (as discussed in Section 6.5). It could, however, be indicative of a change occurring within the cratering process as the silicate content of the target is increased beyond 50 wt.$\%$. Further impacts into targets with a silicate content in the range of $50 - 80$ wt.$\%$ would provide greater insight into this. If this scatter is the result of a change in the impact process within silicate-dominated targets, the increased scatter seen for impacts of basalt projectiles into 50 wt.$\%$ silicate content targets suggests that the impact of basalt projectiles into silicate-dominated targets would be enhanced even further. This would have substantial consequences for the analysis of craters within the Northern Lowland Plains. The increased uncertainty induced from the scatter would suggest that it would be harder to infer the quantity of ice within this region from the crater properties alone.

When considering the Northern Lowlands of Mars, the similarity observed for the trends in crater diameter and volume in Chapter 6 as the quantity of silicate within the target changes shows that without further investigations, crater size alone may not provide sufficient data to infer information regarding the quantity of ice within the region. Despite this, the increased depth observed within

silicate-dominated targets (particularly at lower impact energies) may provide some information regarding the quantity of ice within the region surrounding smaller Martian craters. Crater morphology may provide a means to investigate this region. In particular, profiles taken across silicate-dominated targets appear to show a drastic change only for the central pit region, whereas craters formed within a 50 wt$\%$ content target show typically two transitions. The first of these being from the central pit to the inner crater and a second from the inner crater to a shallow spallation region. Despite this, however, the lack of these transitions within craters formed by the impact of a basalt projectile suggest these features may be related to the difference in density between the projectile and target rather than the properties of the target alone. Whilst inferring detail regarding the quantity of ice within the Martian North Polar region is difficult at this stage, the identification of the central depressions and transitions within the profiles may provide some information regarding terraced craters on the Martian surface. The occurrence of transitions within profiles of craters formed by the impact of a copper projectile may indicate terraced craters to form by the impact of a high-density (or iron/metallic) meteorite whereas other craters are formed by the impact of carbonaceous or stony meteorites.

However, caution is needed. Whilst the presence of ice may alter crater depth, as discussed in the earlier chapters on cratering processes, subsequent infilling may mean the crater forms presented today on the surface of Mars may not show the original crater floor. For more detailed comparisons to be made between Martian craters and those formed within the laboratory setting, this requires accounting for. Similarly, as indicated within Section 6.6, laboratory experiments are conducted within the strength-dominated regime. Hence, the result can only be applied smaller craters on Mars (with diameters ≤ 8 km).

8.4 Phobos

The work presented within Chapter 7 focused on investigating the origin of the Martian moons focusing on the hypothesised geological and mineralogical properties of the Phobosian regolith. The investigation covered a range of impact velocities ($652 - 1620$ m/s) using custom projectiles. This led to the projectile transitioning through what are assumed to be different stages of projectile emplacement during impact. Analysis of the material collected from shots which produced ejecta (shots 4, 5, and 6 - with shot 1 producing rebounded projectile fragments) was able to identify projectile material amongst target material. Focusing on the shots thought to have undergone typical cratering and ejecta formation processes (shots 4, 5, and 6), XRF analysis of the collected ejecta found projectile material in the range of $260\ (\pm 166)$ to $1407\ (\pm 199)$ ppm. Comparing this to the range previously found from numerical investigations it is found to be highly similar, with the upper limit here being ≈ 200 ppm higher than in the numerical estimates [271]. However, this is about the magnitude of the uncertainty in the experimental measurements. Potential ways to narrow and confirm this range are discussed in the next section. If we consider the impacts where no ejecta is thought to have been produced, several implications present themselves for the upcoming MMX mission.

At the slowest speeds ($650\ \mathrm{m/s}$), the collected fragments following the shot are thought to be rebounded projectile material, rather than ejecta. This is largely due to the lack of a substantial impact feature present on the target surface (as seen in Figure 7.11) and the extremely high levels of projectile material detected within XRF analysis - a value of $7833 \pm 1594\ \mathrm{ppm}$. Whilst the high level of projectile material detected may be a sampling bias due to the analysed sample consisting of only a few grains, there should be no preference as a result of any collection bias for ejecta vs. rebounded material in this shot. Thus, the collected sample should be representative of the total sample produced. Given the low escape velocity of Phobos ($11.4\ \mathrm{m/s}$) rebounded material is likely to escape the surface. However, this material is unlikely to escape the Mars system entirely and may well re-impact the surface of Phobos at a later date at a velocity set by the orbital speed of Phobos around Mars ($\approx 2.1\ \mathrm{km/s}$).

This assumption (that the ejecta samples collected are truly representative) has also been applied to the results from shots 2 and 3. These shots (at speeds of $720\ \mathrm{m/s}$ and $860\ \mathrm{m/s}$) produced no measurable quantity of ejecta material, leading to the conclusion that the majority of the projectile became emplaced during the impact. This extremely high concentration of projectile material and the lack of measurable ejecta, implies that whilst previous investigations have suggested that gardening processes have tended towards an approximately uniform distribution of Martian material over the surface of Phobos, this may not be the case for impacts at slower velocities. These results suggest that there may exist regions on the surface of Phobos which possess much higher concentrations of emplaced Martian material, indicating that care should be taken when selecting sampling sites for the MMX lander. In the highest speed impacts ($1000 - 1600\ \mathrm{m/s}$), there is a central pit on the target which may contain some projectile material. This region has not be analyses here, thus the potential quantity of projectile material within this region is unquantified. Projectile material was also positively identified within the ejecta via the elemental tracer used. At these speeds and above, the normal process of crater formation is now occurring, and the spread of impactor material across the Phobosian surface is proceeding as presumed in various numerical models [271, 274, 276].

It has long been considered that determining the fraction of the Phobosian surface that is Martian, would potentially be a discriminator when discussing possible origins of Phobos and its surface evolution. However, given the results here which indicate that there may be different local concentrations due to Martian meteorite impact speed, this becomes more problematic. Additionally, before full conclusions can be drawn or further implications for MMX can be made, more work is required.

8.5 Possible Future Improvements in Experimental Design

Much of the future work stemming from this thesis originates from the results presented in Chapter 5 and 7. In these chapters, novel methods were developed in an attempt to investigate the cratering processes in permafrost materials and on the Phobosian surface respectively. Due to the time constraints of the project, however, the scope and extent of these investigations were reduced. Initial

plans for the project involved a series of further impacts mirroring those presented in Chapter 6 but onto permafrost-rich targets constructed from the MGS-1 simulant. The cementing nature of this material, however, led to the development of a new method for target formation. It required a way to implant water-ice within the MGS-1 material with as little interaction as possible between the MGS-1 simulant and liquid water. For this, the method discussed in Section 5.6 was developed to vapour diffuse the water into a set MGS-1 matrix. Due to the extra time spent on developing this method, the planned shots were unable to be performed as part of the analysis presented within this thesis. Hence, further investigations would involve carrying out this shot programme to investigate the cratering process within an MGS-1 material. Impacts would be carried out into both permafrost and dry targets, to enable the identification of effects due to ice within the coherent target blocks.

Following this, the next stage would be additional development of the method. This would involve both the automation of the process but which the water is added to the block within the cryogenic vacuum chamber and the introduction of CO_2. Automation is needed because the current design introduces a water-vapour-nitrogen mixture to the chamber to induce vapour diffusion. This is controlled by hand with the valves for both the water reservoir and nitrogen supply being adjusted manually to retain some level of control over the pressure. This is to ensure that the pressure within the chamber remains within the range suitable for vapour diffusion to occur. However, this is a time consuming and difficult requirement to achieve due to the response delay in the pressure gauge and the difficulty with identifying an ideal equilibrium point. The addition of motorized gas control valves and electric actuators to the chamber, along with additional sensors to monitor the gas flow rate around the block and the quantity of water flowing into the chamber, would provide a much higher level of control over the process. The addition of CO_2, alongside the water vapour, would generate conditions much more analogous to the Martian surface. With a sufficiently efficient cryogenic system, it would also enable generation of CO_2-ice alongside the water-ice, providing the means to investigate how changes to this ratio may influence the crater formation process on the Martian surface.

Additional future work resulting from this thesis can also arise from the work presented in Chapter 7. This work forms only an initial experimental investigation into the identification of Martian material on the surface of Phobos. Hence, there is substantial space for improvements and follow-up work that were unable to be completed due to the time constraints of this project. In order to aid in the post-shot identification of the projectile material used, a europium-based elemental tracer was included within the projectile material. Issues with this, however, were identified during the XRF analysis of the collected ejecta. Whilst initial scans confirmed the presence of europium and this projectile material within the collected ejecta, the obtained values varied considerably for consecutive scans. This is thought to be due to the overlapping spectral peaks within XRF analysis for iron, europium, and manganese, all of which are present within the doped MGS-1 projectile. The variation was further enhanced due to the small sample size, changing the distribution of material during scans where the sample was set to spin. Whilst this was overcome for the analysis by restricting the spinning of the sample, for further work changes to the doping agent would significantly reduce potential errors.

This would be particularly useful for samples collected from slower speed shots. When selecting a doping agent, however, consideration of both contamination and the compounds already present within the projectile and target materials must be made. Whilst rare-Earth metals provide good elemental tracers due to their low abundance within terrestrial samples, prior use of these within the LGG would lead to high levels of contamination and many possess spectral overlaps with more common elements during spectroscopic analysis. One alternative may be the isotopic doping of the projectile sample, allowing emplaced projectile material to be identified through scattering processes (e.g. neutron scattering, mass spectroscopy processes, etc.). In addition, an improved capture system should be designed to increase the solid angle seen from the target and thus increase the fraction of ejecta that is collected.

Additionally, when undertaking subsequent shots for this investigation, as well as increasing the upper impact speed limit to $\approx 3\ \mathrm{km/s}$ it would be useful to consider repeated shots at approximately equal speeds. This would allow for a comparison of projectile emplacement and ejecta contamination under approximately constant conditions; allowing for outliers to be identified and accounted for. Further work would also involve a more in-depth analysis of the post impact targets. For this, changes would be required to the production of the target blocks or a new method would be required to extract the formed crater. Whilst the targets presented a coherent block easily handled pre-shot, they proved highly friable and often fractured during attempts to cut them down to size for analysis. Hence, extracting the formed impact feature (particularly those resulting from higher speed shots) is a delicate and time consuming task. The analysis of the blocks undertaken within this thesis also encountered difficulties when attempting to identify projectile material within the craters and upon the target surface. Due to the size of the formed impact features, mapping the target within the SEM was impractical with a single map taking $\approx 350\ \mathrm{hours}\,(15\ \mathrm{days})$ to complete. Within future investigations, internal scanning and scattering techniques (e.g. neutron scattering, CT-scanning, etc.) may provide a means to identify and located projectile material without requiring post-shot alterations to the target block.

8.6 Topics for Further Investigation

The results presented within this thesis indicate the need for several further investigations into the impact cratering processes related to the Martian system. The targets used within Chapter 6 contained either $50\ \mathrm{wt}\%$ or $80\ \mathrm{wt}\%$ silicate content. Hence, it is difficult to precisely say why the increase in scatter was observed, particularly within crater depths (which appeared to show no trend within silicate-dominated targets). Further investigations impacting targets with a silicate content between the range used within this thesis may provide further insight into this. Additionally, the gradual increase of silicate content would indicate whether the observed scatter increases uniformly with an increasing silicate content or appears after a threshold silicate content is passed. This could be carried out using the same method described in Chapter 6 by varying the quantity of silicate and ice

within the targets. Further investigations impacting silicate-dominated targets with a range of projectile materials and sizes would also provide further insight into the central pit-like features seen within targets impacted with copper projectiles. This may provide further understanding for the formation of terraced craters on the Martian surface.

Further investigations may also stem from the work presented in Section 5.6. Whilst previous studies have investigated the deposition of CO_2-ice within Martian simulant materials [247], the work presented here may allow for the combination of water-ice and CO_2-ice within a Martian material to investigate how the precise ratio of these influences the cratering process. This is particularly applicable to the high-latitude polar regions on Mars where both water-ice and CO_2-ice is present throughout the surface.

Further development of the shell projectiles utilised within Chapter 7 may allow for the use of a wider range of projectiles within impact studies. Custom designs would reduce the requirements currently placed on projectile studies (with coherent projectiles required to fit within a sabot). Additionally, alterations to the current design (i.e. increased structural supports or the utilisation of higher strength resin - this process is difficult to assess due to the proprietary nature of many 3D-printer resins) would enable their use at higher velocities before in-flight break-up occurs. Current models were designed for used within a smoothbore barrel, limiting their use for shots where the target is placed within the blast tank of the Kent LGG (Section 4.1). Thickening of the shell walls, however, may allow for the recessing of channels within the sabot. In effect this would place the rifling on the outer surface of the projectile required to increase accuracy to allow the projectile to reach the target chamber, with the residual atmosphere within the LGG during firing inducing the spining motion. Whilst this process would be far less effective than the rifling within the barrel (due to the typically low $(0.5 - 50\ \mathrm{mbar})$ pressures within the gun during shots), it may provide sufficient stability to the projectile to allow the use of custom sabots for shots within the target chamber whilst maintaining a relatively large quantity of projectile material.

The current design of shell additionally allows the use of liquid projectiles to be considered. Whilst the friction fit of the lid used within Chapter 7 would likely prove insufficient to hold a liquid projectile within the sabot, the careful application of adhesive to the countersunk ring would secure a liquid projectile; opening up the opportunity for further work utilising organic or biologically relevant compounds to study their potential delivery and survivability during impact processes (providing the contamination of the adhesive and shell are accounted for). This has been done previously by drilling holes into sabots and adding lids (see [280]), but 3D printing such shells and lids would permit finer control of the process. This work, however, would require the use of a high-resolution 3D printer to ensure print quality was maintained over shell prints. Extensive testing would also be required to ensure shell reliability.

8.7 Closing Remarks

The work presented in this thesis aimed to investigate two main aspects of cratering within the Mars system. It involved the development of numerous new techniques to achieve this, as well as the impact testing and chemical analysis of samples used. This work presented a multi-disciplinary project and triggered a range of future applications to impact investigations and potential further studies related to Mars and its moons. It has shown that the presence of volatiles (such as water-ice) in the target is important in determining the size and shape of an impact crater. Further, the nature of the silicate simulant also influences the final craterform. These are important factors that need to be allowed for if Martian craters (particularly within the Northern Lowlands) are to be properly understood. The ability to study experimentally the placement of impactor material on Phobos has also been shown. This demonstrates a need to consider carefully the impact speed in such process, by at speeds in the hypervelocity regime suggests impact delivery of Martian material to Phobos is at levels predicted by models.

Bibliography

[1] Osinski GR, Pierazzo E. Impact cratering: processes and products. In: Osinski GR, Pierazzo E, editors. Impact cratering processes and products. Oxford: Wiley-Blackwell; 2013. p. 1-20.

[2] Kenkmann T, Poelchau MH, Wulf G. Structural geology of impact craters. Journal of Structural Geology. 2014 May;62:156-82. Available from: https://www.sciencedirect.com/science/article/pii/S0191814114000285.

[3] Melosh HJ. Impact Cratering: a geologic process. 1st ed. No. 11 in Oxford monographs on geology and geophysics. New York: Oxford Univ. Press [u.a.]; 1996. OCLC: 34429006.

[4] wright SP, Tornabene LL, Ramsey MS. Remote sensing of impact craters. In: Impact cratering processes and products. Oxford: Wiley-Blackwell; 2013. p. 194-210.

[5] Goderis S, Paquay F, Claeys P. Projectile identification in terrestrial impact structures and ejecta material. In: Osinski GR, Pierazzo E, editors. Impact cratering processes and products. Oxford: Wiley-Blackwell; 2013. p. 223-39.

[6] Daly RT, Schultz PH. How much of the impactor (and its water) ends up in Vesta's regolith? Lunar and Planetary Science Conference; 2014. p. 2070.

[7] Osinski GR, Grieve RAF, Tornabene LL. Excavation and impact ejecta emplacement. In: Osinski GR, Pierazzo E, editors. Impact cratering processes and products. Oxford: Wiley-Blackwell; 2013. p. 43-59.

[8] Carr MH, Head JW. Geologic history of Mars. Earth and Planetary Science Letters. 2010 Jun;294(3-4):185-203. Available from: https://linkinghub.elsevier.com/retrieve/pii/S0012821X09003847.

[9] Platz T, Michael G, Tanaka KL, Skinner JA, Fortezzo CM. Crater-based dating of geological units on Mars: Methods and application for the new global geological map. Icarus. 2013 Jul;225(1):806-27. Available from: https://linkinghub.elsevier.com/retrieve/pii/S0019103513001863.

[10] de Villers G, King Jr DT, Marzen LJ. A Study of Candidate Marine Target Impact Craters in Arabia Terra, Mars. Meteoritics & Planetary Science. 2010 Jun;54(6):947-64. Avail-

able from: https://onlinelibrary-wiley-com.chain.kent.ac.uk/doi/full/10.1111/j.1945-5100.2010.01068.x.

[11] Geologic Map of Mars | U.S. Geological Survey; 2014. Available from: https://www.usgs.gov/media/images/geologic-map-mars.

[12] Khakimov O, Ortiqov O, Ramazanova N, Okbutaev B, Mukhammadieva O, Abdinazarov U, et al. UNVEILING GEOLOGICAL HISTORY THROUGH STRATIGRAPHY AND MINERALOGY. afts. 2024 Dec;2(31):305-10. Available from: https://www.arhivzatehnickenauke.com/article/424.

[13] Bibring JP, Langevin Y, Mustard JF, Poulet F, Arvidson R, Gendrin A, et al. Global Mineralogical and Aqueous Mars History Derived from OMEGA/Mars Express Data. Science. 2006 Apr;312(5772):400-4. Available from: https://www.science.org/doi/10.1126/science.1122659.

[14] Tanaka KL. The stratigraphy of Mars. J Geophys Res. 1986 Nov;91(B13). Available from: https://agupubs.onlinelibrary.wiley.com/doi/10.1029/JB091iB13p0E139.

[15] Smith DE, Zuber MT, Frey HV, Garvin JB, Head JW, Muhleman DO, et al. Topography of the Northern Hemisphere of Mars from the Mars Orbiter Laser Altimeter. Science. 1998 Mar;279(5357):1686-92. Available from: https://www.science.org/doi/10.1126/science.279.5357.1686.

[16] Black BA, Stewart ST. Excess ejecta craters record episodic ice-rich layers at middle latitudes on Mars. J Geophys Res. 2008 Feb;113(E2):E02015. Available from: http://doi.wiley.com/10.1029/2007JE002888.

[17] Dickeson ZI, Davis JM. Martian oceans. Astronomy & Geophysics. 2020 Jun;61(3):3.11-3.17. Available from: https://academic.oup.com/astrogeo/article/61/3/3.11/5836123.

[18] Costard F, Séjourné A, Kelfoun K, Clifford S, Lavigne F, Di Pietro I, et al. Modeling tsunami propagation and the emplacement of thumbprint terrain in an early Mars ocean: TSUNAMIS ON MARS. J Geophys Res Planets. 2017 Mar;122(3):633-49. Available from: http://doi.wiley.com/10.1002/2016JE005230.

[19] Head JW, Hiesinger H, Ivanov MA, Kreslavsky MA, Pratt S, Thomson BJ. Possible Ancient Oceans on Mars: Evidence from Mars Orbiter Laser Altimeter Data. Science. 1999 Dec;286(5447):2134-7. Available from: https://www.science.org/doi/10.1126/science.286.5447.2134.

[20] Senft LE, Stewart ST. Impact crater formation in icy layered terrains on Mars. Meteoritics & Planetary Science. 2008 Dec;43(12):1993-2013. Available from: http://doi.wiley.com/10.1111/j.1945-5100.2008.tb00657.x.

[21] Jones AP, McEwen AS, Tornabene LL, Baker VR, Melosh HJ, Berman DC. A geomorphic analysis of Hale crater, Mars: The effects of impact into ice-rich crust. Icarus. 2011 Jan;211(1):259-72. Available from: https://linkinghub.elsevier.com/retrieve/pii/S0019103510003933.

[22] Schwenzer SP, Abramov O, Allen CC, Clifford SM, Cockell CS, Filiberto J, et al. Puncturing Mars: How impact craters interact with the Martian cryosphere. Earth and Planetary Science Letters. 2012 Jun;335-336:9-17. Available from: https://linkinghub.elsevier.com/retrieve/pii/S0012821X12001987.

[23] Barlow NG, Perez CB. Martian impact crater ejecta morphologies as indicators of the distribution of subsurface volatiles. J Geophys Res. 2003;108(E8):5085. Available from: http://doi.wiley.com/10.1029/2002JE002036.

[24] Schaefer EI, Head JW, Kadish SJ. Vaduz, an unusual fresh crater on Mars: Evidence for impact into a recent ice-rich mantle: VADUZ-EVIDENCE FOR AN ICE-RICH MANTLE. Geophys Res Lett. 2011 Apr;38(7):n/a-n/a. Available from: http://doi.wiley.com/10.1029/2010GL046605.

[25] Schon SC, Head JW. Decameter-scale pedestal craters in the tropics of Mars: Evidence for the recent presence of very young regional ice deposits in Tharsis. Earth and Planetary Science Letters. 2012 Feb;317-318:68-75. Available from: https://linkinghub.elsevier.com/retrieve/pii/S0012821X11005164.

[26] Dundas CM, Byrne S. Modeling sublimation of ice exposed by new impacts in the martian mid-latitudes. Icarus. 2010 Apr;206(2):716-28. Available from: https://linkinghub.elsevier.com/retrieve/pii/S001910350900390X.

[27] Reufer A, Thomas N, Benz W, Byrne S, Bray V, Dundas C, et al. Models of high velocity impacts into dust-covered ice: Application to Martian northern lowlands. Planetary and Space Science. 2010 Aug;58(10):1160-8. Available from: https://linkinghub.elsevier.com/retrieve/pii/S0032063310001108.

[28] Weiss DK, Head JW. Evidence for stabilization of the ice-cemented cryosphere in earlier martian history: Implications for the current abundance of groundwater at depth on Mars. Icarus. 2017 May;288:120-47. Available from: https://linkinghub.elsevier.com/retrieve/pii/S0019103516304535.

[29] Johnsson A, Reiss D, Hauber E, Hiesinger H, Zanetti M. Evidence for very recent meltwater and debris flow activity in gullies in a young mid-latitude crater on Mars. Icarus. 2014 Jun;235:37-54. Available from: https://linkinghub.elsevier.com/retrieve/pii/S0019103514001225.

[30] Prettyman TH. Composition and structure of the Martian surface at high southern latitudes from neutron spectroscopy. J Geophys Res. 2004;109(E5):E05001. Available from: http://doi.wiley.com/10.1029/2003JE002139.

[31] Garvin JB, Sakimoto SEH, Frawley JJ, Schnetzler C. North Polar Region Craterforms on Mars: Geometric Characteristics from the Mars Orbiter Laser Altimeter. Icarus. 2000 Apr;144(2):329-52. Available from: https://linkinghub.elsevier.com/retrieve/pii/S001910359996298X.

[32] Zuber MT, Smith DE, Solomon SC, Abshire JB, Afzal RS, Aharonson O, et al. Observations of the North Polar Region of Mars from the Mars Orbiter Laser Altimeter. Science. 1998 Dec;282(5396):2053-60. Available from: https://www.science.org/doi/10.1126/science.282.5396.2053.

[33] Arvidson RE, Bonitz RG, Robinson ML, Carsten JL, Volpe RA, Trebi-Ollennu A, et al. Results from the Mars Phoenix Lander Robotic Arm experiment. J Geophys Res. 2009 Jan;114(E1):2009JE003408. Available from: https://agupubs.onlinelibrary.wiley.com/doi/10.1029/2009JE003408.

[34] Archer PD, Franz HB, Sutter B, Arevalo RD, Coll P, Eigenbrode JL, et al. Abundances and implications of volatile-bearing species from evolved gas analysis of the Rocknest aeolian deposit, Gale Crater, Mars. J Geophys Res Planets. 2014 Jan;119(1):237-54. Available from: http://doi.wiley.com/10.1002/2013JE004493.

[35] Blake DF, Morris RV, Kocurek G, Morrison SM, Downs RT, Bish D, et al. Curiosity at Gale Crater, Mars: Characterization and Analysis of the Rocknest Sand Shadow. Science. 2013 Sep;341(6153):1239505. Available from: https://www.science.org/doi/10.1126/science.1239505.

[36] Cull S, Arvidson RE, Mellon MT, Skemer P, Shaw A, Morris RV. Compositions of subsurface ices at the Mars Phoenix landing site. Geophysical Research Letters. 2010 Dec;37(24):2010GL045372. Available from: https://agupubs.onlinelibrary.wiley.com/doi/10.1029/2010GL045372.

[37] Burtt DG, Stern JC, Webster CR, Hofmann AE, Franz HB, Sutter B, et al. Highly enriched carbon and oxygen isotopes in carbonate-derived CO_2 at Gale crater, Mars. Proc Natl Acad Sci USA. 2024 Oct;121(42):e2321342121. Available from: https://pnas.org/doi/10.1073/pnas.2321342121.

[38] Meng X, Xu Y, Xiao L, Xiao Z. Permittivity Estimation of Subsurface Deposits in the Elysium–Utopia Region on Mars with *MRO* Shallow Radar Sounder Data. AJ. 2020 Mar;159(4):156. Available from: https://iopscience.iop.org/article/10.3847/1538-3881/ab774c.

[39] Dried out river valley network on Mars;. Available from: https://www.esa.int/ESA_Multimedia/Images/2019/02/Dried_out_river_valley_network_on_Mars.

[40] Carr MH. Martian oceans, valleys and climate. Astron Geophys. 2000 Jun;41(3):3.20-3.26. Available from: https://academic.oup.com/astrogeo/article-lookup/doi/10.1046/j.1468-4004.2000.00320.x.

[41] Fairén AG, Dohm JM, Baker VR, de Pablo MA, Ruiz J, Ferris JC, et al. Episodic flood inundations of the northern plains of Mars. Icarus. 2003 Sep;165(1):53-67. Available from: https://linkinghub.elsevier.com/retrieve/pii/S0019103503001441.

[42] R V, G S, S S. Comparison of analogous terrestrial and Martian drainage systems: a remote sensing based study. Beijing, China; 2014. p. 926035. Available from: http://proceedings.spiedigitallibrary.org/proceeding.aspx?doi=10.1117/12.2068897.

[43] Kraal ER, Van Dijk M, Postma G, Kleinhans MG. Martian stepped-delta formation by rapid water release. Nature. 2008 Feb;451(7181):973-6. Available from: https://www.nature.com/articles/nature06615.

[44] Hoke MRT, Hynek BM, Di Achille G, Hutton EWH. The effects of sediment supply and concentrations on the formation timescale of martian deltas. Icarus. 2014 Jan;228:1-12. Available from: https://linkinghub.elsevier.com/retrieve/pii/S0019103513004089.

[45] Lapôtre MGA, Ielpi A. The Pace of Fluvial Meanders on Mars and Implications for the Western Delta Deposits of Jezero Crater. AGU Advances. 2020 Jun;1(2):e2019AV000141. Available from: https://agupubs.onlinelibrary.wiley.com/doi/10.1029/2019AV000141.

[46] HiRISE | A Terraced Fan and Valley in a Crater (PSP_005583_1700);. Available from: https://www.uahirise.org/PSP_005583_1700.

[47] Rare martian lake delta spotted by Mars Express;. Available from: https://www.esa.int/Science_Exploration/Space_Science/Mars_Express/Rare_martian_lake_delta_spotted_by_Mars_Express.

[48] Duy DV, Tanaka H, Larson M, Viet NT. A Theory for Estuarine Delta Formation with Finite Beach Length under Sediment Supplied from the River. JMSE. 2022 Jul;10(7):947. Available from: https://www.mdpi.com/2077-1312/10/7/947.

[49] Digging Deeper to Find Life on Ocean Worlds - NASA Science; 2023. Section: Science-enabling Technology. Available from: https://science.nasa.gov/science-research/science-enabling-technology/digging-deeper-to-find-life-on-ocean-worlds/.

[50] Zimmerman W, Blake D, Harris W, Morookian JM, Randall D, Reder LJ, et al. MSL Chemistry and Mineralogy X-ray Diffraction X-ray Fluorescence (CheMin) Instrument. In: 2013 IEEE Aerospace Conference. Big Sky, MT: IEEE; 2013. p. 1-15. Available from: http://ieeexplore.ieee.org/document/6496835/.

[51] Allwood AC, Wade LA, Foote MC, Elam WT, Hurowitz JA, Battel S, et al. PIXL: Planetary Instrument for X-Ray Lithochemistry. Space Sci Rev. 2020 Dec;216(8):134. Available from: http://link.springer.com/10.1007/s11214-020-00767-7.

[52] mars nasa gov. Images from the Mars Perseverance Rover - NASA;. Available from: https://mars.nasa.gov/mars2020/multimedia/raw-images/.

[53] Martian 'Blueberries' - NASA Science; 2015. Section: Mars. Available from: https://science.nasa.gov/resource/martian-blueberries-2/.

[54] Catalog Page for PIA19081;. Available from: https://photojournal.jpl.nasa.gov/catalog/PIA19081.

[55] Achilles CN, Downs RT, Ming DW, Rampe EB, Morris RV, Treiman AH, et al. Mineralogy of an active eolian sediment from the Namib dune, Gale crater, Mars: In Situ Mineralogy of the Bagnold Dunes. J Geophys Res Planets. 2017 Nov;122(11):2344-61. Available from: http://doi.wiley.com/10.1002/2017JE005262.

[56] Levin RL, Lyddy DJ. Possible liquid water ponds on the martian surface. In: 2007 IEEE AEROSPACE CONFERENCE, VOLS 1-9. IEEE Aerospace Conference Proceedings. IEEE; Panasonic; Aerosp Corp; IET; dSPACE; CALTECH; Amer Inst Aeronaut & Astronaut; ASES; 2007. p. 272-91.

[57] Eberl DD. On the formation of Martian blueberries. American Mineralogist. 2022 Jan;107(1):153-5. Available from: https://pubs.geoscienceworld.org/ammin/article/107/1/153/610336/On-the-formation-of-Martian-blueberries.

[58] Benison KC. A Martian analog in Kansas: Comparing Martian strata with Permian acid saline lake deposits. Geol. 2006;34(5):385. Available from: https://pubs.geoscienceworld.org/geology/article/34/5/385-388/129547.

[59] Carter J, Poulet F, Bibring JP, Mangold N, Murchie S. Hydrous minerals on Mars as seen by the CRISM and OMEGA imaging spectrometers: Updated global view. JGR Planets. 2013 Apr;118(4):831-58. Available from: https://agupubs.onlinelibrary.wiley.com/doi/10.1029/2012JE004145.

[60] Mars_MGS_colorhillshade_mola_1024.jpg (JPEG Image, 1024 × 512 pixels);. Available from: https://astropedia.astrogeology.usgs.gov/download/Mars/GlobalSurveyor/MOLA/thumbs/Mars_MGS_colorhillshade_mola_1024.jpg.

[61] Ori GG, Marinangeli L, Baliva A, Bressan M, Strom RG. Fluid dynamics of liquids on Titans surface. Planetary and Space Science. 1998 Oct;46(9-10):1417-21. Available from: https://linkinghub.elsevier.com/retrieve/pii/S0032063397001256.

[62] Carter J, Riu L, Poulet F, Bibring JP, Langevin Y, Gondet B. A Mars orbital catalog of aqueous alteration signatures (MOCAAS). Icarus. 2023 Jan;389:115164. Available from: https://linkinghub.elsevier.com/retrieve/pii/S0019103522002664.

[63] Jones E. Identifying an index of subsurface volatiles on Mars through an analysis of impact crater morphometry using principal component analysis: CRATER PRINCIPAL COMPONENT ANALYSIS. J Geophys Res Planets. 2015 Dec;120(12):2084-101. Available from: http://doi.wiley.com/10.1002/2015JE004882.

[64] Morino C, Conway S, Philippe M, Peignaux C, Svennevig K, Lucas A, et al. Permafrost molards as an analogue for ejecta-ice interactions at Hale Crater, Mars. Icarus. 2023 Feb;391:115363. Available from: https://linkinghub.elsevier.com/retrieve/pii/S0019103522004559.

[65] Soare RJ, Conway SJ, Dohm JM, El-Maarry MR. Possible open-system (hydraulic) pingos in and around the Argyre impact region of Mars. Earth and Planetary Science Letters. 2014 Jul;398:25-36. Available from: https://linkinghub.elsevier.com/retrieve/pii/S0012821X14002842.

[66] Jawin ER, Head JW. Patterns of late Amazonian deglaciation from the distribution of martian paraglacial features. Icarus. 2021 Feb;355:114117. Available from: https://linkinghub.elsevier.com/retrieve/pii/S0019103520304619.

[67] Barlow NG. Constraining geologic properties and processes through the use of impact craters. Geomorphology. 2015 Jul;240:18-33. Available from: https://linkinghub.elsevier.com/retrieve/pii/S0169555X14004541.

[68] Barlow NG, Boyce JM, Cornwall C. Martian Low-Aspect-Ratio Layered Ejecta (LARLE) craters: Distribution, characteristics, and relationship to pedestal craters. Icarus. 2014 Sep;239:186-200. Available from: https://linkinghub.elsevier.com/retrieve/pii/S0019103514002905.

[69] Squyres SW, Carr MH. Geomorphic Evidence for the Distribution of Ground Ice on Mars. Science. 1986 Jan;231(4735):249-52. Available from: https://www.science.org/doi/10.1126/science.231.4735.249.

[70] Boynton WV, Feldman WC, Squyres SW, Prettyman TH, Brückner J, Evans LG, et al. Distribution of Hydrogen in the Near Surface of Mars: Evidence for Subsurface Ice Deposits. Science. 2002 Jul;297(5578):81-5. Available from: https://www.science.org/doi/10.1126/science.1073722.

[71] Barlow NG, Boyce JM, Costard FM, Craddock RA, Garvin JB, Sakimoto SEH, et al. Standardizing the nomenclature of Martian impact crater ejecta morphologies. J Geophys Res. 2000 Nov;105(E11):26733-8. Available from: http://doi.wiley.com/10.1029/2000JE001258.

[72] Lobban C, Finney JL, Kuhs WF. The structure of a new phase of ice. Nature. 1998 Jan;391(6664):268-70. Available from: https://www.nature.com/articles/34622.

[73] Hansen TC. The everlasting hunt for new ice phases. Nat Commun. 2021 May;12(1):3161. Available from: https://www.nature.com/articles/s41467-021-23403-6.

[74] Dundas CM, Bramson AM, Ojha L, Wray JJ, Mellon MT, Byrne S, et al. Exposed subsurface ice sheets in the Martian mid-latitudes. Science. 2018 Jan;359(6372):199-201. Available from: https://www.science.org/doi/10.1126/science.aao1619.

[75] Soare RJ, Burr DM, Wan Bun Tseung JM. Possible pingos and a periglacial landscape in northwest Utopia Planitia. Icarus. 2005 Apr;174(2):373-82. Available from: https://linkinghub.elsevier.com/retrieve/pii/S0019103504004105.

[76] Arfstrom J, Hartmann WK. Martian flow features, moraine-like ridges, and gullies: Terrestrial analogs and interrelationships. Icarus. 2005 Apr;174(2):321-35. Available from: https://linkinghub.elsevier.com/retrieve/pii/S0019103504004002.

[77] Barlow NG. Impact craters in the northern hemisphere of Mars: Layered ejecta and central pit characteristics. Meteoritics & Planetary Science. 2006;41(10):1425 1436.

[78] Interactive Mapping of Mars;. Available from: https://imars.uwo.ca/tutorial/glacial.

[79] HiRISE | Knobs near Reull Vallis (ESP_017286_1430);. Available from: https://www.uahirise.org/ESP_017286_1430.

[80] HiRISE | Possible Layers in Pedestal Crater in Amazonis Region (ESP_045462_1920);. Available from: https://www.uahirise.org/ESP_045462_1920.

[81] HiRISE | Fresh Double-Layered Ejecta Crater (PSP_009160_2350);. Available from: https://www.uahirise.org/PSP_009160_2350.

[82] Kadish SJ, Barlow NG, Head JW. Latitude dependence of Martian pedestal craters: Evidence for a sublimation-driven formation mechanism: LATITUDE DEPENDENCE OF PEDESTAL CRATERS. J Geophys Res. 2009 Oct;114(E10):n/a-n/a. Available from: http://doi.wiley.com/10.1029/2008JE003318.

[83] Mouginis-Mark PJ. Cratering on Mars with almost no atmosphere or volatiles: Pangboche crater. Meteorit Planet Sci. 2015 Jan;50(1):51-62. Available from: http://doi.wiley.com/10.1111/maps.12400.

[84] Orosei R, Lauro SE, Pettinelli E, Cicchetti A, Coradini M, Cosciotti B, et al. Radar evidence of subglacial liquid water on Mars. Science. 2018 Aug;361(6401):490-3. Available from: https://www.science.org/doi/10.1126/science.aar7268.

[85] Steinberg Y, Smith IB, Aharonson O. Physical properties of subsurface water ice deposits in Mars's Mid-Latitudes from the shallow radar. Icarus. 2025 Nov;441:116716. Available from: https://linkinghub.elsevier.com/retrieve/pii/S0019103525002647.

[86] Catalog Page for PIA11720;. Available from: https://photojournal.jpl.nasa.gov/catalog/PIA11720.

[87] Catalog Page for PIA10910;. Available from: https://photojournal.jpl.nasa.gov/catalog/PIA10910.

[88] Zenhäusern G, Wójcicka N, Stähler SC, Collins GS, Daubar IJ, Knapmeyer M, et al. An estimate of the impact rate on Mars from statistics of very-high-frequency marsquakes. Nat Astron. 2024 Jun;8(9):1138-47. Available from: https://www.nature.com/articles/s41550-024-02301-z.

[89] Daubar IJ, Atwood-Stone C, Byrne S, McEwen AS, Russell PS. The morphology of small fresh craters on Mars and the Moon: Fresh Crater d/D on Mars and the Moon. J Geophys Res Planets. 2014 Dec;119(12):2620-39. Available from: http://doi.wiley.com/10.1002/2014JE004671.

[90] Peel SE, Burr DM, Tran L. Formation of Central Pits in Impact Craters on Mars: A Statistical Investigation of Proposed Mechanisms. J Geophys Res Planets. 2019 Feb;124(2):437-53. Available from: https://onlinelibrary.wiley.com/doi/abs/10.1029/2018JE005738.

[91] Luther R, Artemieva N, Wünnemann K. The effect of atmospheric interaction on impact ejecta dynamics and deposition. Icarus. 2019 Nov;333:71-86. Available from: https://linkinghub.elsevier.com/retrieve/pii/S0019103519303288.

[92] Caudill CM, Osinski GR, Tornabene LL. Ejecta deposits of Bakhuysen Crater, Mars. Icarus. 2018 Nov;314:175-94. Available from: https://linkinghub.elsevier.com/retrieve/pii/S0019103517305420.

[93] DeLatte DM, Crites ST, Guttenberg N, Tasker EJ, Yairi T. Segmentation Convolutional Neural Networks for Automatic Crater Detection on Mars. IEEE J Sel Top Appl Earth Observations Remote Sensing. 2019 Aug;12(8):2944-57. Available from: https://ieeexplore.ieee.org/document/8734854/.

[94] Boyce JM, Wilson L, Barlow NG. Origin of the outer layer of martian low-aspect ratio layered ejecta craters. Icarus. 2015 Jan;245:263-72. Available from: https://linkinghub.elsevier.com/retrieve/pii/S0019103514004564.

[95] Barlow NG. Crater size-frequency distributions and a revised Martian relative chronology. Icarus. 1988 Aug;75(2):285-305. Available from: https://linkinghub.elsevier.com/retrieve/pii/0019103588900061.

[96] Robbins SJ, Hynek BM. A new global database of Mars impact craters >1 km: 1. Database creation, properties, and parameters: MARS CRATER DATABASE-CONSTRUCTION. J Geophys Res. 2012 May;117(E5):n/a-n/a. Available from: http://doi.wiley.com/10.1029/2011JE003966.

[97] Smith DE, Zuber MT, Frey HV, Garvin JB, Head JW, Muhleman DO, et al. Mars Orbiter Laser Altimeter: Experiment summary after the first year of global mapping of Mars. J Geophys Res. 2001 Oct;106(E10):23689-722. Available from: http://doi.wiley.com/10.1029/2000JE001364.

[98] Kelley SP, Sherlock SC. The geochronology of impact craters. In: Osinski GR, Pierazzo E, editors. Impact cratering processes and products. Oxford: Wiley-Blackwell; 2013. p. 240-53.

[99] Robbins SJ, Runyon K, Singer KN, Bray VJ, Beyer RA, Schenk P, et al. Investigation of Charon's Craters With Abrupt Terminus Ejecta, Comparisons With Other Icy Bodies, and Formation Implications: Abrupt Terminus Ejecta Craters on Charon. J Geophys Res Planets. 2018 Jan;123(1):20-36. Available from: http://doi.wiley.com/10.1002/2017JE005287.

[100] Senft LE, Stewart ST. Modeling the morphological diversity of impact craters on icy satellites. Icarus. 2011 Jul;214(1):67-81. Available from: https://linkinghub.elsevier.com/retrieve/pii/S0019103511001503.

[101] Burchell MJ, Johnson E. Impact craters on small icy bodies such as icy satellites and comet nuclei. Monthly Notices of the Royal Astronomical Society. 2005 Jun;360(2):769-81. Available from: https://academic.oup.com/mnras/article-lookup/doi/10.1111/j.1365-2966.2005.09122.x.

[102] Hiraoka K, Arakawa M, Yoshikawa K, Nakamura AM. Laboratory experiments of crater formation on ice–silicate mixture targets. Advances in Space Research. 2007 Jan;39(3):392-9. Available from: https://linkinghub.elsevier.com/retrieve/pii/S0273117705005880.

[103] Arakawa M. Impact Experiments on Porous Icy-Silicate Cylindrical Blocks and the Implication for Disruption and Accumulation of Small Icy Bodies. Icarus. 2002 Aug;158(2):516-31. Available from: https://linkinghub.elsevier.com/retrieve/pii/S0019103502968934.

[104] Arakawa M, Tomizuka D. Ice–silicate fractionation among icy bodies due to the difference of impact strength between ice and ice–silicate mixture. Icarus. 2004 Jul;170(1):193-201. Available from: https://linkinghub.elsevier.com/retrieve/pii/S0019103504000739.

[105] Koschny D, Grun E. Impacts into Ice–Silicate Mixtures: Crater Morphologies, Volumes, Depth-to-Diameter Ratios, and Yield. Icarus. 2001 Dec;154(2):391-401. Available from: https://linkinghub.elsevier.com/retrieve/pii/S0019103501967077.

[106] Harriss KH, Burchell MJ. Hypervelocity impacts into ice-topped layered targets: Investigating the effects of ice crust thickness and subsurface density on crater morphology. Meteorit Planet Sci. 2017 Jul;52(7):1505-22. Available from: http://doi.wiley.com/10.1111/maps.12913.

[107] Zahnle K, Schenk P, Levison H, Dones L. Cratering Rates in the Outer Solar System. Icarus. 2003 Jun;163(2):263-89.

[108] Hiraoka K, Arakawa M, Setoh M, Nakamura AM. Measurements of target compressive and tensile strength for application to impact cratering on ice-silicate mixtures. J Geophys Res. 2008 Feb;113(E2):E02013. Available from: http://doi.wiley.com/10.1029/2007JE002926.

[109] Moon S, Paige DA, Siegler MA, Russell PS. Geomorphic Evidence for the Presence of Ice Deposits in the Permanently Shadowed Regions of Scott-E Crater on the Moon. Geophys Res Lett. 2021 Jan;48(2). Available from: https://onlinelibrary.wiley.com/doi/10.1029/2020GL090780.

[110] Miljković K, Mason NJ, Zarnecki JC. Ejecta fragmentation in impacts into gypsum and water ice. Icarus. 2011 Aug;214(2):739-47. Available from: https://linkinghub.elsevier.com/retrieve/pii/S0019103511002107.

[111] Murakami Y, Nakamura AM, Yokoyama K, Seto Y, Hasegawa S. Collisional disruption of highly porous targets in the strength regime: Effects of mixture. Planetary and Space Science. 2020 Mar;182:104819. Available from: https://linkinghub.elsevier.com/retrieve/pii/S0032063319301035.

[112] Schultz PH, Ernst CM, Anderson JLB. Expectations for Crater Size and Photometric Evolution from the Deep Impact Collision. Space Sci Rev. 2005 Mar;117(1-2):207-39. Available from: http://link.springer.com/10.1007/s11214-005-3383-7.

[113] Kurosawa K, Takada S. Impact cratering mechanics: A forward approach to predicting ejecta velocity distribution and transient crater radii. Icarus. 2019 Jan;317:135-47. Available from: https://linkinghub.elsevier.com/retrieve/pii/S0019103517307728.

[114] Richardson JE, Melosh HJ, Artemeiva NA, Pierazzo E. Impact Cratering Theory and Modeling for the Deep Impact Mission: From Mission Planning to Data Analysis. Space Sci Rev. 2005 Mar;117(1-2):241-67. Available from: http://link.springer.com/10.1007/s11214-005-3393-5.

[115] Osinski GR, Tornabene LL, Grieve RAF. Impact ejecta emplacement on terrestrial planets. Earth and Planetary Science Letters. 2011 Oct;310(3-4):167-81. Available from: https://linkinghub.elsevier.com/retrieve/pii/S0012821X11004675.

[116] Runyon KD, Barnouin OS. Preliminary laboratory investigations of ejecta emplacement dynamics and morphology with planetary applications. Planetary and Space Science.

2018 Oct;160:39-55. Available from: https://linkinghub.elsevier.com/retrieve/pii/S0032063317303094.

[117] Prieur NC, Rolf T, Luther R, Wünnemann K, Xiao Z, Werner SC. The effect of target properties on transient crater scaling for simple craters: Target Properties and Simple Craters. J Geophys Res Planets. 2017 Aug;122(8):1704-26. Available from: http://doi.wiley.com/10.1002/2017JE005283.

[118] Yamamoto S, Wada K, Okabe N, Matsui T. Transient crater growth in granular targets: An experimental study of low velocity impacts into glass sphere targets. Icarus. 2006 Jul;183(1):215-24. Available from: https://linkinghub.elsevier.com/retrieve/pii/S0019103506000650.

[119] Jones E, Osinski GR. Using martian single and double layered ejecta craters to probe subsurface stratigraphy. Icarus. 2015 Feb;247:260-78. Available from: https://linkinghub.elsevier.com/retrieve/pii/S0019103514005557.

[120] Schenk PM. Central pit and dome craters: Exposing the interiors of Ganymede and Callisto. J Geophys Res. 1993 Apr;98(E4):7475-98. Available from: http://doi.wiley.com/10.1029/93JE00176.

[121] Osinski GR, Grieve RAF, Marion C, Chanou A. Impact melting. In: Osinski GR, Pierazzo E, editors. Impact cratering processes and products. Oxford: Wiley-Blackwell; 2013. p. 125-45.

[122] French BM. Traces of Catastrophe: A Handbook of Shock-Metamorphic Effects in Terrestrial Meteorite Impact Structures. Houston, Texas: Lunar and Planetary Institute; 1998.

[123] Galilei G. Sidereus Nuncius; 1610.

[124] Koeberl C. Craters on the Moon from Galileo to Wegener: a Short History of the Impact Hypothesis, and Implication for the Study of Terrestrial Impact Craters. Earth, Moon, and Planets. 1999;85/86:209-24. Available from: http://link.springer.com/10.1023/A:1017020032451.

[125] Hooke R. Micrographia: Some Physiological Desriptions of Minute Bodies Made by Magnifying Glasses with Observations and Inquiries Thereupon. London: London: Printed by Jo. Martyn, and Ja. Allestry, Printers to the Royal Society; 1665.

[126] Gifford AC. The Origin of Surface Features on the Moon. Journal of the Royal Astronomical Society of Canada. 1931 Feb;25:70.

[127] Fresh Craters on the Moon and Earth [Text.Article]. NASA Earth Observatory; 2009. Available from: https://earthobservatory.nasa.gov/images/39769/fresh-craters-on-the-moon-and-earth.

[128] Newsom HE, Wright SP, Misra S, Hagerty JJ. Comparison of simple impact craters: A case study of Metero and Lonar craters. In: Osinski GR, Pierazzo E, editors. Impact cratering processes and products. Oxford: Wiley-Blackwell; 2013. p. 271-89.

[129] Kenkmann T, Collins GS, Wünnemann K. The modification stage of crater formation. In: Osinski GR, Pierazzo E, editors. Impact cratering processes and products. Oxford: Wiley-Blackwell; 2013. p. 60-75.

[130] Michel P, Morbidelli A. Population of impactors and the impact cratering rate in the inner Solar System. In: Osinski GR, Pierazzo E, editors. Impact cratering processes and products. Oxford: Wiley-Blackwell; 2013. p. 21-31.

[131] Bottke W. Interpreting the Elliptical Crater Populations on Mars, Venus, and the Moon. Icarus. 2000 May;145(1):108-21. Available from: https://linkinghub.elsevier.com/retrieve/pii/S0019103599963236.

[132] Burchell MJ, Mackay NG. Crater ellipticity in hypervelocity impacts on metals. J Geophys Res. 1998 Sep;103(E10):22761-74. Available from: https://agupubs.onlinelibrary.wiley.com/doi/10.1029/98JE02143.

[133] Oberbeck VR. Laboratory simulation of impact cratering with high explosives. J Geophys Res. 1971 Aug;76(23):5732-49. Available from: http://doi.wiley.com/10.1029/JB076i023p05732.

[134] Adushkin VV, Khristoforov BD. Craters of Large-Scale Surface Explosions. Combustion, Explosion, and Shock Waves. 2004 Nov;40(6):674-8. Available from: https://doi.org/10.1023/B:CESW.0000048270.62239.01.

[135] Luccioni B, Ambrosini D, Nurick G, Snyman I. Craters produced by underground explosions. Computers & Structures. 2009 Nov;87(21):1366-73. Available from: https://www.sciencedirect.com/science/article/pii/S0045794909001710.

[136] Formby SA, Wharton RK. Blast characteristics and TNT equivalence values for some commercial explosives detonated at ground level. Journal of Hazardous Materials. 1996 Oct;50(2):183-98. Available from: https://www.sciencedirect.com/science/article/pii/0304389496017918.

[137] Treaty banning nuclear weapon tests in the atmosphere, in outer space and under water; 1963. Available from: https://treaties.un.org/pages/showDetails.aspx?objid=08000002801313d9.

[138] National Nuclear Security Administration;. Available from: https://www.energy.gov/nnsa/national-nuclear-security-administration.

[139] Smirnov NN, Kondratyev KA. Evaluation of craters formation in hypervelocity impact of debris particles on solid structures. Acta Astronautica. 2009 Dec;65(11):1796-803. Available from: https://www.sciencedirect.com/science/article/pii/S0094576509002318.

[140] Graham GA, Kearsley AT, Grady MM, Wright IP, Herbert MK, McDonnell JAM. Natural and simulated hypervelocity impacts into solar cells. International Journal of Impact Engineering. 1999 Dec;23(1):319-30. Available from: https://linkinghub.elsevier.com/retrieve/pii/S0734743X99000834.

[141] Kearsley AT, Drolshagen G, McDonnell JAM, Mandeville JC, Moussi A. Impacts on Hubble Space Telescope solar arrays: Discrimination between natural and man-made particles. Advances in Space Research. 2005 Jan;35(7):1254-62. Available from: https://linkinghub.elsevier.com/retrieve/pii/S0273117705006605.

[142] Payne JE, Myers WS, Ehrgott JQ, Rickman DD, Thomas CD, Windham JE. Investigation of relationships between soil type and condition and crater size for shallow-buried explosive charges. International Journal of Protective Structures. 2019 Jun;10(2):135-53. Available from: http://journals.sagepub.com/doi/10.1177/2041419618798382.

[143] Afriyie G, Braimah A, Rayhani MT. Effect of explosive cratering on embankment dams. International Journal of Geotechnical Engineering. 2018 Mar;12(2):200-8. _eprint: https://doi.org/10.1080/19386362.2016.1262308. Available from: https://doi.org/10.1080/19386362.2016.1262308.

[144] Zhou X, Bai C, Zhang Y, Wang Z. Inverse analysis of explosives based on crater size. Shock Waves. 2017 Jan;27(1):27-35. Available from: https://doi.org/10.1007/s00193-016-0643-2.

[145] Ambrosini RD, Luccioni BM, Danesi RF, Riera JD, Rocha MM. Size of craters produced by explosive charges on or above the ground surface. Shock Waves. 2002 Jul;12(1):69-78. Available from: https://doi.org/10.1007/s00193-002-0136-3.

[146] Van Ginneken M, Harvey RP, Goderis S, Artemieva N, Boslough M, Maeda R, et al. The identification of airbursts in the past: Insights from the BIT-58 layer. Earth and Planetary Science Letters. 2024 Feb;627:118562. Available from: https://linkinghub.elsevier.com/retrieve/pii/S0012821X23005721.

[147] Sweden's Siljan Ring [Text.Article]. NASA Earth Observatory; 2021. Available from: https://earthobservatory.nasa.gov/images/148577/swedens-siljan-ring.

[148] Violent Formation for Mistastin Lake [Text.Article]. NASA Earth Observatory; 2021. Available from: https://earthobservatory.nasa.gov/images/148491/violent-formation-for-mistastin-lake.

[149] Vredefort Crater [Text.Article]. NASA Earth Observatory; 2018. Available from: https://earthobservatory.nasa.gov/images/92689/vredefort-crater.

[150] Serra da Cangalha Crater, Brazil [Text.Article]. NASA Earth Observatory; 2008. Available from: https://earthobservatory.nasa.gov/images/8568/serra-da-cangalha-crater-brazil.

[151] Osinski GR, Grieve RAF. Comparison of mid-size terrestrial complex impact structures: A case study. In: Osinski GR, Pierazzo E, editors. Impact cratering processes and products. Oxford: Wiley-Blackwell; 2013. p. 290-305.

[152] Ferrière L, Osinski GR. Shock metamorphism. In: Osinski GR, Pierazzo E, editors. Impact cratering processes and products. Oxford: Wiley-Blackwell; 2013. p. 106-24.

[153] Grieve RAF, Therriault AM. Impactites: their characteristics and spatial distribution. In: Osinski GR, Pierazzo E, editors. Impact cratering processes and products. Oxford: Wiley-Blackwell; 2013. p. 90-105.

[154] Morgan JV, Rebolledo-Vieyra M. Geophysical studies of impact craters. In: Osinski GR, Pierazzo E, editors. Impact cratering processes and products. Oxford: Wiley-Blackwell; 2013. p. 211-22.

[155] Kirsimäe K, Osinski GR. Impact-induced hydrothermal activity. In: Osinski GR, Pierazzo E, editors. Impact cratering processes and products. Oxford: Wiley-Blackwell; 2013. p. 76-89.

[156] Melosh HJ. The contact and compression stage of impact cratering. In: Osinski GR, Pierazzo E, editors. Impact cratering processes and products. Oxford: Wiley-Blackwell; 2013. p. 32-42.

[157] Ivanov BA, Artemieva NA, Pierazzo E. Impact cratering and material models: Subsurface volatiles on Mars. In: Workshop on the role of volatiles and atmospheres on Martian impact craters. vol. 1273 of LPI Contributions; 2005. p. 55-6.

[158] Johnson BC, Bowling TJ, Melosh HJ. Jetting during vertical impacts of spherical projectiles. Icarus. 2014 Aug;238:13-22. Available from: https://linkinghub.elsevier.com/retrieve/pii/S0019103514002474.

[159] Miller GH. Jetting in Oblique, Asymmetric Impacts. Icarus. 1998 Jul;134(1):163-75. Available from: https://linkinghub.elsevier.com/retrieve/pii/S0019103598959450.

[160] Tandy JD, Price MC, Wozniakiewicz PJ, Cole MJ, Alesbrook LS, Avdellidou C. Impact flash evolution of CO $_2$ ice, water ice, and frozen Martian and lunar regolith simulant targets. Meteorit Planet Sci. 2020 Oct;55(10):2301-19. Available from: https://onlinelibrary.wiley.com/doi/10.1111/maps.13581.

[161] Walsh JM, Shreffler RG, Willig FJ. Limiting Conditions for Jet Formation in High Velocity Collisions. Journal of Applied Physics. 1953 Mar;24(3):349-59. Available from: https://pubs.aip.org/aip/jap/article/24/3/349-359/160328.

[162] Harlow FH. Formation and Penetration of High-Speed Collapse Jets. Phys Fluids. 1966;9(10):1951. Available from: https://pubs.aip.org/aip/pfl/article/9/10/1951-1959/850666.

[163] Melosh HJ. Impact ejection, spallation, and the origin of meteorites. Icarus. 1984 Aug;59(2):234-60. Available from: https://linkinghub.elsevier.com/retrieve/pii/0019103584900265.

[164] Kurosawa K, Okamoto T, Genda H. Hydrocode modeling of the spallation process during hypervelocity impacts: Implications for the ejection of Martian meteorites. Icarus. 2018 Feb;301:219-34. Available from: https://linkinghub.elsevier.com/retrieve/pii/S001910351730249X.

[165] Chappaz L, Melosh HJ, Vaquero M, Howell KC. Transfer of Impact Ejecta Material from the Surface of Mars to Phobos and Deimos. Astrobiology. 2013 Oct;13(10):963-80. Available from: http://www.liebertpub.com/doi/10.1089/ast.2012.0942.

[166] Melosh HJ, Ivanov BA. IMPACT CRATER COLLAPSE. Annu Rev Earth Planet Sci. 1999 May;27(1):385-415. Available from: https://www.annualreviews.org/doi/10.1146/annurev.earth.27.1.385.

[167] Robbins SJ, Schenk PM, Riggs JD, Parker AH, Bray VJ, Beddingfield CB, et al. Depths of Pluto's and Charon's craters, and their simple-to-complex transition. Icarus. 2021 Mar;356:113902. Available from: https://linkinghub.elsevier.com/retrieve/pii/S0019103520302815.

[168] Silber EA, Osinski GR, Johnson BC, Grieve RAF. Effect of impact velocity and acoustic fluidization on the simple-to-complex transition of lunar craters. JGR Planets. 2017 May;122(5):800-21. Available from: https://agupubs.onlinelibrary.wiley.com/doi/10.1002/2016JE005236.

[169] Chandnani M, Herrick RR, Kramer GY. Geologic Investigation of Deep Simple Craters in the Lunar Simple-to-Complex Transition. JGR Planets. 2019 Oct;124(10):2482-504. Available from: https://agupubs.onlinelibrary.wiley.com/doi/10.1029/2018JE005903.

[170] Robbins SJ, Hynek BM. A new global database of Mars impact craters >1 km: 2. Global crater properties and regional variations of the simple-to-complex transition diameter. J Geophys Res. 2012 Jun;117(E6):2011JE003967. Available from: https://agupubs.onlinelibrary.wiley.com/doi/10.1029/2011JE003967.

[171] Chandnani M, Herrick RR, Kramer GY. Geologic Analyses of the Causes of Morphological Variations in Lunar Craters Within the Simple-to-Complex Transition. JGR Planets. 2019 May;124(5):1238-65. Available from: https://agupubs.onlinelibrary.wiley.com/doi/10.1029/2018JE005729.

[172] Chandnani M, Herrick RR. Influence of Target Properties on Wall Slumping in Lunar Impact Craters Within the Simple-To-Complex Transition. JGR Planets. 2023

Jan;128(1):e2022JE007369. Available from: https://agupubs.onlinelibrary.wiley.com/doi/10.1029/2022JE007369.

[173] Prieur NC, Rolf T, Wünnemann K, Werner SC. Formation of Simple Impact Craters in Layered Targets: Implications for Lunar Crater Morphology and Regolith Thickness. JGR Planets. 2018 Jun;123(6):1555-78. Available from: https://agupubs.onlinelibrary.wiley.com/doi/10.1029/2017JE005463.

[174] Heyer T, Hiesinger H, Reiss D, Erkeling G, Bernhardt H, Luesebrink D, et al. The Multi-Temporal Database of Planetary Image Data (MUTED): A web-based tool for studying dynamic Mars. Planetary and Space Science. 2018 Sep;159:56-65. Available from: https://linkinghub.elsevier.com/retrieve/pii/S0032063317304038.

[175] Siewert J, Ferlito C. Mechanical erosion by flowing lava. Contemporary Physics. 2008 Jan;49(1):43-54. Available from: http://www.tandfonline.com/doi/abs/10.1080/00107510802077388.

[176] Armstrong J, Leovy C. Long term wind erosion on Mars. Icarus. 2005 Jul;176(1):57-74. Available from: https://linkinghub.elsevier.com/retrieve/pii/S0019103505000242.

[177] Khawja S, Ernst RE, Samson C, Byrne PK, Ghail RC, MacLellan LM. Tesserae on Venus may preserve evidence of fluvial erosion. Nat Commun. 2020 Nov;11(1):5789. Available from: https://www.nature.com/articles/s41467-020-19336-1.

[178] Haeberli W, Hallet B, Arenson L, Elconin R, Humlum O, Kääb A, et al. Permafrost creep and rock glacier dynamics. Permafrost Periglac Process. 2006 Jul;17(3):189-214. Available from: https://onlinelibrary.wiley.com/doi/10.1002/ppp.561.

[179] Durham WB, Pathare AV, Stern LA, Lenferink HJ. Mobility of icy sand packs, with application to Martian permafrost. Geophys Res Lett. 2009 Dec;36(23):L23203. Available from: http://doi.wiley.com/10.1029/2009GL040392.

[180] Mangold N, Allemand P, Duval P, Geraud Y, Thomas P. Experimental and theoretical deformation of ice–rock mixtures: Implications on rheology and ice content of Martian permafrost. Planetary and Space Science. 2002 Apr;50(4):385-401. Available from: https://linkinghub.elsevier.com/retrieve/pii/S0032063302000053.

[181] Fendyke S, Price MC, Burchell MJ. Hydrocode modelling of hypervelocity impacts on ice. Advances in Space Research. 2013 Aug;52(4):705-14. Available from: https://linkinghub.elsevier.com/retrieve/pii/S0273117713002226.

[182] Robbins SJ, Singer KN, Bray VJ, Schenk P, Lauer TR, Weaver HA, et al. Craters of the Pluto-Charon system. Icarus. 2017 May;287:187-206. Available from: https://linkinghub.elsevier.com/retrieve/pii/S0019103516306133.

[183] Sizemore HG, Schmidt BE, Buczkowski DA, Sori MM, Castillo-Rogez JC, Berman DC, et al. A Global Inventory of Ice-Related Morphological Features on Dwarf Planet Ceres: Implications for the Evolution and Current State of the Cryosphere. J Geophys Res Planets. 2019 Jul;124(7):1650-89. Available from: https://onlinelibrary.wiley.com/doi/abs/10.1029/2018JE005699.

[184] Grey IDS, Burchell MJ. Hypervelocity impact craters in ammonia rich ice. Icarus. 2004 Apr;168(2):467-74. Available from: https://linkinghub.elsevier.com/retrieve/pii/S0019103503003919.

[185] Alzate N, Barlow NG. Central pit craters on Ganymede. Icarus. 2011 Feb;211(2):1274-83. Available from: https://linkinghub.elsevier.com/retrieve/pii/S0019103510003945.

[186] Viola D, McEwen AS, Dundas CM, Byrne S. Subsurface volatile content of martian double-layer ejecta (DLE) craters. Icarus. 2017 Mar;284:325-43. Available from: https://linkinghub.elsevier.com/retrieve/pii/S0019103516303864.

[187] Barlow NG, Ferguson SN, Horstman RM, Maine A. Comparison of central pit craters on Mars, Mercury, Ganymede, and the Saturnian satellites. Meteorit Planet Sci. 2017 Jul;52(7):1371-87. Available from: https://onlinelibrary.wiley.com/doi/10.1111/maps.12857.

[188] Schenk P, Sizemore H, Schmidt B, Castillo-Rogez J, De Sanctis M, Bowling T, et al. The central pit and dome at Cerealia Facula bright deposit and floor deposits in Occator crater, Ceres: Morphology, comparisons and formation. Icarus. 2019 Mar;320:159-87. Available from: https://www.sciencedirect.com/science/article/pii/S001910351730862X.

[189] Williams NR, Bell JF, Christensen PR, Farmer JD. Evidence for an explosive origin of central pit craters on Mars. Icarus. 2015 May;252:175-85. Available from: https://linkinghub.elsevier.com/retrieve/pii/S001910351400685X.

[190] Hughson KHG, Russell CT, Schmidt BE, Chilton HT, Sizemore HG, Schenk PM, et al. Fluidized Appearing Ejecta on Ceres: Implications for the Mechanical Properties, Frictional Properties, and Composition of its Shallow Subsurface. J Geophys Res Planets. 2019 Jul;124(7):1819-39. Available from: https://onlinelibrary.wiley.com/doi/abs/10.1029/2018JE005666.

[191] Shrine N, Burchell MJ, Grey IDS. Velocity Scaling of Impact Craters in Water Ice over the Range 1 to 7.3 km/s. Icarus. 2002 Feb;155(2):475-85. Available from: https://linkinghub.elsevier.com/retrieve/pii/S001910350196734X.

[192] Suzuki AI, Kurita K. Fluidized Ejecta Morphologies and Degradation Processes of Martian Impact Craters. Journal of Geography (Chigaku Zasshi). 2016;125(1):13-33. Available from: https://www.jstage.jst.go.jp/article/jgeography/125/1/125_125.13/_article/-char/ja/.

[193] Bland MT, Bray VJ. The inevitability of large shallow craters on Callisto and Ganymede: Implications for crater depth-diameter trends. Icarus. 2024 Jan;408:115811. Available from: https://linkinghub.elsevier.com/retrieve/pii/S0019103523003901.

[194] Schenk PM. Crater formation and modification on the icy satellites of Uranus and Saturn: Depth/diameter and central peak occurrence. J Geophys Res. 1989 Apr;94(B4):3813-32. Available from: http://doi.wiley.com/10.1029/JB094iB04p03813.

[195] Caussi ML, Dombard AJ, Korycansky DG, White OL, Moore JM, Schenk PM. Dome Craters on Ganymede and Callisto May Form by Topographic Relaxation of Pit Craters Aided by Remnant Impact Heat. JGR Planets. 2024 Jul;129(7):e2023JE008258. Available from: https://agupubs.onlinelibrary.wiley.com/doi/10.1029/2023JE008258.

[196] Moore JM, Malin MC. Dome craters on Ganymede. Geophysical Research Letters. 1988 Mar;15(3):225-8. Available from: https://agupubs.onlinelibrary.wiley.com/doi/10.1029/GL015i003p00225.

[197] Mare Serpentis (Jun 02, 2016); 2013. Available from: https://www.geo.fu-berlin.de/en/geol/fachrichtungen/planet/press/archiv2016/mare_serpentis1/index.html.

[198] Potter RWK. Investigating the onset of multi-ring impact basin formation. Icarus. 2015 Nov;261:91-9. Available from: https://linkinghub.elsevier.com/retrieve/pii/S001910351500353X.

[199] LROC PDS Release Number 5 | Lunar Reconnaissance Orbiter Camera;. Available from: http://lroc.sese.asu.edu/posts/306.

[200] Catalog Page for PIA00562;. Available from: https://photojournal.jpl.nasa.gov/catalog/PIA00562.

[201] Johnson BC, Andrews-Hanna JC, Collins GS, Freed AM, Melosh HJ, Zuber MT. Controls on the Formation of Lunar Multiring Basins. JGR Planets. 2018 Nov;123(11):3035-50. Available from: https://onlinelibrary.wiley.com/doi/10.1029/2018JE005765.

[202] Barnouin OS, Ernst CM, Susorney HCM. The remarkable Hokusai Crater, Mercury. Lunar and Planetary Science Conference XLVI. Houston, Texas; 2015. p. 2672.

[203] Sugita S. Initiation of Run-Out Flows on Venus by Oblique Impacts. Icarus. 2002 Feb;155(2):265-84. Available from: https://linkinghub.elsevier.com/retrieve/pii/S0019103501967314.

[204] Ernst CM, Chabot NL, Barnouin OS. Examining the Potential Contribution of the Hokusai Impact to Water Ice on Mercury. J Geophys Res Planets. 2018 Oct;123(10):2628-46. Available from: http://doi.wiley.com/10.1029/2018JE005552.

[205] Weissman PR, Stern SA. The Impactor Flux in the Pluto-Charon System. Icarus. 1994 Oct;111(2):378-86.

[206] Johnson JR, Baker VR. Surface Property Variations in Venusian Fluidized Ejecta Blanket Craters. Icarus. 1994 Jul;110(1):33-70. Available from: https://linkinghub.elsevier.com/retrieve/pii/S0019103584711067.

[207] NASA - Orientale Basin [Image Feature]. Brian Dunbar;. Available from: https://www.nasa.gov/mission_pages/LRO/multimedia/lroimages/lroc-20100618-orientale.html.

[208] Butler BJ, Muhleman DO, Slade MA. Mercury: full-disk radar images and the detection and stability of ice at the North Pole. J Geophys Res. 1993;98(E8):15003. Available from: http://doi.wiley.com/10.1029/93JE01581.

[209] Moses JI, Rawlins K, Zahnle K, Dones L. External Sources of Water for Mercury's Putative Ice Deposits. Icarus. 1999 Feb;137(2):197-221. Available from: https://linkinghub.elsevier.com/retrieve/pii/S0019103598960365.

[210] Fastook JL, Head JW, Deutsch AN. Glaciation on Mercury: Accumulation and flow of ice in permanently shadowed circum-polar crater interiors. Icarus. 2019 Jan;317:81-93. Available from: https://linkinghub.elsevier.com/retrieve/pii/S0019103517306061.

[211] Herrick RR, Phillips RJ. Implications of a Global Survey of Venusian Impact Craters. Icarus. 1994 Oct;111(2):387-416. Available from: https://linkinghub.elsevier.com/retrieve/pii/S0019103584711523.

[212] Ong L, Asphaug EI, Korycansky D, Coker RF. Volatile retention from cometary impacts on the Moon. Icarus. 2010 Jun;207(2):578-89. Available from: https://linkinghub.elsevier.com/retrieve/pii/S0019103509005016.

[213] Bland PA, Artemieva NA, Collins GS, Bottke WF, Bussey DBJ, Joy KH. Asteroids on the Moon: Projectile survival during low velocity impacts. Lunar and Planetary Science Conference; 2008. p. 2045.

[214] Daly RT, Schultz PH. Predictions for impactor contamination on Ceres based on hypervelocity impact experiments. Geophys Res Lett. 2015 Oct;42(19):7890-8. Available from: https://onlinelibrary.wiley.com/doi/abs/10.1002/2015GL065601.

[215] Li L, Yue Z, Di K, Peng M. Observations of Martian layered ejecta craters and constraints on their formation mechanisms. Meteorit Planet Sci. 2015 Mar;50(3):508-22. Available from: https://onlinelibrary.wiley.com/doi/abs/10.1111/maps.12438.

[216] Zhang Y. H $_2$ O and Other Volatiles in the Moon, 50 Years and on. ACS Earth Space Chem. 2020 Sep;4(9):1480-99. Available from: https://pubs.acs.org/doi/10.1021/acsearthspacechem.9b00305.

[217] Wada K, Barnouin OS. The formation of fluidized ejecta on Mars by granular flows. Meteoritics & Planetary Science. 2006 Oct;41(10):1551 1569.

[218] Xiao Z, Komatsu G. Impact craters with ejecta flows and central pits on Mercury. Planetary and Space Science. 2013 Jul;82-83:62-78. Available from: https://linkinghub.elsevier.com/retrieve/pii/S0032063313000743.

[219] Xiao Z, Zeng Z, Komatsu G. A global inventory of central pit craters on the Moon: Distribution, morphology, and geometry. Icarus. 2014 Jan;227:195-201. Available from: https://linkinghub.elsevier.com/retrieve/pii/S0019103513004107.

[220] Catalog Page for PIA20350;. Available from: https://photojournal.jpl.nasa.gov/catalog/PIA20350.

[221] 33. Isis (Central Pit Crater) Ganymede, Jupiter;. Available from: https://www.lpi.usra.edu/publications/slidesets/3dsolarsystem/slide_33.html.

[222] PILOT - Planetary Image Locator Tool - USGS Astrogeology Science Center - NASA Archive of Raw Planet Images of Moon, Mars, Jupiter, Saturn, Mercury . . .;. Available from: https://pilot.wr.usgs.gov/#polygon.

[223] Geissler P, McEwen A, Phillips C, Keszthelyi L, Spencer J. Surface changes on Io during the Galileo mission. Icarus. 2004 May;169(1):29-64. Available from: https://linkinghub.elsevier.com/retrieve/pii/S001910350300321X.

[224] Williams DA, Keszthelyi LP, Crown DA, Yff JA, Jaeger WL, Schenk PM, et al. Volcanism on Io: New insights from global geologic mapping. Icarus. 2011 Jul;214(1):91-112. Available from: https://linkinghub.elsevier.com/retrieve/pii/S0019103511001710.

[225] de Pater I, Keane JT, de Kleer K, Davies AG. A 2020 Observational Perspective of Io. Annu Rev Earth Planet Sci. 2021 May;49(1):643-78. Available from: https://www.annualreviews.org/doi/10.1146/annurev-earth-082420-095244.

[226] Catalog Page for PIA01658;. Available from: https://photojournal.jpl.nasa.gov/catalog/PIA01658.

[227] Rogers JA, Bass NT, Wiest ML, Wantz Z, Wilkerson JW, Lacy TE. The pursuit of hypervelocities: A review of two-stage light gas gun aeroballistic ranges. International Journal of Impact Engineering. 2024 Mar;185:104861. Available from: https://linkinghub.elsevier.com/retrieve/pii/S0734743X23003706.

[228] Crozier WD, Hume W. High-Velocity, Light-Gas Gun. Journal of Applied Physics. 1957 Aug;28(8):892-4. Available from: https://pubs.aip.org/jap/article/28/8/892/161711/High-Velocity-Light-Gas-Gun.

[229] Francesconi A, Pavarin D, Bettella A, Angrilli F. A special design condition to increase the performance of two-stage light-gas guns. International Journal of Impact Engineering. 2008 Dec;35(12):1510-5. Available from: https://linkinghub.elsevier.com/retrieve/pii/S0734743X08001577.

[230] Tang W, Wang Q, Wei B, Li J, Li J, Shang J, et al. Performance and Modeling of a Two-Stage Light Gas Gun Driven by Gaseous Detonation. Applied Sciences. 2020 Jun;10(12):4383. Available from: https://www.mdpi.com/2076-3417/10/12/4383.

[231] Burchell MJ, Cole MJ, McDonnell JAM, Zarnecki JC. Hypervelocity impact studies using the 2 MV Van de Graaff accelerator and two-stage light gas gun of the University of Kent at Canterbury. Meas Sci Technol. 1999 Jan;10(1):41-50. Available from: https://iopscience.iop.org/article/10.1088/0957-0233/10/1/011.

[232] Murtaugh M, Rogers JA, Allaire D, Lacy TE. Empirical Models for Predicting Two-Stage Light Gas Gun Muzzle Velocity. J dynamic behavior mater. 2024 Oct. Available from: https://link.springer.com/10.1007/s40870-024-00441-x.

[233] Lexow B, Wickert M, Thoma K, Schäfer F, Poelchau MH, Kenkmann T. The extra-large light-gas gun of the Fraunhofer EMI: Applications for impact cratering research: The extra-large light-gas gun of the Fraunhofer EMI. Meteoritics & Planetary Science. 2013 Jan;48(1):3-7. Available from: http://doi.wiley.com/10.1111/j.1945-5100.2012.01427.x.

[234] Lexow B, Wickert M, Thoma K, Schäfer F, Poelchau MH, Kenkmann T. The extra-large light-gas gun of the Fraunhofer EMI: Applications for impact cratering research. Meteorit & Planetary Scien. 2013 Jan;48(1):3-7. Available from: https://onlinelibrary.wiley.com/doi/10.1111/j.1945-5100.2012.01427.x.

[235] Price MC, Cole MJ, Harriss KH, Alesbrook LS, Burchell MJ, Wozniakiewicz PJ. A new compact, self-compressing, vertical one and two-stage gas gun at the University of Kent. International Journal of Impact Engineering. 2024 Feb;184:104828. Available from: https://linkinghub.elsevier.com/retrieve/pii/S0734743X23003378.

[236] Niemes S, Braun JR. Speed of Sound Measurement of Hydrogen Isotopologues Containing Tritium for Reference Gas Sample Verification. Fusion Science and Technology. 2024 May;80(3-4):558-62. Available from: https://www.tandfonline.com/doi/full/10.1080/15361055.2023.2209087.

[237] X-ray fluorescence (XRF);. Available from: https://rigaku.com/resources/techniques/x-ray-fluorescence-xrf.

[238] X-rays;. Available from: http://hyperphysics.phy-astr.gsu.edu/hbase/quantum/xterm.html.

[239] Cannon KM, Britt DT, Smith TM, Fritsche RF, Batcheldor D. Mars global simulant MGS-1: A Rocknest-based open standard for basaltic martian regolith simulants. Icarus. 2019 Jan;317:470-8. Available from: https://linkinghub.elsevier.com/retrieve/pii/S0019103518303038.

[240] Quinteros VS, Mikesell TD, Griffiths L, Jerves AX. Geotechnical laboratory testing of lunar simulants and the importance of standardization. Icarus. 2024 Jan;408:115812. Available from: https://linkinghub.elsevier.com/retrieve/pii/S0019103523003913.

[241] Allen CC, Morris RV, Jager KM, Golden DC, Lindstrom DJ, Lindstrom MM, et al. Martian Regolith Simulant JSC Mars-1. Lunar and Planetary Science Conference XXIX. Houston, Texas; 1998. p. 1960.

[242] Landsman ZA, Schultz CD, Britt DT, Peppin M, Kobrick RL, Metzger PT, et al. Phobos regolith simulants PGI-1 and PCA-1. Advances in Space Research. 2021 May;67(10):3308-27. Available from: https://linkinghub.elsevier.com/retrieve/pii/S0273117721000612.

[243] Allen CC, Jager KM, Morris RV, Lindstrom DJ, Lindstrom MM, Lockwood JP. Martian soil stimulant available for scientific, educational study. Eos Trans AGU. 1998;79(34):405-5. Available from: http://doi.wiley.com/10.1029/98EO00309.

[244] Metzger PT, Britt DT, Covey S, Schultz C, Cannon KM, Grossman KD, et al. Measuring the fidelity of asteroid regolith and cobble simulants. Icarus. 2019 Mar;321:632-46. Available from: https://linkinghub.elsevier.com/retrieve/pii/S0019103518302902.

[245] Particle Size Conversion Table;. Available from: https://www.sigmaaldrich.com/GB/en/support/calculators-and-apps/particle-size-conversion-table.

[246] Thomas M. Supplementary Cementing Materials in Concrete. CRC Press; 2017.

[247] Mc Keown LE, Bourke MC, McElwaine JN. Experiments On Sublimating Carbon Dioxide Ice And Implications For Contemporary Surface Processes On Mars. Sci Rep. 2017 Oct;7(1):14181. Available from: https://www.nature.com/articles/s41598-017-14132-2.

[248] Duarte KD, Schmidt BE, Chilton HT, Hughson KHG, Sizemore HG, Ferrier KL, et al. Landslides on Ceres: Diversity and Geologic Context. J Geophys Res Planets. 2019 Dec;124(12):3329-43. Available from: https://onlinelibrary.wiley.com/doi/abs/10.1029/2018JE005673.

[249] Burchell MJ. Cratering on icy bodies. In: Gudipati MS, Castillo-Rogez J, editors. The science of Solar System ices. New York, NY: Springer; 2013. p. 253-78.

[250] Stephan K, Jaumann R, Wagner R. Geology of icy bodies. In: Gudipati MS, Castillo-Rogez J, editors. The science of Solar System ices. New York, NY: Springer; 2013. p. 279-367.

[251] Bray VJ, Collins GS, Morgan JV, Schenk PM. The effect of target properties on crater morphology: Comparison of central peak craters on the Moon and Ganymede. Meteoritics &

Planetary Science. 2008 Dec;43(12):1979-92. Available from: http://doi.wiley.com/10.1111/j.1945-5100.2008.tb00656.x.

[252] Moore JM, Asphaug E, Sullivan RJ, Klemaszewski JE, Bender KC, Greeley R, et al. Large Impact Features on Europa: Results of the Galileo Nominal Mission. Icarus. 1998 Sep;135(1):127-45. Available from: https://www.sciencedirect.com/science/article/pii/S0019103598959735.

[253] Moore JM, Schenk PM, Bruesch LS, Asphaug E, McKinnon WB. Large impact features on middle-sized icy satellites. Icarus. 2004 Oct;171(2):421-43. Available from: https://linkinghub.elsevier.com/retrieve/pii/S0019103504001666.

[254] Grey IDS, Burchell MJ. Hypervelocity impact cratering on water ice targets at temperatures ranging from 100 K to 253 K. J Geophys Res. 2003;108(E3):5019. Available from: http://doi.wiley.com/10.1029/2002JE001899.

[255] Lange MA, Ahrens TJ. Impact cratering in ice- and ice-silicate targets: An experimental assessment. Lunar and Planetary Science Conference; 1982. p. 415-6.

[256] Koschny D, Kargl G, Rott M. Experimental studies of the cratering process in porous ice targets. Advances in Space Research. 2001 Jan;28(10):1533-7. Available from: https://linkinghub.elsevier.com/retrieve/pii/S0273117701003660.

[257] Burchell M, Johnson E, Grey I. Estimating Crater Size for Hypervelocity Impacts on Small Icy Bodies (e.g. Comet Nucleus). In: Koeberl C, Dypvik H, Burchell MJ, Claeys P, editors. Cratering in Marine Environments and on Ice. Berlin, Heidelberg: Springer Berlin Heidelberg; 2004. p. 197-210. Series Title: Impact Studies. Available from: http://link.springer.com/10.1007/978-3-662-06423-8_11.

[258] Burchell MJ, Brooke-Thomas W, Leliwa-Kopystynski J, Zarnecki JC. Hypervelocity Impact Experiments on Solid CO2Targets. Icarus. 1998 Jan;131(1):210-22. Available from: https://linkinghub.elsevier.com/retrieve/pii/S0019103597958577.

[259] Igneous Rocks;. Available from: https://www2.nau.edu/gaud/RiodeFlag/ignsrck.htm.

[260] Citron RI, Genda H, Ida S. Formation of Phobos and Deimos via a giant impact. Icarus. 2015 May;252:334-8. Available from: https://linkinghub.elsevier.com/retrieve/pii/S0019103515000639.

[261] Hyodo R, Genda H, Charnoz S, Rosenblatt P. On the Impact Origin of Phobos and Deimos. I. Thermodynamic and Physical Aspects. ApJ. 2017 Aug;845(2):125. Available from: https://iopscience.iop.org/article/10.3847/1538-4357/aa81c4.

[262] Pätzold M, Andert T, Jacobson R, Rosenblatt P, Dehant V. Phobos: Observed bulk properties. Planetary and Space Science. 2014 Nov;102:86-94. Available from: https://linkinghub.elsevier.com/retrieve/pii/S0032063314000087.

[263] Guo X, Yan J, Andert T, Yang X, Pätzold M, Hahn M, et al. A lighter core for Phobos? A&A. 2021 Jul;651:A110. Available from: https://www.aanda.org/10.1051/0004-6361/202038844.

[264] Ramsley KR, Head JW. The Origins and Geological Histories of Deimos and Phobos: Hypotheses and Open Questions. Space Sci Rev. 2021 Dec;217(8):86. Available from: https://link.springer.com/10.1007/s11214-021-00864-1.

[265] Craddock RA. Are Phobos and Deimos the result of a giant impact? Icarus. 2011 Feb;211(2):1150-61. Available from: https://linkinghub.elsevier.com/retrieve/pii/S0019103510004100.

[266] Poggiali G, Matsuoka M, Barucci MA, Brucato JR, Beck P, Fornasier S, et al. Phobos and Deimos surface composition: search for spectroscopic analogues. Monthly Notices of the Royal Astronomical Society. 2022 Aug;516(1):465-76. Available from: https://academic.oup.com/mnras/article/516/1/465/6660653.

[267] Catalog Page for PIA10368;. Available from: https://photojournal.jpl.nasa.gov/catalog/PIA10368.

[268] Duxbury TC, Zakharov AV, Hoffmann H, Guinness EA. Spacecraft exploration of Phobos and Deimos. Planetary and Space Science. 2014 Nov;102:9-17. Available from: https://linkinghub.elsevier.com/retrieve/pii/S0032063313003322.

[269] Kirsch E, McKenna-Lawlor SMP, Afonin VV, Keppler E, Livi S, Rosenbauer H, et al. Signatures of the Martian moon Phobos in the fluxes of energetic particles as measured by experiment SLED onboard Phobos 2. Planetary and Space Science. 1993 Jun;41(6):435-40. Available from: https://linkinghub.elsevier.com/retrieve/pii/003206339390003K.

[270] Fanale FP, Salvail JR. Loss of water from Phobos. Geophys Res Lett. 1989 Apr;16(4):287-90. Available from: http://doi.wiley.com/10.1029/GL016i004p00287.

[271] Ramsley KR, Head JW. Mars impact ejecta in the regolith of Phobos: Bulk concentration and distribution. Planetary and Space Science. 2013 Oct;87:115-29. Available from: https://linkinghub.elsevier.com/retrieve/pii/S0032063313002328.

[272] Wiegert P, Galiazzo MA. Meteorites from Phobos and Deimos at Earth? Planetary and Space Science. 2017 Aug;142:48-52. Available from: https://linkinghub.elsevier.com/retrieve/pii/S0032063316304019.

[273] Ivanov AV. Is the Kaidun Meteorite a Sample from Phobos? Solar System Research. 2004 Mar;38(2):97-107. Available from: http://link.springer.com/10.1023/B:SOLS.0000022821.22821.84.

[274] Hyodo R, Kurosawa K, Genda H, Usui T, Fujita K. Transport of impact ejecta from Mars to its moons as a means to reveal Martian history. Sci Rep. 2019 Dec;9(1):19833. Available from: http://www.nature.com/articles/s41598-019-56139-x.

[275] Ramsley KR, Head JW. The origin of Phobos grooves from ejecta launched from impact craters on Mars: Tests of the hypothesis. Planetary and Space Science. 2013 Jan;75:69-95. Available from: https://linkinghub.elsevier.com/retrieve/pii/S003206331200298X.

[276] Thomas PC. Ejecta Emplacement on the Martian Satellites. Icarus. 1998 Jan;131(1):78-106. Available from: https://linkinghub.elsevier.com/retrieve/pii/S0019103597958589.

[277] Space Resource Technologies;. Available from: https://spaceresourcetech.com/.

[278] Burchell MJ, Cole MJ, Price MC, Kearsley AT. Experimental investigation of impacts by solar cell secondary ejecta on silica aerogel and aluminum foil: Implications for the Stardust Interstellar Dust Collector. Meteorit & Planetary Scien. 2012 Apr;47(4):671-83. Available from: https://onlinelibrary.wiley.com/doi/10.1111/j.1945-5100.2011.01294.x.

[279] Sun Y, Jiang T, Zhuang Y, Zhang H, Britt DT, Zhu MH. A laboratory study of the photometric properties of Mars Global Soil Simulant MGS-1 and its variants. Planetary and Space Science. 2023 Mar;227:105639. Available from: https://linkinghub.elsevier.com/retrieve/pii/S0032063323000089.

[280] Burchell MJ, Bowden SA, Cole M, Price MC, Parnell J. Survival of Organic Materials in Hypervelocity Impacts of Ice on Sand, Ice, and Water in the Laboratory. Astrobiology. 2014 Jun;14(6):473-85. Available from: http://www.liebertpub.com/doi/10.1089/ast.2013.1007.

Appendix A

Chapter 6 Depth Profiles

A.1 50 wt% Kiln Dried Sand Craters

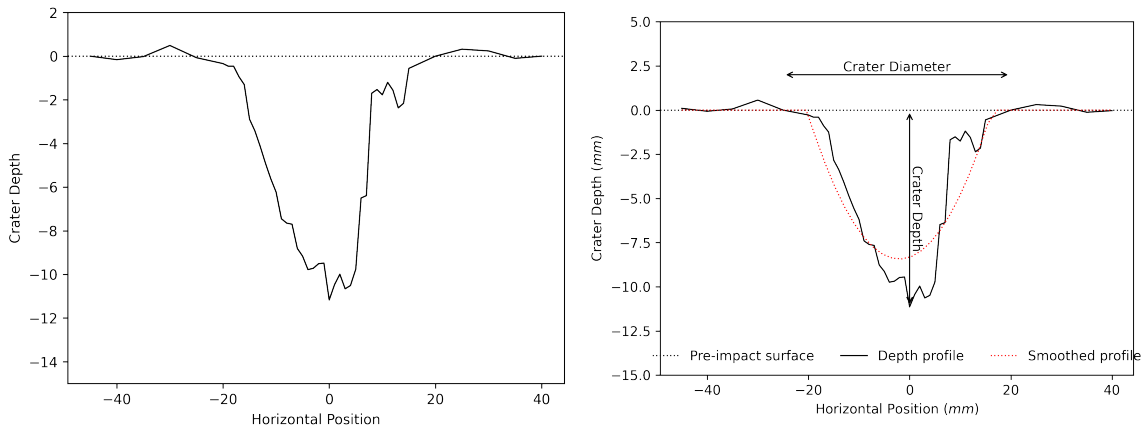

Figure A.1: Depth profiles taken across the crater formed during shot 1 (speed 2.22 km/s). The left column shows the raw profiles and the right column shows the corrected profiles and fitted parabolas for calculating volume.

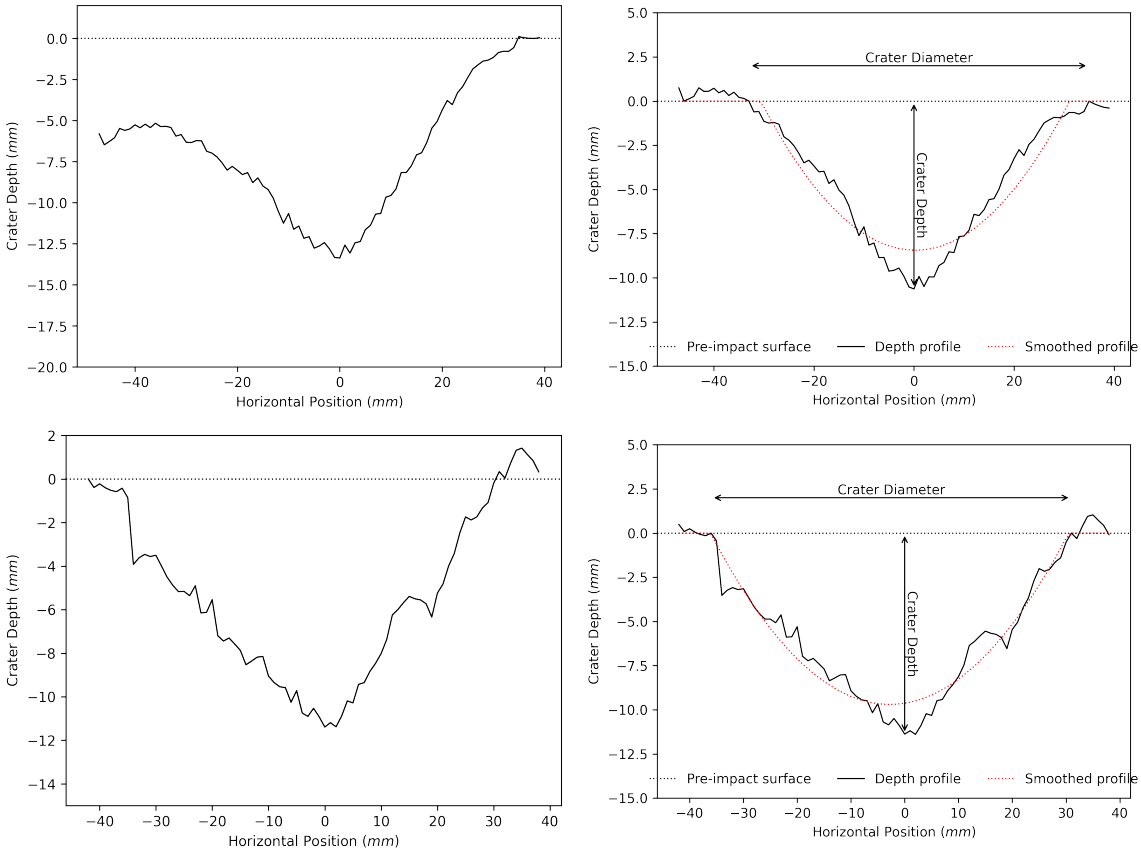

Figure A.2: Depth profiles taken across the crater formed during shot 2 (speed 2.97 km/s). The left column shows the raw profiles and the right column shows the corrected profiles and fitted parabolas for calculating volume.

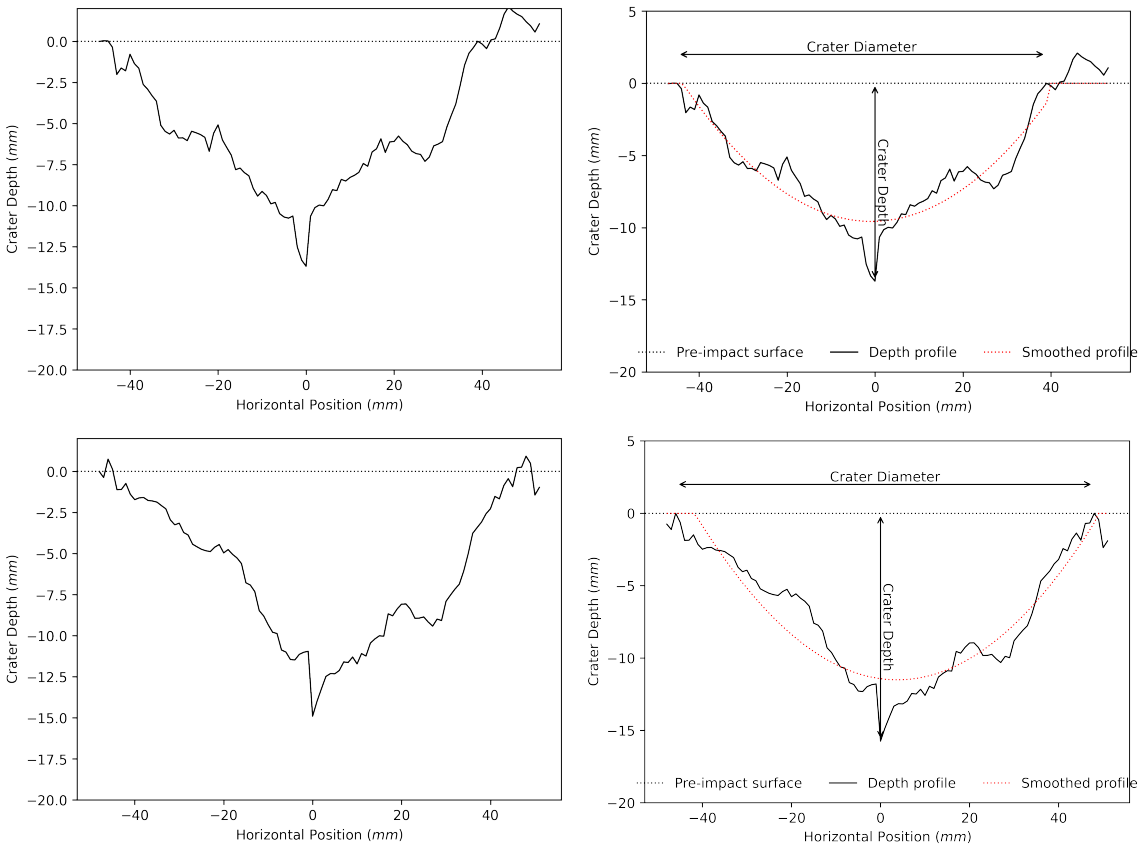

Figure A.3: Depth profiles taken across the crater formed during shot 3 (speed $4.12\ \mathrm{km/s}$). The left column shows the raw profiles and the right column shows the corrected profiles and fitted parabolas for calculating volume.

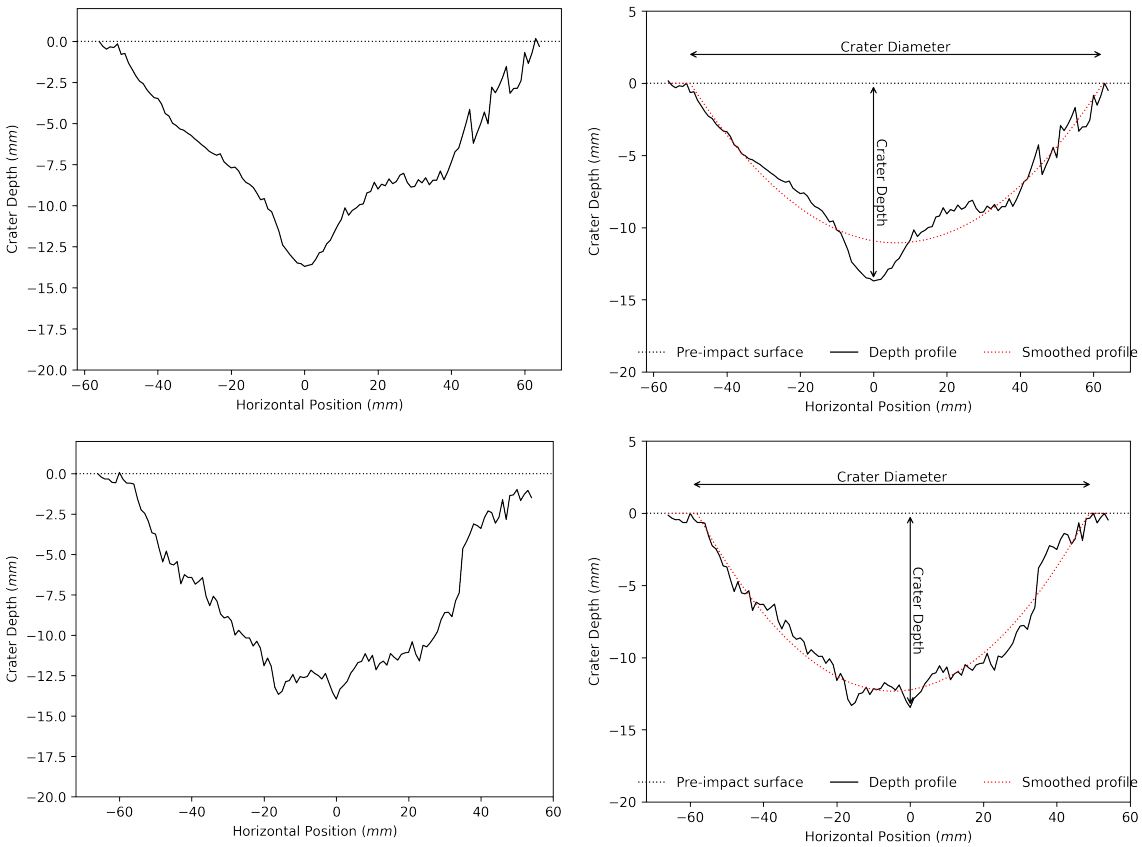

Figure A.4: Depth profiles taken across the crater formed during shot 4 (speed 4.74 km/s). The left column shows the raw profiles and the right column shows the corrected profiles and fitted parabolas for calculating volume.

A.2 50 wt% JSC Mars-1 Craters

A.2.1 Copper Projectiles

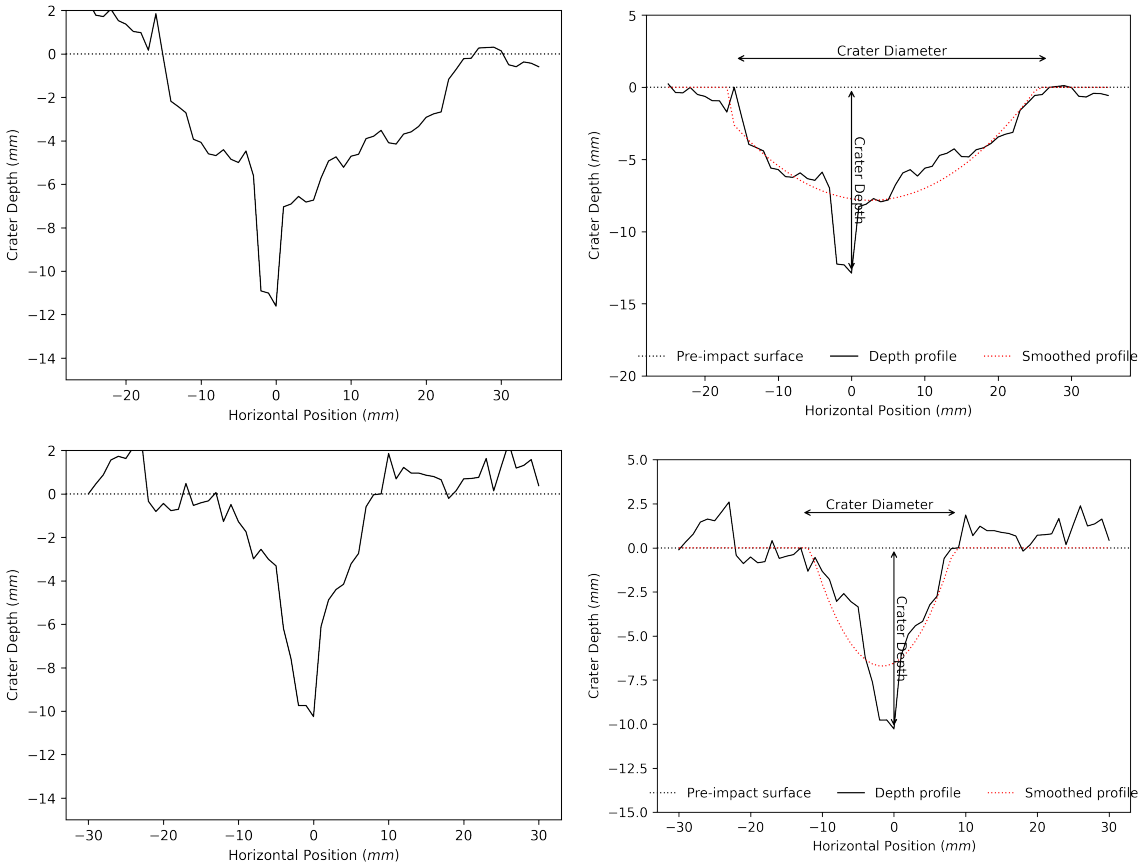

Figure A.5: Depth profiles taken across the crater formed during shot 5 (speed 1.98 km/s). The left column shows the raw profiles and the right column shows the corrected profiles and fitted parabolas for calculating volume.

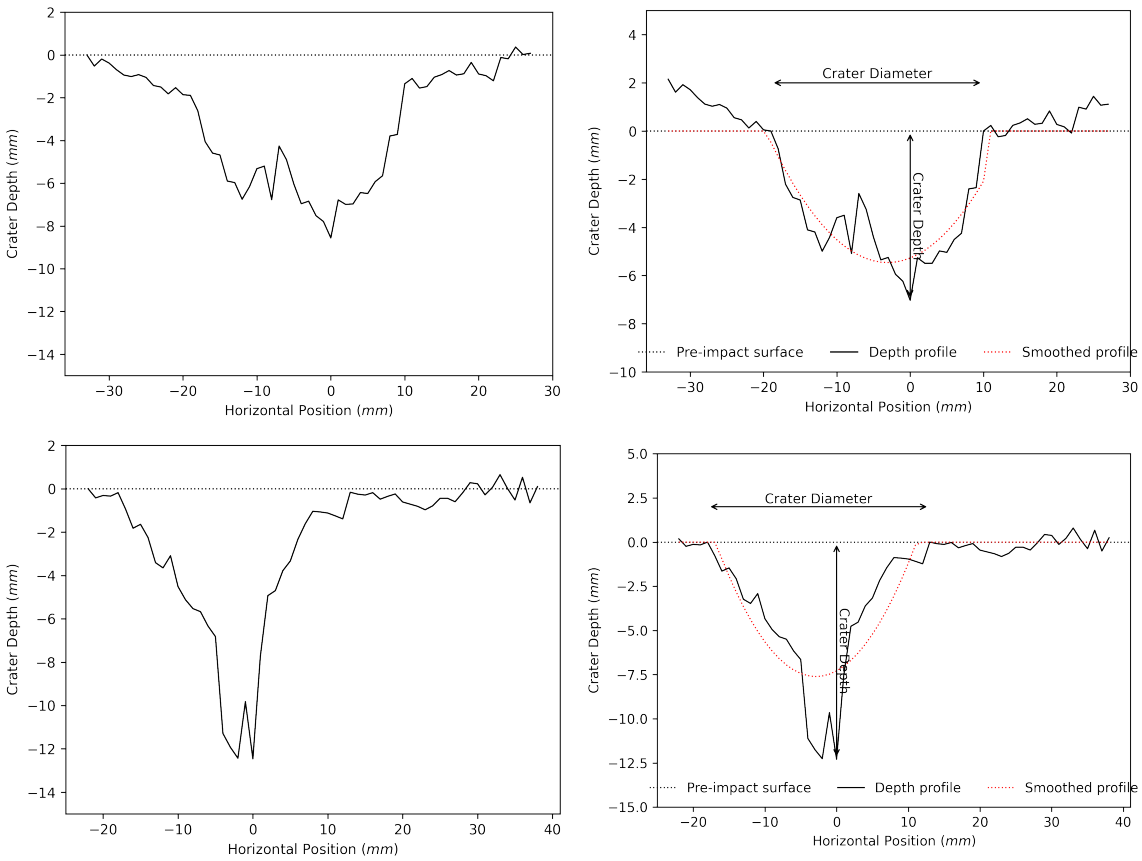

Figure A.6: Depth profiles taken across the crater formed during shot 6 (speed $2.13\ \mathrm{km/s}$). The left column shows the raw profiles and the right column shows the corrected profiles and fitted parabolas for calculating volume.

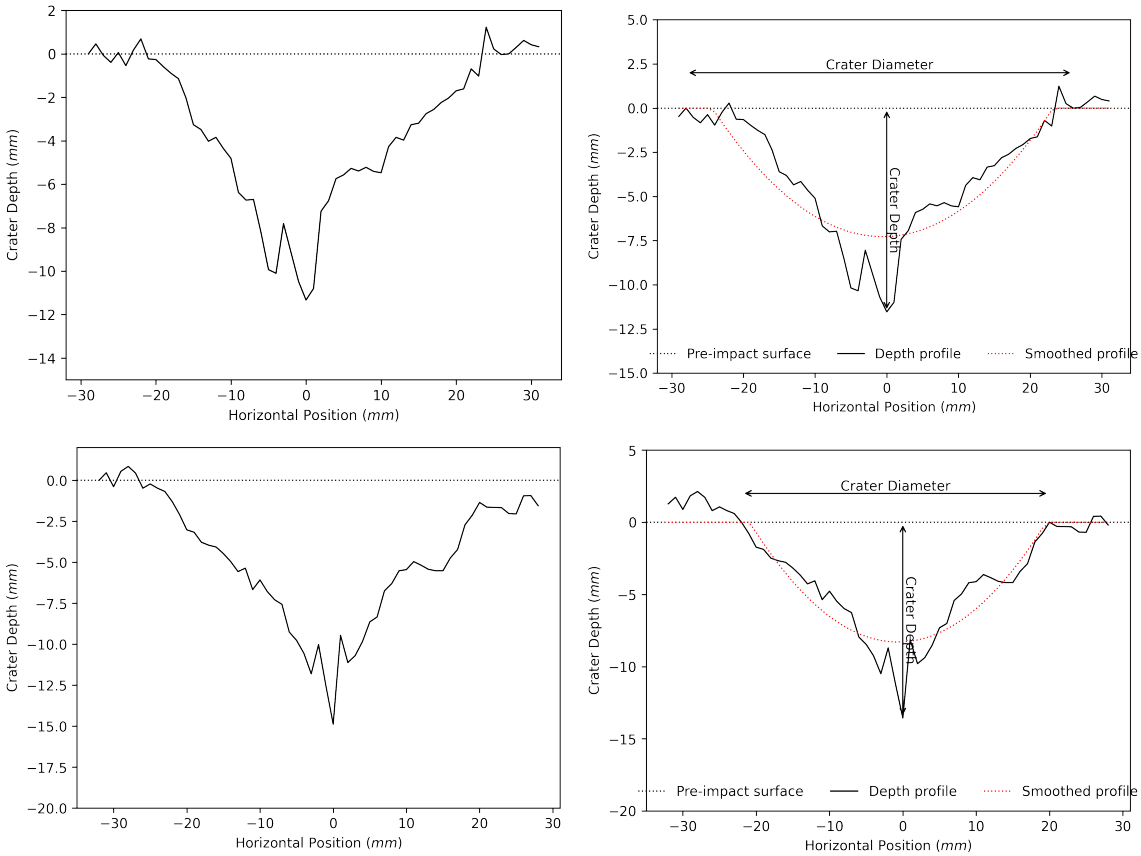

Figure A.7: Depth profiles taken across the crater formed during shot 7 (speed 3.32 km/s). The left column shows the raw profiles and the right column shows the corrected profiles and fitted parabolas for calculating volume.

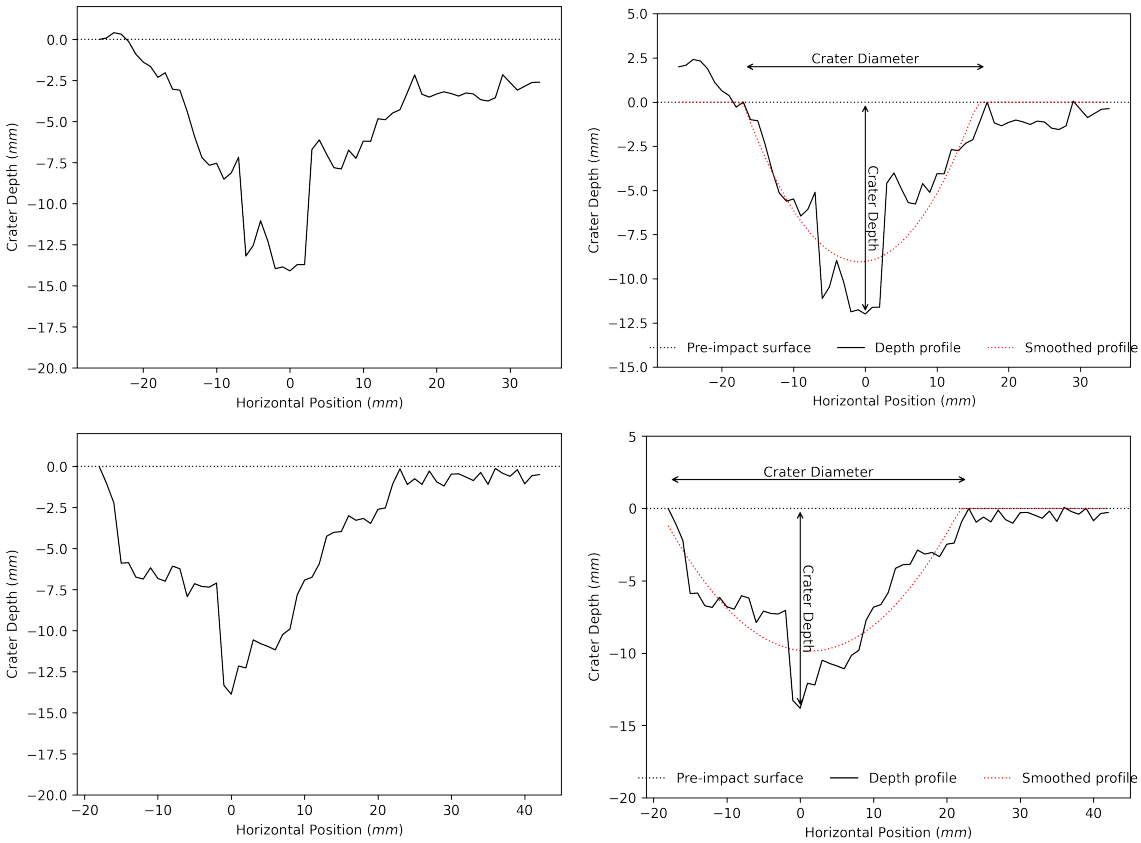

Figure A.8: Depth profiles taken across the crater formed during shot 8 (speed 3.67 km/s). The left column shows the raw profiles and the right column shows the corrected profiles and fitted parabolas for calculating volume.

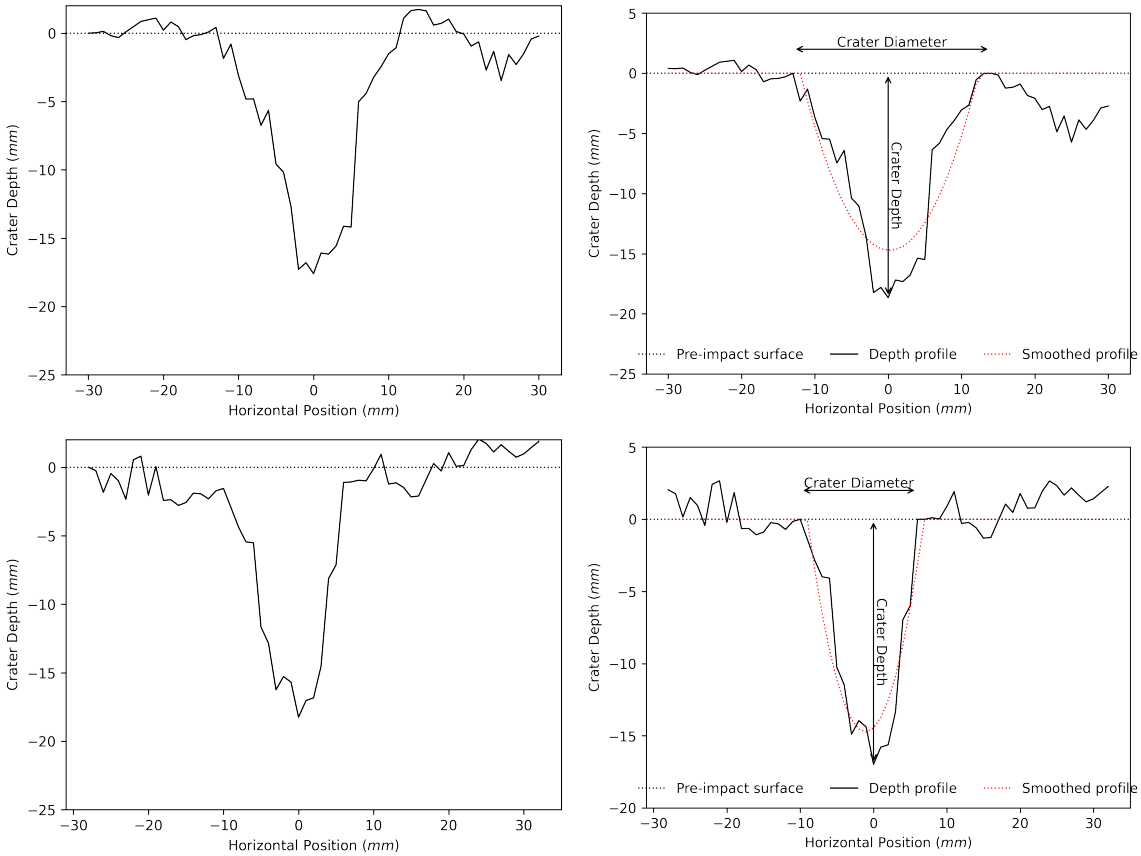

Figure A.9: Depth profiles taken across the crater formed during shot 9 (speed 4.30 km/s). The left column shows the raw profiles and the right column shows the corrected profiles and fitted parabolas for calculating volume.

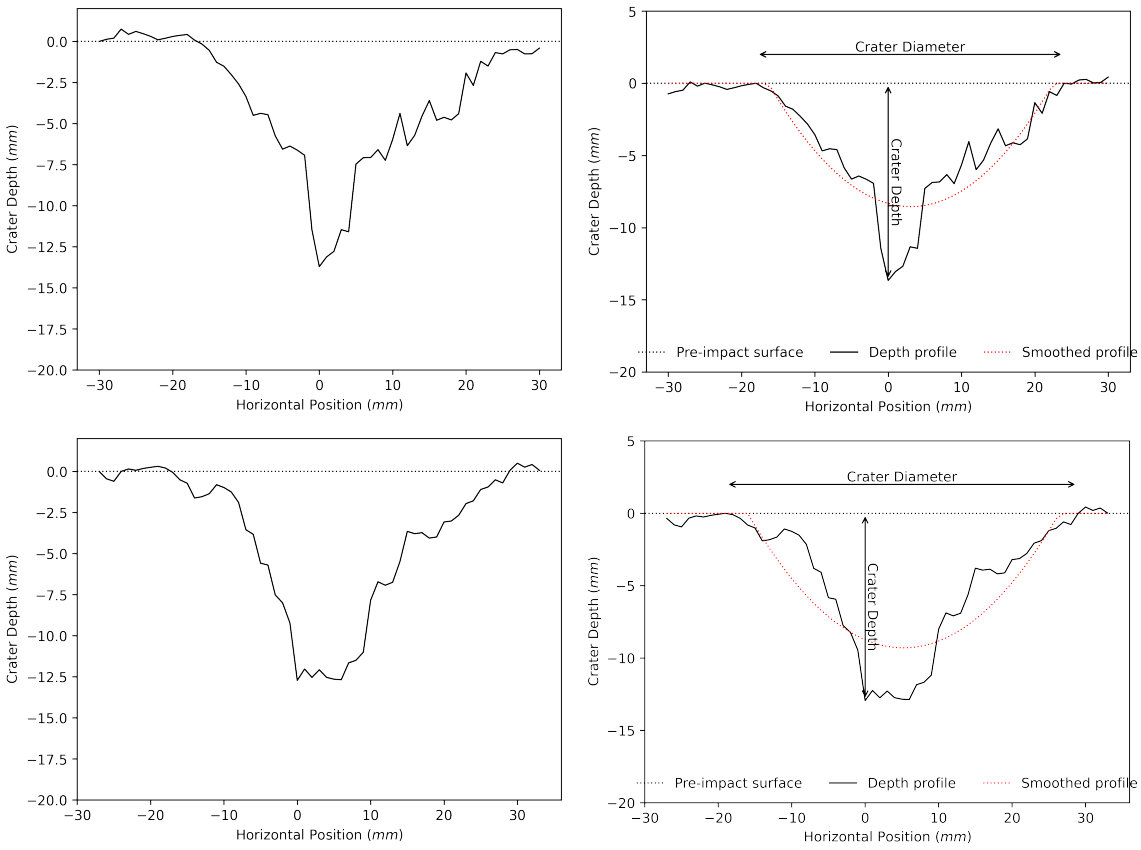

Figure A.10: Depth profiles taken across the crater formed during shot 10 (speed 4.47 km/s). The left column shows the raw profiles and the right column shows the corrected profiles and fitted parabolas for calculating volume.

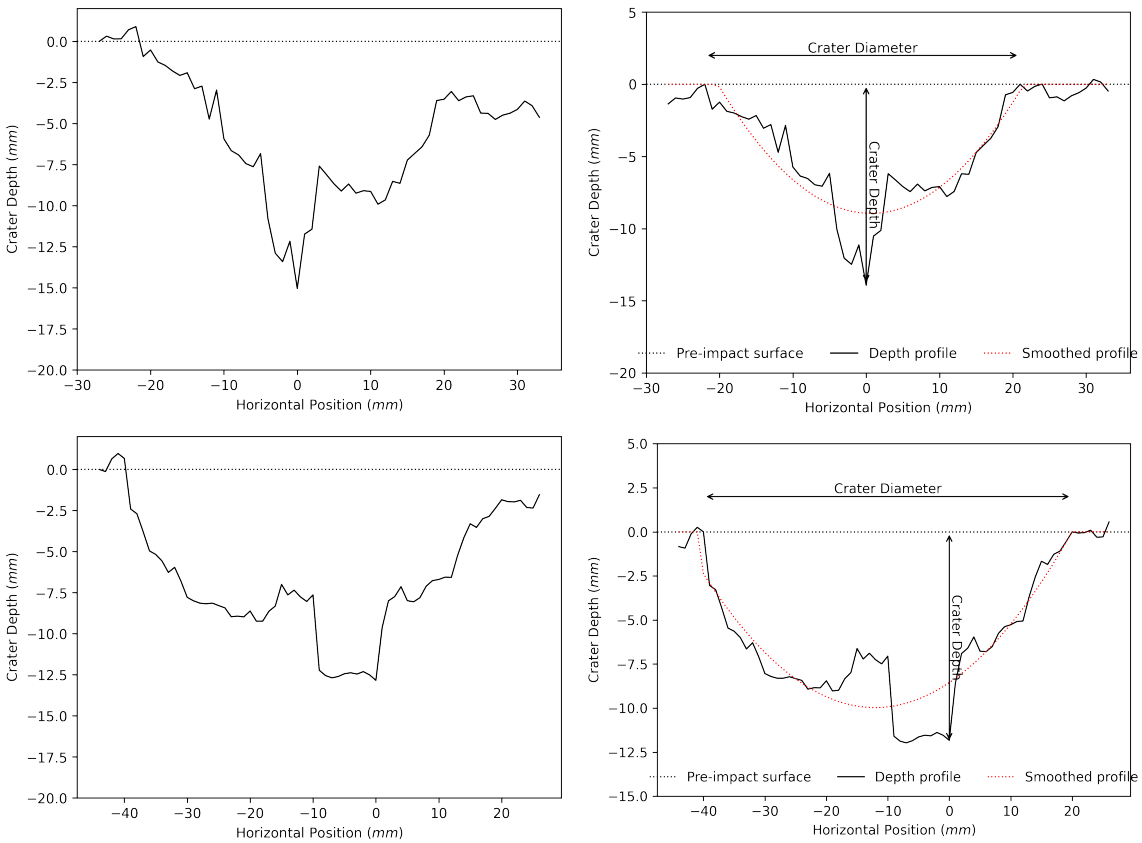

Figure A.11: Depth profiles taken across the crater formed during shot 11 (speed 4.60 km/s). The left column shows the raw profiles and the right column shows the corrected profiles and fitted parabolas for calculating volume.

A.2.2 Basalt Projectiles

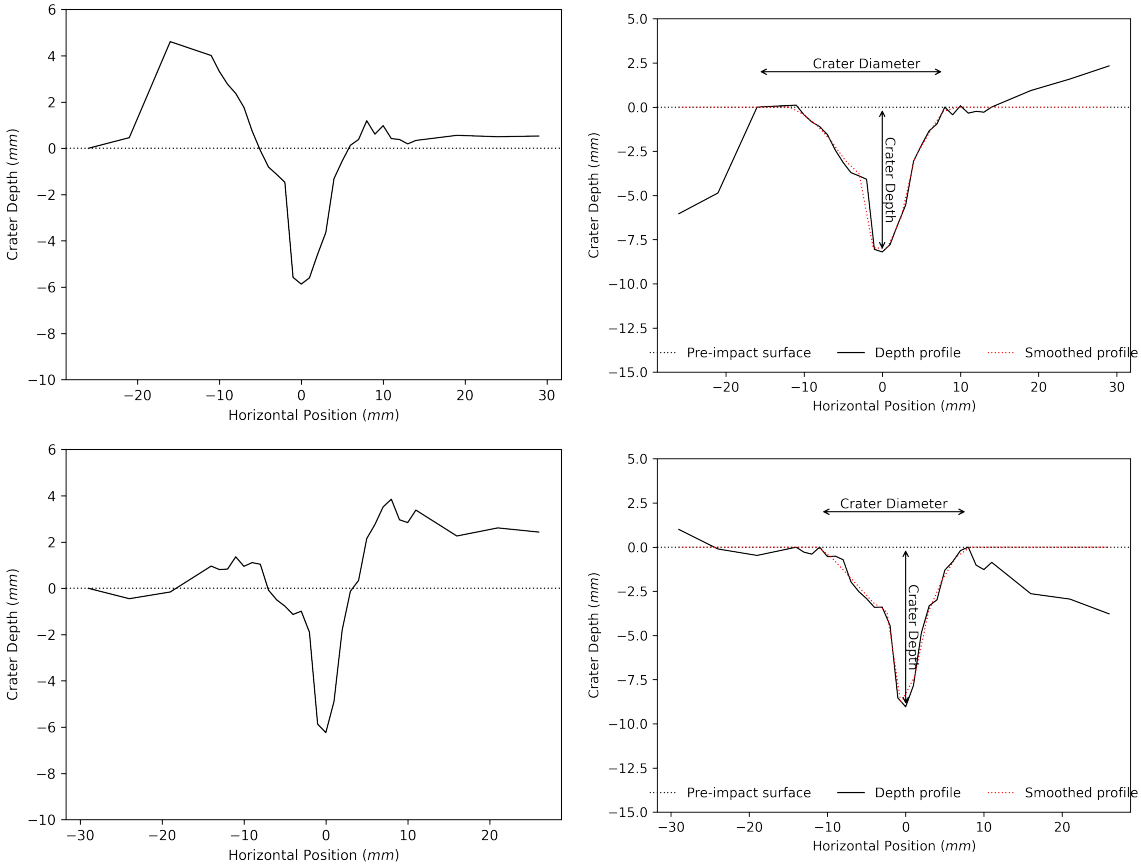

Figure A.12: Depth profiles taken across the crater formed during shot 12 (speed $1.83\ \mathrm{km/s}$). The left column shows the raw profiles and the right column shows the corrected profiles and fitted parabolas for calculating volume.

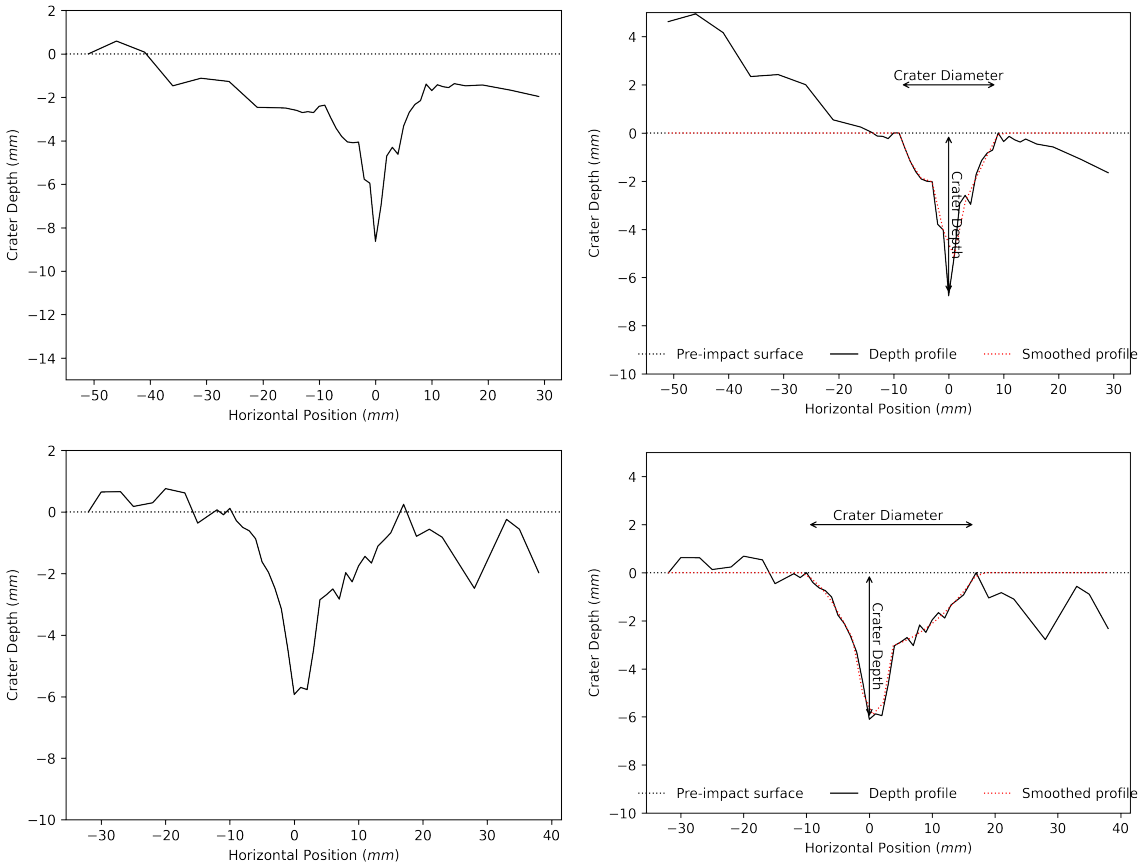

Figure A.13: Depth profiles taken across the crater formed during shot 13 (speed 2.11 km/s). The left column shows the raw profiles and the right column shows the corrected profiles and fitted parabolas for calculating volume.

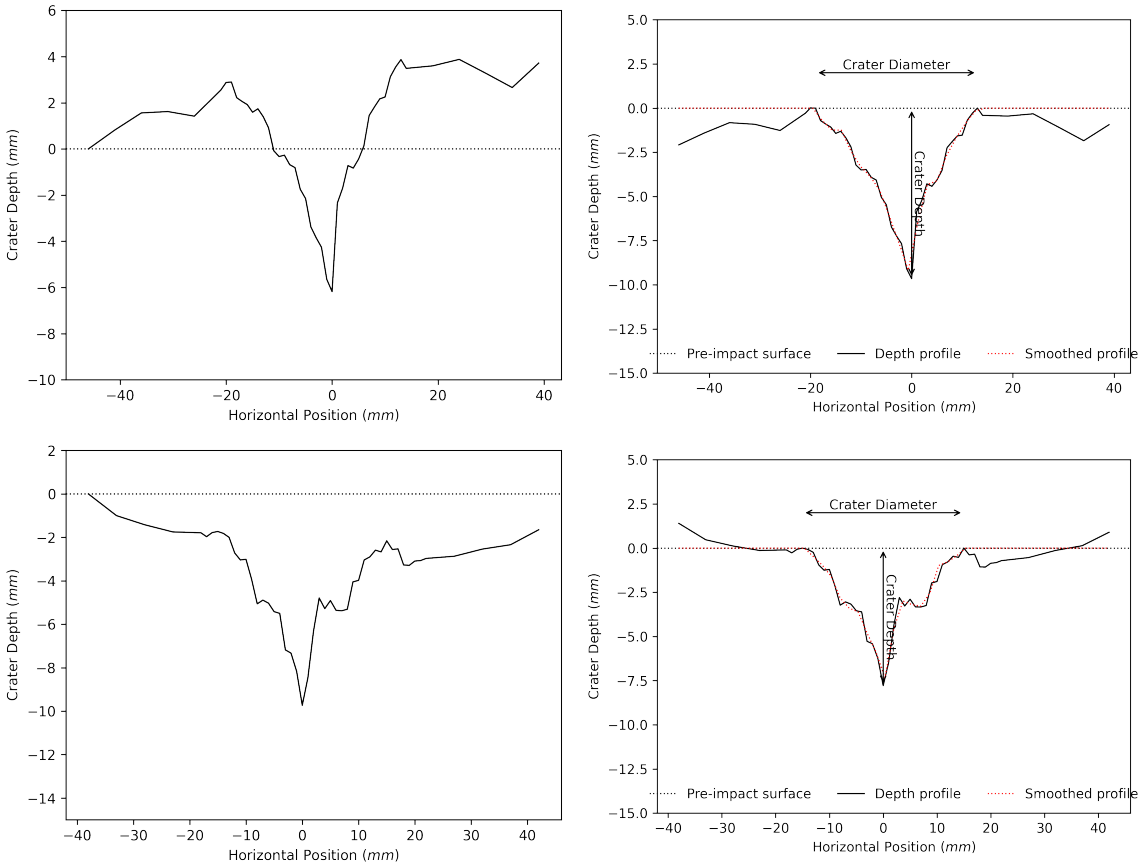

Figure A.14: Depth profiles taken across the crater formed during shot 14 (speed $3.25\ \mathrm{km/s}$). The left column shows the raw profiles and the right column shows the corrected profiles and fitted parabolas for calculating volume.

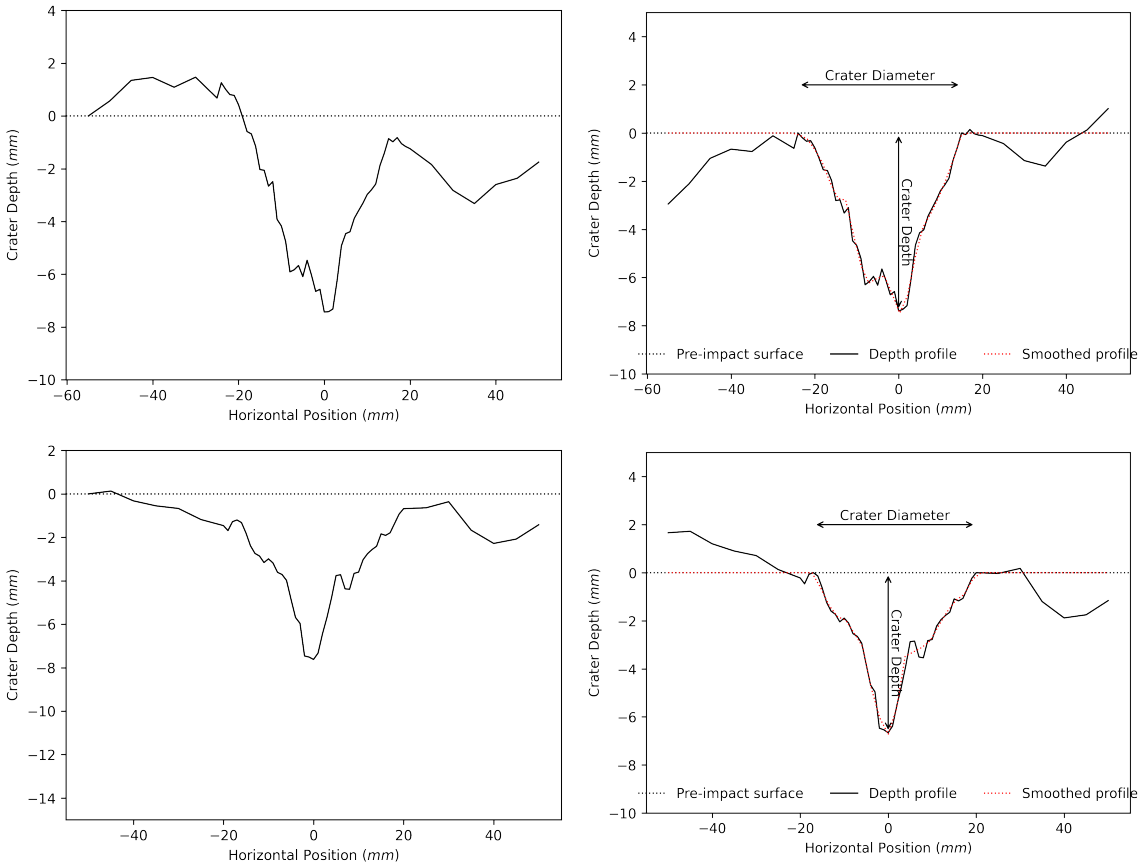

Figure A.15: Depth profiles taken across the crater formed during shot 15 (speed $3.53\ \mathrm{km/s}$). The left column shows the raw profiles and the right column shows the corrected profiles and fitted parabolas for calculating volume.

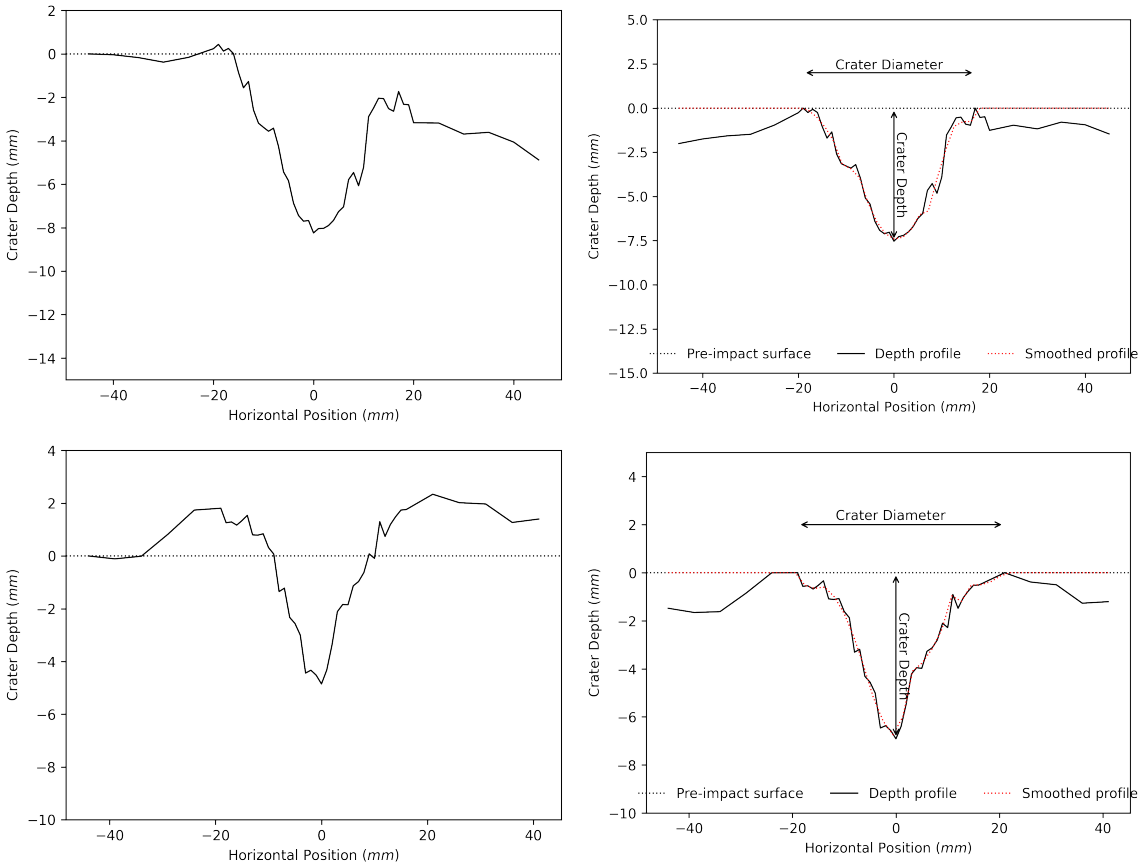

Figure A.16: Depth profiles taken across the crater formed during shot 16 (speed $3.67\ \mathrm{km/s}$). The left column shows the raw profiles and the right column shows the corrected profiles and fitted parabolas for calculating volume.

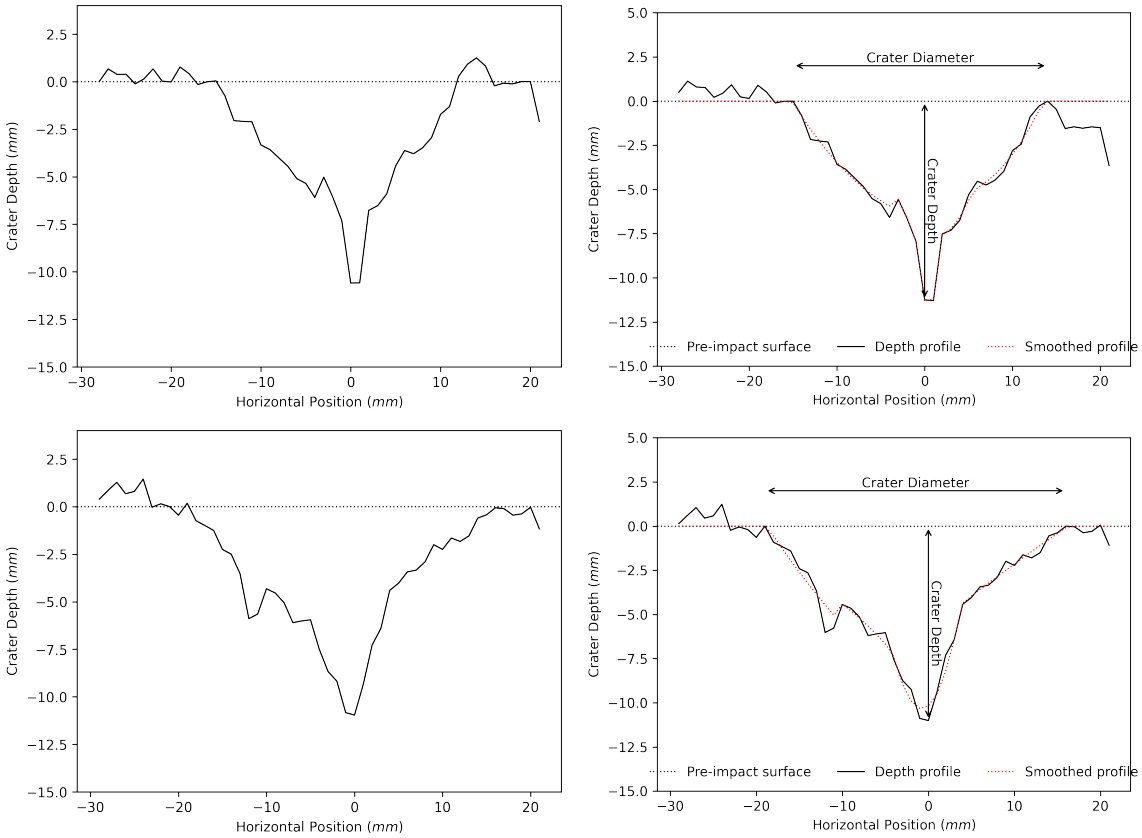

Figure A.17: Depth profiles taken across the crater formed during shot 17 (speed 4.89 km/s). The left column shows the raw profiles and the right column shows the corrected profiles and fitted parabolas for calculating volume.

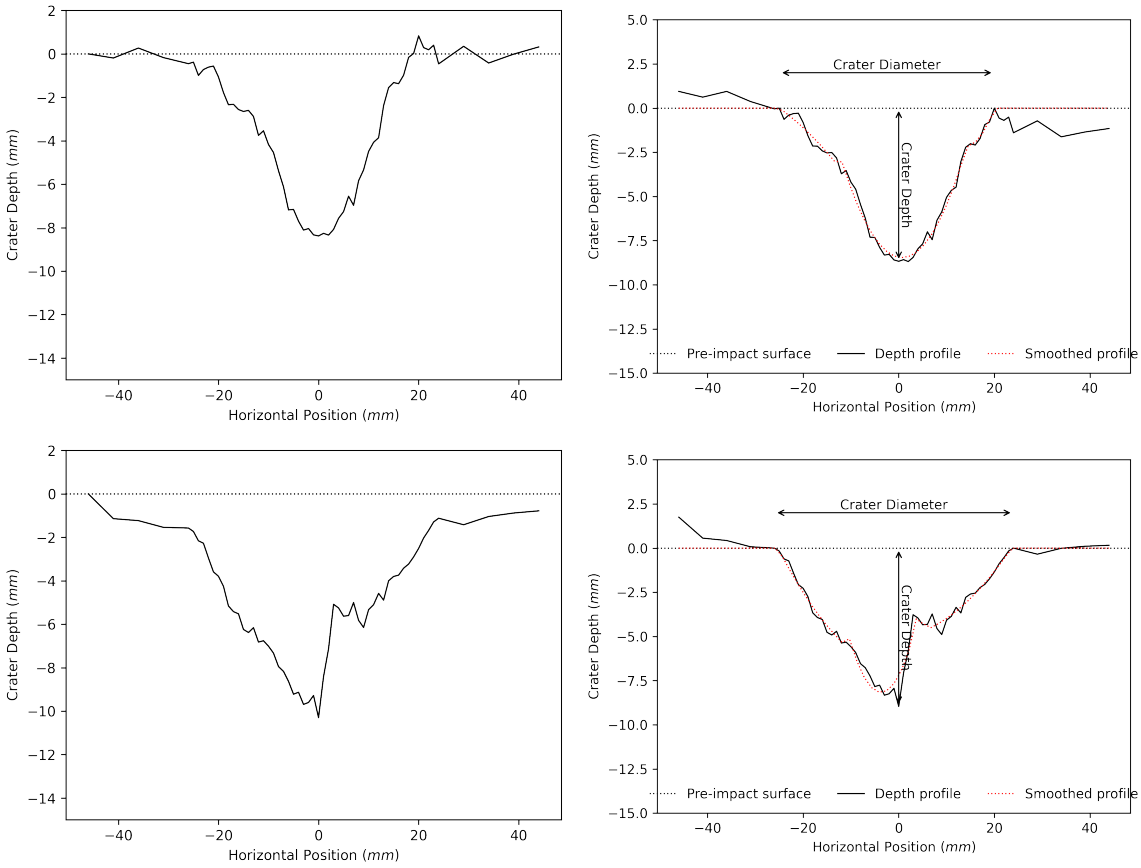

Figure A.18: Depth profiles taken across the crater formed during shot 18 (speed 4.97 km/s). The left column shows the raw profiles and the right column shows the corrected profiles and fitted parabolas for calculating volume.

A.3 80 wt% JSC Mars-1 Craters

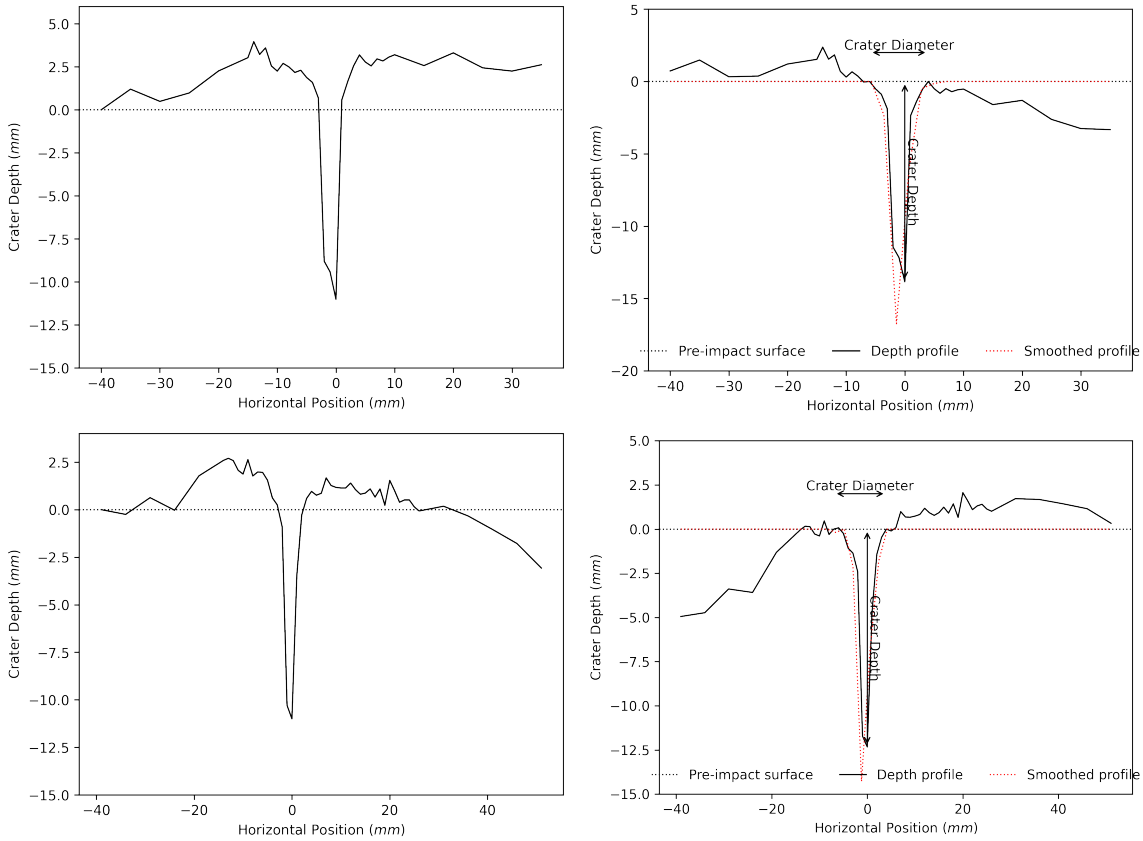

Figure A.19: Depth profiles taken across the crater formed during shot 19 (speed $0.95\ \mathrm{km/s}$). The left column shows the raw profiles and the right column shows the corrected profiles and fitted parabolas for calculating volume.

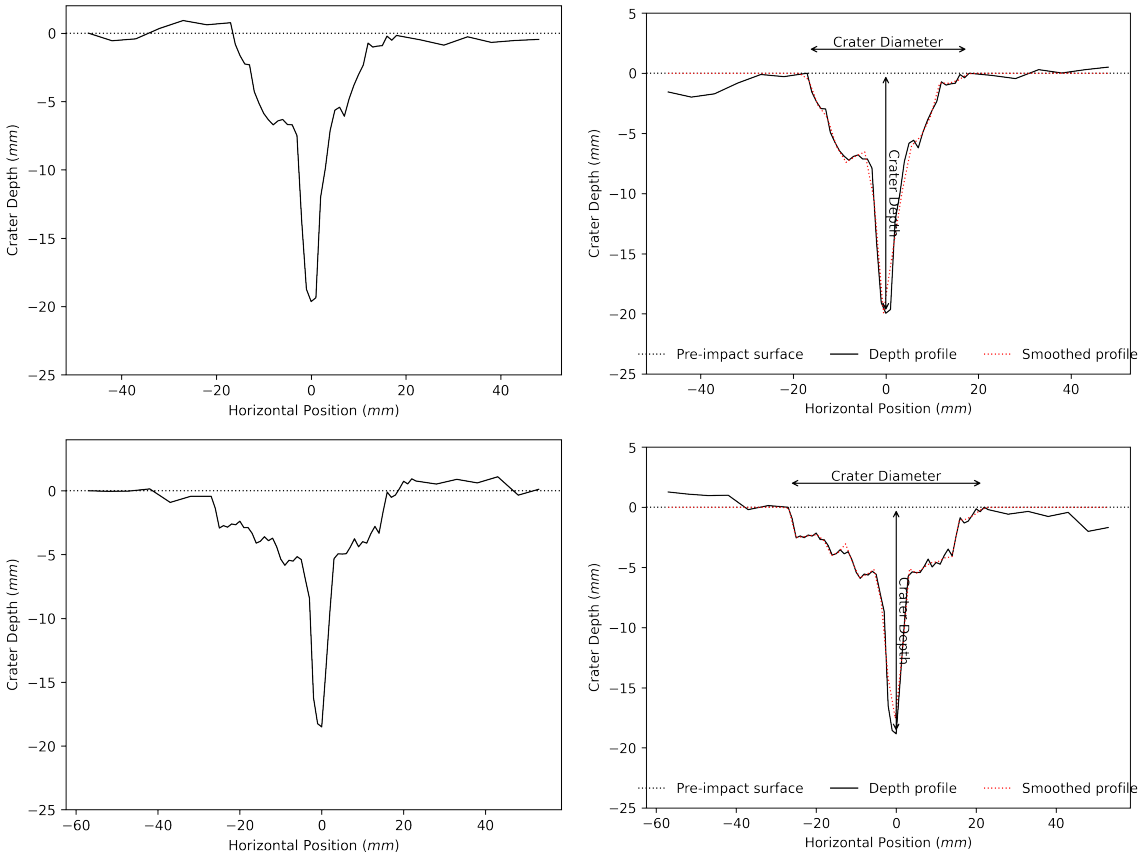

Figure A.20: Depth profiles taken across the crater formed during shot 20 (speed $1.80\ \mathrm{km/s}$). The left column shows the raw profiles and the right column shows the corrected profiles and fitted parabolas for calculating volume.

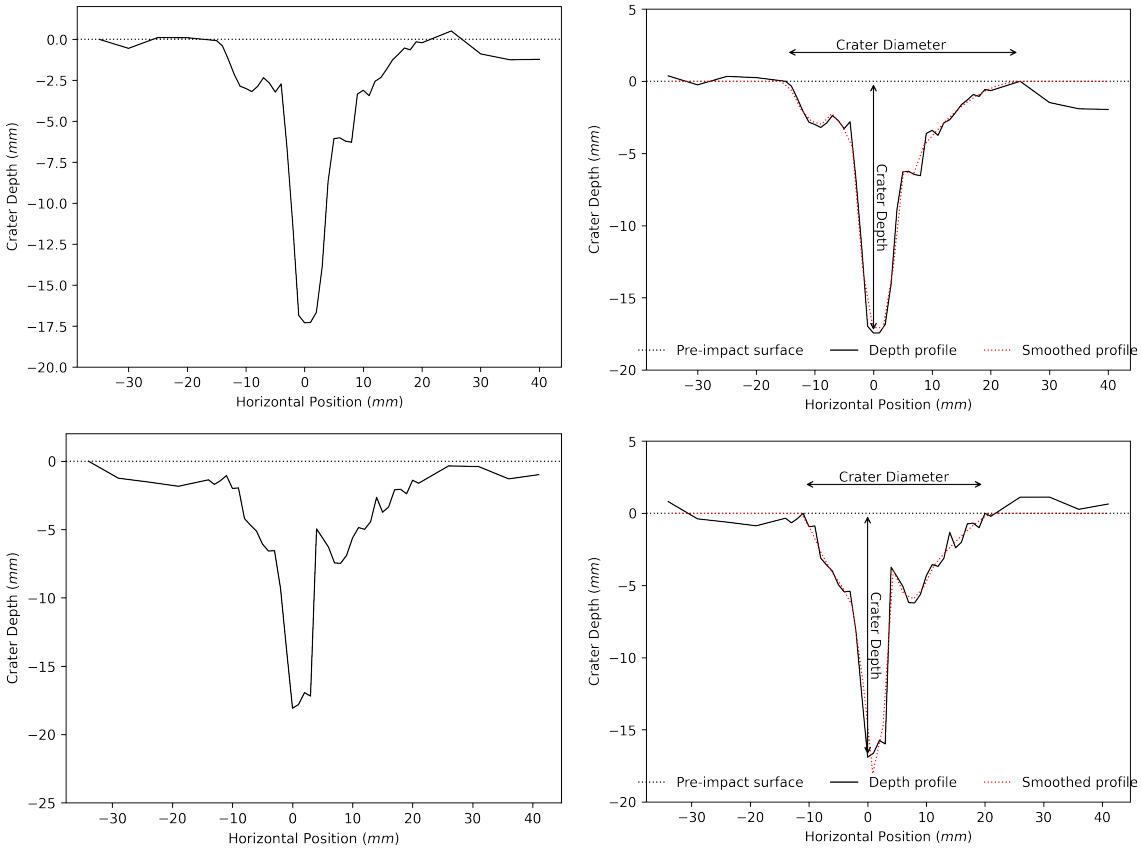

Figure A.21: Depth profiles taken across the crater formed during shot 21 (speed $2.04\ \mathrm{km/s}$). The left column shows the raw profiles and the right column shows the corrected profiles and fitted parabolas for calculating volume.

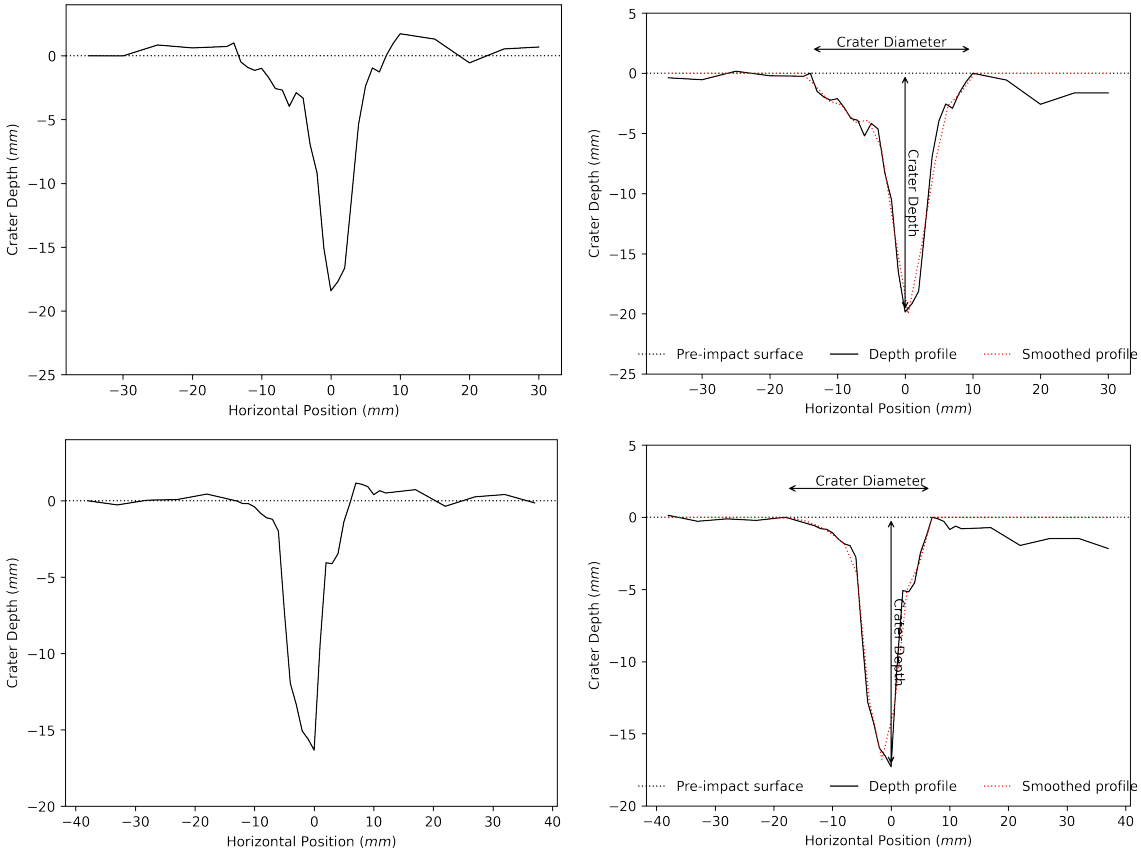

Figure A.22: Depth profiles taken across the crater formed during shot 22 (speed $2.46\ \mathrm{km/s}$). The left column shows the raw profiles and the right column shows the corrected profiles and fitted parabolas for calculating volume.

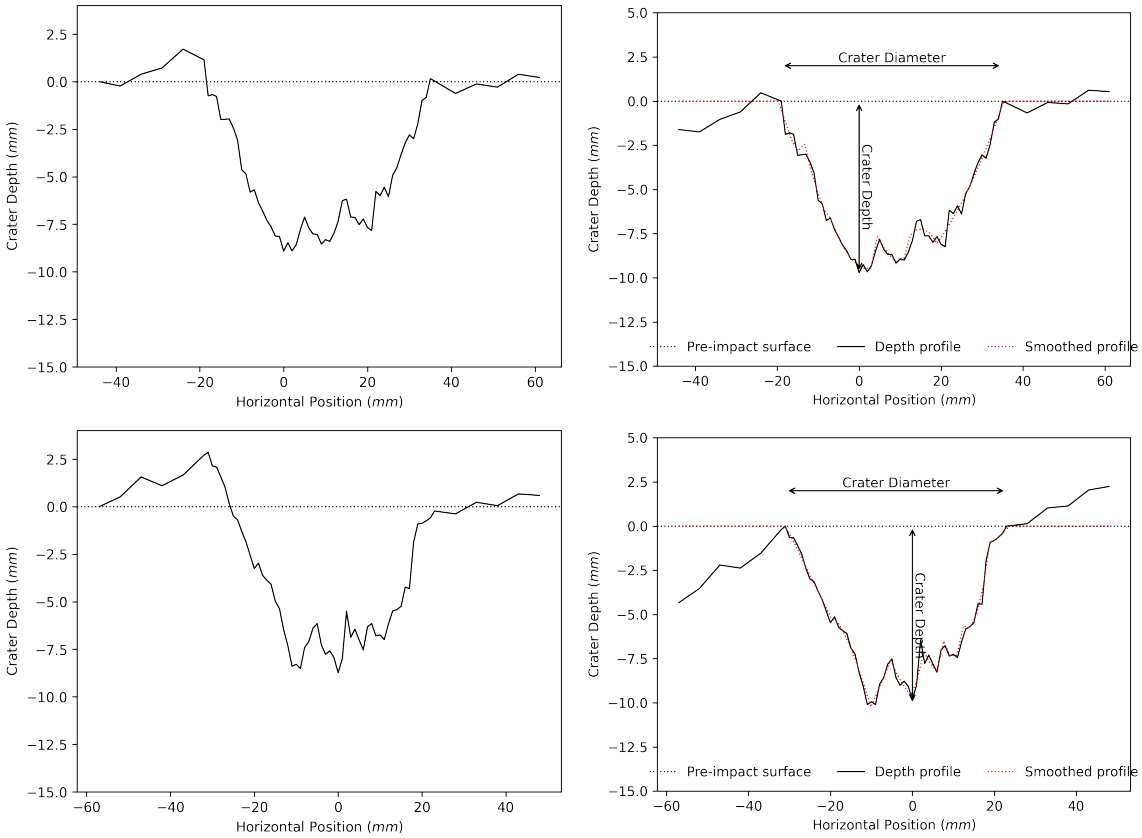

Figure A.23: Depth profiles taken across the crater formed during shot 23 (speed $2.89\ \mathrm{km/s}$). The left column shows the raw profiles and the right column shows the corrected profiles and fitted parabolas for calculating volume.

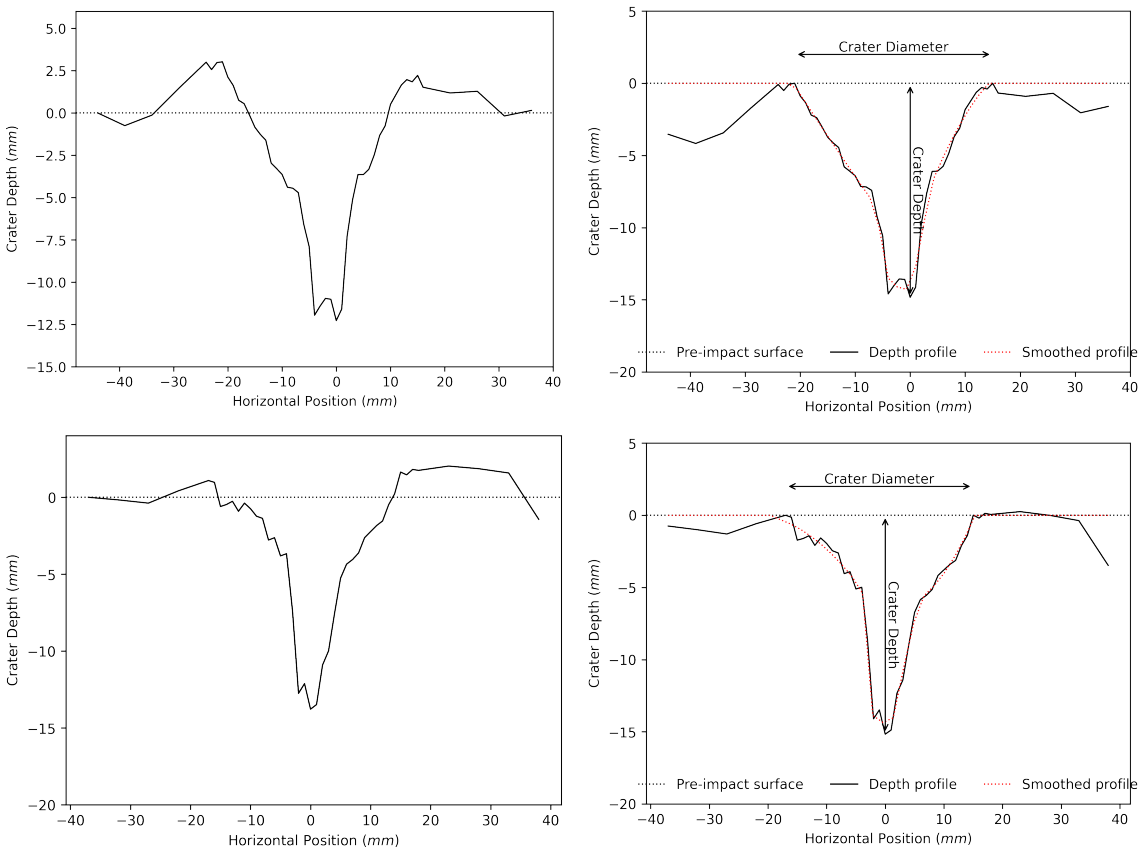

Figure A.24: Depth profiles taken across the crater formed during shot 24 (speed $3.72\ \mathrm{km/s}$). The left column shows the raw profiles and the right column shows the corrected profiles and fitted parabolas for calculating volume.

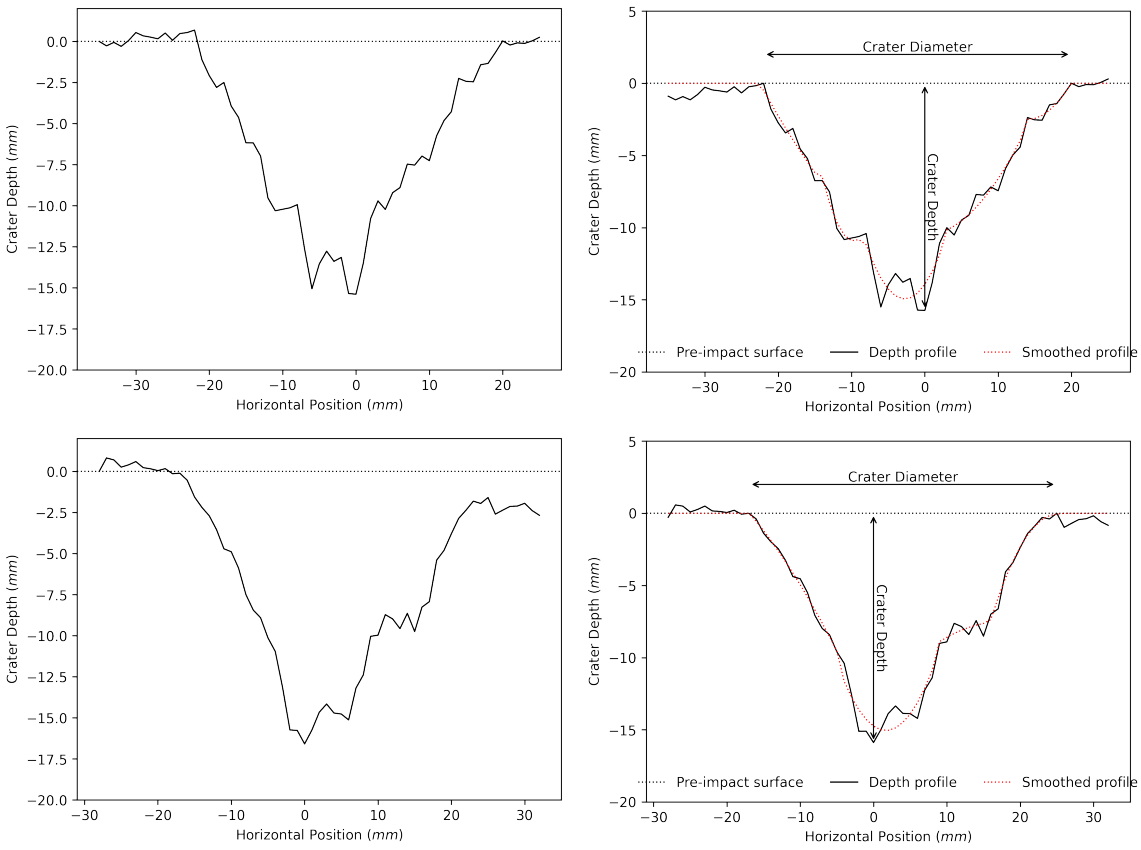

Figure A.25: Depth profiles taken across the crater formed during shot 25 (speed $3.86\ \mathrm{km/s}$). The left column shows the raw profiles and the right column shows the corrected profiles and fitted parabolas for calculating volume.

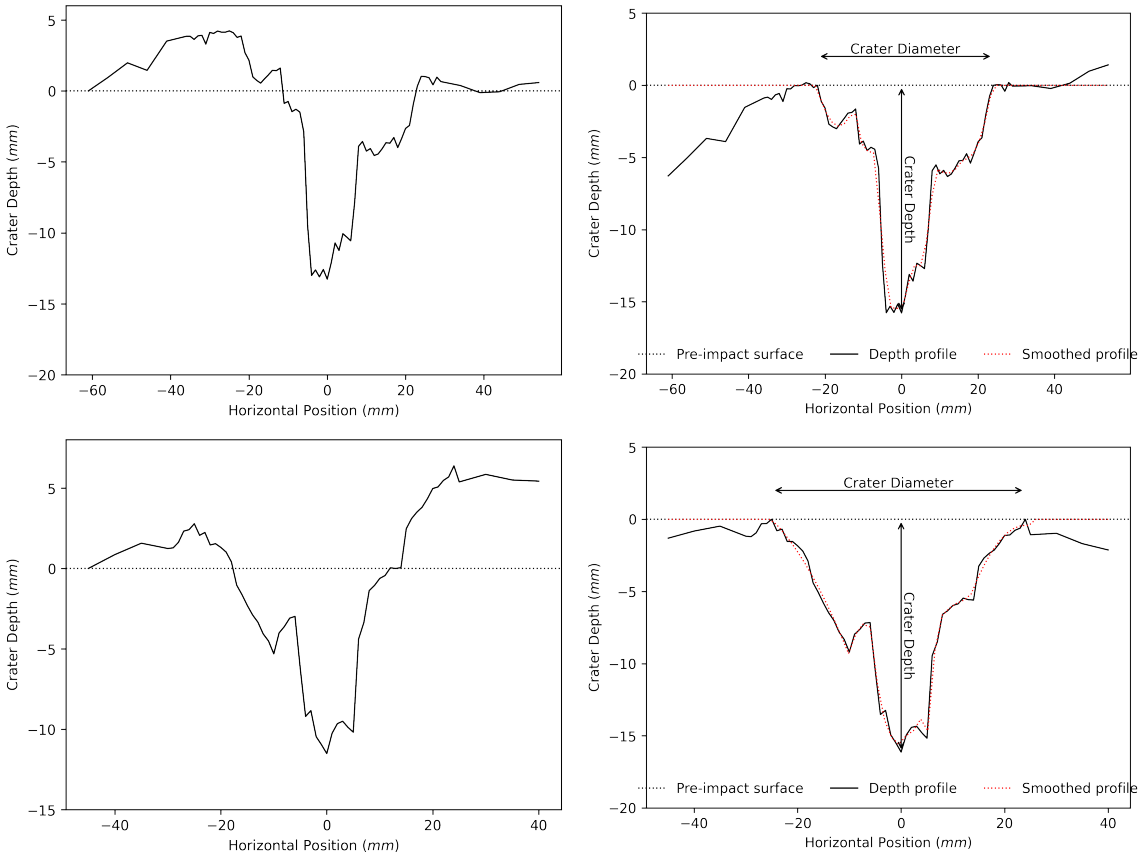

Figure A.26: Depth profiles taken across the crater formed during shot 26 (speed $4.95\ \mathrm{km/s}$). The left column shows the raw profiles and the right column shows the corrected profiles and fitted parabolas for calculating volume.